Politecnico di Torino

Master of Science in Civil Engineering

Master of Science Thesis

Characterization of fracture surfaces in brittle rocks

Supervisors:
Prof. Monica Barbero
Prof. Mauro Borri Brunetto
Eng. Lorenzo Milan

Candidate:
Alessandro Parziale

December 2023

Abstract

It is well known that the rock mass mechanical properties, both in terms of deformability and strength, are deeply influenced by the presence of discontinuities. Their characterization is of paramount importance in any engineering design of rock related projects. This thesis presents an experimental campaign aimed at investigating the geometrical and mechanical characteristics of fracture surfaces obtained by tensile splitting. Four different rocks have been considered: Balma Syenite, Absolute Black Gabbro, Pink Porriño Granite and Carrara marble.

Prismatic samples have been tested for determining the deformability properties, by means of unconfined compression tests. Then, for each sample a tensile fracture has been induced by means of Brasilian-like tests. Ultrasonic tests have been performed on both intact and fractured specimens to evaluate the influence of the presence of the fracture on the propagation of the sonic waves.

The geometrical characteristics of the induced fractures have been investigated by analyzing the roughness of a number of orthogonal profiles. Several mathematical methods have been used to quantify the roughness of the profiles. The results have been used to compare the estimation of the Joint Roughness Coefficient given by several empirical laws found in the literature. Moreover, tilt tests have been performed to evaluate the base friction angle of the different rock types.

With the aim to assess the effect of the fracture process on the mineral distribution on the exposed faces, saw cut surfaces and rough fractures have been analyzed by processing their photographs.

Contents

1 Introduction **25**
- 1.1 Reasons and objectives of the thesis . . . 25
- 1.2 Structure of the thesis . . . 27

2 Rock discontinuities **29**
- 2.1 Definition and typology . . . 29
- 2.2 Characterization of discontinuities . . . 29
- 2.3 Mechanical behavior of the discontinuities . . . 38
  - 2.3.1 Shear strength . . . 38
  - 2.3.2 Deformability . . . 42
- 2.4 Roughness parameters . . . 43
  - 2.4.1 Root–mean square of slopes: Z_2 . . . 43
  - 2.4.2 Roughness profile index: R_p . . . 44
  - 2.4.3 Structure function of the profile: SF . . . 45
  - 2.4.4 Fractal dimension: D . . . 45
- 2.5 Ultrasonic test on rock . . . 46
  - 2.5.1 Wave propagation . . . 46
  - 2.5.2 Beam spread . . . 46
  - 2.5.3 Interference . . . 47
  - 2.5.4 Absorption and scattering . . . 47
  - 2.5.5 Elastic constants . . . 48

3 Experimental campaign **49**
- 3.1 Rock lithotypes . . . 49
  - 3.1.1 Syenite . . . 49
  - 3.1.2 Absolute Black granite . . . 49
  - 3.1.3 Pink Porriño granite . . . 50
  - 3.1.4 Carrara marble . . . 51
  - 3.1.5 QAPF diagram . . . 51
- 3.2 Ultrasonic tests on intact rock specimens . . . 53
  - 3.2.1 Test procedure . . . 53
  - 3.2.2 Test results . . . 55
- 3.3 Unconfined compression tests . . . 58
  - 3.3.1 Test procedure . . . 58
  - 3.3.2 Test results . . . 63
  - 3.3.3 Evaluation of the deformability parameters . . . 66
- 3.4 Splitting tests . . . 68
  - 3.4.1 Test procedure . . . 68
  - 3.4.2 Test results . . . 70
- 3.5 Ultrasonic tests on fractured rock specimens . . . 71
  - 3.5.1 Test procedure . . . 71

3.5.2 Test results . . . 73
3.6 Tilt test . . . 76
3.6.1 Test procedure . . . 76
3.6.2 Test results . . . 79
3.7 Discussion of the results . . . 80

4 Analysis of fracture surfaces **83**
4.1 Method and procedure . . . 83
4.2 Results . . . 87
4.2.1 Roughness parameters . . . 87
4.2.2 JRC estimation from roughness parameters . . . 92
4.2.3 JRC estimation from qualitative comparison with standard profiles . . . 97
4.3 Discussion of the results . . . 98

5 Image analysis of surfaces **101**
5.1 Image acquisition procedure . . . 101
5.2 Mineralogical composition: results . . . 103
5.3 Mismatching of the two faces of the fracture: results . . . 108
5.4 Discussion of the results . . . 109

6 Conclusion **111**

A Ultrasonic tests on intact rock specimens **115**

B Unconfined compression tests **135**

C Ultrasonic tests on fractured rock specimens **143**

D Mineralogical composition **155**

List of Figures

1.1 Comparison between lab and in situ scale . . . 25
1.2 Modes of failure in rock slopes. (a) planar sliding; (b) wedge sliding; (c) slumping; (d) toppling. [2] . . . 26
1.3 Transition from non-violent spalling (a) to bursting through buckling (b), interaction with structure (c) and dilational yield (d) [3]. . . . 26

2.1 (a) Joints in a rock mass. Source: `https://tinyurl.com/4d6aswzj`; (b) Bedding planes in a rock mass. Source: `https://tinyurl.com/2u4utdwc`; (c) Schistosity in a rock mass. Source: `https://tinyurl.com/3rxvp8jz`; (d) Fault in a Sandstone deposit. Source: `https://tinyurl.com/ywajyaah`. . . . 30
2.2 Orientation of a plane in the space given by dip and dip direction [7]. . . . 31
2.3 Spacing measurement of parallel discontinuities [7]. . . . 32
2.4 Persistence measurement of parallel discontinuities [7]. . . . 32
2.5 Definition of large–scale roughness (waviness) and small–scale roughness (unevenness) of rock discontinuities [8]. . . . 33
2.6 Barton profilometer. . . . 33
2.7 Standard roughness profiles and corresponding range of JRC [9]. . . . 34
2.8 Correlation chart for Schmidt hammer test - ISRM (1978) [7]. . . . 35
2.9 Aperture of an open discontinuity - ISRM (1978) [7]. . . . 35
2.10 Filled discontinuity - ISRM (1978) [7]. . . . 36
2.11 Examples of block shape - ISRM (1978) [7]. . . . 37
2.12 Transition from intact to heavily jointed rock mass with increasing scale of the problem [10]. . . . 38
2.13 Shear strength of a rock specimen as function of normal stress. (a) intact rock; (b) smooth joint; (c) rough joint with a roughness angle of i, assuming $\phi_b = \phi_j$ [12]. . . . 39
2.14 Shear stress vs shear displacement for a certain normal stress obtained through direct shear test on the same material with rough and smooth joints [13]. . . . 39
2.15 Patton saw-tooth model [11]. . . . 40
2.16 Comparison between Barton criterion and Mohr-Coulomb criterion [14]. . . . 41
2.17 Stress-strain typical response of in-situ rock mass [6]. . . . 42
2.18 Typical stress-relative displacement relationship: (a) σ_n vs u_n; (b) τ vs u_s [6]. . . . 43
2.19 One of the sources of error using a profilometer to acquire a roughness profile (a): profilometer applied on a rough surface; (b): zoomed-in view of the pins, unable to capture the real profile features [8]. . . . 44
2.20 Three roughness profiles with the same mean inclination angle [17]. . . . 44
2.21 P-waves and S-waves propagation inside a medium. Source: `https://tinyurl.com/35xbjv79` . . . 46
2.22 beam spread phenomenon in ultrasonic wave propagation [21] . . . 47

3.1 Syenite texture. Scale in millimeters. . . . 49
3.2 Absolute Black texture. Scale in millimeters. . . . 50

3.3 Porriño texture. Scale in millimeters. 50
3.4 Carrara texture. Scale in millimeters. 51
3.5 QAPF diagram. Red: Syenite family; Blue: Gabbro family; Green: Granite family. 52
3.6 Ultrasonic testing instrument Pundit PL-200. 53
3.7 (a): P-wave Proceq transducer; (b): S-wave transducer Parametrics-NDT V151. . 54
3.8 (a): Setup for P-waves velocity measurement on Pink Porriño sample; (b): Setup for S-waves velocity measurement on Absolute Black sample. 54
3.9 Definition of the directions of propagation in the sample and local reference system. 54
3.10 (a): Scheme of wave transmission in direction "a" of the rock sample; (b): Scheme of wave transmission in direction "b" and "c" of the rock sample. 54
3.11 Recorded signal of P-waves in direction "a" for Absolute Black sample 1. 55
3.12 Recorded signal of P-waves in direction "b" for Absolute Black sample 1. 55
3.13 Recorded signal of P-waves in direction "c" for Absolute Black sample 1. 55
3.14 Recorded signal on vibration plane "x" of S-waves in direction "a" for Absolute Black sample 1. 56
3.15 Recorded signal on vibration plane "z" of S-waves in direction "a" for Absolute Black sample 1. 56
3.16 Recorded signal on vibration plane "z" of S-waves in direction "b" for Absolute Black sample 1. 56
3.17 Recorded signal on vibration plane "z" of S-waves in direction "c" for Absolute Black sample 1. 57
3.18 Surface grinding process on the contact surfaces - Porriño granite sample. 58
3.19 Displacement measuring devices size [24]. 59
3.20 LVDT HBM DD1 2.5 mm transducer for axial displacements. 59
3.21 LVDT HBM WI/2mm-T transducer for radial displacements. 60
3.22 HBM MX840B measuring amplifier module. 60
3.23 instrumented sample of Syenite. 61
3.24 force vs time of a typical test. F_{50} : force corresponding to a stress equal to the 50% of the UCS; F_{70} : force corresponding to a stress equal to the 70% of the UCS. 62
3.25 Complete setup for compression test - Syenite specimen. 62
3.26 Syenite sample 1. blue: force vs time; red: radial strain vs time. 63
3.27 Syenite sample 1. blue: stress vs axial strain; red: stress vs radial strain. 63
3.28 Absolute Black sample 1. blue: force vs time; red: radial strain vs time. 64
3.29 Absolute Black sample 1. blue: stress vs axial strain; red: stress vs radial strain. 64
3.30 Porriño sample 1. blue: force vs time; red: radial strain vs time. 64
3.31 Porriño sample 1. blue: stress vs axial strain; red: stress vs radial strain. 65
3.32 Carrara sample 1. blue: force vs time; red: radial strain vs time. 65
3.33 Carrara sample 1. blue: stress vs axial strain; red: stress vs radial strain. 65
3.34 Syenite samples. blue: Young's modulus vs number of points in the fit interval; red: Poisson's ratio vs number of points in the fit interval. 66
3.35 Absolute Black samples. blue: Young's modulus vs number of points in the fit interval; red: Poisson's ratio vs number of points in the fit interval. 66
3.36 Porriño samples. blue: Young's modulus vs number of points in the fit interval; red: Poisson's ratio vs number of points in the fit interval. 67
3.37 Carrara samples. blue: Young's modulus vs number of points in the fit interval; red: Poisson's ratio vs number of points in the fit interval. 67
3.38 Crack modes in fracture mechanics [27]. 68
3.39 Specimen setup of the splitting test. 68
3.40 ZwickRoell mechanical press used for splitting test. 69
3.41 Final setup under the loading machine used to perform the splitting test. 69
3.42 Cracked sample of Syenite. 70

3.43 Schematic wave transmission in direction “a” at the crack interface of the sample. 71
3.44 load test on rubber bands. 72
3.45 load-elongation experimental curve and polynomial approximation curve. 72
3.46 (a): Setup of P-waves velocity measurement on Carrara fractured sample (flat surfaces); (b): Setup of S-waves velocity measurement on Porriño fractured sample (rough surfaces). 73
3.47 Recorded signal of P-waves in direction “a” for Absolute Black sample 1 (rough surfaces). 73
3.48 Recorded signal of P-waves in direction “b” for Absolute Black sample 1 (flat surfaces). 74
3.49 Recorded signal on vibration plane “x” of S-waves in direction “a” for Absolute Black sample 1 (rough surfaces). 74
3.50 Recorded signal on vibration plane “x” of S-waves in direction “b” for Absolute Black sample 1 (flat surfaces). 74
3.51 Recorded signal on vibration plane “z” of S-waves in direction “a” for Absolute Black sample 1 (rough surfaces). 74
3.52 Recorded signal on vibration plane “z” of S-waves in direction “b” for Absolute Black sample 1 (flat surfaces). 75
3.53 Rigid table with hinged supports. 76
3.54 Tilt test apparatus with wood ring to keep fixed the bottom half specimen, stopping barrier for the upper half, camera support on the edge and hook to lift the plane. 76
3.55 Complete setup of tilt tests apparatus. 77
3.56 CatmanEasy software for the real–time acquisition of the LVDT sensor measurements. 77
3.57 (a) Tilt test in progress; (b) Sliding has already occurred and the test is finished. 78

4.1 Scheme of survey directions for the acquisition of roughness profiles. 83
4.2 Geometrical setup for the acquisition of roughness profiles. (a) markers in direction “c”; (b) markers in direction “b” 84
4.3 Reconstituted specimen of Carrara with geometrical setup for the acquisition of roughness profiles. 84
4.4 Example of profile acquisition with profilometer. On the left and right side there are the stopping supports (rectangular steel tubes). 85
4.5 Example of profile digitization with Epson Precision 1200U image scanner. . . . 85
4.6 Example of scanned image with a resolution of 1200 DPI. 86
4.7 Example of profile vector obtained from processing the image with a Matlab code. Units in millimeters. 86
4.8 Roughness parameter Z_2 for Syenite. (a) numbers; (b) letters. 87
4.9 Roughness parameter R_p for Syenite. (a) numbers; (b) letters. 87
4.10 Roughness parameter SF for Syenite. (a) numbers; (b) letters. 88
4.11 Roughness parameter D for Syenite. (a) numbers; (b) letters. 88
4.12 Roughness parameter Z_2 for Porriño. (a) numbers; (b) letters. 88
4.13 Roughness parameter R_p for Porriño. (a) numbers; (b) letters. 88
4.14 Roughness parameter SF for Porriño. (a) numbers; (b) letters. 89
4.15 Roughness parameter D for Porriño. (a) numbers; (b) letters. 89
4.16 Roughness parameter Z_2 for Absolute Black. (a) numbers; (b) letters. 89
4.17 Roughness parameter R_p for Absolute Black. (a) numbers; (b) letters. 89
4.18 Roughness parameter SF for Absolute Black. (a) numbers; (b) letters. 90
4.19 Roughness parameter D for Absolute Black. (a) numbers; (b) letters. 90
4.20 Roughness parameter Z_2 for Carrara. (a) numbers; (b) letters. 90
4.21 Roughness parameter R_p for Carrara. (a) numbers; (b) letters. 90

4.22 Roughness parameter SF for Carrara. (a) numbers; (b) letters. 91
4.23 Roughness parameter D for Carrara. (a) numbers; (b) letters. 91
4.24 JRC obtained from Z_2 for Porriño 92
4.25 JRC obtained from Rp for Porriño 92
4.26 JRC obtained from SF for Porriño 93
4.27 JRC obtained from D for Porriño 93
4.28 JRC obtained from Z_2 for Syenite 93
4.29 JRC obtained from Rp for Syenite 93
4.30 JRC obtained from SF for Syenite 94
4.31 JRC obtained from D for Syenite 94
4.32 JRC obtained from Z_2 for Absolute Black 94
4.33 JRC obtained from Rp for Absolute Black 94
4.34 JRC obtained from SF for Absolute Black 95
4.35 JRC obtained from D for Absolute Black 95
4.36 JRC obtained from Z_2 for Carrara 95
4.37 JRC obtained from Rp for for Carrara 95
4.38 JRC obtained from SF for Carrara 96
4.39 JRC obtained from D for Carrara 96

5.1 Setup of the camera in the Photographic Lab. 101
5.2 Photos of the two sides of a splitting fracture in a Porriño sample. (a): side A; (b): side B. 102
5.3 Geometrical setup to find the center of the Porriño sample. 102
5.4 Cropped image of the fracture surface of Porriño sample 1. (a): side A; (b): side B. 103
5.5 Cropped image of the fracture surface of Syenite sample 1. (a): side A; (b): side B. 103
5.6 Color extraction using ImageJ of Porriño sample 1. Saw-cut surface. (a) black; (b) grey; (c) pink; (d) white. 104
5.7 Color extraction using ImageJ of Porriño sample 1. Fracture surface (side "A"). (a) black; (b) grey; (c) pink; (d) white. 105
5.8 Color extraction using ImageJ of the Syenite sample 1. Saw–cut surface. (a) black; (b) grey; (c) pink; (d) white. 106
5.9 Color extraction using ImageJ of the Syenite sample 1. Fracture surface. (a) black; (b) grey; (c) pink; (d) white. 107
5.10 Image correlation of the Porriño sample 1. (a) low correlation (24.1%); (b) total correlation (100.0%). 108
5.11 Mismatching of the two faces of the fracture in Porriño samples. (a) Porriño 1; (b) Porriño 2; (c) Porriño 3. 108
5.12 Mismatching of the two faces of the fracture in Syenite samples. (a) Syenite 1; (b) Syenite 2; (c) Syenite 3. 109

A.1 Recorded signal of P-waves in direction "a" for Absolute Black sample 2 115
A.2 Recorded signal of P-waves in direction "b" for Absolute Black sample 2 115
A.3 Recorded signal of P-waves in direction "c" for Absolute Black sample 2 116
A.4 Recorded signal on vibration plane "x" of S-waves in direction "a" for Absolute Black sample 2 116
A.5 Recorded signal on vibration plane "z" of S-waves in direction "a" for Absolute Black sample 2 116
A.6 Recorded signal on vibration plane "z" of S-waves in direction "b" for Absolute Black sample 2 116
A.7 Recorded signal on vibration plane "z" of S-waves in direction "c" for Absolute Black sample 2 117
A.8 Recorded signal of P-waves in direction "a" for Absolute Black sample 3 117

A.9 Recorded signal of P-waves in direction “b” for Absolute Black sample 3 117
A.10 Recorded signal of P-waves in direction “c” for Absolute Black sample 3 117
A.11 Recorded signal on vibration plane “x” of S-waves in direction “a” for Absolute Black sample 3 118
A.12 Recorded signal on vibration plane “z” of S-waves in direction “a” for Absolute Black sample 3 118
A.13 Recorded signal on vibration plane “z” of S-waves in direction “b” for Absolute Black sample 3 118
A.14 Recorded signal on vibration plane “z” of S-waves in direction “c” for Absolute Black sample 3 118
A.15 Recorded signal of P-waves in direction “a” for Syenite sample 1 119
A.16 Recorded signal of P-waves in direction “b” for Syenite sample 1 119
A.17 Recorded signal of P-waves in direction “c” for Syenite sample 1 119
A.18 Recorded signal on vibration plane “x” of S-waves in direction “a” for Syenite sample 1 119
A.19 Recorded signal on vibration plane “z” of S-waves in direction “a” for Syenite sample 1 120
A.20 Recorded signal on vibration plane “z” of S-waves in direction “b” for Syenite sample 1 120
A.21 Recorded signal on vibration plane “z” of S-waves in direction “c” for Syenite sample 1 120
A.22 Recorded signal of P-waves in direction “a” for Syenite sample 2 120
A.23 Recorded signal of P-waves in direction “b” for Syenite sample 2 121
A.24 Recorded signal of P-waves in direction “c” for Syenite sample 2 121
A.25 Recorded signal on vibration plane “x” of S-waves in direction “a” for Syenite sample 2 121
A.26 Recorded signal on vibration plane “z” of S-waves in direction “a” for Syenite sample 2 121
A.27 Recorded signal on vibration plane “z” of S-waves in direction “b” for Syenite sample 2 122
A.28 Recorded signal on vibration plane “z” of S-waves in direction “c” for Syenite sample 2 122
A.29 Recorded signal of P-waves in direction “a” for Syenite sample 3 122
A.30 Recorded signal of P-waves in direction “b” for Syenite sample 3 122
A.31 Recorded signal of P-waves in direction “c” for Syenite sample 3 123
A.32 Recorded signal on vibration plane “x” of S-waves in direction “a” for Syenite sample 3 123
A.33 Recorded signal on vibration plane “z” of S-waves in direction “a” for Syenite sample 3 123
A.34 Recorded signal on vibration plane “z” of S-waves in direction “b” for Syenite sample 3 123
A.35 Recorded signal on vibration plane “z” of S-waves in direction “c” for Syenite sample 3 124
A.36 Recorded signal of P-waves in direction “a” for Porriño sample 1 124
A.37 Recorded signal of P-waves in direction “b” for Porriño sample 1 124
A.38 Recorded signal of P-waves in direction “c” for Porriño sample 1 124
A.39 Recorded signal on vibration plane “x” of S-waves in direction “a” for Porriño sample 1 125
A.40 Recorded signal on vibration plane “z” of S-waves in direction “a” for Porriño sample 1 125

A.41 Recorded signal on vibration plane “z” of S-waves in direction “b” for Porriño sample 1 . . . 125
A.42 Recorded signal on vibration plane “z” of S-waves in direction “c” for Porriño sample 1 . . . 125
A.43 Recorded signal of P-waves in direction “a” for Porriño sample 2 . . . 126
A.44 Recorded signal of P-waves in direction “b” for Porriño sample 2 . . . 126
A.45 Recorded signal of P-waves in direction “c” for Porriño sample 2 . . . 126
A.46 Recorded signal on vibration plane “x” of S-waves in direction “a” for Porriño sample 2 . . . 126
A.47 Recorded signal on vibration plane “z” of S-waves in direction “a” for Porriño sample 2 . . . 127
A.48 Recorded signal on vibration plane “z” of S-waves in direction “b” for Porriño sample 2 . . . 127
A.49 Recorded signal on vibration plane “z” of S-waves in direction “c” for Porriño sample 2 . . . 127
A.50 Recorded signal of P-waves in direction “a” for Porriño sample 3 . . . 127
A.51 Recorded signal of P-waves in direction “b” for Porriño sample 3 . . . 128
A.52 Recorded signal of P-waves in direction “c” for Porriño sample 3 . . . 128
A.53 Recorded signal on vibration plane “x” of S-waves in direction “a” for Porriño sample 3 . . . 128
A.54 Recorded signal on vibration plane “z” of S-waves in direction “a” for Porriño sample 3 . . . 128
A.55 Recorded signal on vibration plane “z” of S-waves in direction “b” for Porriño sample 3 . . . 129
A.56 Recorded signal on vibration plane “z” of S-waves in direction “c” for Porriño sample 3 . . . 129
A.57 Recorded signal of P-waves in direction “a” for Carrara sample 1 . . . 129
A.58 Recorded signal of P-waves in direction “b” for Carrara sample 1 . . . 129
A.59 Recorded signal of P-waves in direction “c” for Carrara sample 1 . . . 130
A.60 Recorded signal on vibration plane “x” of S-waves in direction “a” for Carrara sample 1 . . . 130
A.61 Recorded signal on vibration plane “z” of S-waves in direction “a” for Carrara sample 1 . . . 130
A.62 Recorded signal on vibration plane “z” of S-waves in direction “b” for Carrara sample 1 . . . 130
A.63 Recorded signal on vibration plane “z” of S-waves in direction “c” for Carrara sample 1 . . . 131
A.64 Recorded signal of P-waves in direction “a” for Carrara sample 2 . . . 131
A.65 Recorded signal of P-waves in direction “b” for Carrara sample 2 . . . 131
A.66 Recorded signal of P-waves in direction “c” for Carrara sample 2 . . . 131
A.67 Recorded signal on vibration plane “x” of S-waves in direction “a” for Carrara sample 2 . . . 132
A.68 Recorded signal on vibration plane “z” of S-waves in direction “a” for Carrara sample 2 . . . 132
A.69 Recorded signal on vibration plane “z” of S-waves in direction “b” for Carrara sample 2 . . . 132
A.70 Recorded signal on vibration plane “z” of S-waves in direction “c” for Carrara sample 2 . . . 132
A.71 Recorded signal of P-waves in direction “a” for Carrara sample 3 . . . 133
A.72 Recorded signal of P-waves in direction “b” for Carrara sample 3 . . . 133
A.73 Recorded signal of P-waves in direction “c” for Carrara sample 3 . . . 133

A.74 Recorded signal on vibration plane “x” of S-waves in direction “a” for Carrara sample 3 . . . 133
A.75 Recorded signal on vibration plane “z” of S-waves in direction “a” for Carrara sample 3 . . . 134
A.76 Recorded signal on vibration plane “z” of S-waves in direction “b” for Carrara sample 3 . . . 134
A.77 Recorded signal on vibration plane “z” of S-waves in direction “c” for Carrara sample 3 . . . 134

B.1 Syenite sample 2. blue: force vs time; red: radial strain vs time. . . . 135
B.2 Syenite sample 2. blue: stress vs axial strain; red: stress vs radial strain. . . . 135
B.3 Syenite sample 3. blue: force vs time; red: radial strain vs time. . . . 136
B.4 Syenite sample 3. blue: stress vs axial strain; red: stress vs radial strain. . . . 136
B.5 Absolute Black sample 2. blue: force vs time; red: radial strain vs time. . . . 137
B.6 Absolute Black sample 2. blue: stress vs axial strain; red: stress vs radial strain. 137
B.7 Absolute Black sample 3. blue: force vs time; red: radial strain vs time. . . . 138
B.8 Absolute Black sample 3. blue: stress vs axial strain; red: stress vs radial strain. 138
B.9 Porriño sample 2. blue: force vs time; red: radial strain vs time. . . . 139
B.10 Porriño sample 2. blue: stress vs axial strain; red: stress vs radial strain. . . . 139
B.11 Porriño sample 3. blue: force vs time; red: radial strain vs time. . . . 140
B.12 Porriño sample 3. blue: stress vs axial strain; red: stress vs radial strain. . . . 140
B.13 Carrara sample 2. blue: force vs time; red: radial strain vs time. . . . 141
B.14 Carrara sample 2. blue: stress vs axial strain; red: stress vs radial strain. . . . 141
B.15 Carrara sample 3. blue: force vs time; red: radial strain vs time. . . . 142
B.16 Carrara sample 3. blue: stress vs axial strain; red: stress vs radial strain. . . . 142

C.1 Recorded signal of P-waves in direction “a” for Absolute Black sample 2 (rough surfaces). . . . 143
C.2 Recorded signal on vibration plane “x” of S-waves in direction “a” for Absolute Black sample 2 (rough surfaces). . . . 143
C.3 Recorded signal on vibration plane “z” of S-waves in direction “a” for Absolute Black sample 2 (rough surfaces). . . . 144
C.4 Recorded signal of P-waves in direction “a” for Absolute Black sample 3 (rough surfaces). . . . 144
C.5 Recorded signal on vibration plane “x” of S-waves in direction “a” for Absolute Black sample 3 (rough surfaces). . . . 144
C.6 Recorded signal on vibration plane “z” of S-waves in direction “a” for Absolute Black sample 3 (rough surfaces). . . . 144
C.7 Recorded signal of P-waves in direction “a” for Syenite sample 1 (rough surfaces). 145
C.8 Recorded signal of P-waves in direction “b” for Syenite sample 1 (flat surfaces). . 145
C.9 Recorded signal on vibration plane “x” of S-waves in direction “a” for Syenite sample 1 (rough surfaces). . . . 145
C.10 Recorded signal on vibration plane “x” of S-waves in direction “b” for Syenite sample 1 (flat surfaces). . . . 146
C.11 Recorded signal on vibration plane “z” of S-waves in direction “a” for Syenite sample 1 (rough surfaces). . . . 146
C.12 Recorded signal on vibration plane “z” of S-waves in direction “b” for Syenite sample 1 (flat surfaces). . . . 146
C.13 Recorded signal of P-waves in direction “a” for Syenite sample 2 (rough surfaces). 146
C.14 Recorded signal on vibration plane “x” of S-waves in direction “a” for Syenite sample 2 (rough surfaces). . . . 147

C.15 Recorded signal on vibration plane "z" of S-waves in direction "a" for Syenite sample 2 (rough surfaces). 147
C.16 Recorded signal of P-waves in direction "a" for Syenite sample 3 (rough surfaces). 147
C.17 Recorded signal on vibration plane "x" of S-waves in direction "a" for Syenite sample 3 (rough surfaces). 147
C.18 Recorded signal on vibration plane "z" of S-waves in direction "a" for Syenite sample 3 (rough surfaces). 148
C.19 Recorded signal of P-waves in direction "a" for Porriño sample 1 (rough surfaces). 148
C.20 Recorded signal of P-waves in direction "b" for Porriño sample 1 (flat surfaces). . 148
C.21 Recorded signal on vibration plane "x" of S-waves in direction "a" for Porriño sample 1 (rough surfaces). 148
C.22 Recorded signal on vibration plane "x" of S-waves in direction "b" for Porriño sample 1 (flat surfaces). 149
C.23 Recorded signal on vibration plane "z" of S-waves in direction "a" for Porriño sample 1 (rough surfaces). 149
C.24 Recorded signal on vibration plane "z" of S-waves in direction "b" for Porriño sample 1 (flat surfaces). 149
C.25 Recorded signal of P-waves in direction "a" for Porriño sample 2 (rough surfaces). 149
C.26 Recorded signal on vibration plane "x" of S-waves in direction "a" for Porriño sample 2 (rough surfaces). 150
C.27 Recorded signal on vibration plane "z" of S-waves in direction "a" for Porriño sample 2 (rough surfaces). 150
C.28 Recorded signal of P-waves in direction "a" for Porriño sample 3 (rough surfaces). 150
C.29 Recorded signal on vibration plane "x" of S-waves in direction "a" for Porriño sample 3 (rough surfaces). 150
C.30 Recorded signal on vibration plane "z" of S-waves in direction "a" for Porriño sample 3 (rough surfaces). 151
C.31 Recorded signal of P-waves in direction "a" for Carrara sample 1 (rough surfaces). 151
C.32 Recorded signal of P-waves in direction "b" for Carrara sample 1 (flat surfaces). 151
C.33 Recorded signal on vibration plane "x" of S-waves in direction "a" for Carrara sample 1 (rough surfaces). 151
C.34 Recorded signal on vibration plane "x" of S-waves in direction "b" for Carrara sample 1 (flat surfaces). 152
C.35 Recorded signal on vibration plane "z" of S-waves in direction "a" for Carrara sample 1 (rough surfaces). 152
C.36 Recorded signal on vibration plane "z" of S-waves in direction "b" for Carrara sample 1 (flat surfaces). 152
C.37 Recorded signal of P-waves in direction "a" for Carrara sample 2 (rough surfaces). 152
C.38 Recorded signal on vibration plane "x" of S-waves in direction "a" for Carrara sample 2 (rough surfaces). 153
C.39 Recorded signal on vibration plane "z" of S-waves in direction "a" for Carrara sample 2 (rough surfaces). 153
C.40 Recorded signal of P-waves in direction "a" for Carrara sample 3 (rough surfaces). 153
C.41 Recorded signal on vibration plane "x" of S-waves in direction "a" for Carrara sample 3 (rough surfaces). 153
C.42 Recorded signal on vibration plane "z" of S-waves in direction "a" for Carrara sample 3 (rough surfaces). 154

D.1 Color extraction using ImageJ of Porriño sample 2. Fracture surface. (a) black; (b) grey; (c) pink; (d) white. 155
D.2 Color extraction using ImageJ of Porriño sample 3. Fracture surface. (a) black; (b) grey; (c) pink; (d) white. 156

D.3 Color extraction using ImageJ of the Syenite sample 1. Fracture surface. (a) black; (b) grey; (c) pink; (d) white. 157
D.4 Color extraction using ImageJ of the Syenite sample 1. Fracture surface. (a) black; (b) grey; (c) pink; (d) white. 158

List of Tables

2.1 Persistence classification according to ISRM (1978) [7]. 32
2.2 Aperture classification by ISRM (1978) [7]. 36
2.3 Seepage classification by ISRM (1978) [7]. 36
2.4 Number of sets classification by ISRM (1978) [7]. 37
2.5 Block size classification by ISRM (1978) [7]. 37

3.1 Dimensions and weights of the samples. 51
3.2 Arrival times of P-waves and S-waves trough the intact rock specimens. 57
3.3 Dynamic deformability parameters obtained from ultrasonic propagation tests; E: Young's modulus; ν: Poisson's ratio. 57
3.4 geometrical data and loads applied to the samples. 61
3.5 Static deformability parameters obtained from the unconfined compression tests; E: Young's modulus; ν: Poisson's ratio. 67
3.6 Splitting test: breaking loads. 70
3.7 Arrival times of P-waves and S-waves trough the fractured rock specimens. . . . 75
3.8 Normal and tangential stiffness of the fracture. 75
3.9 Results of tilt tests. 79
3.10 Average tilt angle and standard deviation for each lithotype. 79

4.1 Statistical distribution of roughness parameters - Syenite 91
4.2 Relationship between correlation and equation used to compute JRC 92
4.3 JRC from the qualitative comparison with the standard profiles provided by [9] . 97
4.4 JRC from the qualitative comparison with the standard profiles provided by ISRM [9] 98
4.5 Normal and tangential stiffness of the fracture for each lithotype. 99

5.1 Mineral–color correlation adopted for Syenite and Porriño samples. 104
5.2 Mineral composition of Porriño samples. 105
5.3 Mineral composition of Syenite samples. 106

Chapter 1

Introduction

1.1 Reasons and objectives of the thesis

Rock masses are natural formations defined as blocks of rock material often separated by discontinuities [1]. In certain instances, these surfaces exhibit predominant behavior, leading to various types of instability. Attention must be paid in the evaluation of the mechanical behavior of an existing rock mass through laboratory samples, since it can differ significantly due to the presence of weakness zones at a macroscopic scale, as shown in fig. 1.1. Therefore, the characterization of discontinuities systems plays a fundamental role in the strength and deformability evaluation at the site scale. The hydraulic properties of the rock mass are also determined by the characteristics of the discontinuity systems. The phenomenon is dominated by the opening, filling, and roughness of the wall surfaces. Hydraulic conductivity is directly proportional to the opening and inversely proportional to the roughness, making the path of water tortuous.

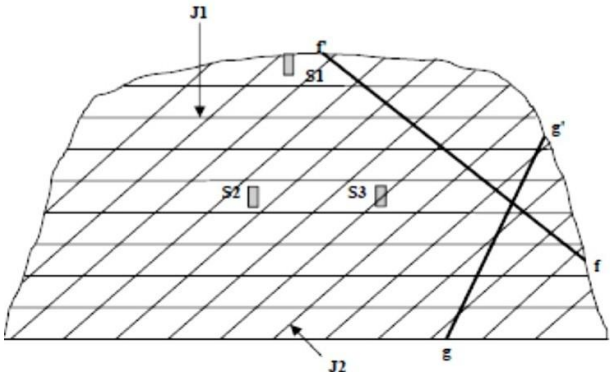

Figure 1.1: Comparison between lab and in situ scale

In many fields of rock mechanics, the correct assessment of the rock mass properties is of paramount importance for successful design of engineering works. Rock slopes can be subject to mass movements or collapses, both due to natural and anthropogenic causes. With increasing activities such as tourism, infrastructure development, construction of dams and roads, the instability scenarios on rock slopes have been increased over the last century. Therefore, it is crucial not to make incorrect assessment against instability mechanisms to avoid environmental consequences and safeguard human life.

Fig. 1.2 shows common failure mechanisms associated with rock slopes, including sliding along a discontinuity plane (planar sliding), sliding in a direction determined by the intersection of two discontinuity planes (three-dimensional wedge sliding), rotation of rock blocks around an axis horizontal and perpendicular to the slope (slumping) and overturning mechanism when the center of gravity is outside the base of the block (toppling). Frequently, mechanisms result

from the combination of these elementary kinematics. In the engineering design practice, it is essential to provide detailed information about the structure, as well as the geo-morphological and hydrological conditions. This ensure to obtain a geomechanical model that represents, in a simplified form, the behavior of the complex interaction of the rock mass.

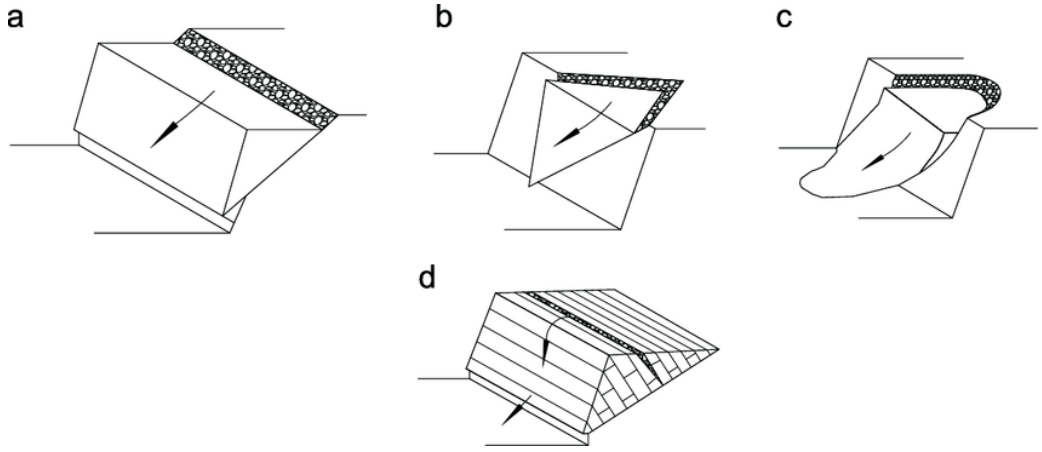

Figure 1.2: Modes of failure in rock slopes. (a) planar sliding; (b) wedge sliding; (c) slumping; (d) toppling. [2]

In deep tunneling with elevated in-situ stresses, rocks can fail in a brittle manner via tensile fracture near the opening due to the presence of low confinement. The fracture propagates and the release of slabs from the wall of the excavation can be more or less violent. Usually it is not violent in the case of progressive and stable release of energy, as shown in fig. 1.3 (a). Spalling can also develop without release of energy and material until a buckling instability takes place, resulting in a violent phenomenon called rockburst, as shown in fig. 1.3 (b). The same phenomenon can interact with retaining structures in a structurally controlled strain burst, as shown in fig. 1.3 (c). If the supports are adequate to the problem and the slabs are anchored with bolts within the rockmass, that is usually the case, the fractures can propagate into the rockmass leading to failure inside the rock mass, as shown in fig. 1.3 (d).

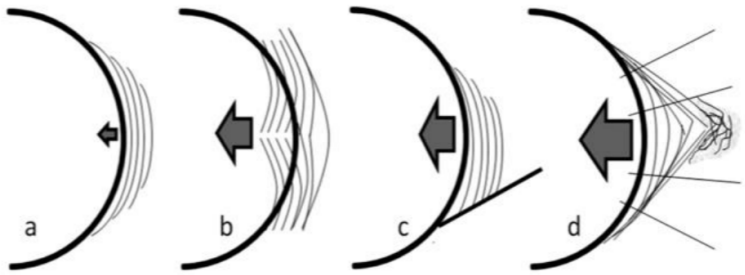

Figure 1.3: Transition from non-violent spalling (a) to bursting through buckling (b), interaction with structure (c) and dilational yield (d) [3].

An important consideration about this problem was made by Suorineni during the 2014 SOMP (Society of Mining Professors) Annual Meeting, when he wrote the following state [4]:

> We need to stand-up to rockbursts (SU_2R), just as the medical scientists are standing up to cancer (SU_2C).

Suorineni's statement still hold true after almost 10 years because the mechanism is not fully understood yet, and everything we can do is to use the best available design tools and then to monitor, mitigate, and identify potential high-risk areas.

In general, the evaluation of shear strength of a discontinuity has evolved over time. Initially, few parameters were considered, such as the applied normal stress, the friction angle and the inclination of asperities (Patton, 1966). Then an improved criterion was made by taking into account also the roughness of the joint trough the Joint Roughness Coefficient (Barton, 1973) and the Joint Compressive Strength, obtainable by directly testing the compressive resistance of the joint using the Schmidt hammer.

In this context, this thesis has the role to investigate and characterize the influence of the fracturing process in rock lithotypes that are likely to have brittle behavior, through a wide experimental campaign aimed at obtaining the deformability of the rocks and the characterization of many roughness profiles on the fracture surfaces.

For this reason, in the following pages, we will first explore how these weakness elements are formed. Considering prismatic specimens of four different rock types, Balma Syenite, Absolute Black Gabbro, Pink Porriño Granite and Carrara marble, the deformability characteristics will be obtained trough static and dynamic testing.

Subsequently, tensile fractures will be induced in the specimens and the analysis of these surfaces will be conducted using a profilometer to collect many profiles and using mathematical parameters to characterize their roughness. Several empirical correlations, available in literature, that correlate those parameters and the Joint Roughness Coefficient will be used. Throughout history many researcher have focused on this topic, contributing significant insights to the field and some of them will be compared.

Tilt tests will be conducted on the smooth surfaces in order to evaluate the base friction angle of each different lithotype.

Finally an image analysis will be performed on saw cut and rough surfaces to analyze differences in the relative abundance of minerals caused by the fracturing process.

1.2 Structure of the thesis

In this section, we will outline the structure of the thesis. The document is organized into the following chapters:

1. Introduction: Introduction to the role of discontinuities in the influence of strength and deformability properties of a rock mass, with reasons and objectives of the thesis.

2. Rock discontinuities: This chapter provides an overview of the existing literature about the rock discontinuities and the theoretical frameworks that inform the research.

3. Experimental campaign: This chapter presents the mechanical experimental campaign conducted on the rock specimens, focusing on ultrasonic propagation tests, unconfined compression tests, splitting tests and tilt tests.

4. Analysis of fracture surfaces: This chapter outlines the characterization of the fracture surfaces through the geometrical analysis of many roughness profiles and their consequent mathematical description, checking the goodness of the correlations with the mechanical parameter JRC .

5. Image analysis of surfaces: This chapter discusses the effect of the fracture process on the mineral distribution on the saw cut surfaces and rough fractures, by processing their photographs.

6. Conclusion: The final chapter summarizes the key findings, contributions to the field, and suggests directions for future research.

7. Bibliography: This section lists all the sources and references cited throughout the thesis.

Chapter 2

Rock discontinuities

2.1 Definition and typology

The term "Discontinuity" in Rock Mechanics is referred to a separation within a rock mass, usually characterized by very low or negligible tensile strength [5]. It is a very broad term that involves varies typologies, for example according to rock type or genesis. The formation of these features within the rock mass may be attributed to geological or anthropogenic origin.
In the following, the typologies will be individually explained:

Joint: it has geological origin and it is the most common type of discontinuity present in a rock mass. It can be generated by shear or tensile stress. A group of joints, parallel or sub-parallel, is defined as a set: they intersect to form systems and they can be open, filled, or cemented. Often, they form parallel to sedimentation planes or cleavage planes.

Bedding plane: it divides sedimentary rocks into distinct layers or strata, marking interruptions in the rock mass deposition process. Since the deposition process is very slow, these planes typically exhibit long-lasting characteristics. Bedding planes may contain materials with different grain sizes compared to the sediments forming the rock mass. Cohesion can exist between the layers, otherwise the shear resistance is entrusted only on friction. Due to the depositional process, particles within the rock may exhibit a preferred orientation, leading to the formation of planes of weakness aligned parallel to the bedding planes [6].

Cleavage plane: flat and parallel surfaces within the intact material generated by a geological process. Mainly lithology and stress conditions are responsible of shearing, extension and compression, as for example in metamorphic rocks where preferential surfaces of structural weakness are generated by high temperatures and/or pressures. Moreover, cleavage is typically associated with faults and folds, and it is well-visible in schist and medium to coarse-grained metamorphic rocks that tend to split easily into thin sheets. In addition, it can create strong anisotropy in the strength and the deformability of a rock mass.

Fault: discontinuity where big visible displacement has occurred. They can affect large areas with a thickness in the order of meters or can involve only a small area and a thickness in the order of millimeters in the case of local fault. More in general faults are zones of low shear strength where slip may occur.

2.2 Characterization of discontinuities

Discontinuities are present in rock masses in the form of sets or families, or as individual features in the particular case of a single plane observed. Data related to these parameters are collected

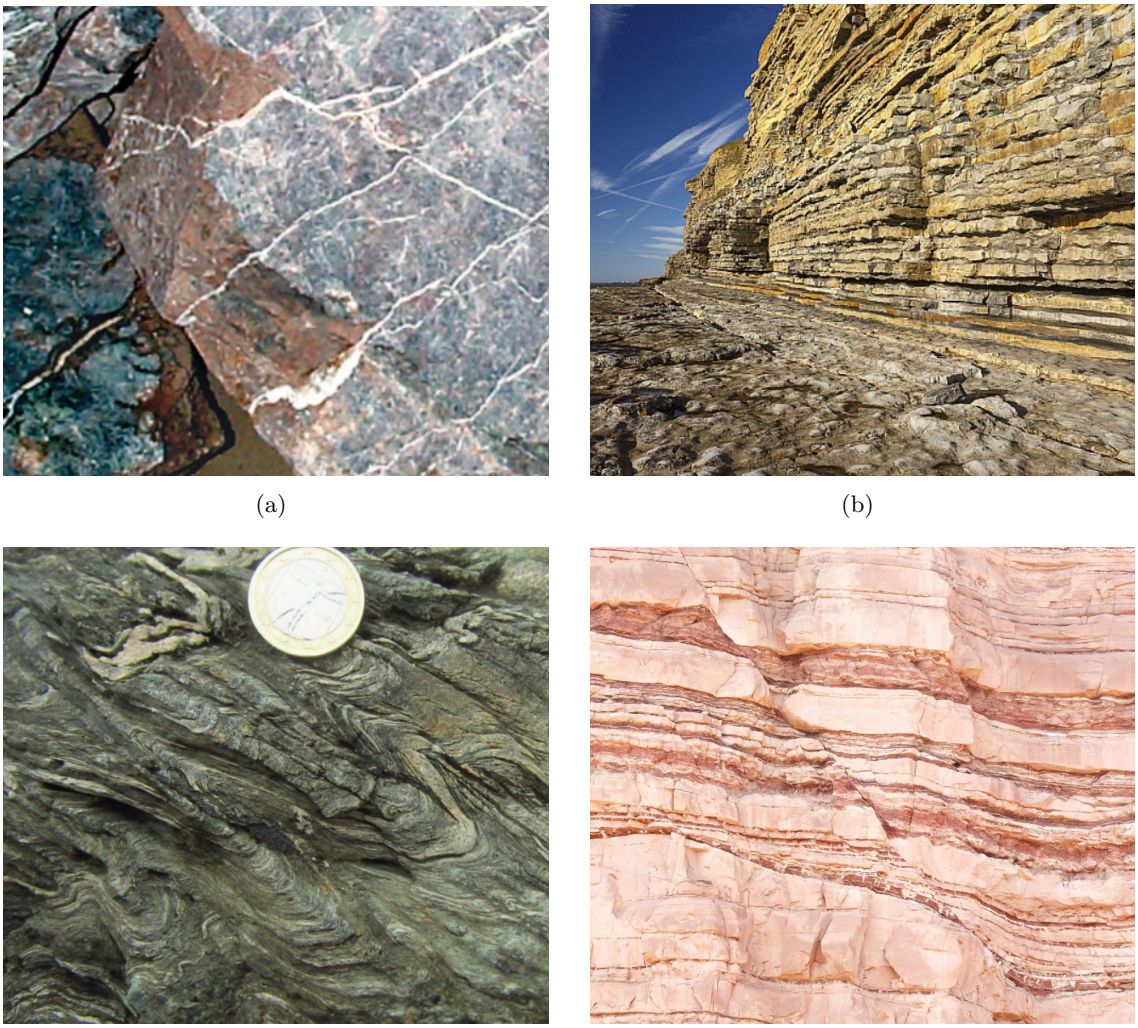

(a) (b)

(c) (d)

Figure 2.1: (a) Joints in a rock mass. Source: `https://tinyurl.com/4d6aswzj`; (b) Bedding planes in a rock mass. Source: `https://tinyurl.com/2u4utdwc`; (c) Schistosity in a rock mass. Source: `https://tinyurl.com/3rxvp8jz`; (d) Fault in a Sandstone deposit. Source: `https://tinyurl.com/ywajyaah`.

directly on-site through traditional surveying techniques or by employing more innovative measurement instruments. For instance, photogrammetric surveys or laser scanning of the surveyed rock faces could provide a complete set of geometric information. The ISRM published the "Suggested methods for the quantitative description of discontinuities in rock masses", where ten parameters are introduced to describe the characteristics of discontinuities [7]:

1. *Orientation*: described by dip direction (or the azimuth) and dip of the steepest line in the plane of discontinuity.
2. *Spacing:* orthogonal distance between nearby discontinuities. It is common to refer to the mean spacing of a set of discontinuities.
3. *Persistence:* trace length observed on a exposed face.
4. *Roughness:* roughness of a discontinuity. It is very relevant for the shear strength of the discontinuity.
5. *Wall strength:* compressive strength of the walls of a discontinuity.

6. *Aperture:* measure of the perpendicular distance between the two walls of the discontinuity.

7. *Filling:* internal material that fills the discontinuity, typically different from the host rock.

8. Seepage: water flow visible in the discontinuity sets.

9. *Number of sets:* number of discontinuity sets affecting the rock mass.

10. *Block size:* size of the block resulting by the intersection of different sets or systems.

In the following, these aspects of the description of the discontinuities are presented in more detail.

Orientation. Usually described by the dip direction α or azimuth measured clockwise from the north and by the dip ψ of the steepest line with respect to the horizontal. Fig. 2.2 shows a schematic orientation in space of a plane. The mutual geometrical interaction between the orientation of different sets of discontinuities, determine the shape and the size of individual blocks in the rock mass [6]. The orientation is measured on site by the geologist compass. The orientation representative of a set of discontinuities is provided by analyzing the measures taken on different discontinuities affecting the rock mass analyzed. If a systematic geological survey is performed, the orientations are analyzed by a statistical procedure, which provides the sets of discontinuities and their relative representative values of dip and dip direction.

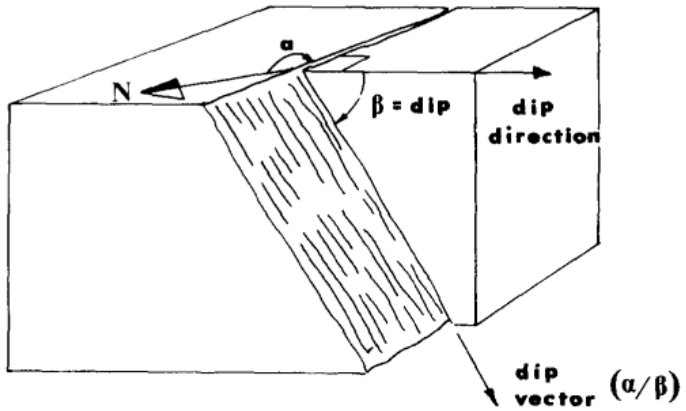

Figure 2.2: Orientation of a plane in the space given by dip and dip direction [7].

Spacing. It is the distance between nearby discontinuities belonging to the same set, measured along the scanline. From the spacing it is possible to define the linear frequency λ which is the reciprocal of the mean spacing or in other words, the number of discontinuities intersected by a unit length scanline [6]. A schematic of the spacing measurement is given in fig. 2.3. The frequency λ varies with the scanline angle, so it is important to specify its corresponding direction with respect to the normal to the set, to correlate it with the normal frequency of a set. The correlation is given by:

$$\lambda_s = \lambda_n \cos\theta \tag{2.1}$$

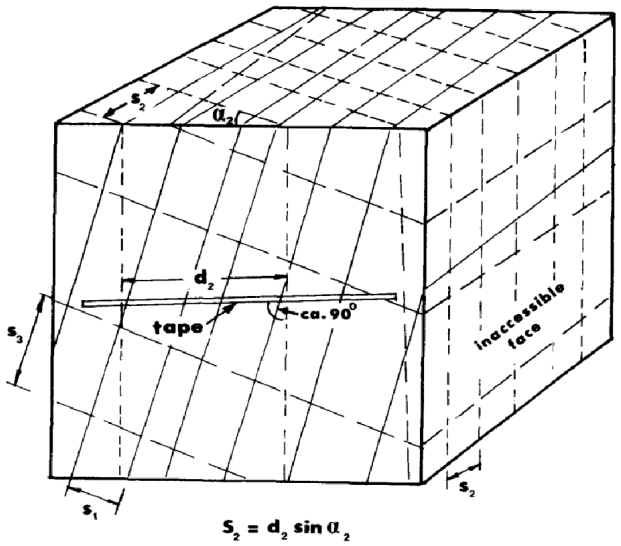

Figure 2.3: Spacing measurement of parallel discontinuities [7].

Persistence. It is quantified from the exposed rock face, observing the trace lengths of the discontinuities. A sketch is proposed in fig. 2.4. The persistence has great influence on the shear strength developed in the plane of the discontinuity [6]. A classification of the persistence given by ISRM is proposed in table 2.1.

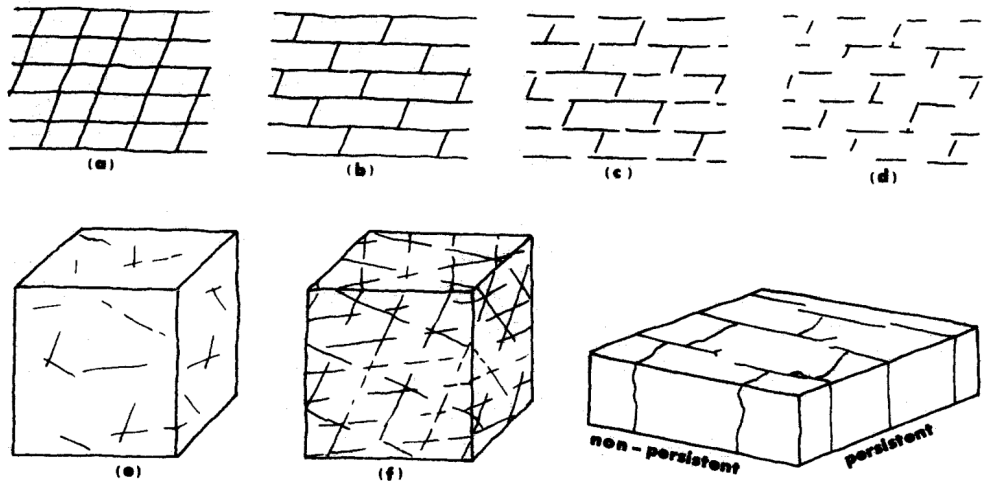

Figure 2.4: Persistence measurement of parallel discontinuities [7].

Table 2.1: Persistence classification according to ISRM (1978) [7].

Very low persistence	< 1 m
Low persistence	1 - 3 m
Medium persistence	3 - 10 m
High persistence	10 - 20 m
Very high persistence	> 20 m

Roughness. The roughness contributes to shear resistance, especially in the case of contacting surfaces with no relative movement. It is usually defined as a combination of the roughness at microscopic-scale, the roughness at the laboratory scale and waviness of the mean profile at the macro-scale, as schematized in fig. 2.5. The first component tends to break

during sliding, while the macroscopic one causes dilation during sliding. The roughness has great influence on the initial direction of sliding [6]. Its influence decreases with increasing opening of the fracture.

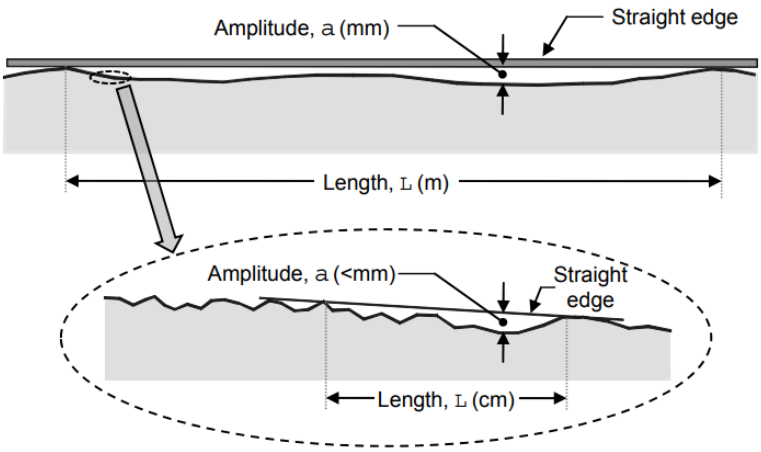

Figure 2.5: Definition of large–scale roughness (waviness) and small–scale roughness (unevenness) of rock discontinuities [8].

To acquire a roughness profile, several techniques were developed during the years: laser scanner, near-surface photogrammetry or the most simple, a profilometer such as the so-called Barton comb, shown in fig. 2.6. It consists in a instrument with very thin steel wires that allows to follow the roughness profile of the sample under testing and to obtain, with a pen on paper, a copy of the profile.
Once a profile is acquired along the discontinuity, it is possible to compare it with the typical profiles provided by ISRM [9], reported in fig. 2.7. Each standard profile is associated with a range of JRC that can be used to assess the peak strength of a rock joint. Whatever is the adopted technique, the comparison remains only qualitative. On the contrary, the computation of roughness parameters uniquely identifies the acquired profile allowing a standardized analysis of the surfaces. This latter aspect will be further discussed in the subsection 2.4.

Figure 2.6: Barton profilometer.

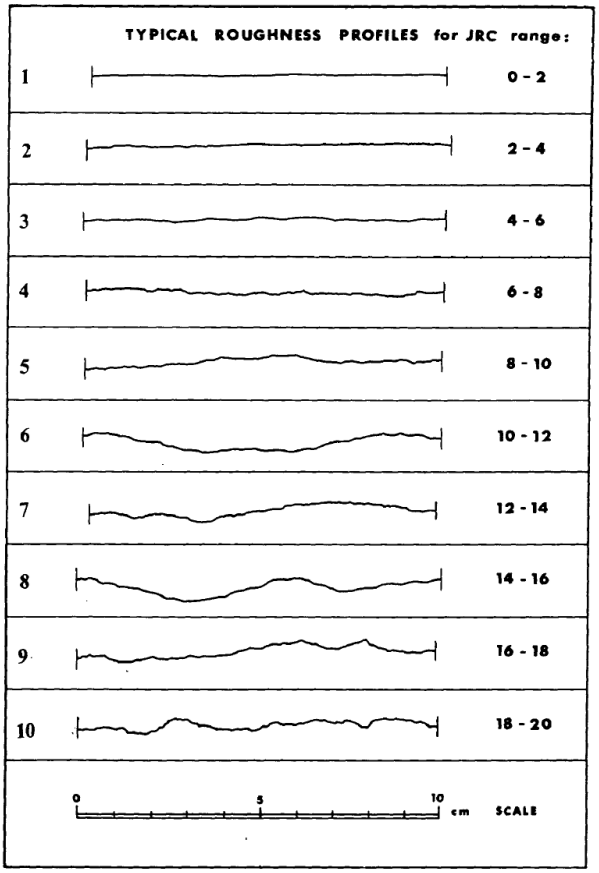

Figure 2.7: Standard roughness profiles and corresponding range of JRC [9].

Wall strength. The compressive strength of the discontinuity faces is very important in the evaluation of the shear strength of the discontinuity itself. The asperities start to damage when the stress overcome locally the strength of the wall material. Usually, the Schmidt hammer is used to evaluate the compressive strength of the walls of the discontinuities. The hammer is applied perpendicularly to the wall and the test is repeated in groups of 10 per discontinuity. The mean value of these tests is used to estimate the JCS (Joint Compressive Strength) according to ISRM (1978) [7] with the graph shown in fig. 2.8.

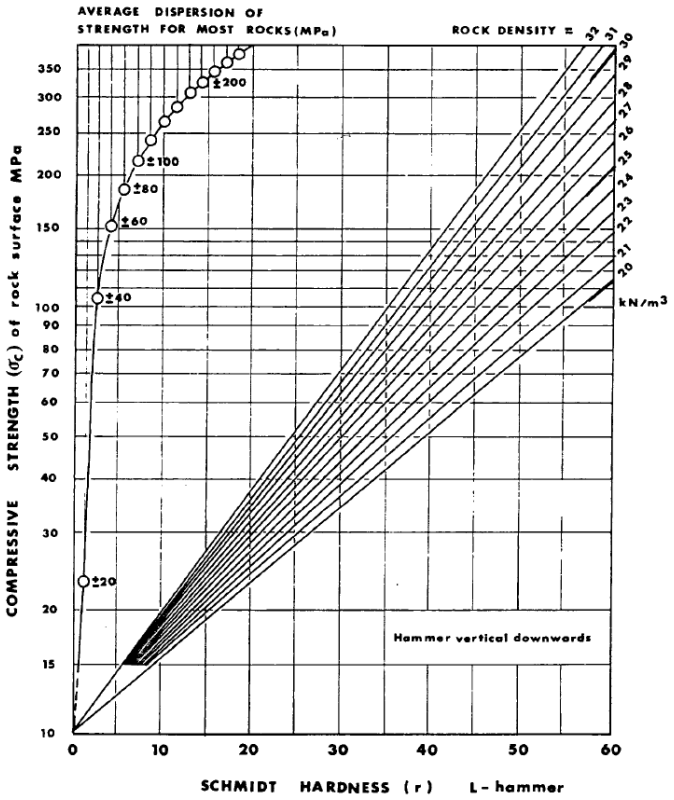

Figure 2.8: Correlation chart for Schmidt hammer test - ISRM (1978) [7].

Aperture. It is the perpendicular distance between the discontinuity faces in the case of an open discontinuity, as shown in fig. 2.9. In the case of a closed discontinuity or a filled discontinuity, it is common to refer to the width. The areal variation of the aperture influences the mechanical properties of the rock mass, but also the hydraulic conductivity of the fracture. A list of suggested aperture dimensions is provided by ISRM [7] in table 2.2.

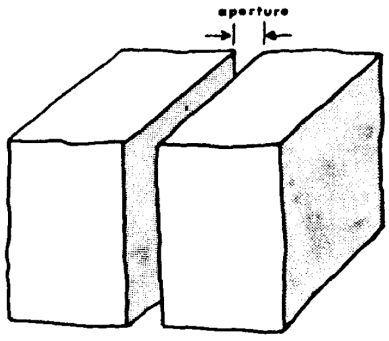

Figure 2.9: Aperture of an open discontinuity - ISRM (1978) [7].

Table 2.2: Aperture classification by ISRM (1978) [7].

Aperture	Description	
< 0.1 mm	Very tight	
0.1 - 0.25 mm	Tight	"Closed" features
0.25 - 0.5 mm	Partly open	
0.5 - 2.5 mm	Open	
2.5 - 10 mm	Moderately wide	"Gapped" features
> 10 mm	Wide	
1 - 10 cm	Very wide	
10 - 100 cm	Extremely wide	"Open" features
> 1 m	Cavernous	

Filling. It is the material that fills the space between the discontinuity walls in the case of a filled discontinuity. It can be of various nature such as clay, silt, quartz, or calcite. Usually, filling materials are weaker than the host rock and they have great influence on the shear strength. Moreover their behavior is greatly affected by the water content.

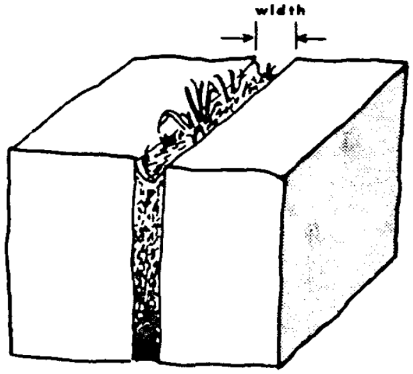

Figure 2.10: Filled discontinuity - ISRM (1978) [7].

Seepage. In a rock mass water seepage can usually take place through the discontinuities. In particular cases, i.e. for sedimentary rocks, it could take place also through the pores. A classification given by ISRM (1978) [7], is proposed in table 2.3.

Table 2.3: Seepage classification by ISRM (1978) [7].

Seepage rating	Description
I	The discontinuity is very tight and dry, water flow along it does not appear possible
II	The discontinuity is dry with no evidence of water flow
III	The discontinuity is dry but shows evidence of water flow, i.e. rust staining,etc.
IV	The discontinuity is damp but no free water is present
V	The discontinuity shows seepage, occasional drops of water, but no continuous flow.
VI	The discontinuity shows a continuous flow of water (Estimate l/min and describe pressure i.e. low, medium, high)

Number of sets. It is a fundamental parameter in the definition of the behavior of the rock mass. A large number of discontinuity sets can strongly affect strength and deformability

of a rock mass. The classification proposed by ISRM (1978) [7] is presented in table 2.4.

Table 2.4: Number of sets classification by ISRM (1978) [7].

Seepage rating	Description
I	massive, occasional random joints
II	one joint set
III	one joint set plus random
IV	two joint sets
V	two joint sets plus random
VI	three joint sets
VII	three joint sets plus random
VIII	four or more joint sets
IX	crushed rock, earth-like

Block size. The block size is influenced by the number of sets, the persistence and the spacing of the discontinuities. A classification proposed by ISRM (1978) [7] is reported in table 2.5. Some examples of block shape are shown in fig. 2.11.

Table 2.5: Block size classification by ISRM (1978) [7].

Block size rating	Description
I	*massive* = few joints or very wide spacing
II	*blocky* = approximately equidimensional
III	*tabular* = one dimension considerably smaller than the other two
IV	*columnar* = one dimension considerably larger than the other two
V	*irregular* = wide variations of block size and shape
VI	*crushed* = heavily jointed to "sugar cube"

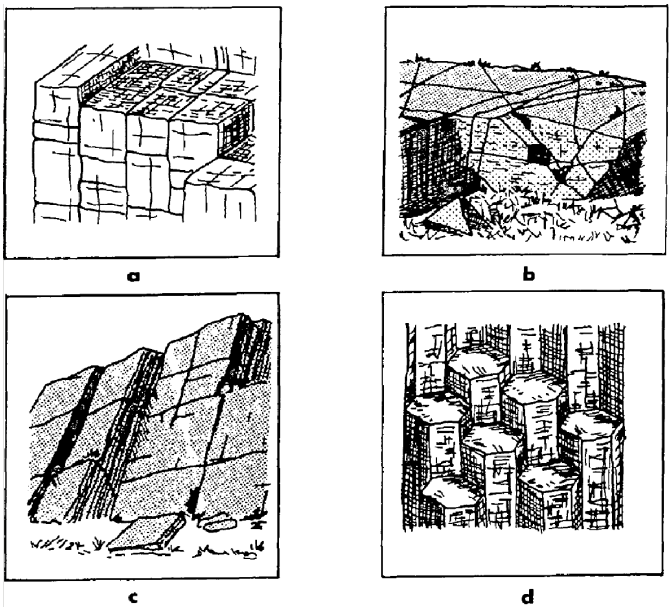

Figure 2.11: Examples of block shape - ISRM (1978) [7].

2.3 Mechanical behavior of the discontinuities

Discontinuities have great impact on the strength characteristics of a rock mass, that can be treated as a continuum or a discontinuum material depending on the scale of the engineering problem (e.g. unstable volume, diameter of excavation), as shown in fig. 2.12. The choice of the model depends on the ratio between the characteristic volume of the representative block size and the structure to be analyzed. If the block size is small compared to the structure, the equivalent continuum approach can be used, while if the block has the same size of the structure being analyzed, the discontinuum approach is more suitable.

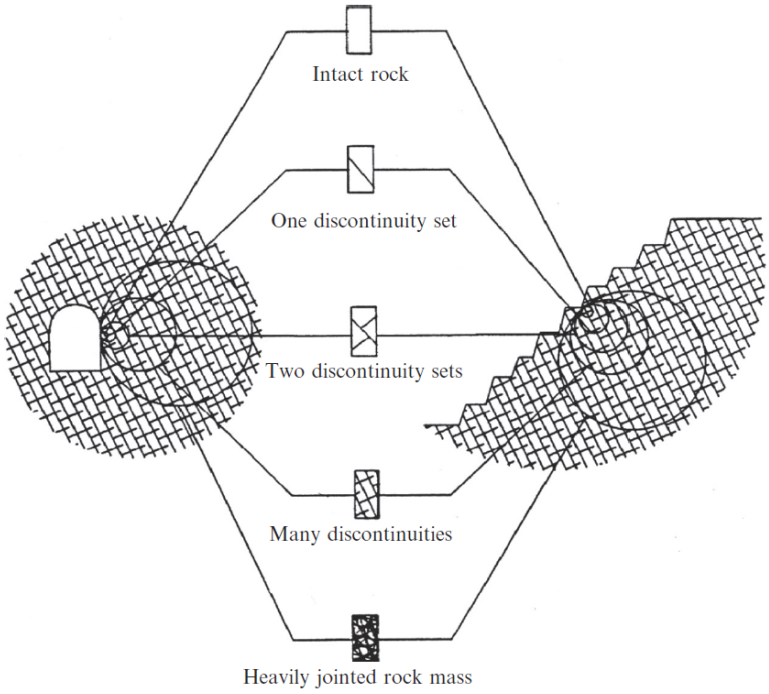

Figure 2.12: Transition from intact to heavily jointed rock mass with increasing scale of the problem [10].

2.3.1 Shear strength

Considering an intact rock specimen under shearing, according to the Mohr–Coulomb criterion the failure envelope can be represented by a straight-line inclined by an angle ϕ_b in the $\tau - \sigma_n$ plane, as shown in fig. 2.13(a). The intercept with the vertical axis is the contribution of cohesion. Considering instead a rock specimen with a smooth horizontal joint, the envelope is a different straight line without any value of cohesion and inclined by an angle ϕ_j, as shown in fig. 2.13(b). In the last case in fig. 2.13(c), a rough joint is assumed and a bilinear envelope is used to reproduce the strength contribution of the roughness (angle i), up to the breaking of the asperities, according to the Patton saw-tooth model [11].

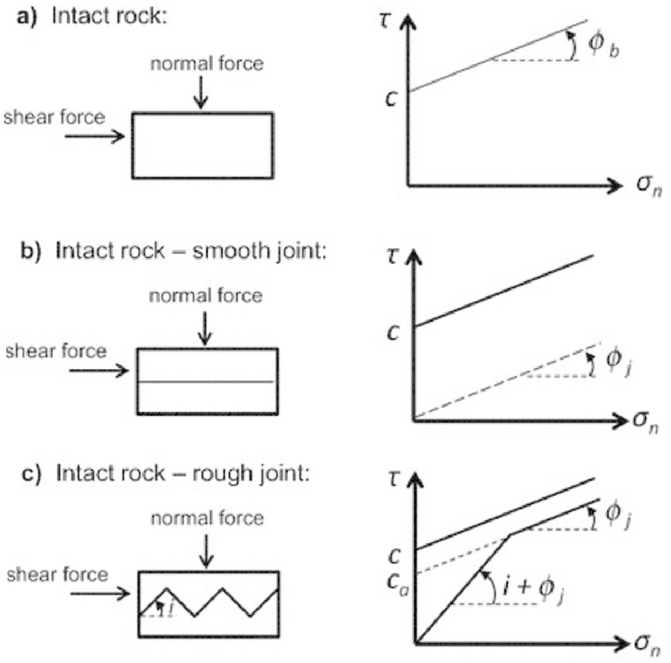

Figure 2.13: Shear strength of a rock specimen as function of normal stress. (a) intact rock; (b) smooth joint; (c) rough joint with a roughness angle of i, assuming $\phi_b = \phi_j$ [12].

Moreover, a sample with a rough joint shows a peak in the shear stress - shear displacement graph, followed by a loose of strength (softening) down to the residual condition. This is typical of materials with fragile behavior. On the contrary a sample with a smooth joint reveals hardening behavior as ductile materials. The comparison is presented in fig. 2.14.

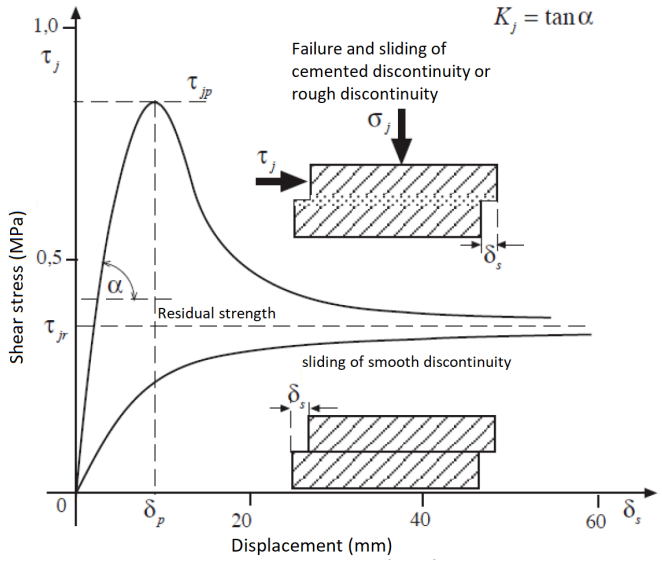

Figure 2.14: Shear stress vs shear displacement for a certain normal stress obtained through direct shear test on the same material with rough and smooth joints [13].

A natural discontinuity surface in hard rock is never as smooth as a sawn surface, the one used for determining the basal friction angle [10]. The roughness of the discontinuity influences the shear strength of the surface, for example according to the Patton saw-tooth model. This was one of the first model developed in literature based on a simple dilatancy mechanism shown in fig. 2.15 and described by eq. 2.2. The inclination of the asperities is responsible of the

increase in the shear strength up to the failure of the material and the consequent smoothing of the interface. A strong limitation comes from the assumption of a constant angle which is difficult to be estimated as representative for the whole mechanism.

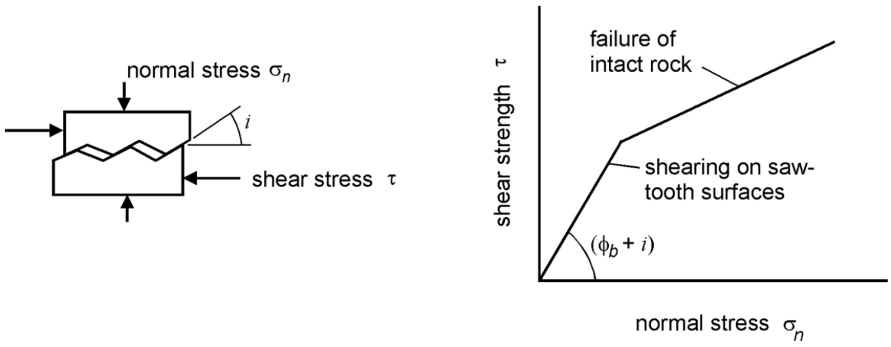

Figure 2.15: Patton saw-tooth model [11].

The limit value of shear stress is given by:

$$\tau = \sigma_n \tan(\phi_b + i) \tag{2.2}$$

where ϕ_b is the basal friction angle and i is the angle of the saw-tooth face. Eq. 2.2 is not valid for high compressive stresses, since in that case the teeth start to break off, due to local peaks of stress. On the contrary for low confining stress, the friction of the surface offers a further contribution to the shearing resistance of the rock.
To overcome these limitations, Barton in 1973 [14] proposed a non-linear criterion for rock joints which better represents the real behavior that is more gradual than abrupt, as was for Patton. The equation is written as follow:

$$\tau = \sigma_n \tan\left(\phi_r + \text{JRC}\ \log_{10}\left(\frac{\text{JCS}}{\sigma_n}\right)\right) \tag{2.3}$$

where JRC is the Joint Roughness Coefficient and JCS is the Joint-wall Compressive Strength. The step forward consists in the expression of the parameter i which is not constant anymore but depends on the two parameters JRC and JCS and on the applied normal stress. The JCS can be estimated using the Schmidt hammer directly on the joint, while JRC is a roughness index introduced by Barton in 1973 to quantify the surface roughness along a discontinuity. A comparison between the Barton criterion and the Mohr-Coulomb one is depicted in fig. 2.16.

Both values of JRC and JCS obtained from laboratory samples are not representative of the in-situ conditions but should be corrected for the scale effect as proposed by Barton and Bandis in 1983 [15]:

$$\text{JRC}_{\ n} = \text{JRC}_{\ 0}\left(\frac{L_n}{L_0}\right)^{-0.02JRC_0} \tag{2.4}$$

$$\text{JCS}_{\ n} = \text{JCS}_{\ 0}\left(\frac{L_n}{L_0}\right)^{-0.03JRC_0} \tag{2.5}$$

where $\text{JRC}_{\ 0}$, JCS_0 and L_0, that is the characteristic length of the discontinuity, are referred to the laboratory scale, while $\text{JRC}_{\ n}$, JCS_n and L_n are referred to the real site scale.

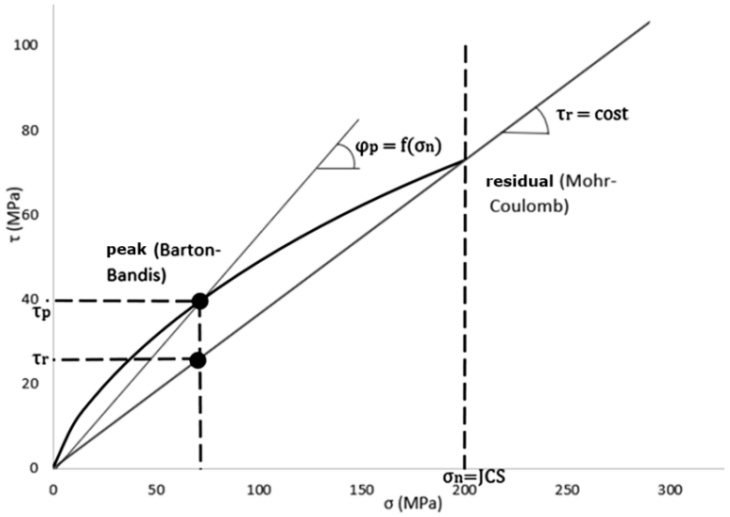

Figure 2.16: Comparison between Barton criterion and Mohr-Coulomb criterion [14].

2.3.2 Deformability

The discontinuities play also an important role in the deformability of the rock mass. In fig. 2.17 a plot of the stress-strain response of a rock mass containing discontinuities is presented with the various deformability moduli that can be defined [6]:

Initial tangent modulus: slope of the tangent to the initial concave upward section of the curve.

Elastic modulus: slope of the tangent to the linear section, usually specified as the 50% of the peak strength.

Recovery modulus: slope of the tangent to the unloading part of the response curve.

Deformation modulus: slope of the secant line between the origin and a specified stress level, usually assumed as the 50% of the peak strength.

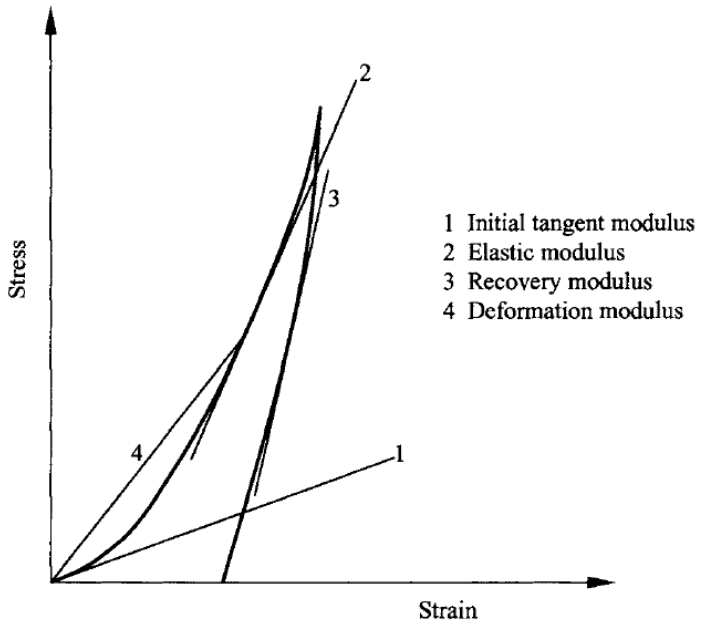

Figure 2.17: Stress-strain typical response of in-situ rock mass [6].

The deformability of a discontinuity is defined by the stiffness in the normal direction k_n and in the tangential direction k_t. They depends by the normal stress, the roughness and the filling material. Basically, the normal stiffness can be defined by the slope of the normal stress–relative normal displacement curve:

$$k_n = \frac{d\sigma_n}{du_n} \tag{2.6}$$

where σ_n is the applied normal stress on the discontinuity and u_n is the relative normal displacement. In the same way, the tangential stiffness can be defined as the slope of the shear stress–relative shear displacement curve:

$$k_s = \frac{d\tau}{du_s} \tag{2.7}$$

where τ is the shear stress on the discontinuity and u_n is the relative shear displacement. Fig. 2.18 shows the typical stress–relative displacement behavior of a discontinuity. Measuring the closure with different levels of applied normal stress, allows to define the response of a discontinuity that tends towards an asymptote corresponding to the complete sealing of the fracture. On the contrary, applying shear stress the relative shear displacement increases indefinitely [6].

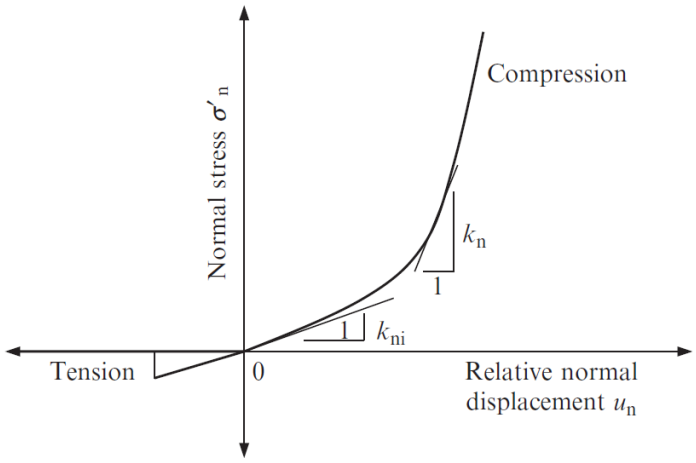

(a)

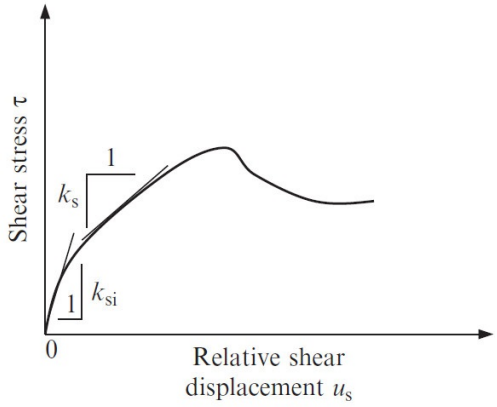

(b)

Figure 2.18: Typical stress-relative displacement relationship: (a) σ_n vs u_n; (b) τ vs u_s [6].

2.4 Roughness parameters

Statistical parameters are used to evaluate quantitatively the roughness of the profiles. Using empirical equations it is possible to correlate the roughness parameters with the JRC , which is necessary to assess the peak strength of the rock. One of the most affecting parameters on the empirical relationships is the sampling interval, so they are derived based on the sampling interval. One of the main reasons of this influence was investigated by Tatone and Grasselli in 2010 [8], as shown in fig. 2.19. In this document only the correlations for a sampling interval of 1 mm will be presented, since it is the resolution of the profilometer used in chapter 4.

2.4.1 Root–mean square of slopes: Z_2

Between the non-directional roughness parameters, Z_2 is one of the most used [16]. It is a statistical parameters that describes the root-mean square of the first derivative values of the profile. The equation is reported in the following:

$$Z_2 = \sqrt{\frac{1}{L}\int_{x=0}^{x=L}\left(\frac{dz}{dx}\right)^2 dx} = \sqrt{\frac{1}{L}\sum_{i=1}^{N-1}\frac{(z_{i+1}-z_i)^2}{(x_{i+1}-x_i)^2}} = \sqrt{\frac{1}{L}\sum_{i=1}^{N-1}(\tan\alpha_i)^2} \tag{2.8}$$

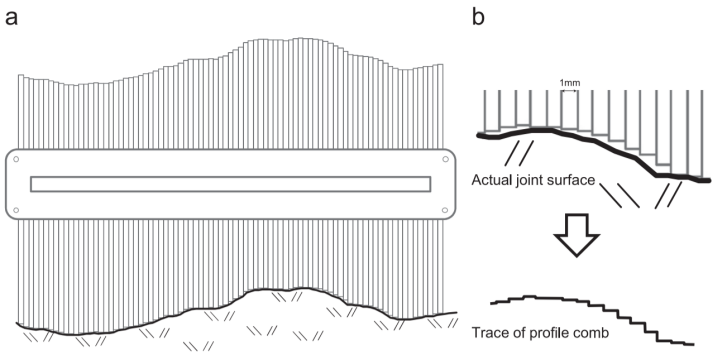

Figure 2.19: One of the sources of error using a profilometer to acquire a roughness profile (a): profilometer applied on a rough surface; (b): zoomed-in view of the pins, unable to capture the real profile features [8].

where L is the projected length of the profile, N is the number of discrete points of the profile and x_i, z_i their coordinates.
This parameter is strongly influenced by the sampling interval: increasing the sampling interval Z_2 increases while decreasing the sampling interval Z_2 decreases. Moreover, this parameter has some limitations in its definition, since it is based only on the mean inclination angle without considering the amplitudes. An example is shown in fig. 2.20 [17] where three different profiles with equal Z_2 parameter are compared.

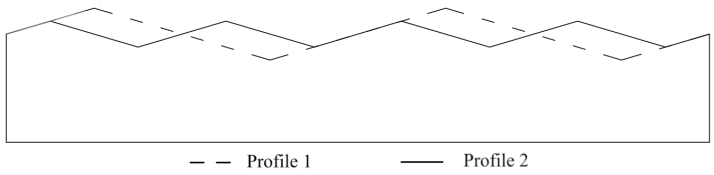

Figure 2.20: Three roughness profiles with the same mean inclination angle [17].

In literature, several empirical correlations between the parameters Z_2 and JRC were developed during the years. The following regression equations are provided by Yu and Vayssade [18]:

$$\text{JRC} = 64.22Z_2 - 2.31 \tag{2.9}$$

$$\text{JRC} = 66.86\tan(Z_2) - 2.57 \tag{2.10}$$

$$\text{JRC} = 51.31\sqrt{Z_2} - 11.78 \tag{2.11}$$

$$\text{JRC} = 21.32\log_{10}(Z_2) + 26.57 \tag{2.12}$$

An alternative was developed by Tatone and Grasselli in 2010 [8]:

$$\text{JRC} = 55.03(Z_2)^{0.74} - 6.1 \tag{2.13}$$

2.4.2 Roughness profile index: R_p

The roughness parameter R_p is also widely used for 2D analysis. In particular, it is defined as the ratio between the real profile length L_t and the nominal profile length L_n, as described in

the following equation:

$$R_p = \frac{L_t}{L_n} = \frac{\sum_{i=1}^{N-1} \sqrt{(x_{i+1} - x_i)^2 + (z_{i+1} - z_i)^2}}{L_n} \tag{2.14}$$

where L_n is the projected length of the profile, N is the number of discrete points of the profile and x_i, z_i their coordinates.
High values of R_p indicates highly rough profiles. This method is also strongly influenced by the sampling interval adopted in the acquisition of the profile. Two correlations with JRC are provided from Yu and Vayssade [18]:

$$\text{JRC} = 95.23\sqrt{R_p - 1} - 2.62 \tag{2.15}$$

$$\text{JRC} = 702.67\sqrt{R_p - 1} - 699.99 \tag{2.16}$$

Another correlation with JRC is provided by Tatone and Grasselli in 2010 [8]:

$$\text{JRC} = \left(0.0338 + \frac{0.00107}{\ln(R_p)}\right)^{-1} \tag{2.17}$$

2.4.3 Structure function of the profile: SF

The roughness parameter SF is defined as the structure function of the profile, as presented in the following equation:

$$SF = \frac{1}{L_n} \sum_{i=1}^{N-1} (z_{i+1} - z_i)^2 (x_{i+1} - x_i) = (Z_2 \Delta x)^2 \tag{2.18}$$

where L_n is the projected length of the profile, N is the number of discrete points of the profile and x_i, z_i their coordinates.
The following correlations with JRC , provided by Yu and Vayssade [18] are available:

$$\text{JRC} = 63.69\sqrt{SF} - 2.31 \tag{2.19}$$

$$\text{JRC} = 10.66 \log_{10}(SF) + 26.49 \tag{2.20}$$

2.4.4 Fractal dimension: D

According to Li and Wuang [19], the fractal dimension D describes the degree of variation of a profile from a reference line. The typical range of D goes from 1 for a perfectly smooth profile, up to 2 for an extremely rough profile. To estimate the value of D, the $h - L$ method firstly proposed by Xie and Pariseau [20] has been used.

$$D = \frac{\log_{10} 4}{\log_{10} 2(1 + \cos[\arctan(2h/L)])} \tag{2.21}$$

where L and h are defined as the average base length and the average height of high–order asperities of a joint, respectively.

$$h = \frac{1}{M} \sum_{i=1}^{M} h_i; \qquad L = \frac{1}{M} \sum_{i=1}^{M} L_i$$

A correlation between D and JRC is provided by Li and Huang [19]:

$$\text{JRC} = 118.89(D - 1)^{0.4343} \tag{2.22}$$

2.5 Ultrasonic test on rock

In order to estimate the dynamic elastic properties of the intact rock at the lab scale, the ultrasonic test is one of the most used non-destructive method since it is simple and very fast to be applied. Ultrasonic testing utilizes high frequency sound energy that propagates inside the material and the gradual loss of wave intensity traveling through the medium, also known as attenuation, is directly linked to micro-fabric changes in the material. It is the result of different processes acting together: beam spread, interference, absorption and scatter.

2.5.1 Wave propagation

Usually the test is performed either with compressional waves or shear waves. Compressional waves generate particle movements in the same direction of the propagation, while shear waves generate particle motion perpendicular to the direction of propagation. Fig. 2.21 shows the particle motion versus the direction of propagation for compressional waves and shear waves. Compression waves typically have a higher speed of propagation compared to shear waves in the

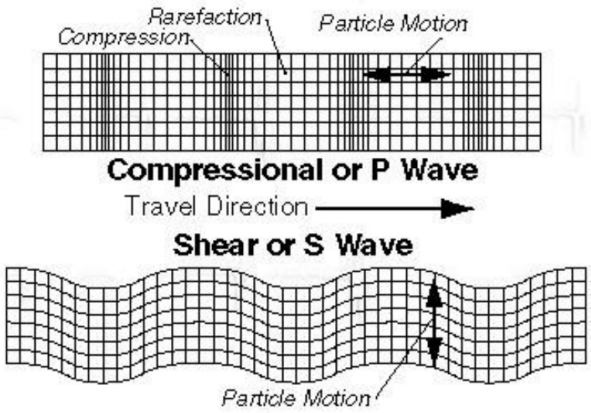

Figure 2.21: P-waves and S-waves propagation inside a medium. Source: `https://tinyurl.com/35xbjv79`

same material. This is because they cause changes in volume (that means changes in density), which are typically faster to transmit through a medium. On the contrary, shear waves produce only changes in the shape of the traveled medium, without changing volume. Moreover the velocity of propagation is proportional to the stiffness of the material in the direction of particle motion.

2.5.2 Beam spread

The beam spread is due to the divergence of the wave during its propagation and can be quantified by the whole angle of the wave θ in the far field, expressed by:

$$\sin\frac{\theta}{2} = C\lambda/d = CV/fd \tag{2.23}$$

where C is a commonly used constant for calculation of theoretical beam shapes that depends on how far the receiver get the signal emitted from the transducer (e.g. $C = 0.56$ if the amplitude has dropped by one half or $C = 1.08$ if the amplitude has dropped by one tenth), λ is the wavelength, d is the diameter of the transducer, f is the frequency and V is the wave velocity. As can be seen from the formula, influence factors of the beam spread are also the frequency and the diameter of the probe, so that increasing both the effect will be reduced. In any case the transducers should be aligned in the centerline of the wave to collect the maximum

amplitude. The "far field" is the zone in which the signal amplitude decreases monotonically with the increasing distance and it is located outside the "near field" that is the zone in which the signal amplitude fluctuates significantly, due to the influence of constructive and destructive interference, as shown in fig. 2.22.

The cause of this phenomenon is the alignment of the particle inside the medium, that is not

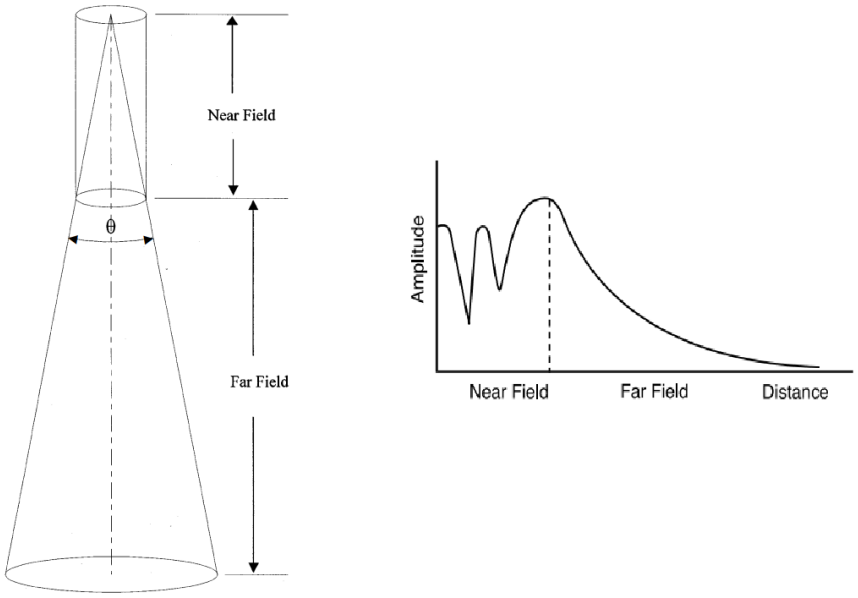

Figure 2.22: beam spread phenomenon in ultrasonic wave propagation [21]

always consistent with the propagation direction of the wave, therefore it results in a partial transfer of energy in different directions, with a certain angle. Selecting appropriate frequency and diameter of the transducer, this effect can be minimized.

2.5.3 Interference

In the "near field" zone, close to the source, important fluctuations of the signal amplitude take place. According to the Huygen's principle, this is due to constructive and destructive interferences of waves with different phases. For a flat and circular transducer the extension of the near field can be approximated by:

$$N = d^2/4\lambda = d^2 f/4V \tag{2.24}$$

The receiver should be placed as far as possible from the near field to avoid influences of this type.

2.5.4 Absorption and scattering

The absorption effect is due to the direct conversion of the wave energy into heat due to internal friction induced by the vibration. The scattering is a complex process that takes place at the microscopic interfaces such as grain boundaries or fissures within the medium. For a polycristalline material, according to [22], both the phenomena are proportional to the frequency and they can be described by a polynomial function α where the first term is referred to the absorption while the second term is referred to the scattering process:

$$\alpha = k_1 f^2 + k_2 d_g^y f^x \tag{2.25}$$

with k_1 and k_2 positive constants, y depending on the type of dominant scattering process and x positive constant higher than 2. Since, the absorption is proportional to the square of the

frequency while the scattering is proportional to a power higher than 2 of the frequency, this latter is the predominant phenomenon.

Therefore, considering also the low frictional effects induced by very low strains, the overall attenuation can be considered function only of the scattering process.

2.5.5 Elastic constants

The dynamic elastic properties can be assessed, starting from the results of ultrasonic tests in terms of velocity of elastic waves and using the following equations for isotropic and ideal elastic rocks:

$$\nu_d = \frac{(v_p/v_s)^2 - 2}{2[(v_p/v_s)^2 - 1]} \tag{2.26}$$

$$E_d = \frac{\rho v_p^2 (1 - 2\nu_d)(1 + \nu_d)}{1 - \nu_d} \tag{2.27}$$

$$G_d = \rho v_s^2 \tag{2.28}$$

where ν_d is the dynamic Poisson's ratio, ρ is the density of the material, v_p is the P-wave velocity, v_s is the S-wave velocity, E_d is the dynamic elastic modulus, G_d is the dynamic shear modulus.

Chapter 3

Experimental campaign

3.1 Rock lithotypes

The study will be focused on four different lithotypes, considering magmatic or metamorphic rocks that are likely to have brittle behavior around deep tunnels excavations, due to high stress releases. Three samples for each selected lithotype were provided by Generalmarmi in Collegno (Torino): Balma Syenite, Absolute Black gabbro, Pink Porriño granite, Carrara marble.

3.1.1 Syenite

The Syenite belongs to the intrusive igneous rock found in the pluton of Valle Cervo in Balma zone (hereinafter referred as "Syenite"). The structure is fine to medium-grained, very similar to the granite but with less quartz content in mineral composition. The massive presence of Potassium Feldspar gives the typical grey/violet color, while the black is given by biotite or pyroxene and the white by plagioclase. The texture is shown in fig. 3.1. The specimens dimensions were approximately 10x10x20 cm and the weights are reported in table 3.1.

Figure 3.1: Syenite texture. Scale in millimeters.

3.1.2 Absolute Black granite

The Absolute Black belongs to the Gabbro's family black granite rocks, intrusive and magmatic formations found in Zimbabwe, South Africa (hereinafter referred as "Black"). The structure

is fine-grained with very few anisotropy. The mineral composition is different from the Syenite, with higher content of Plagioclase instead of alkali feldspar. The texture is shown in fig. 3.2. The specimens dimensions were approximately 10x10x20 cm and the weights are reported in table 3.1.

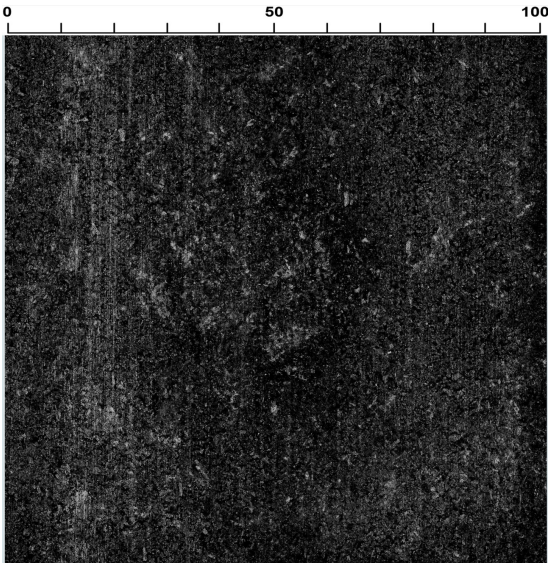

Figure 3.2: Absolute Black texture. Scale in millimeters.

3.1.3 Pink Porriño granite

The Pink Porriño granite belongs to them intrusive and igneous granite rocks quarried near Porriño, in the province of Pontevedra in Galicia, Spain (hereinafter referred as "Porriño"). The structure is medium-grained with a pink background given by the Potassium feldspar and grey, black and white minerals inclusions. The grey color is given by the quartz content, while the black color is given by biotite or pyroxene minerals and the white color by plagioclase, as for the Syenite. The texture is shown in fig. 3.3. The specimens dimensions were approximately 10x10x20 cm and the weights are reported in table 3.1.

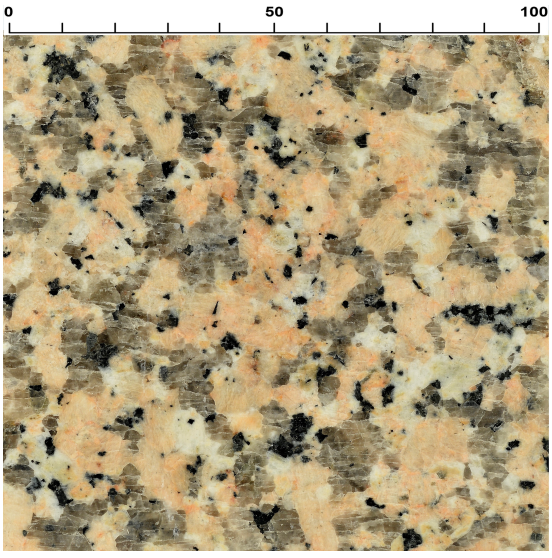

Figure 3.3: Porriño texture. Scale in millimeters.

3.1.4 Carrara marble

The Carrara marble (hereinafter referred as "Carrara") belongs to the Marble's family, metamorphic rocks that recrystallize under high pressures and heat, quarried near the city of Carrara, Italy. The structure is very homogeneous, with a white predominant background, as shown in fig. 3.4. The colour is given by its composition made of calcite crystals and some mica inclusions. The specimens dimensions were approximately 12x12x24 cm and the weights are reported in table 3.1.

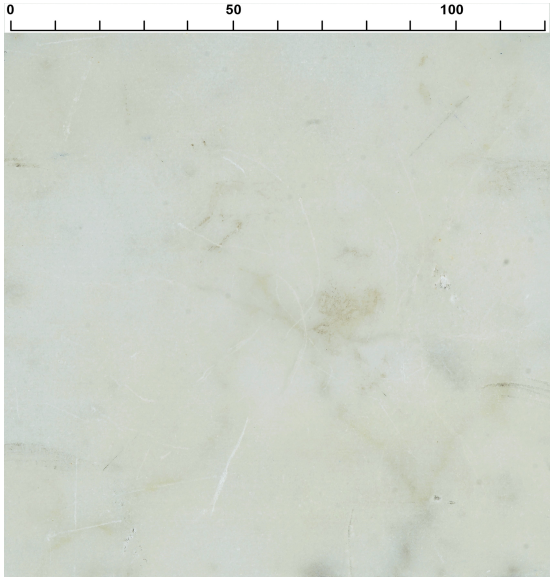

Figure 3.4: Carrara texture. Scale in millimeters.

Table 3.1: Dimensions and weights of the samples.

Lithotype	Sample	Weight kg	Density $\mathrm{kg\,m^{-3}}$
Syenite	1	5.78	2685.2
	2	5.75	2697.6
	3	5.68	2678.9
Absolute Black	1	6.06	3075.0
	2	6.03	3078.1
	3	6.02	3070.3
Pink Porriño	1	5.14	2608.6
	2	5.10	2615.8
	3	5.19	2621.2
Carrara	1	9.80	2733.4
	2	9.60	2698.2
	3	9.54	2692.8

3.1.5 QAPF diagram

The QAPF diagram is a classification tool used in mineralogy, particularly in the field of igneous rock classification. The acronym QAPF stands for Quartz, Alkali Feldspar, Plagioclase Feldspar, and Feldspathoid, that are the main minerals found in magmatic rocks. It is composed by a double triangular diagram which allows to classify the rocks based on the relative proportion of the minerals. Syenite, Absolute Black and Porriño are igneous rocks and can be classified using

the QAPF diagram. In fig. 3.5 the red zone identifies the Syenite family, the blue zone identifies the Gabbro family and the green zone identifies the Granite family.

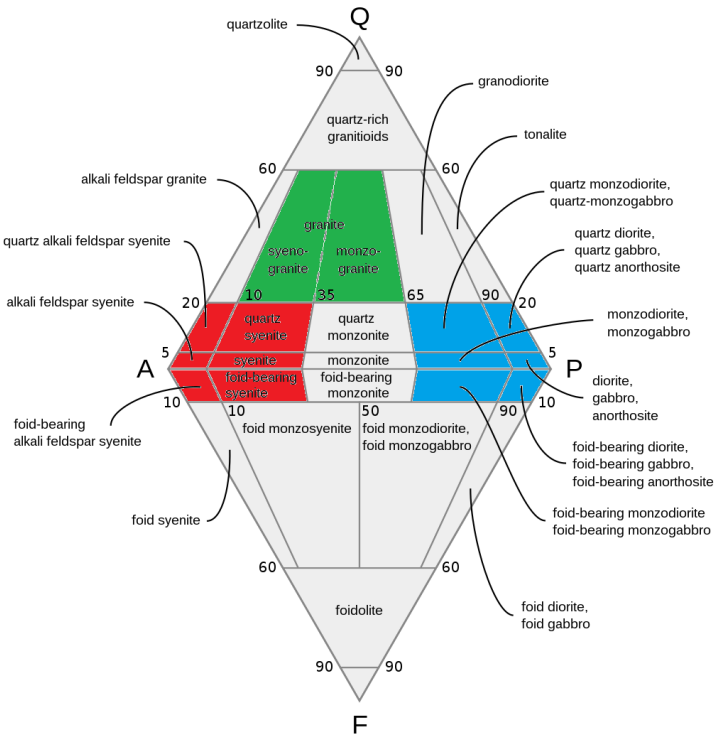

Figure 3.5: QAPF diagram. Red: Syenite family; Blue: Gabbro family; Green: Granite family.

3.2 Ultrasonic tests on intact rock specimens

3.2.1 Test procedure

To investigate the dynamic properties of the specimens and to evaluate the deformability characteristics of the fracture, such as normal and tangential stiffness, an ultrasonic testing instrument has been used. It is the Pundit PL-200 from Proceq SA, provided by MASTRLAB (MAterial and STRucture LABoratory) at Politecnico di Torino. This instrument is a wave generator that includes an oscilloscope to receive the signal and an automatical arrival time determination for both P and S-waves. It has a bandwidth from 20 to 500 kHz with a measuring resolution of 0.1 µs, a pulse voltage from ±100 to ±450 V and a receiver gain from 1 to 10000x (0 to 80 dB). The

Figure 3.6: Ultrasonic testing instrument Pundit PL-200.

tests are performed for both P-waves and S-waves, allowing to determine normal and tangential stiffness properties.
P-waves particle displacements are parallel to the direction of propagation and consequently, sensitive to the normal stiffness. S-waves particles move perpendicularly to the wave direction and so their motion is sensitive to the tangential stiffness [23]. The compression waves are induced by two 250 kHz Proceq transducers with a diameter of 28 mm, shown in fig. 3.7 (a). To allow the measurement of the shear wave velocity, S-waves transducers with a diameter of 41 mm and a frequency of 250 kHz have been used, as shown in fig. 3.7 (b). Both sets of transducers have been provided by the Environmental Engineering Department of Politecnico di Torino (DIATI). To connect the P-waves transducers to the specimen, a gel for ultrasound transmission producted by "La Tecnocarta" has been used, in order to create a suction cup effect acting as a bond with the material, reducing the acoustic impedance and the reflection. The experimental setups are shown in fig. 3.8. The S-waves transducer are attached to the sample surfaces using the phenyl salicylate, a white solid salt that becomes liquid when heated and recrystallizes when cooled. It is also known as "Salol" and it is produced by Sigma-Aldrich. The probes are pressed against the sample until the salt is solified, to release any bubble of air ensuring continuity between the probe itself and the sample. The setup is shown in fig. 3.8 (b).

Three directions of the specimen are defined "a", "b" or "c", as presented in fig. 3.9 with the local reference system. For both P-waves and S-waves, the tests are performed along the main directions of the sample as shown in fig. 3.10 (a) and fig. 3.10 (b): one longitudinal and two transversal directions. Moreover, in the longitudinal direction "a", the S-wave propagation is tested producing the particle vibration in two orthogonal planes, aligning the transducers with the "x" and "z" directions of the local reference system.

In summary, for each sample three P-waves propagation are tested (along dir."a", "b","c") and four S-waves propagation (along dir."a", dir. "b", dir."c" - vibration plane "z", dir."a" - vibration plane "x").

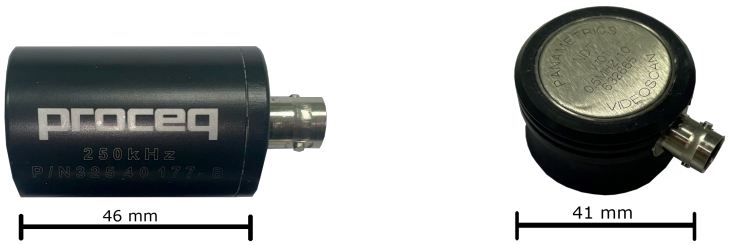

(a) (b)

Figure 3.7: (a): P-wave Proceq transducer; (b): S-wave transducer Parametrics-NDT V151.

(a) (b)

Figure 3.8: (a): Setup for P-waves velocity measurement on Pink Porriño sample; (b): Setup for S-waves velocity measurement on Absolute Black sample.

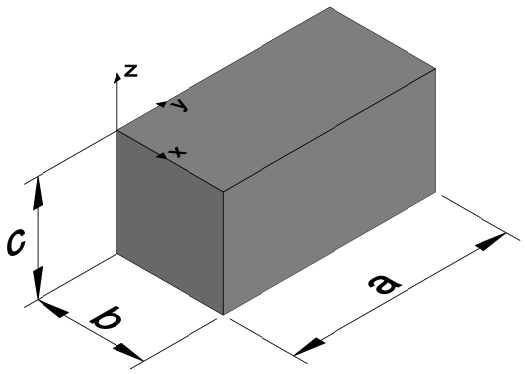

Figure 3.9: Definition of the directions of propagation in the sample and local reference system.

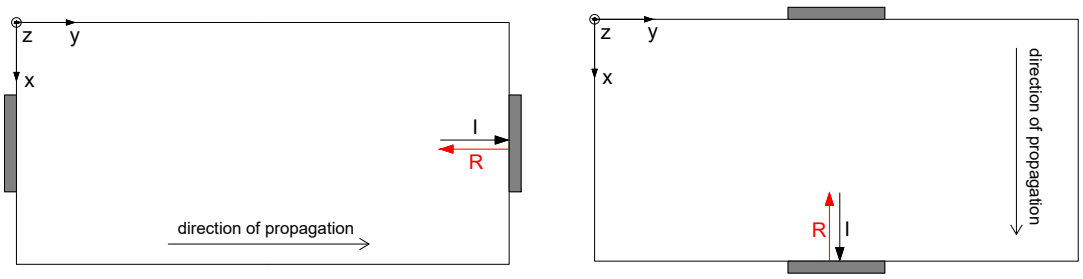

(a) (b)

Figure 3.10: (a): Scheme of wave transmission in direction “a” of the rock sample; (b): Scheme of wave transmission in direction “b” and “c” of the rock sample.

3.2.2 Test results

As an example, the signals resulting from the Pundit ultrasonic instrument for the first sample of Absolute Black are presented in the following pictures. The other waveforms are included in the Appendix A for the sake of readability. The arrival times for each intact rock sample are summarized in the table 3.2. The dynamic deformability properties calculated using eq. 2.27 and eq. 2.26, are reported in table 3.3.

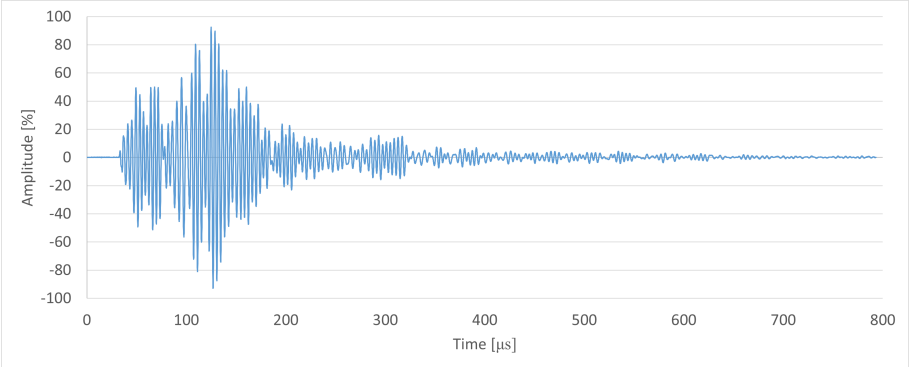

Figure 3.11: Recorded signal of P-waves in direction "a" for Absolute Black sample 1.

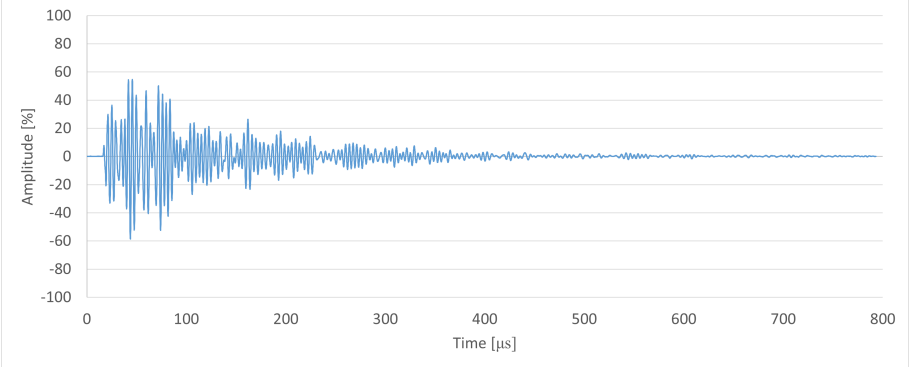

Figure 3.12: Recorded signal of P-waves in direction "b" for Absolute Black sample 1.

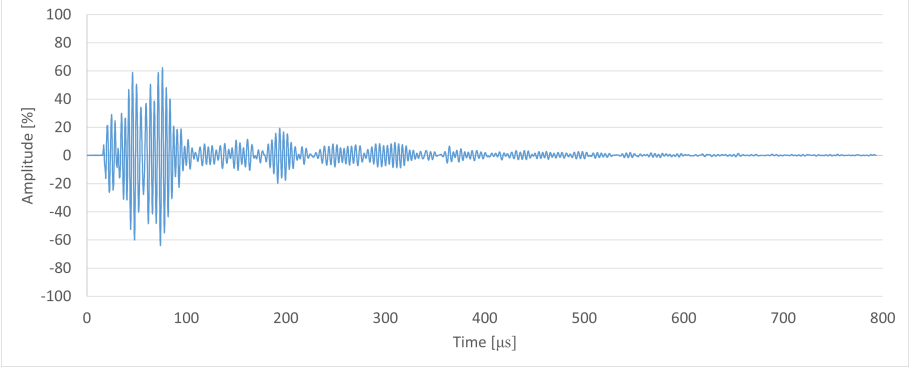

Figure 3.13: Recorded signal of P-waves in direction "c" for Absolute Black sample 1.

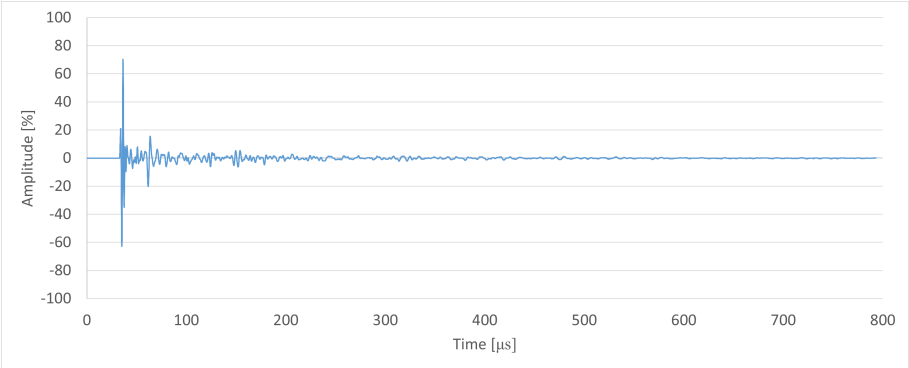

Figure 3.14: Recorded signal on vibration plane "x" of S-waves in direction "a" for Absolute Black sample 1.

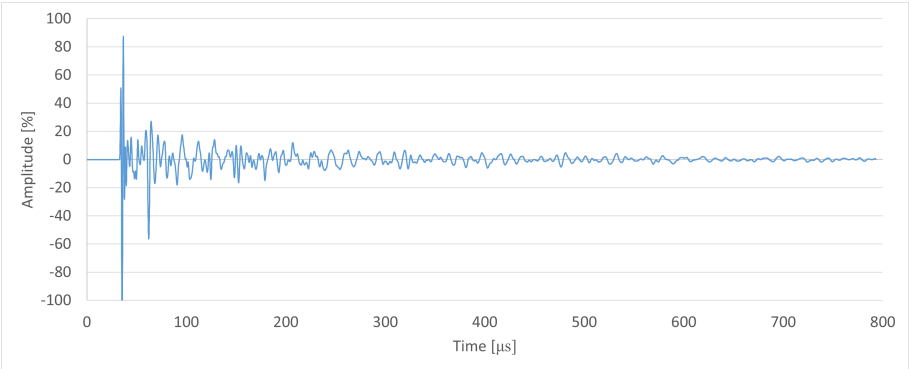

Figure 3.15: Recorded signal on vibration plane "z" of S-waves in direction "a" for Absolute Black sample 1.

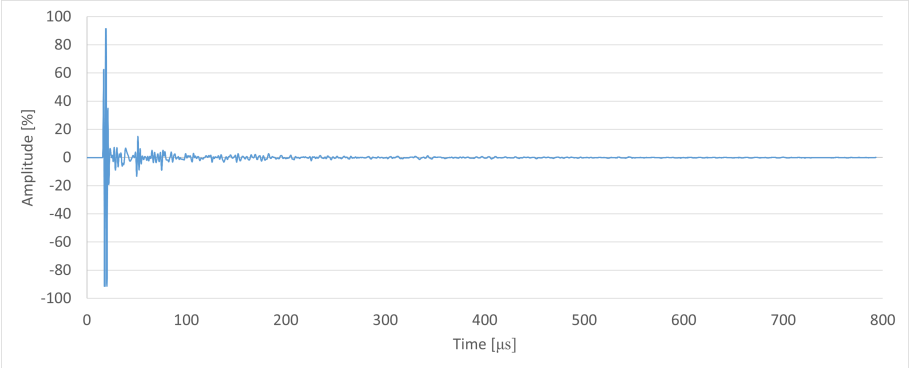

Figure 3.16: Recorded signal on vibration plane "z" of S-waves in direction "b" for Absolute Black sample 1.

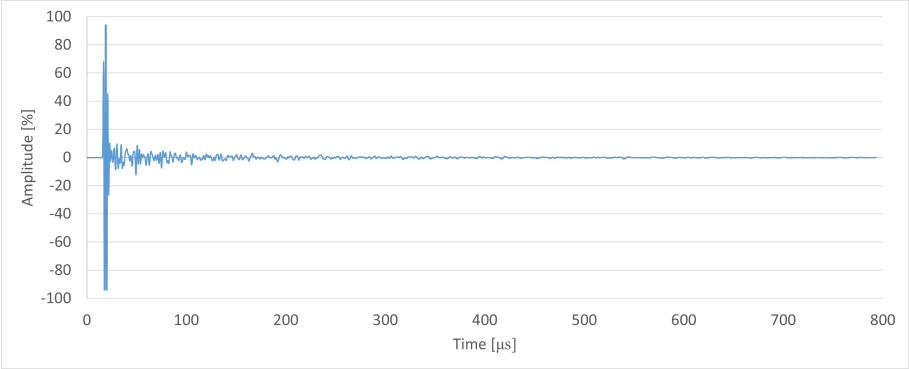

Figure 3.17: Recorded signal on vibration plane "z" of S-waves in direction "c" for Absolute Black sample 1.

Table 3.2: Arrival times of P-waves and S-waves trough the intact rock specimens.

		dir. "a"			dir. "b"		dir. "c"	
Lithotype	Sample	P-wave	S-wave		P-wave	S-wave	P-wave	S-wave
			x	z		z		z
		µs	µs		µs	µs	µs	µs
Syenite	1	38	70	70	21	36	21	37
	2	42	79	79	21	37	19	33
	3	39	72	72	21	36	21	37
Absolute Black	1	32	60	60	16	26	15	25
	2	32	60	60	16	27	16	26
	3	31	58	58	16	27	15	25
Pink Porriño	1	44	80	80	26	45	20	35
	2	44	83	83	26	47	19	33
	3	44	80	81	25	44	20	35
Carrara	1	42	79	79	21	37	21	37
	2	42	78	78	21	36	20	35
	3	41	77	77	20	36	20	35

Table 3.3: Dynamic deformability parameters obtained from ultrasonic propagation tests; E: Young's modulus; ν: Poisson's ratio.

Lithotype	E_d	ν_d
-	GPa	-
Syenite	45.6	0.33
Absolute Black	83.6	0.33
Porriño	35.9	0.33
Carrara	63.1	0.33

3.3 Unconfined compression tests

The unconfined compression test allows to determine the UCS (Unconfined Compressive Strength) of the investigated material. It is a common laboratory test for rocks, in which there is no confinement to the specimen and the axial load is applied by a plate with displacement or force controlled rate. The test is intended to carry out the strength of the material and its deformability.
In this case the tests are performed to characterize the deformability of the materials without arriving to the failure, in order to be able to recover the intact samples after the tests. Since the specimens are not cylindrical, the test is designed according to the UNI EN 14580/2005 for the determination of the static elastic modulus of natural rock prisms [24].

3.3.1 Test procedure

The setup has to be prepared according to the UNI EN 14580/2005 [24], that states the following:

> The specimens shall be prisms with a plan dimension of minimum 50 mm and not less than 10 times the largest cristal grain size. The height to plan dimension ratio shall be between 2 and 4. The material surfaces, in contact with the plates, shall be planar with a tolerance of 0.1 mm and both shall be perpendicular to the axis of the specimen with a tolerance of 0.01 radians.

To meet the latter requirements, the samples were finished with a surface grinder machine on both the contact surfaces. This operation was performed in the Environmental Engineering department (DIATI) at Politecnico di Torino, using the grinding machine shown in fig. 3.18.

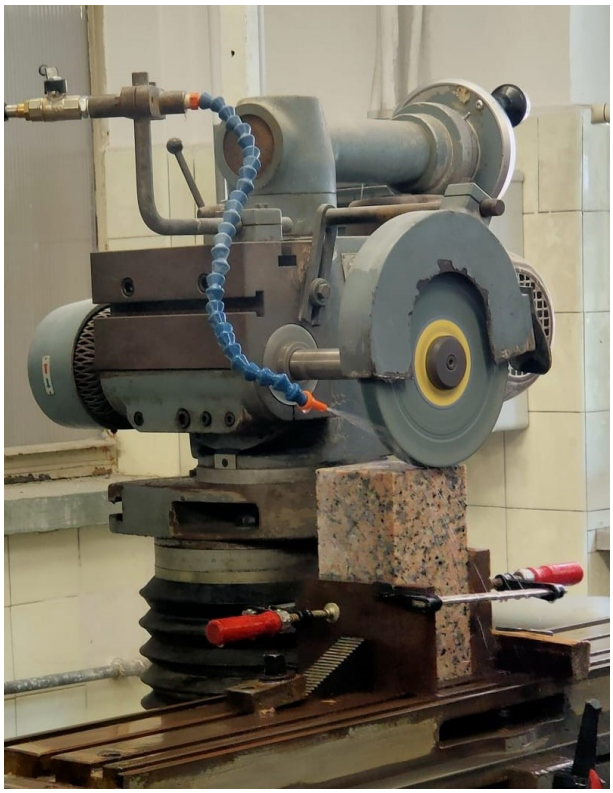

Figure 3.18: Surface grinding process on the contact surfaces - Porriño granite sample.

The compression tests were performed at the MASTRLAB (MAterial and STRucture LABoratory) in the Structural, Building and Geotechnical Engineering department (DISEG) at Po-

litecnico di Torino using a 5000 kN Galdabini testing machine able to control the force through a oil-based hydraulic pressure transducer. Following the aforementioned standard, the strain measuring devices were two, fixed parallel and symmetrical to the axis of the specimen. Moreover they should be longer than the larger plan dimension of the sample, as shown in the scheme in fig. 3.19.

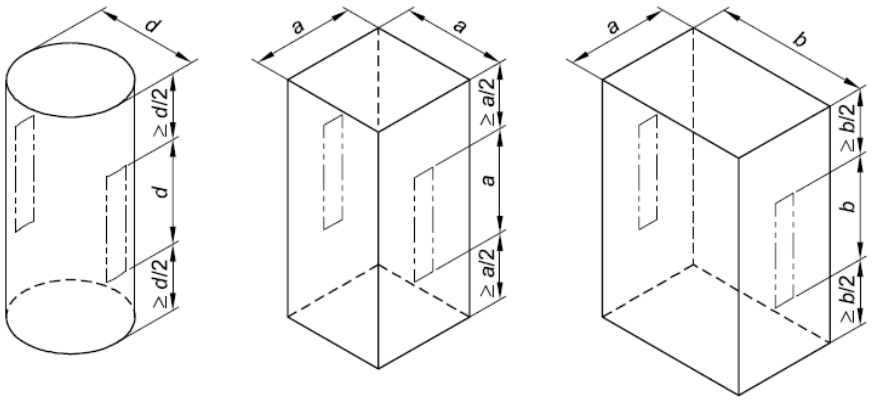

Figure 3.19: Displacement measuring devices size [24].

The sensors utilized to measure the axial and radial displacements are LVDT (Linear Variable Displacement Transducer) from HBM GmbH. In particular, the axial displacements are measured by two DD1 sensors (fig. 3.20), kept in place by two springs, on two parallel faces of the sample with a measurement base of 10 mm. The maximum nominal displacement of the DD1 sensors is ± 2.5 mm and the sensitivity is ± 2.5 mV/V. The data of axial displacements are directly collected by the software linked to the machine itself with a smart sampling frequency, to reduce the quantity of data stored when no significant changes happen. The radial displacements were measured by two LVDT sensors (model WI/2mm-T from HBM), shown in fig. 3.21, placed with a two-component glue on 50 mm measurement bases with a maximum nominal displacement of ± 2 mm and a sensitivity of ± 2 mV/V.

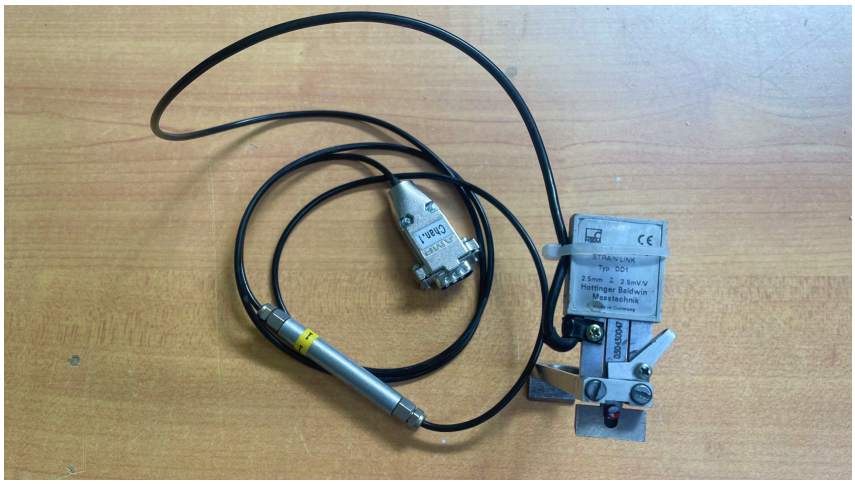

Figure 3.20: LVDT HBM DD1 2.5 mm transducer for axial displacements.

The measuring amplifier module is the MX840B model by HBM, shown in fig. 3.22. The data of the radial displacements are collected by an external data acquisition module in a different time-frame and with a constant frequency of 20 Hz, therefore it will be necessary to resample the axial displacements measurements consistently to the radial measurements and to realign both in a common origin in time. The instrumented sample is shown in fig. 3.23.

Figure 3.21: LVDT HBM WI/2mm-T transducer for radial displacements.

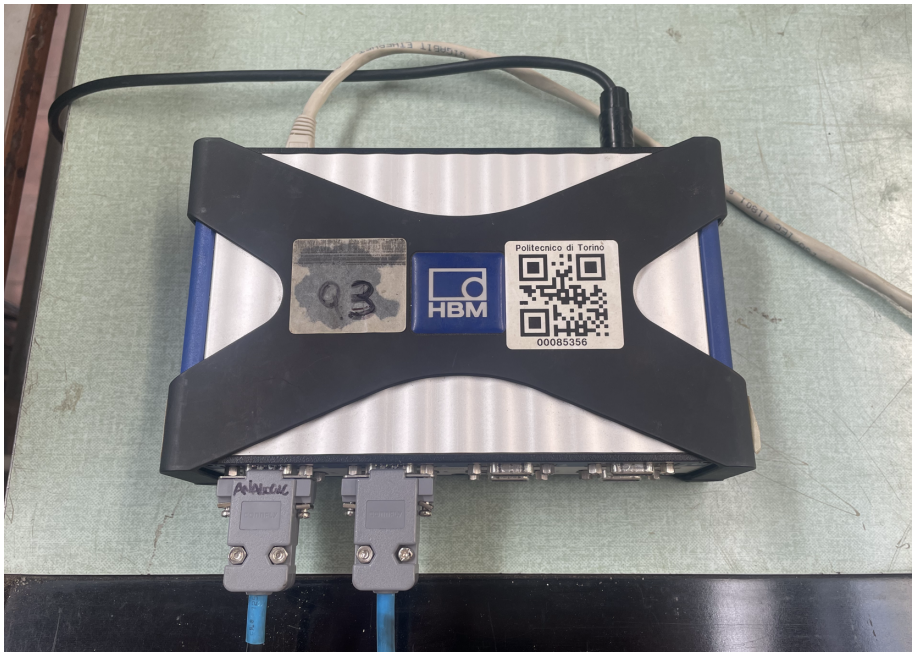

Figure 3.22: HBM MX840B measuring amplifier module.

Usually in this type of test, the specimens are failed to obtain the complete stress-strain response curve that allows the evaluation of the strength and of the deformability at the desired level of stress. But in this case the test is only aimed at obtaining the deformability parameters and moreover the breaking must be avoided because to replicate the brittle phenomenon during tunnels excavation, the specimens need to be splitted with a splitting test that induces a tensile crack. So the UCS remains unknown and it can only be assumed from literature. The loads to be applied to the specimens were calculated based on a percentage of the assumed UCS to remain in the elastic part of the behavior avoiding damages. The geometrical dimensions of the specimens were obtained averaging the measurements of their edges, taken using a digital caliper.
The sample was centered with respect to the plates of the machine and subjected to loading/unloading cycles. The tests were performed in a force-controlled scheme, with a loading rate equal to 0.75 MPa/s for all the specimens, according both to the UNI EN 14580/2005 [24] and to

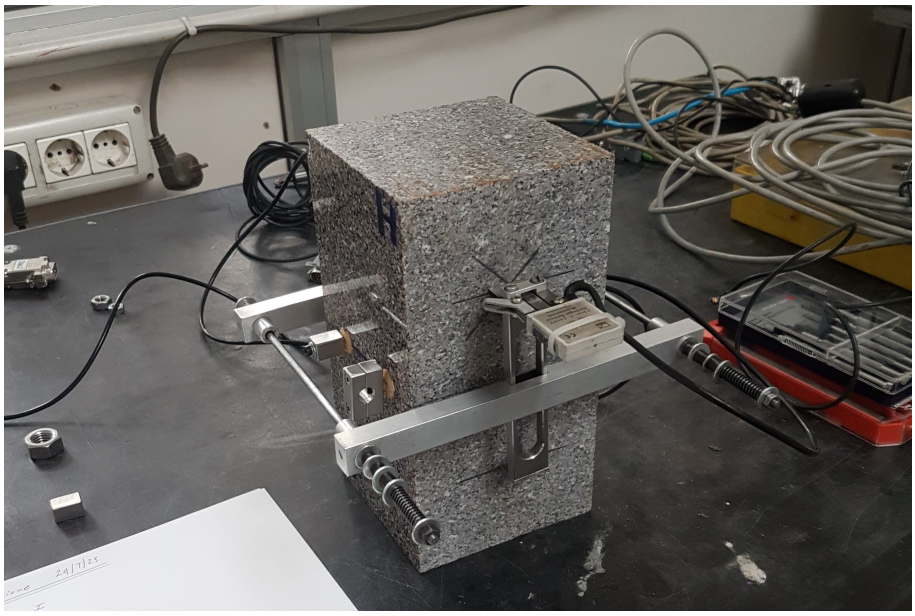

Figure 3.23: instrumented sample of Syenite.

the "Suggested methods for determination of the deformability of rock materials" given in the "Blue Book" by the ISRM (International Society for Rock Mechanics) [9]. Two loading/unloading cycles are recorded, up to the 50 % and 70 % of the assumed value of UCS, respectively, as shown in figure 3.24. The first loading allows the correct adjustment of the specimen-plates contact conditions, while the second loading is used to determine the mechanical parameters. After each loading or unloading step, the force is kept constant for 5 s generating a plateau. Whenever the time-displacements curve showed an abrupt change in its slope during the test, due to a possible overestimation of the strength based on the existing literature, the assumed value of UCS was decreased for the other samples of the same lithotype (not already tested), to avoid damages or microcracks within the material. The section of each sample is used in order to compute the force to be applied to reach the desired level of stress for each step of the test. A summary of the mean area of the sections in contact with the plates, the mean heights and the loads applied to each sample for the two load steps, is presented in the table 3.4.

Table 3.4: geometrical data and loads applied to the samples.

Lithotype	Sample	Area (avg)	height (avg)	UCS	1st Load		2nd Load	
-	-	mm^2	mm	MPa	MPa	kN	MPa	kN
Syenite	1	10761	200.0	150	75	807	105	1130
	2	10770	196.6	150	75	808	105	1131
	3	10464	199.7	150	75	785	105	1099
Absolute Black	1	9829	200.6	270	135	1327	189	1858
	2	9811	199.4	270	135	1324	189	1854
	3	9808	199.8	270	135	1324	189	1854
Pink Porriño	1	9952	197.9	140	70	697	98	975
	2	9814	198.0	140	70	687	98	962
	3	9956	198.9	100	50	498	70	697
Carrara	1	15142	238.7	130	65	984	91	1378
	2	14860	237.6	110	55	817	77	1144
	3	14717	238.9	100	50	736	70	1030

The sample is centered with respect to the plates of the machine and the load is applied with the loading rate previously discussed (0.75 MPa/s). The complete setup is shown in fig. 3.25.

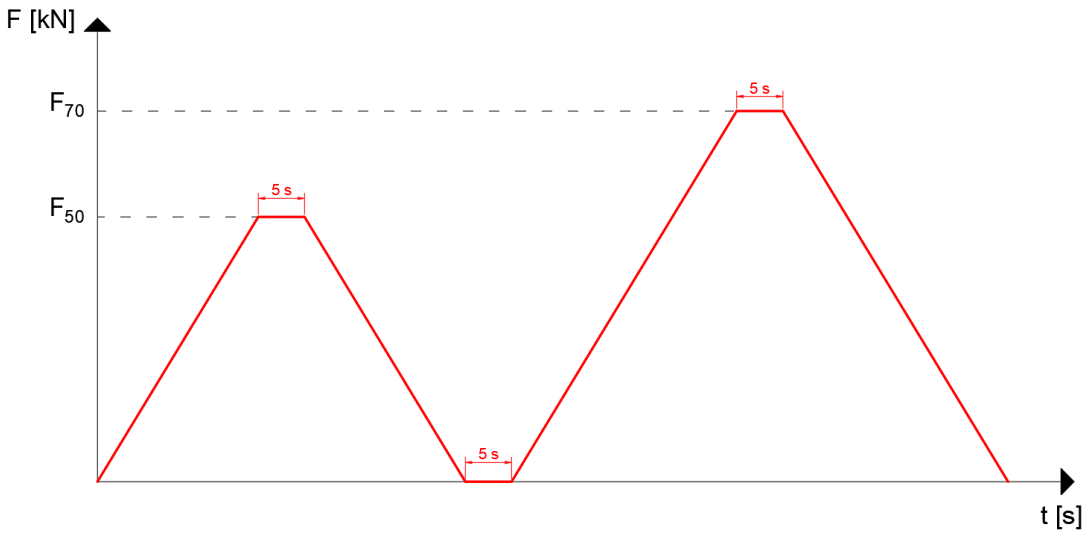

Figure 3.24: force vs time of a typical test. F_{50} : force corresponding to a stress equal to the 50% of the UCS; F_{70} : force corresponding to a stress equal to the 70% of the UCS.

Figure 3.25: Complete setup for compression test - Syenite specimen.

3.3.2 Test results

As already explained, the axial and radial measurements are recorded in two different time-frames and with different sampling frequency. Therefore the alignment, the resampling and consequently the smoothing of the signals obtained from the sensors are performed using a Matlab code based on the moving mean (MM), creating average sections of the recorded signal in time. In particular the utilized sampling interval is equal to 1 s. The alignment of radial and axial deformations is performed referring to the first point of the plateau immediately after the first unloading cycle, which is clearly defined in all the curves. In figures 3.26, 3.28, 3.30, 3.32 the resampling of the force in time is presented with blue points while the resampled and aligned signal in time of the radial displacement is shown with red dots. In the following graphs, the positive values of the radial deformation are conventionally referred to extensions.

In the following figures, the axial stress - axial strain and axial stress - radial strain paths are presented for one sample of each lithotype, referring to the average strain collected by the two pairs of sensors. The other results are included in the Appendix B for the sake of readability.

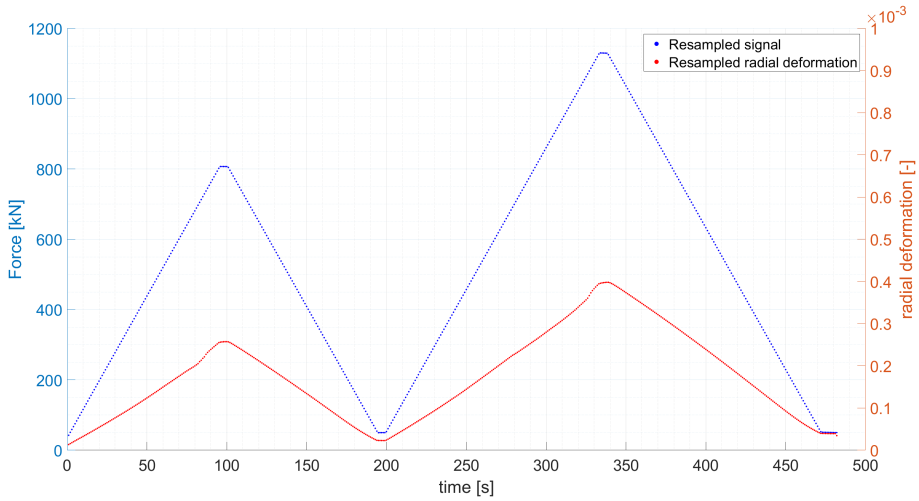

Figure 3.26: Syenite sample 1. blue: force vs time; red: radial strain vs time.

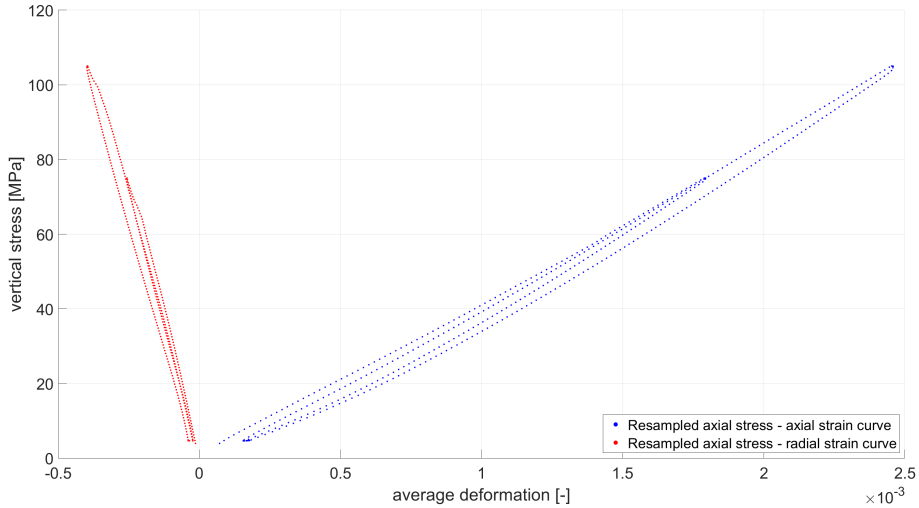

Figure 3.27: Syenite sample 1. blue: stress vs axial strain; red: stress vs radial strain.

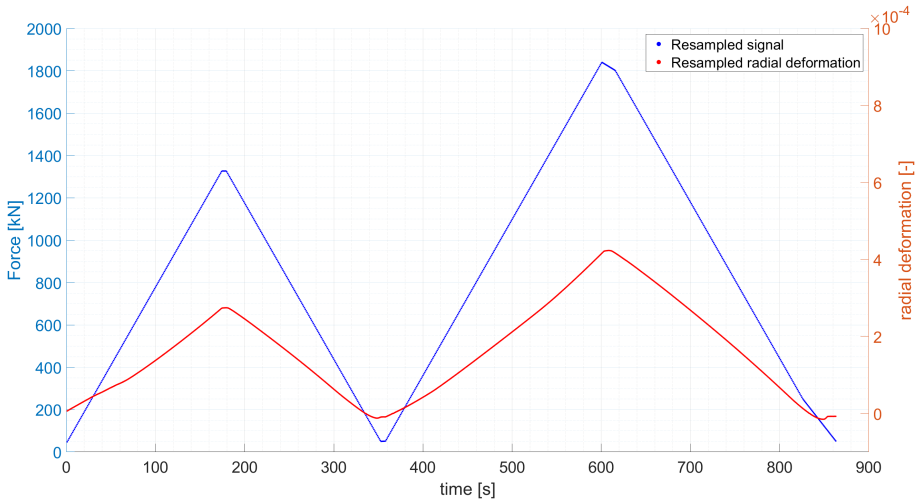

Figure 3.28: Absolute Black sample 1. blue: force vs time; red: radial strain vs time.

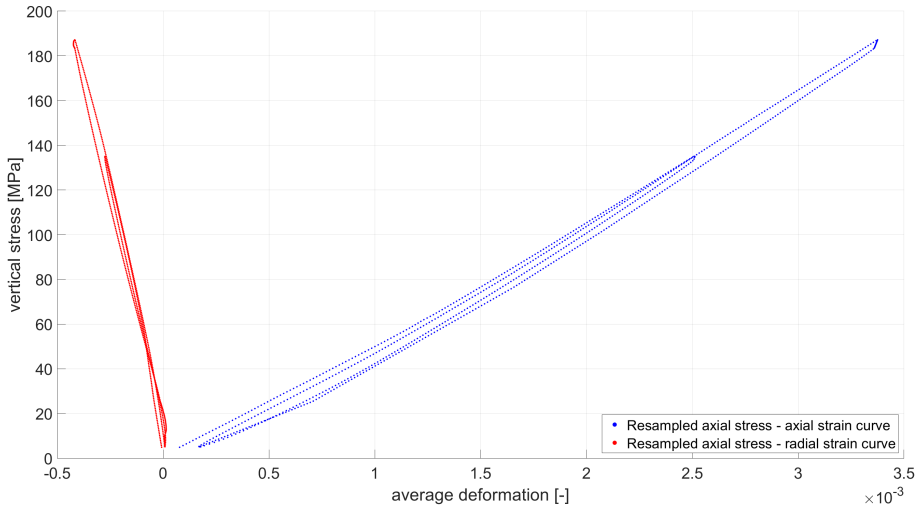

Figure 3.29: Absolute Black sample 1. blue: stress vs axial strain; red: stress vs radial strain.

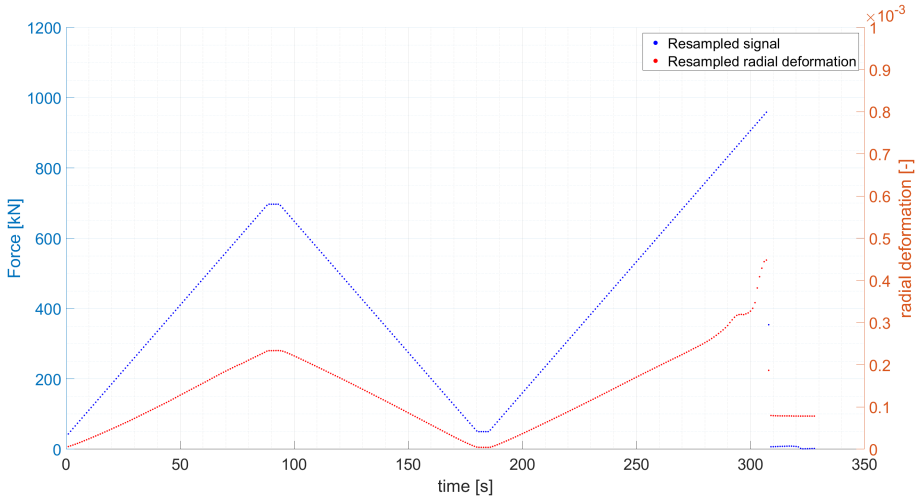

Figure 3.30: Porriño sample 1. blue: force vs time; red: radial strain vs time.

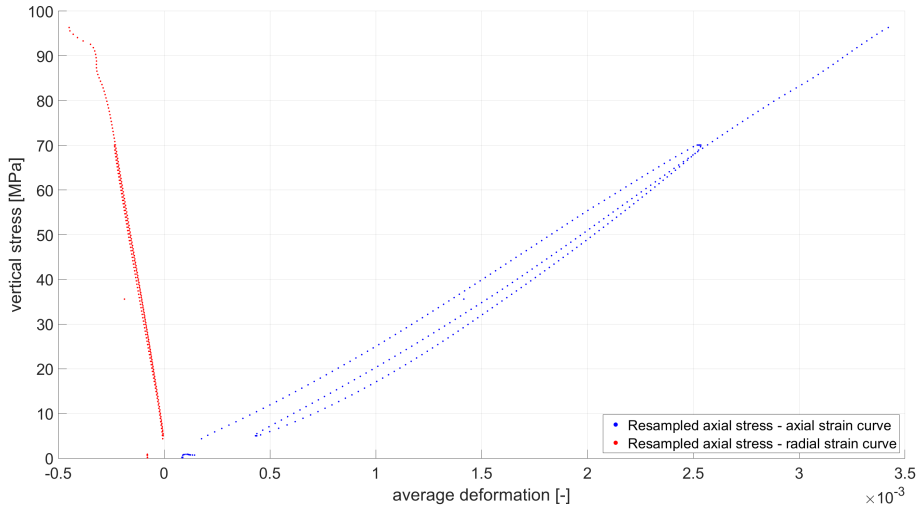

Figure 3.31: Porriño sample 1. blue: stress vs axial strain; red: stress vs radial strain.

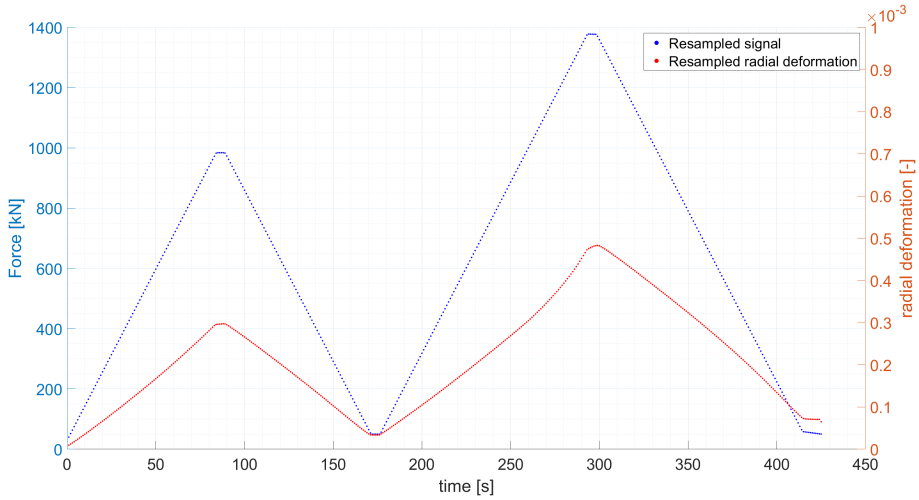

Figure 3.32: Carrara sample 1. blue: force vs time; red: radial strain vs time.

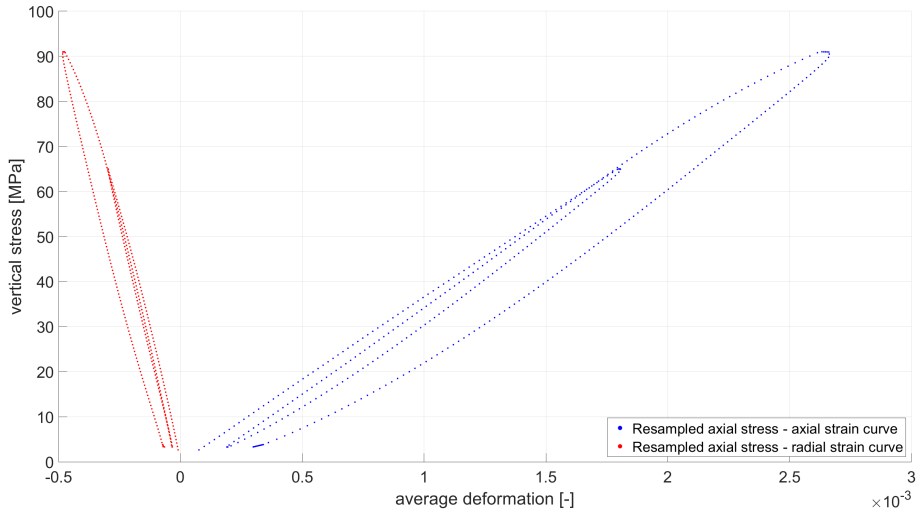

Figure 3.33: Carrara sample 1. blue: stress vs axial strain; red: stress vs radial strain.

3.3.3 Evaluation of the deformability parameters

The tangent elastic modulus is evaluated according to the ISRM suggestions: as the slope of the axial stress - axial strain curve at the 50% of the UCS [9].

$$E_{50} = \left(\frac{d\sigma}{d\varepsilon}\right)_{50} \tag{3.1}$$

The Poisson's coefficient can be evaluated in the same way as the ratio between the slope of the axial stress - axial strain curve and the slope of the axial stress - radial strain curve, both at the 50% of the UCS [9]:

$$\nu_{50} = -\left(\frac{d\varepsilon_r}{d\varepsilon_a}\right)_{50} \tag{3.2}$$

In the theoretical case of a continuous experimental curve, the mathematical derivative as expressed in eq. 3.2 can be used. In the case of discrete measurements, a regression line is used to fit an interval around the point of interest. The influence on the Young's modulus and Poisson's ratio of the number of points considered is shown in thew following figures. Using the converged values of the graphs, the results in terms of Young's modulus and Poisson's ratio for each specimen, are evaluated and summarized in table 3.5.

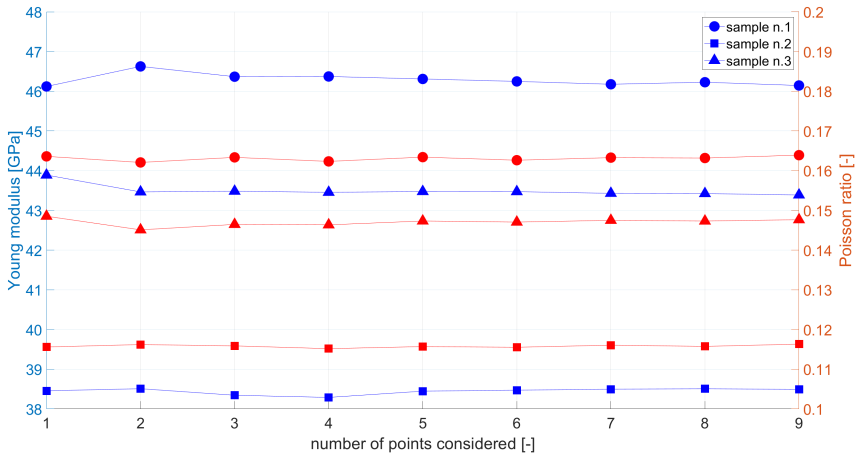

Figure 3.34: Syenite samples. blue: Young's modulus vs number of points in the fit interval; red: Poisson's ratio vs number of points in the fit interval.

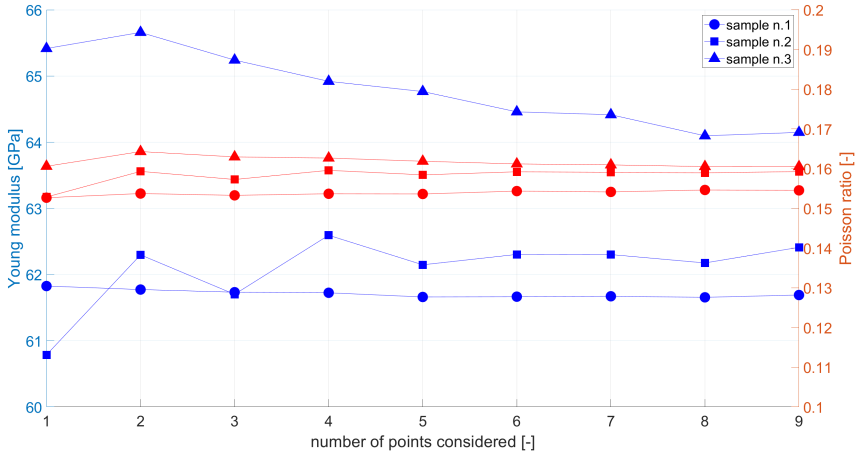

Figure 3.35: Absolute Black samples. blue: Young's modulus vs number of points in the fit interval; red: Poisson's ratio vs number of points in the fit interval.

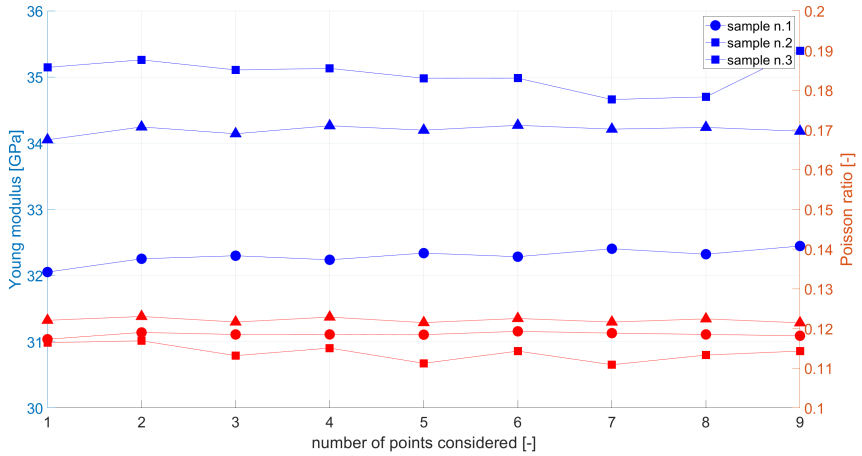

Figure 3.36: Porriño samples. blue: Young's modulus vs number of points in the fit interval; red: Poisson's ratio vs number of points in the fit interval.

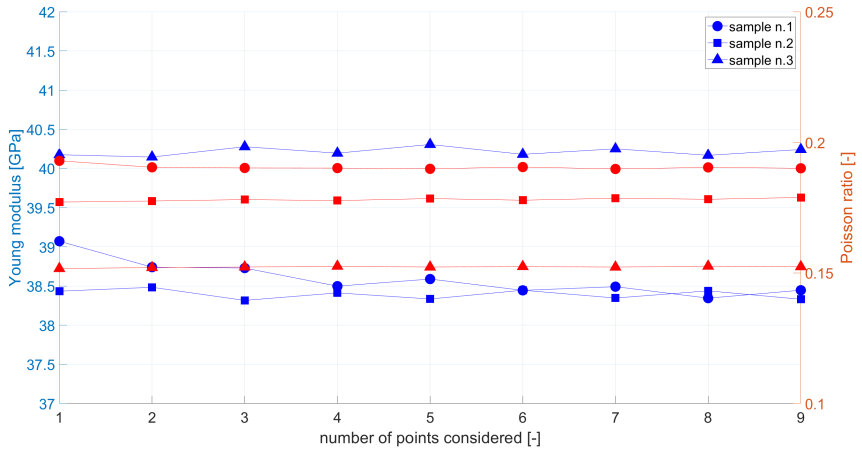

Figure 3.37: Carrara samples. blue: Young's modulus vs number of points in the fit interval; red: Poisson's ratio vs number of points in the fit interval.

Table 3.5: Static deformability parameters obtained from the unconfined compression tests; E: Young's modulus; ν: Poisson's ratio.

Lithotype	Sample	E_{50}	Average	ν_{50}	Average
-	-	GPa	GPa	-	-
Syenite	1	46.3	42.7 ± 3.3	0.16	0.14 ± 0.02
	2	38.3		0.12	
	3	43.5		0.15	
Absolute Black	1	61.7	62.9 ± 1.5	0.16	0.16 ± 0.00
	2	61.9		0.16	
	3	65		0.16	
Porriño	1	32.2	33.8 ± 1.2	0.12	0.12 ± 0.01
	2	35.1		0.11	
	3	34.2		0.12	
Carrara	1	38.7	39.1 ± 0.8	0.19	0.17 ± 0.02
	2	38.4		0.18	
	3	40.2		0.15	

3.4 Splitting tests

3.4.1 Test procedure

In order to reproduce the collapse of boreholes in rocks due to high compressive stress, such as the tunneling excavation, tensile cracks need to be generated. Rockburst and spalling are induced by compressive stresses with a mechanism not very well understood at present, but involving tensile cracking from a microscopic point of view [25]. The aim is to perform a vertical splitting test to generate a clean and sudden crack similar to the wedge splitting test for concrete or concrete-like materials, deeply treated by E. Brühwiler and F.H. Wittmann [26].

Tensile fractures are generated by pulling apart of the two side, as shown in fig. 3.38-Mode I. Shear fractures generated by sliding are shown in fig. 3.38-Mode II and III. Tensile fractures are generally more irregular, while shear stresses tend to destroy asperities, leaving the strength close to residual strength. An important factor is the direction of stresses which influences the anisotropy of the fracture.

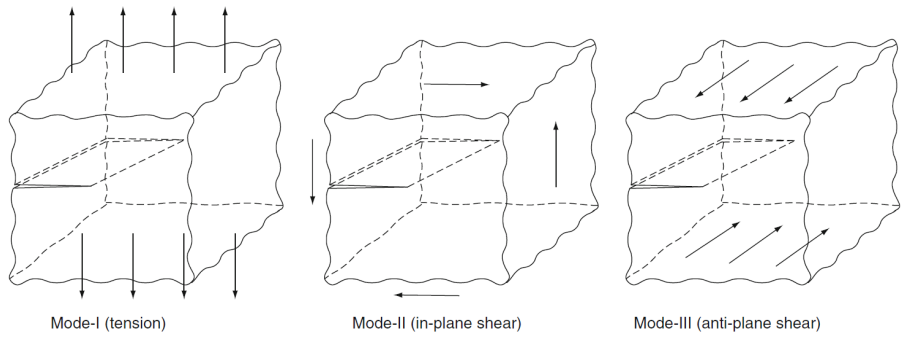

Figure 3.38: Crack modes in fracture mechanics [27].

The idea is to induce an overcoming of the tensile strength of the material with a compressive load, as in the Brazilian test. The Brazilian test is performed on cylindrical specimens with a special load cell that make contact in two opposite points. Since in this case the splitting test is performed on prismatic specimens, to ensure the crack formation along the desired path, two steel rods of 9 mm in diameter, are fixed through an adhesive tape in correspondence of the middle of the direction “a” and aligned with the direction “b” of the specimen, as shown in the setup in fig. 3.39.

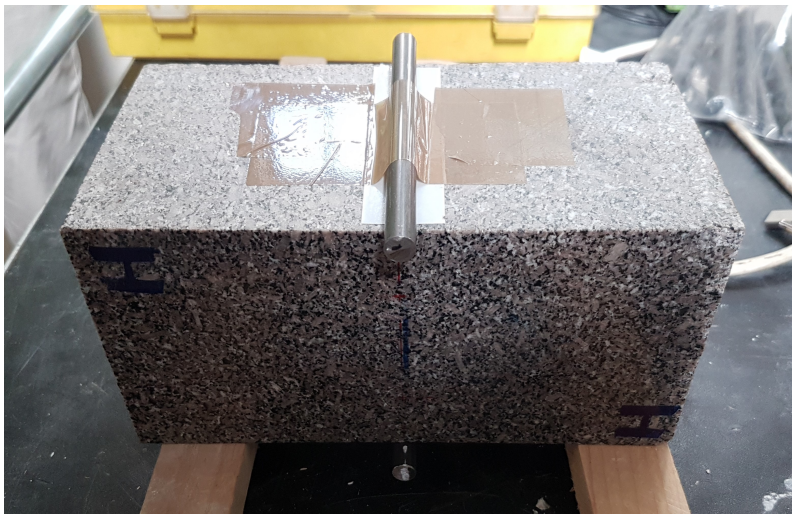

Figure 3.39: Specimen setup of the splitting test.

Figure 3.40: ZwickRoell mechanical press used for splitting test.

Using a force–controlled ZwickRoell mechanical press shown in fig. 3.40 at the MASTRLAB (MAterial and STRucture LABoratory), the sample is loaded in correspondence of the steel rods inducing a tensile crack through the middle section of the block. In order to avoid the tilting of the specimens around the lower or upper steel rod, some deformable polystyrene sheets are used as sealing. The sample under loading is shown in fig. 3.41.

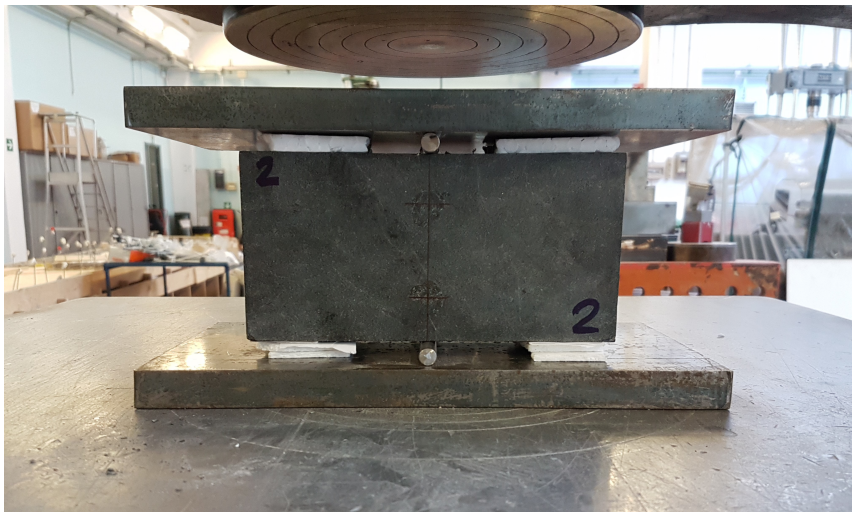

Figure 3.41: Final setup under the loading machine used to perform the splitting test.

3.4.2 Test results

The crack is induced with a constant load rate of 1 kN/s. A picture of the cracked sample after the splitting is reported in fig. 3.42. The breaking loads for each specimen with the average and standard deviation for each lithotype, are presented in the table 3.6. During the splitting of the specimens, the second sample of Syenite started to be inclined during loading and consequently the test was interrupted close to the expected breaking load to fix the setup. This lead to a strange breaking load result after the test was resumed, so it is not considered in the table 3.6 and in the calculation of average and standard deviation of the lithotype.

Figure 3.42: Cracked sample of Syenite.

Table 3.6: Splitting test: breaking loads.

Lithotype	Sample	Breaking load	Average
-	-	kN	kN
Syenite	1	138	127 ± 11
	2	-	
	3	116	
Absolute Black	1	196	167 ± 20
	2	151	
	3	154	
Pink Porriño	1	88	79 ± 7
	2	76	
	3	72	
Carrara	1	34	36 ± 3
	2	41	
	3	34	

3.5 Ultrasonic tests on fractured rock specimens

3.5.1 Test procedure

On the fractured rock samples, the ultrasonic tests are repeated to investigate the influence of the fracturing on the deformability characteristics of the interface generated in the specimen. In this case the wave travels up to the first interface and it is partially reflected by air gaps between the asperities related to not perfect contact between the surfaces, as it is shown in the scheme proposed in fig. 3.43. In literature it has been demonstrated that the reflection of a wave at partially contacting solid-solid interfaces is related to the contact stiffness of the interface [23], which can be quantified as:

$$K = \frac{\omega z}{2}\sqrt{\frac{1}{R_{12}^2} - 1} \tag{3.3}$$

where $z = \rho v$ is the acoustic impedance, $\omega = 2\pi f$ is the angular frequency and R_{12} is the reflection coefficient. The acoustic impedance and the angular frequency are function of the density of the material and of the wave frequency and velocity. The reflection coefficient is expressed by:

$$R_{12} = \frac{R}{I} \tag{3.4}$$

where R is the amplitude of the reflected wave and I is the amplitude of the incident wave.

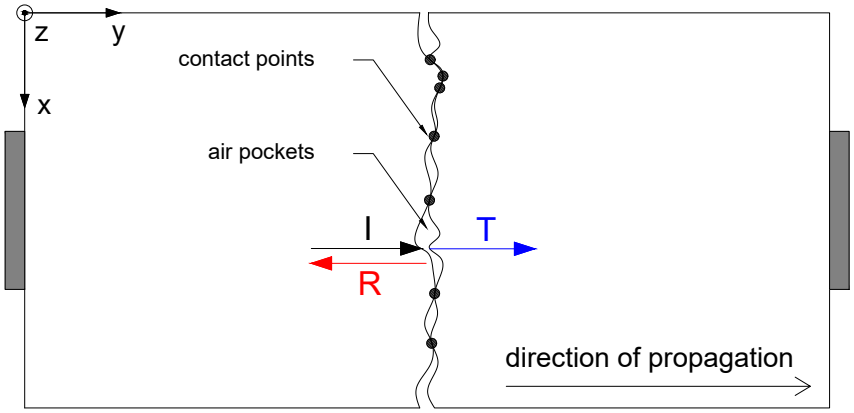

Figure 3.43: Schematic wave transmission in direction “a” at the crack interface of the sample.

The relationship between the amplitude of the incident wave on a interface and those of its generated components, the transmitted wave and the reflected wave, is given by:

$$I = T + R \tag{3.5}$$

With these ingredients the amplitude of the reflected wave can be known starting from the difference between the amplitude of the incident wave and the amplitude of the transmitted one. The amplitude of the incident wave at the interface is estimated from the average of ultrasonic tests performed in the direction “b” and “c” of the sample, since the wavepath is equal in distance being $b = \frac{a}{2}$. Rigorously, the transmitted wave should be quantified at the interface, but considering the difficulty to put a transducer there, the idea is to perform ultrasonic tests along the whole direction “a” on the fractured samples and correct the results accounting for the geometrical dispersion that occurs from the interface to the reading transducer. This correction is made amplifying the signal to compensate the attenuation occurring from the interface to the

receiver, assuming that is the same attenuation occurring from the source to the receiver in the ultrasonic measurement in “b” or “c” direction on the intact samples, since the waves travel within a zone of intact material.
Considering the necessity of carrying-out the test on different specimens applying to the interface the same pressure, rubber bands have been used to keep the two parts of each specimen together in a repeatable manner. The rubber bands were characterized to obtain a load–elongation curve by means of a load test, as shown in fig. 3.44. Holding the band at the top with a bolt and drawing a vertical measuring base of 10 cm along its branches, different weights are applied resulting in different elongation of the measuring bases, allowing the definition of a load–elongation diagram of the rubber band. The experimental curve is presented in fig. 3.45.

Figure 3.44: load test on rubber bands.

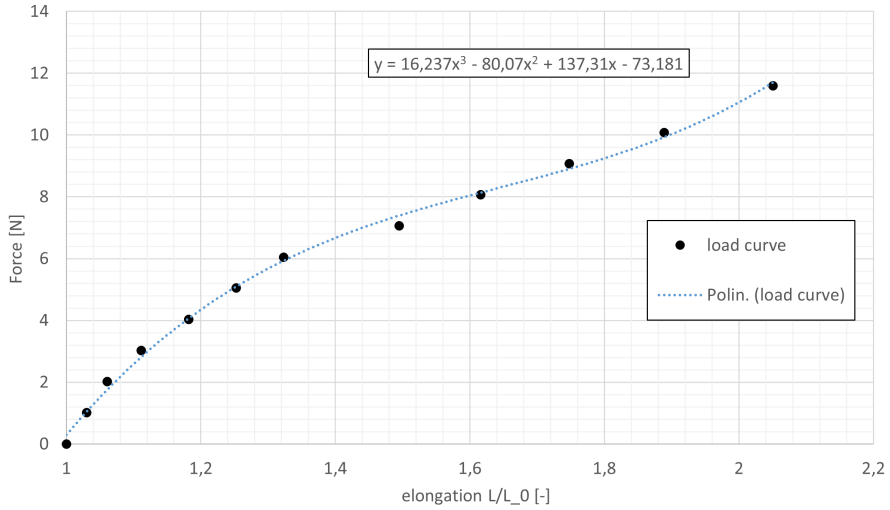

Figure 3.45: load-elongation experimental curve and polynomial approximation curve.

Previous studies on rubber bands, have revealed that are not ideally linear and elastic materials. Mooney [28] and Rivlin [29] deeply investigate the behavior of elastomers and they proposed a two–parameters non–linear constitutive model. The deviation of rubber bands from Hooke's law may be attributed to the molecular structure that does not remain intact after stretching.

The rubber bands are placed around the samples and the length of each marked base is adjusted trying to have the same elongation for each band. The setup is shown in fig. 3.46. Using the experimental curve, approximated with a cubic polynomial function, it is possible to evaluate the elongation necessary for each band to apply a predefined force on the sample that is assumed to be uniformly distributed on the interface area of the sample. For each sample the stress applied was about 5 kPa for a elongation of about 40% for the 10x10x20 cm specimens (Syenite, Absolute Black, Porriño) and about 70% for 12x12x24 cm specimens (Carrara). The ultrasonic measurements are taken once along the direction "a" putting in contact the rough surfaces generated by the fracturing process, and then along the direction "b" putting in contact the flat surfaces representing a perfect contact interface.

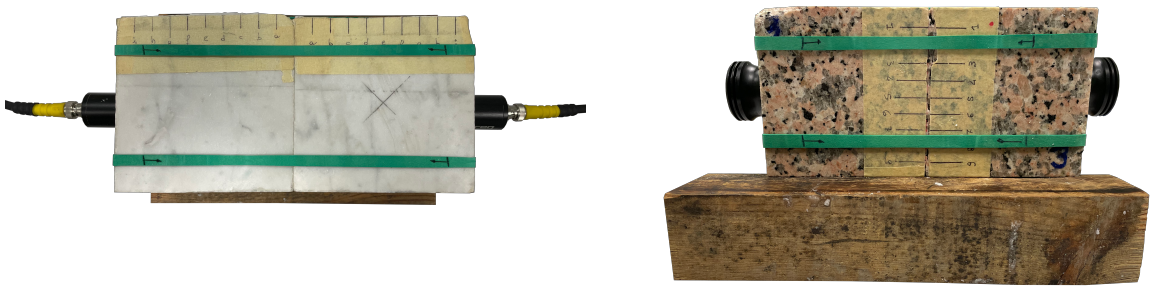

(a) (b)

Figure 3.46: (a): Setup of P-waves velocity measurement on Carrara fractured sample (flat surfaces); (b): Setup of S-waves velocity measurement on Porriño fractured sample (rough surfaces).

3.5.2 Test results

As an example, the signal recorded for the first sample of Absolute Black are presented in the following figures. The other waveforms are included in the Appendix C for the sake of readability.

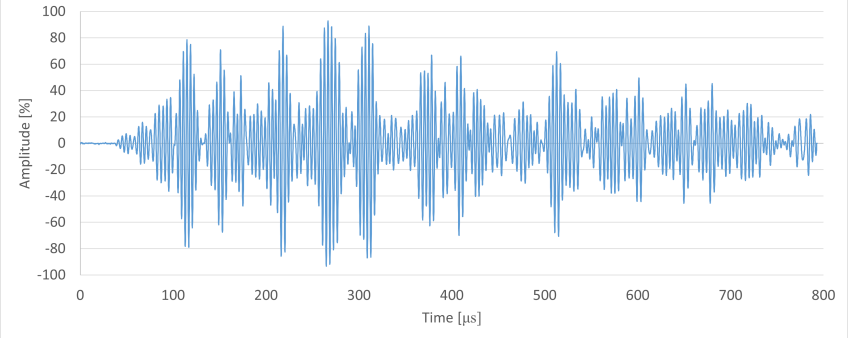

Figure 3.47: Recorded signal of P-waves in direction "a" for Absolute Black sample 1 (rough surfaces).

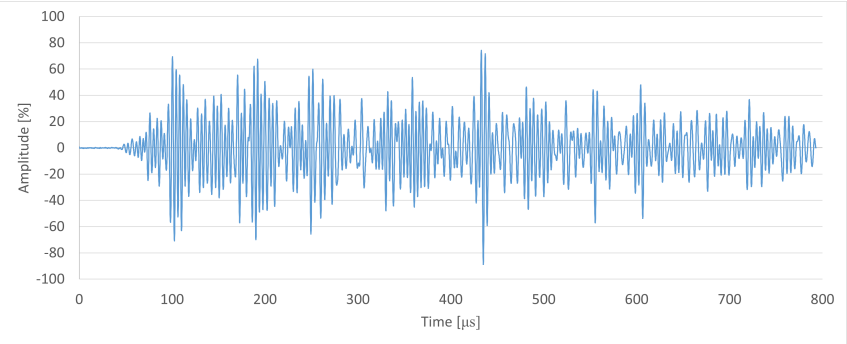

Figure 3.48: Recorded signal of P-waves in direction “b” for Absolute Black sample 1 (flat surfaces).

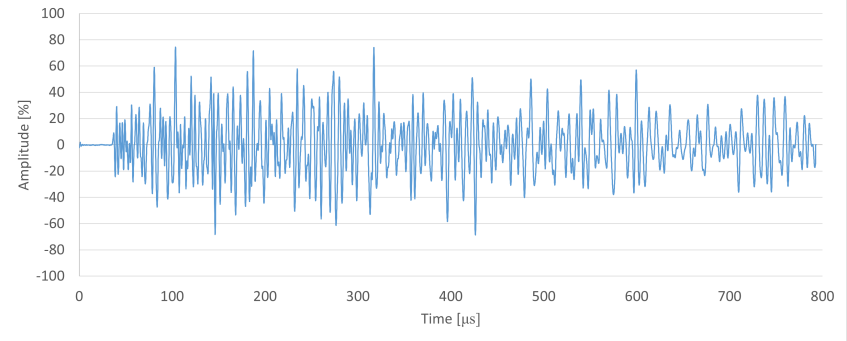

Figure 3.49: Recorded signal on vibration plane “x” of S-waves in direction “a” for Absolute Black sample 1 (rough surfaces).

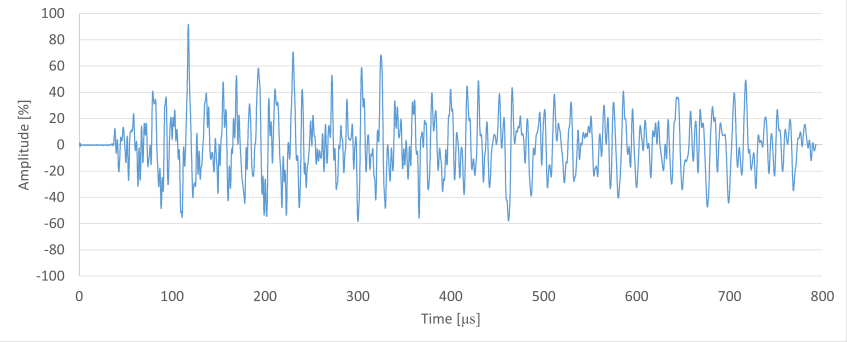

Figure 3.50: Recorded signal on vibration plane “x” of S-waves in direction “b” for Absolute Black sample 1 (flat surfaces).

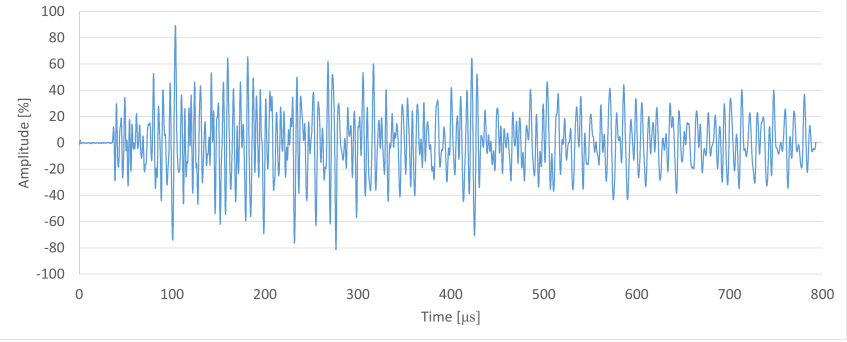

Figure 3.51: Recorded signal on vibration plane “z” of S-waves in direction “a” for Absolute Black sample 1 (rough surfaces).

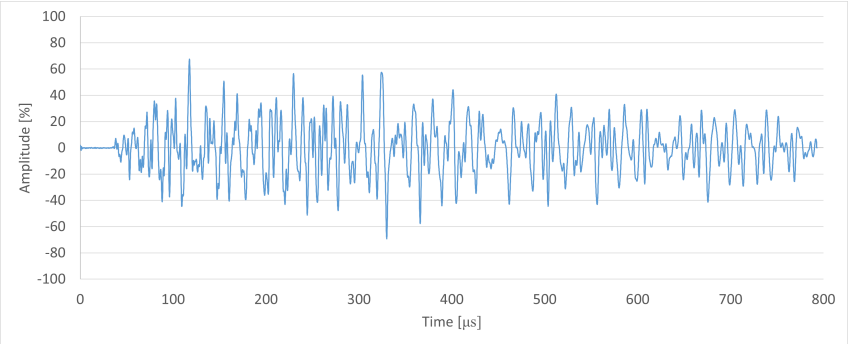

Figure 3.52: Recorded signal on vibration plane "z" of S-waves in direction "b" for Absolute Black sample 1 (flat surfaces).

The arrival times for each fractured rock sample are summarized in table 3.7.

Table 3.7: Arrival times of P-waves and S-waves trough the fractured rock specimens.

		rough surfaces			flat surfaces		
Lithotype	Sample	P-wave	S-wave		P-wave	S-wave	
			x	z		x	z
-	-	µs	µs	µs	µs	µs	µs
Syenite	1	60	96	96	55	100	99
	2	67	107	107	-	-	-
	3	57	103	100	-	-	-
Absolute Black	1	45	77	77	45	77	77
	2	42	73	72	-	-	-
	3	42	74	74	-	-	-
Pink Porriño	1	72	132	132	109	204	181
	2	74	142	141	-	-	-
	3	62	111	111	-	-	-
Carrara	1	49	88	88	52	97	94
	2	52	91	91	-	-	-
	3	55	107	107	-	-	-

The normal and tangential stiffnesses of the interface generated by the crack in the specimen are evaluated using eq. 3.3 based on the theoretical approach presented in subsection Test procedure. The results are summarized in table 3.8.

Table 3.8: Normal and tangential stiffness of the fracture.

Lithotype	Sample	Normal stiffness K_σ	Average	Tangential stiffness K_τ		Average
				x	z	
-	-	TPa m^{-1}	TPa m^{-1}	TPa m^{-1}	TPa m^{-1}	TPa m^{-1}
Syenite	1	45.7	91.5 ± 74.5	21.5	21.3	40.5 ± 22.8
	2	196.5		75.5	69.3	
	3	32.1		30.8	24.6	
Absolute Black	1	37.8	30.2 ± 9.0	49.0	83.4	51.0 ± 14.7
	2	35.1		41.1	41.7	
	3	17.6		46.1	44.9	
Pink Porriño	1	321.1	203.3 ± 104.9	352.1	329.4	270.4 ± 61.1
	2	66.4		190.1	195.2	
	3	222.4		275.7	279.7	
Carrara	1	80.2	95.2 ± 45.0	43.9	48.7	31.0 ± 13.7
	2	156.3		33.8	28.0	
	3	49.1		6.9	24.3	

3.6 Tilt test

3.6.1 Test procedure

The tilt test aims to determine the friction angle between two rock surfaces. The apparatus is composed of an hinged rigid tilting table which can be rotated around an axis. The test consists of placing a rock sample containing a discontinuity the table, in such a way that the lower part is fixed and the upper one is free to move relatively. By gradually rotating the plane around the hinges, it is possible to evaluate the angle at which a relative movement occurs between the two pieces. In order to perform this test, an apparatus was built using a wood rigid plane and two hinges as shown in fig. 3.53.

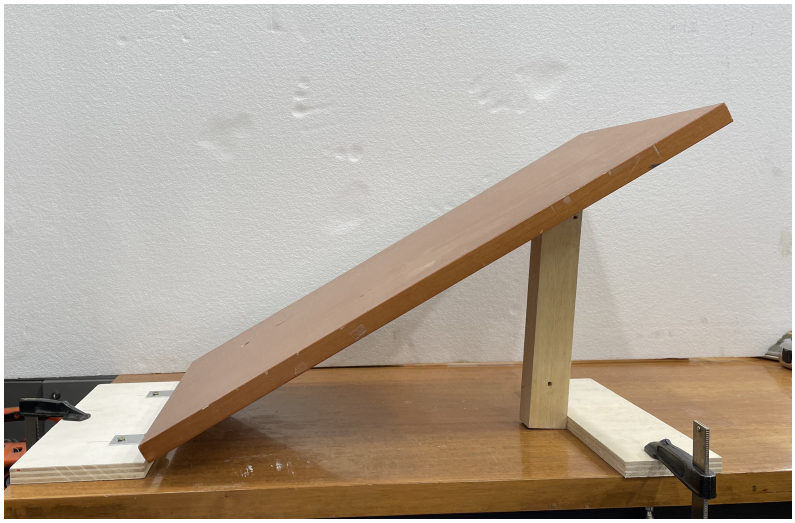

Figure 3.53: Rigid table with hinged supports.

A wood ring fixed on the plane was placed around the lower half specimen to keep it fixed and a stopping barrier was placed at a very short distance to prevent the upper half from toppling. Moreover, a support for the camera was placed on the border of the plane to allows the recording of each test.

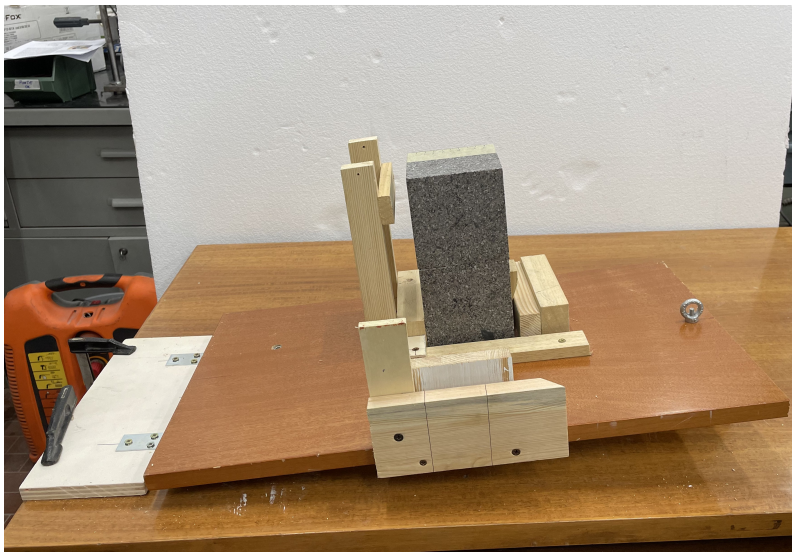

Figure 3.54: Tilt test apparatus with wood ring to keep fixed the bottom half specimen, stopping barrier for the upper half, camera support on the edge and hook to lift the plane.

Since there is an influence on the results given by vibrations induced by the movement [30], the plane was lifted from the hook using a testing machine to allow a very slow and smooth lifting that is not possible to reach with manually operated apparatus.

A LVDT (Linear Variable Displacement Transducer) transducer WA-500mm from HBM was placed in front of the upper rock element to identify the first movement of the block. The complete setup is shown in fig. 3.55. The displacements measured by the transducer are acquired in real–time using *catmanEasy* software shown in fig. 3.56, allowing to stop the tilting as soon as a minimum movement is observed. The tests are performed with a tilting rate of 10°/min as suggested from ISRM [30] for smoothly moving machines.

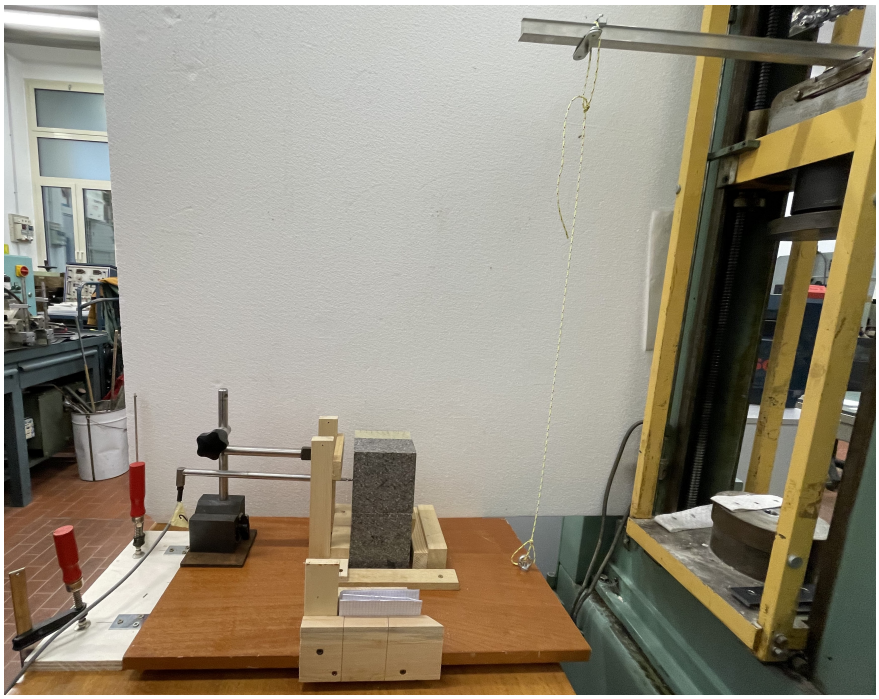

Figure 3.55: Complete setup of tilt tests apparatus.

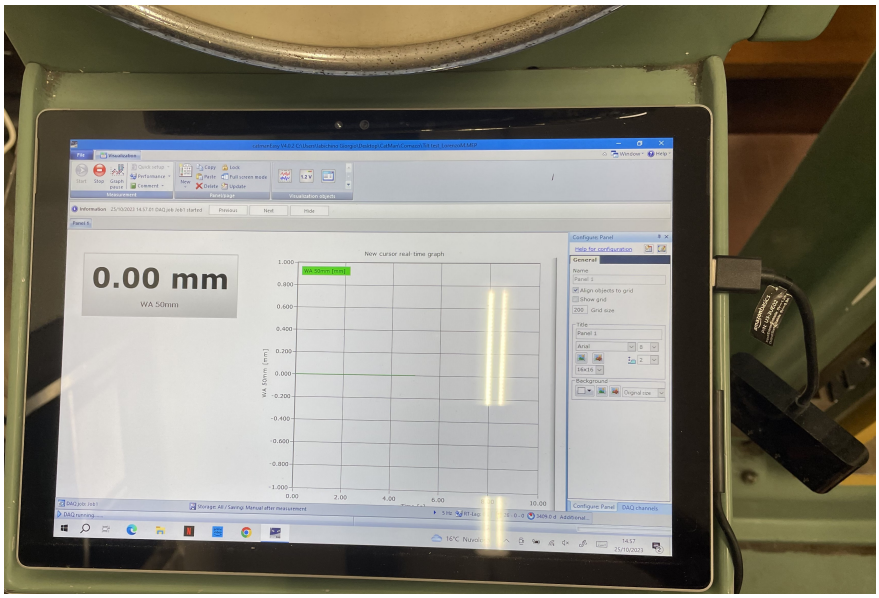

Figure 3.56: CatmanEasy software for the real–time acquisition of the LVDT sensor measurements.

Only smooth discontinuities obtained artificially by cutting the rock block have been tested, determining the base friction angle, since it was not possible to test rough fractures because in that case the upper half specimen rotated before sliding. Fig. 3.57 (a) shows the tilt test in progress. In fig. 3.57 (b) the sliding has already occurred and the test is finished. During the tests, the smartphone inclinometer is used to monitor the slope angle in real–time through a software application. At the end of each test manual measurement were taken to calculate the angle using trigonometry: given the geometry of the setup at the sliding instant, the inclination angle can be evaluated.

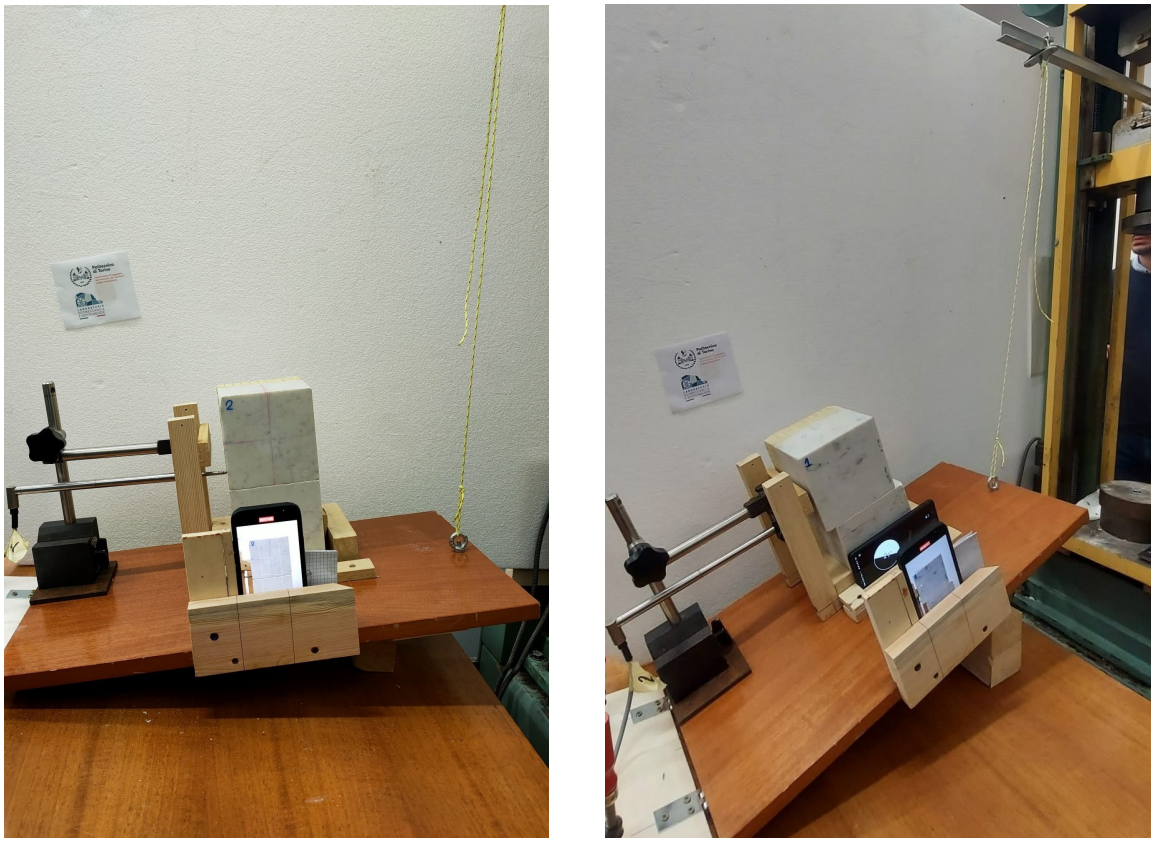

(a) (b)

Figure 3.57: (a) Tilt test in progress; (b) Sliding has already occurred and the test is finished.

3.6.2 Test results

The results are summarized in the following table:

Table 3.9: Results of tilt tests.

Sample	Measurement	H cm	L cm	Angle °
Syenite 1	1	25.2	63.5	23
	2	27.5	63.5	26
	3	27.2	63.5	25
Syenite 2	1	21.5	63.5	20
	2	23.9	63.5	22
	3	23.1	63.5	21
Syenite 3	1	23.8	63.5	22
	2	25.3	63.5	23
	3	25.9	63.5	24
Absolute Black 1	1	25.2	63.5	23
	2	25.6	63.5	24
	3	25.3	63.5	23
Absolute Black 2	1	25.8	63.5	24
	2	21.8	63.5	20
	3	23.9	63.5	22
Absolute Black 3	1	20.6	63.5	19
	2	21.5	63.5	20
	3	22.3	63.5	21
Porriño 1	1	26.0	63.5	24
	2	27.7	63.5	26
	3	27.6	63.5	26
Porriño 2	1	25.1	63.5	23
	2	23.5	63.5	22
	3	26.5	63.5	25
Porriño 3	1	25.9	63.5	24
	2	25.0	63.5	23
	3	26.6	63.5	25
Carrara 1	1	26.8	63.5	25
	2	26.8	63.5	25
	3	25.1	63.5	23
Carrara 2	1	16.4	63.5	15
	2	19.8	63.5	18
	3	21.9	63.5	20
Carrara 3	1	17.6	63.5	16
	2	17.4	63.5	16
	3	17.9	63.5	16

Table 3.10: Average tilt angle and standard deviation for each lithotype.

Sample	Average angle °
Syenite	23 ± 2
Absolute Black	22 ± 2
Porriño	24 ± 1
Carrara	19 ± 4

3.7 Discussion of the results

The data obtained with ultrasonic tests, compression tests and tilt tests are comparable and representative of each lithotype.

The arrival time of the S-waves are coherently higher than those of P-waves and both are reduced by almost half when tests are performed in transversal direction which propagation distance is almost half than the longitudinal one. The lowest arrival times (fastest propagation) were found in the Absolute Black specimens, for both P-waves and S-waves. The highest arrival times (slowest propagation) were found in the Porriño specimens. This is a first indication that Absolute black and Porriño are the most and the least rigid lithotypes, respectively.

Compressive tests further validate this trend, revealing average static elastic moduli of 62.9 ± 1.5 GPa for Absolute Black, 42.7 ± 3.3 GPa for Syenite, 39.1 ± 0.8 GPa for Carrara and 33.8 ± 1.2 GPa for Porriño. Typical values found in literature [10] are in good agreement with the results, and they are listed below:

- 40–120 GPa for Gabbro;
- 50–80 GPa for Granite;
- 20–70 GPa for Syenite;
- 30–80 GPa for Carrara marble.

The dynamic moduli obtained from the ultrasonic propagation tests and presented in table 3.3 follow almost the same trend with slightly higher values, as expected for dynamic testing. The difference between dynamic and static Young's modulus for rocks has been widely studied in literature, suggesting typical ratios between 1 and 2. Generally, the dynamic modulus of elasticity is slightly higher than the static value [6]. The differences are commonly attributed to microcracks and pores within the rock material.

Porriño shows the lowest Poisson's ratio with an average of 0.12 ± 0.01, Carrara has the highest ratio with an average of 0.17 ± 0.02, while Absolute Black and Syenite have intermediate values of 0.16 ± 0.00 and 0.14 ± 0.02, respectively. The values are lower than expected, as also confirmed by literature data for these type of rocks [31], but they are consistent and repeated within each lithotype. The reason could be attributed to the non–conventional shape of the specimens or simply to the internal fabric of the material. The Poisson's ratios obtained through dynamic testing all have the same value of 0.33.

All the lithotypes showed consistent results also in the splitting tests. Carrara marble reveals the lowest average breaking load of 36 ± 3 kN with the lowest variability. Absolute Black lithotype shows the highest resistance with an average breaking load of 167 ± 20 kN. Syenite and Porriño follow with average values of 127 ± 11 kN and 79 ± 7 kN, respectively.

The ultrasonic tests on fractured samples shows consistently higher arrival times than intact rock results (about 40% higher) in the longitudinal direction, due to the influence of the interface generated by the fracture. The interface stiffnesses were presented in table 3.8 for both normal and tangential directions. Since no variability was observed between the two tangential directions, the average values and the standard deviations are referred to both directions.

A possible correlation between the interface stiffness and the deformability modulus of the intact rock material, could exist. In fact Porriño that has the lowest static elastic modulus, shows the highest normal stiffness at the interface of 203.3 ± 104.9 TPa m^{-1} and the highest tangential stiffness of 270.4 ± 61.1 TPa m^{-1}. Carrara shows 95.2 ± 45.0 TPa m^{-1} as normal stiffness and 31.0 ± 13.7 TPa m^{-1} as tangential stiffness. Absolute Black that has the highest static elastic modulus, shows the lowest normal stiffness of 30.2 ± 9.0 TPa m^{-1} and the second lowest tangential stiffness of 51.0 ± 14.7 TPa m^{-1}. Syenite has intermediate values of 91.5 ± 74.5 TPa m^{-1} as normal stiffness and 40.5 ± 22.8 TPa m^{-1} as tangential stiffness. These results will be further discussed in the next chapter in comparison to the roughness results in terms of JRC .

Tilt test results reveal that the Carrara has the lowest base friction angle of $19 \pm 4°$, as expected from its smooth surface and very fine grained composition. Absolute Black that is fine grained too, follows with $22 \pm 2°$. Syenite and Porriño that are medium grained lithotypes have the highest tilt angles of $23 \pm 2°$ and $24 \pm 1°$, respectively.

Chapter 4

Analysis of fracture surfaces

4.1 Method and procedure

The roughness of induced fractures in the specimens has been investigated through the geometrical survey of several orthogonal profiles, minimizing the arbitrariness of the measurements. A standard procedure has been studied and followed to ensure the uniformity of the results for all the samples. The profiles were examined along two orthogonal directions of the fracture surface, according to the scheme of fig. 4.1. The fracture propagation is parallel to the "letters" direction. In the fig. 4.2 the geometrical setup of the survey with equally spaced markers along "letters" and "numbers" direction, is presented. Fig. 4.3 shows a reconstituted sample. A total of 18 profiles for each half specimen (9 for each direction with a spacing of 1 centimeters) were analyzed. The trace length of the profiles were 10 centimeters for Syenite, Absolute Black, Porriño and 12 centimeters for Carrara marble.

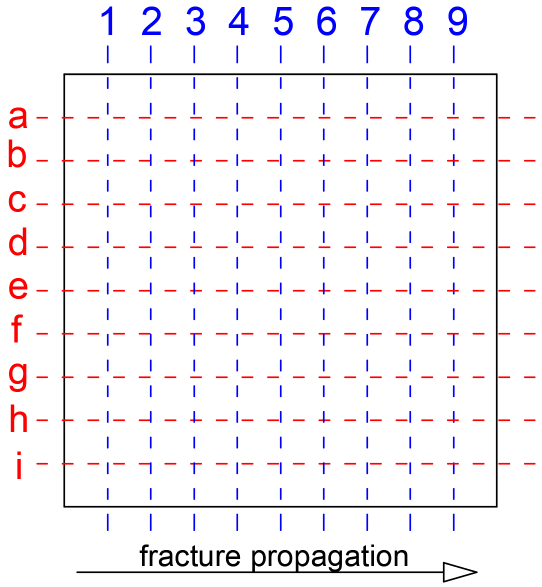

Figure 4.1: Scheme of survey directions for the acquisition of roughness profiles.

The acquisition procedure is summarized in the following steps:

1. Profile acquisition with the profilometer made by many steel pins with a diameter of 1 mm;
2. Profile digitization with a standard image scanner;
3. Vectorialization of the profile from the image.

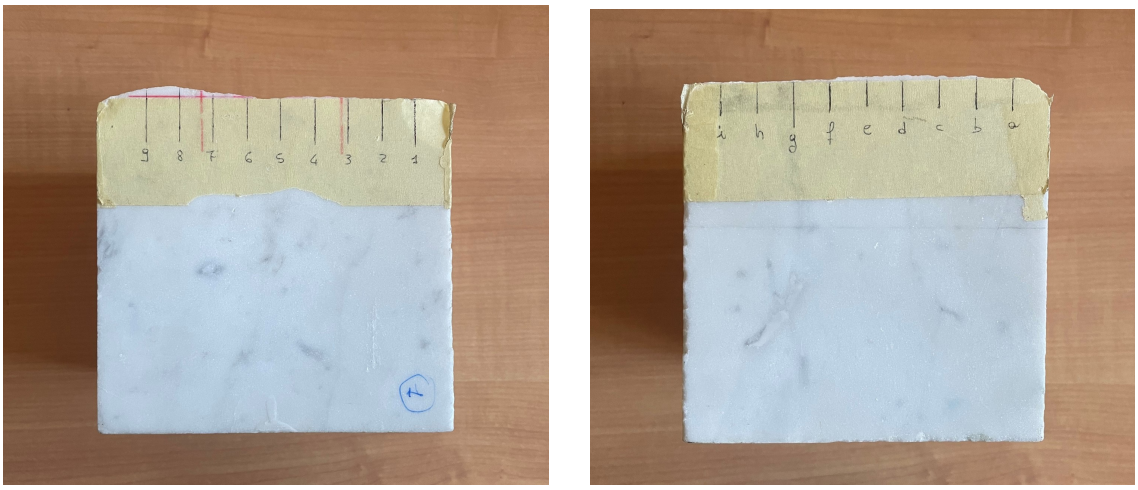

(a) (b)

Figure 4.2: Geometrical setup for the acquisition of roughness profiles. (a) markers in direction "c"; (b) markers in direction "b"

Figure 4.3: Reconstituted specimen of Carrara with geometrical setup for the acquisition of roughness profiles.

Each step is now further described.

1. The profilometer is placed above the profile being analyzed, following its contours by starting always from the same steel pin (marked with an adhesive tape). Two rectangular tubes were placed adjacent to the specimen, acting as horizontally stopping supports. The acquisition setup is shown in fig. 4.4.

2. The profile is digitized with a Epson Precision 1200U scanner, using the software *VueScan*. The scan resolution is set to the maximum of 1200 DPI (Dots Per Inch), the document size is set to A4 and the file is saved in a TIFF format. Fig. 4.5 shows the scanner setup with the profilometer lying on the flatbed. An example of the scan result is shown in fig. 4.6.

3. Each image is then processed with a Matlab code to obtain a discrete roughness profile,

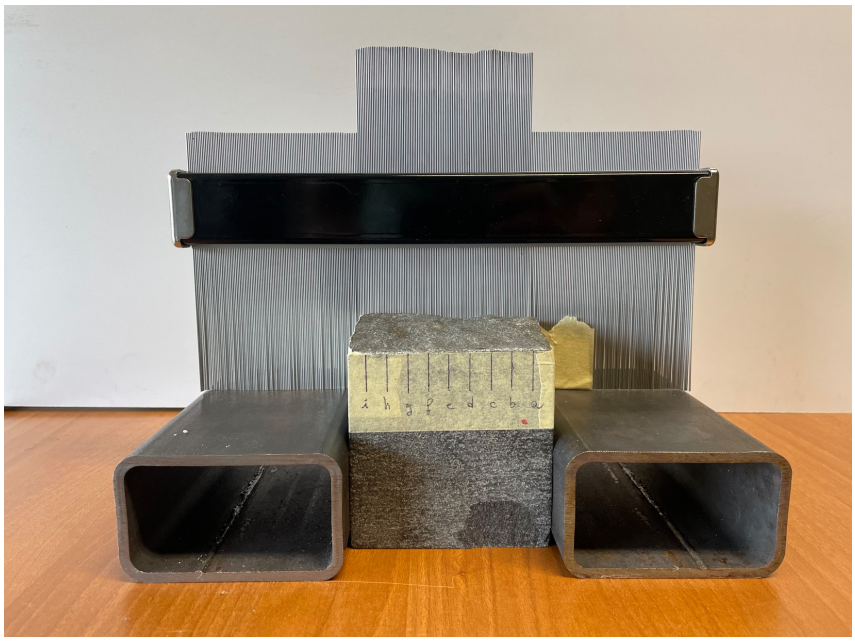

Figure 4.4: Example of profile acquisition with profilometer. On the left and right side there are the stopping supports (rectangular steel tubes).

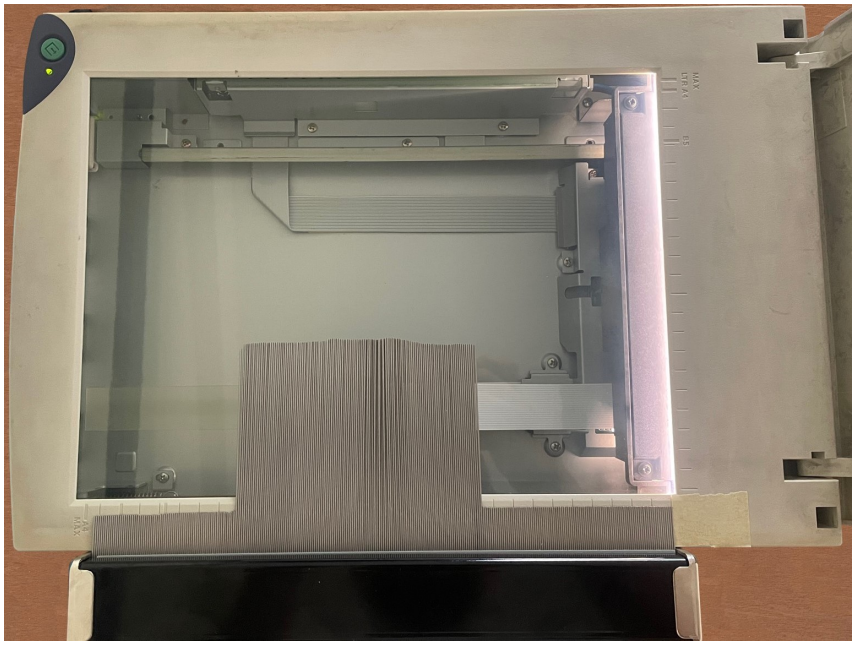

Figure 4.5: Example of profile digitization with Epson Precision 1200U image scanner.

in which the horizontal resolution corresponds to the diameter of the profilometer pins and the height is determined by averaging the acquired image pixels corresponding to the top of the pin. Then the profile is detrended, to obtain a null average of the slopes, as required for the computation of the roughness parameters. The result is a vector of points, shown as an example in fig 4.7 where the two side of the same fracture profile (upper and lower) are overlapped with two different colors. Clearly, they are not perfectly equal due to breaking of particles in the fracturing process but mostly due to the systematic errors during the survey already discussed in chapter 2.

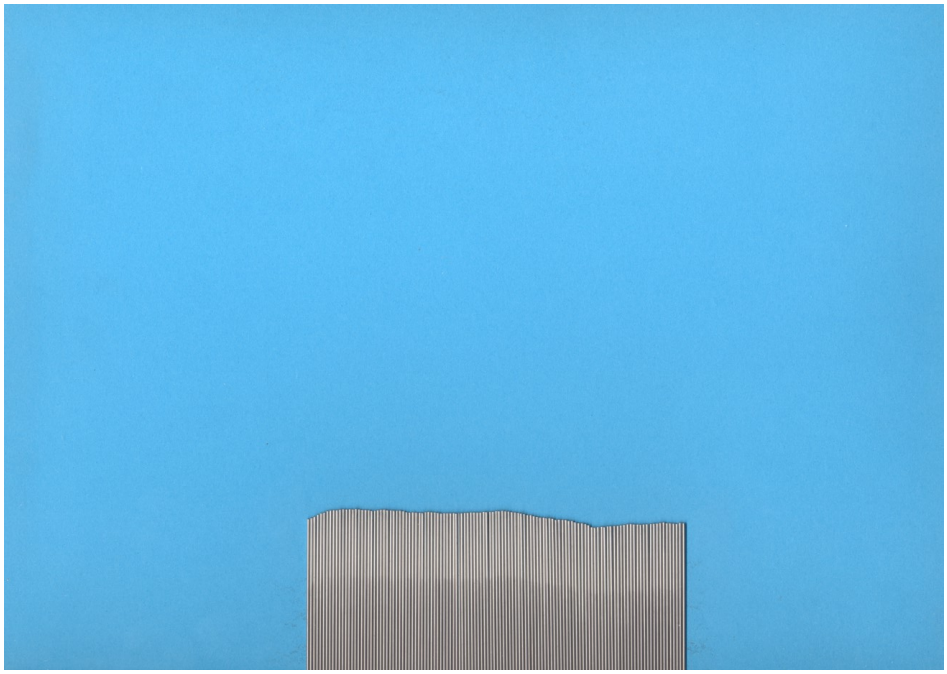

Figure 4.6: Example of scanned image with a resolution of 1200 DPI.

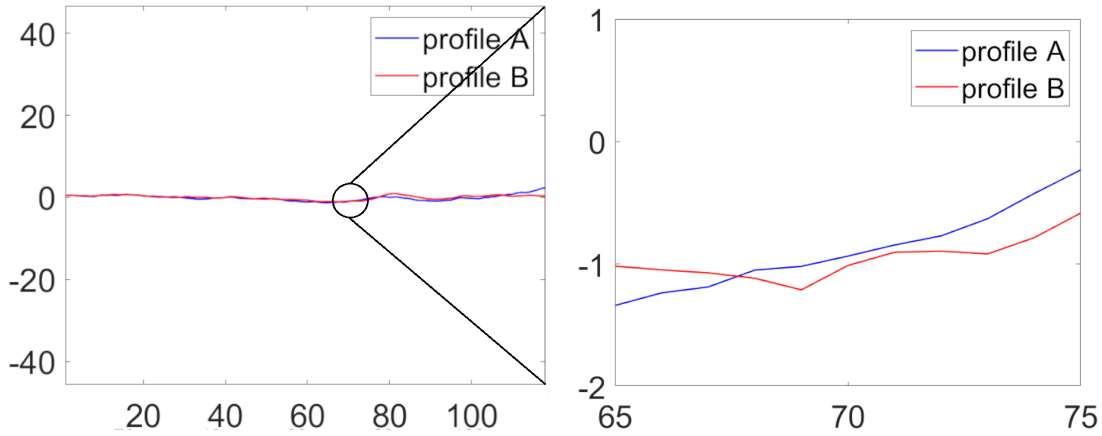

Figure 4.7: Example of profile vector obtained from processing the image with a Matlab code. Units in millimeters.

4.2 Results

4.2.1 Roughness parameters

For each profile, the roughness parameters Z_2, R_p, SF, D are computed using the expressions reported in chapter 2. The calculation shows that no significant variability exists between the two faces of the same rough fracture, therefore the average value of the parameters is assumed between the two sides and it is used in the following graphs and for the correlation with JRC . To have a global overview of each lithotype, all the three specimens are grouped together by direction of analysis for a total of 27 profiles in the direction of "numbers" (hereinafter in the graphs called "NUM") and 27 in the direction of "letters" (hereinafter in the graphs called "LET"). For each lithotype, the computed parameters with their averages and standard deviations are presented in the following graphs and then summarized in table 4.1:

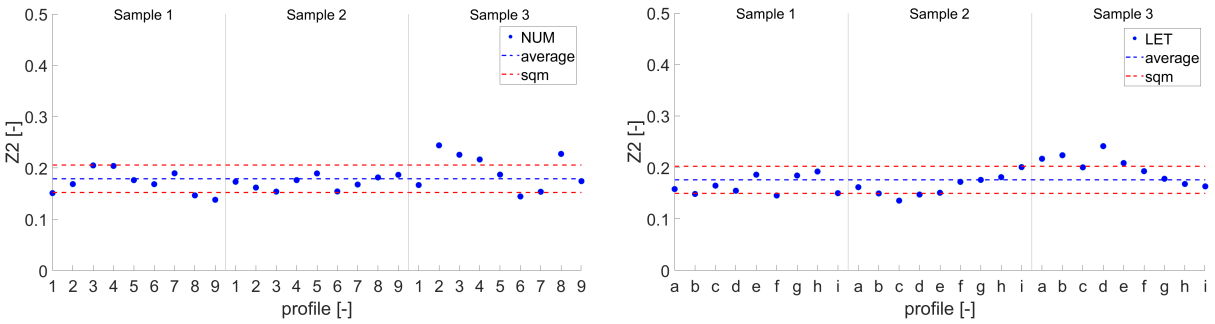

(a) (b)

Figure 4.8: Roughness parameter Z_2 for Syenite. (a) numbers; (b) letters.

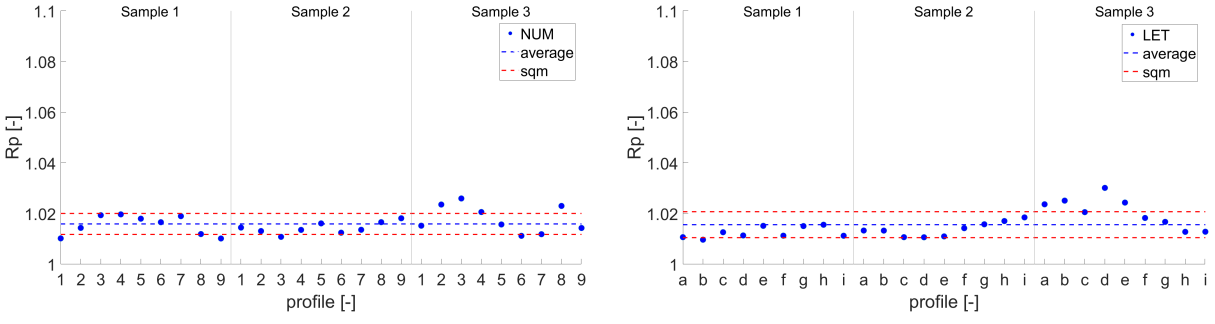

(a) (b)

Figure 4.9: Roughness parameter R_p for Syenite. (a) numbers; (b) letters.

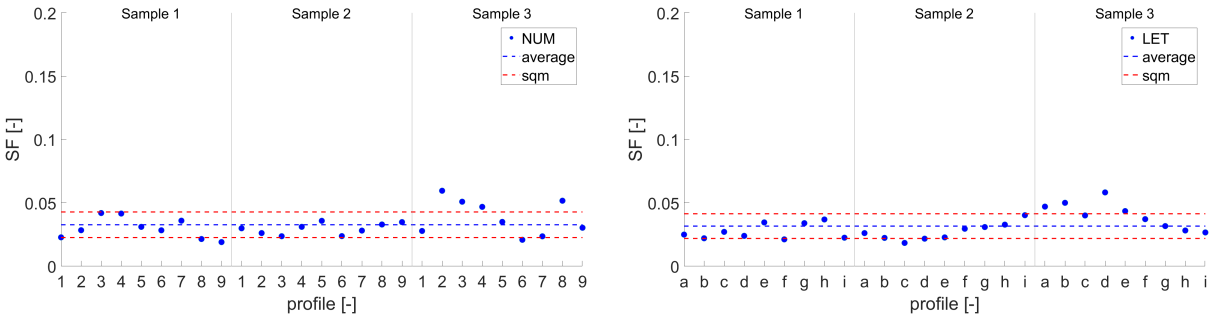

(a) (b)

Figure 4.10: Roughness parameter SF for Syenite. (a) numbers; (b) letters.

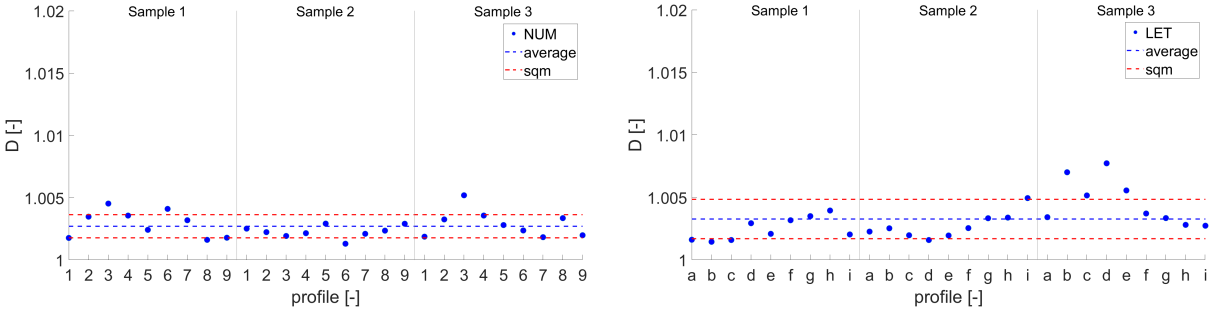

(a) (b)

Figure 4.11: Roughness parameter D for Syenite. (a) numbers; (b) letters.

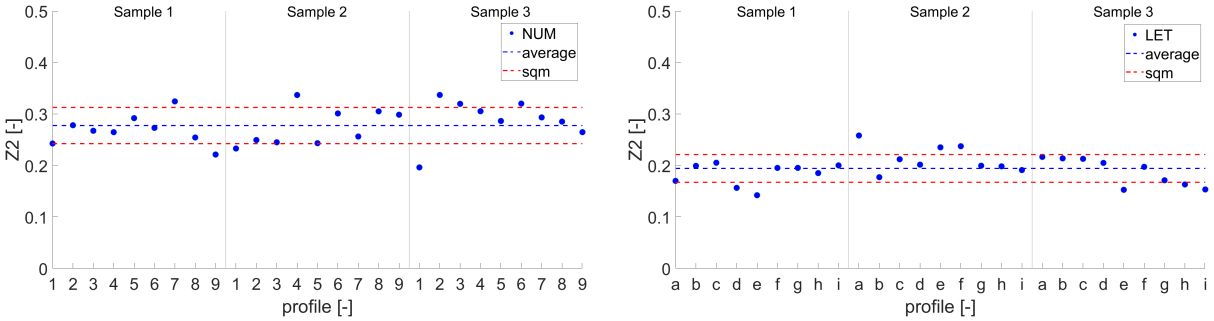

(a) (b)

Figure 4.12: Roughness parameter Z_2 for Porriño. (a) numbers; (b) letters.

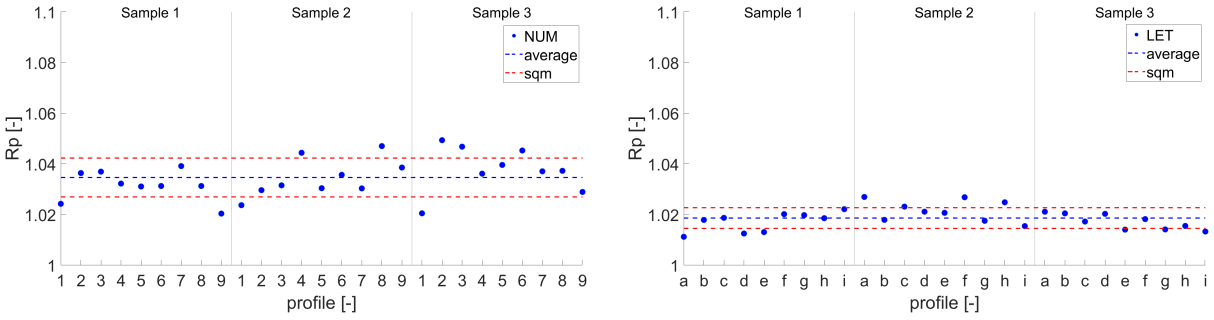

(a) (b)

Figure 4.13: Roughness parameter R_p for Porriño. (a) numbers; (b) letters.

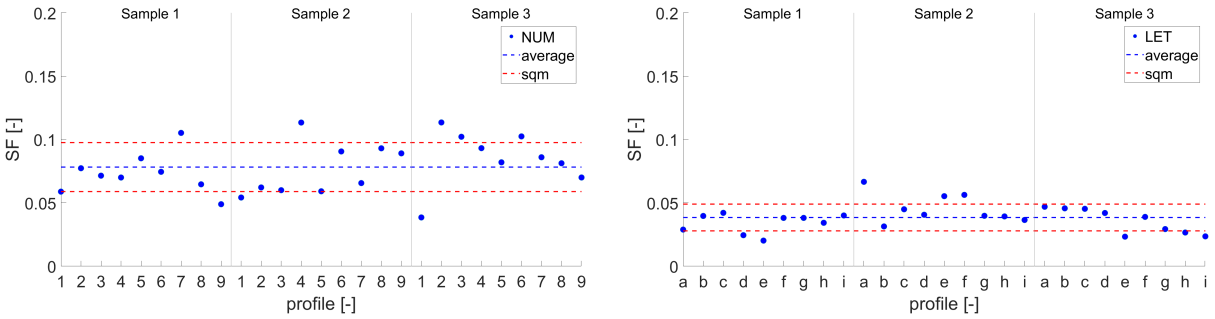

(a) (b)

Figure 4.14: Roughness parameter SF for Porriño. (a) numbers; (b) letters.

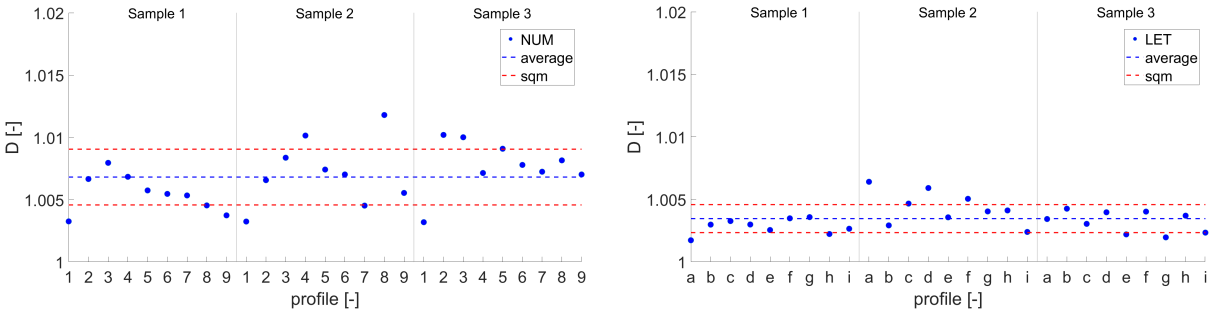

(a) (b)

Figure 4.15: Roughness parameter D for Porriño. (a) numbers; (b) letters.

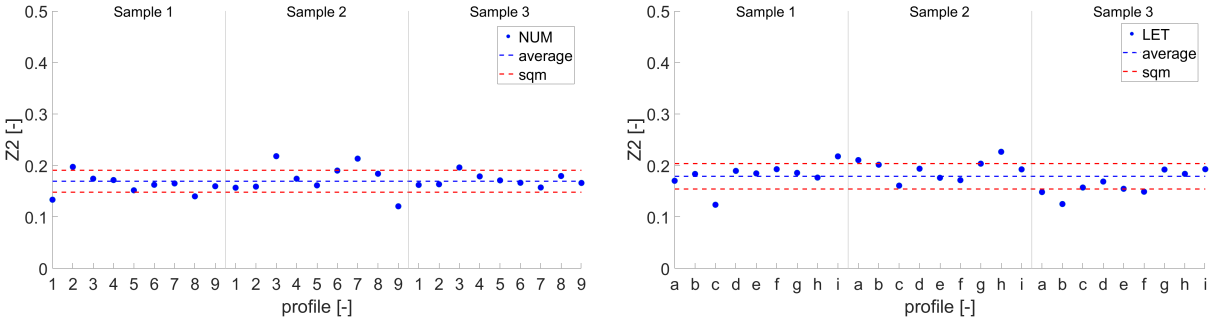

(a) (b)

Figure 4.16: Roughness parameter Z_2 for Absolute Black. (a) numbers; (b) letters.

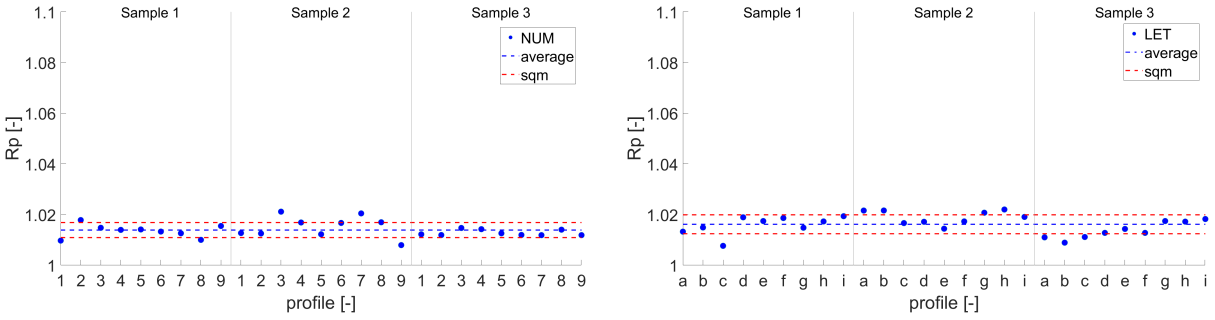

(a) (b)

Figure 4.17: Roughness parameter R_p for Absolute Black. (a) numbers; (b) letters.

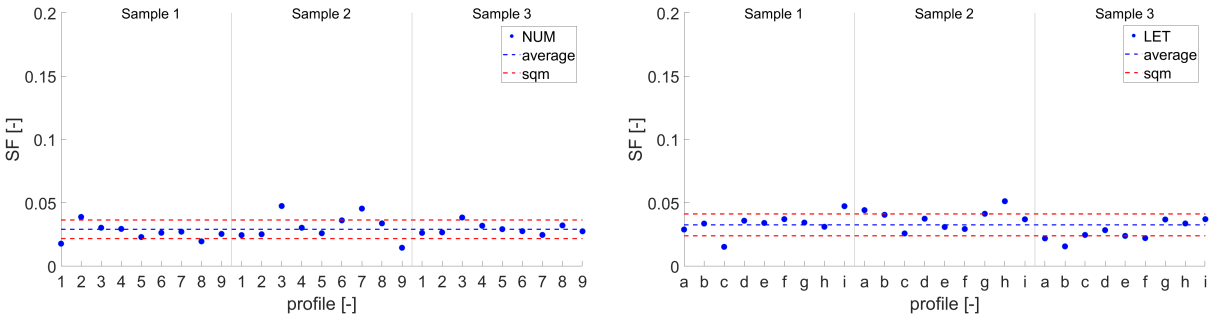

(a) (b)

Figure 4.18: Roughness parameter SF for Absolute Black. (a) numbers; (b) letters.

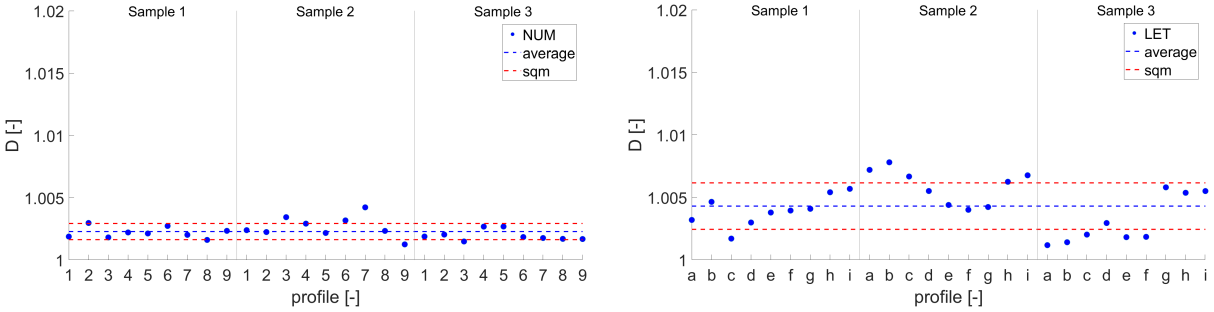

(a) (b)

Figure 4.19: Roughness parameter D for Absolute Black. (a) numbers; (b) letters.

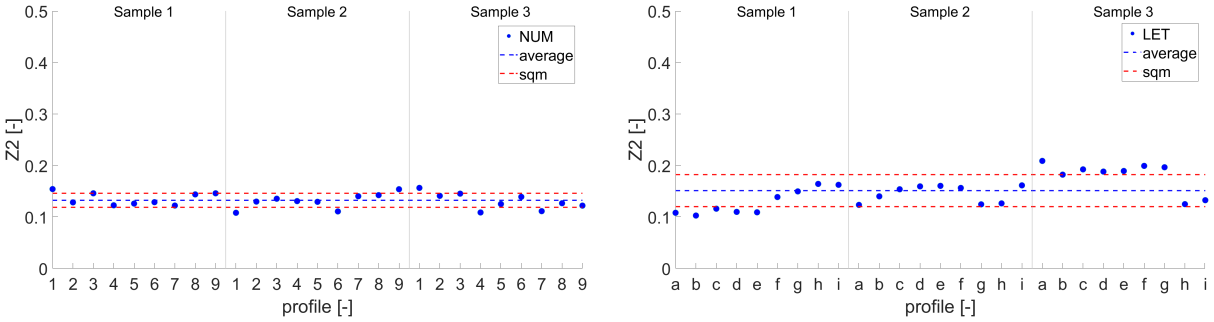

(a) (b)

Figure 4.20: Roughness parameter Z_2 for Carrara. (a) numbers; (b) letters.

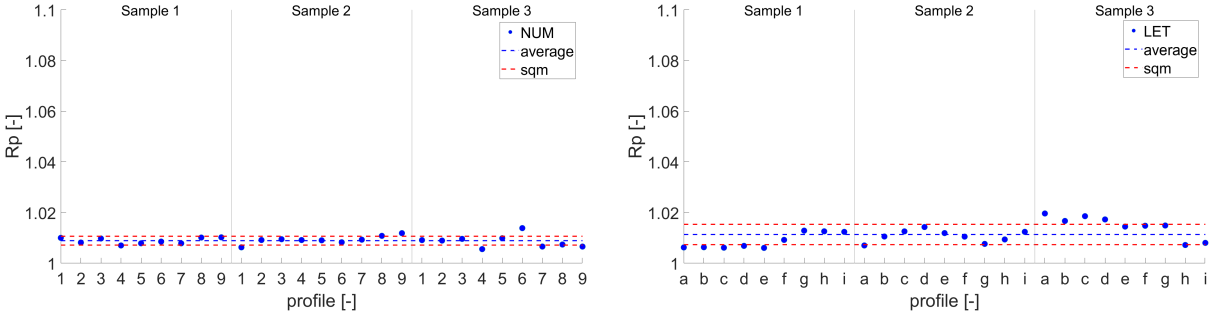

(a) (b)

Figure 4.21: Roughness parameter R_p for Carrara. (a) numbers; (b) letters.

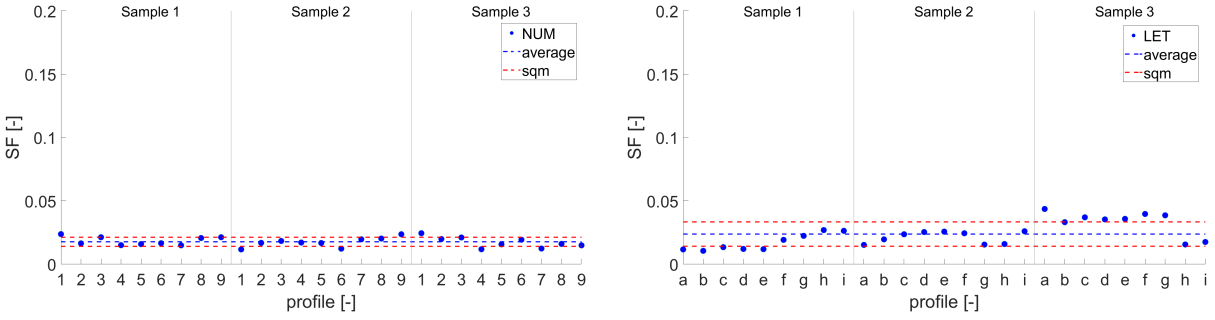

(a) (b)

Figure 4.22: Roughness parameter SF for Carrara. (a) numbers; (b) letters.

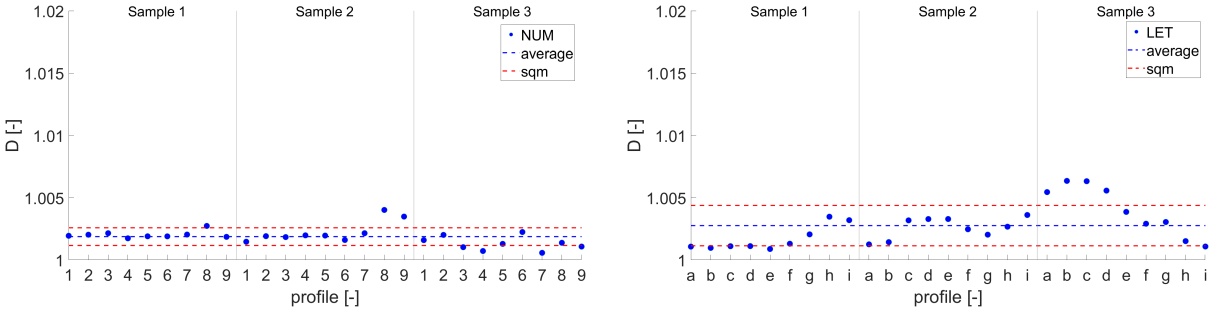

(a) (b)

Figure 4.23: Roughness parameter D for Carrara. (a) numbers; (b) letters.

Table 4.1: Statistical distribution of roughness parameters - Syenite

	Syenite	Porriño	Absolute Black	Carrara
Z_2	0.1776 ± 0.0266	0.2359 ± 0.0521	0.1742 ± 0.0236	0.1417 ± 0.0258
R_p	1.0157 ± 0.0047	1.0266 ± 0.0101	1.0150 ± 0.0036	1.0101 ± 0.0033
SF	0.0322 ± 0.0099	0.0584 ± 0.0253	0.0309 ± 0.0082	0.0207 ± 0.0079
D	1.0030 ± 0.0013	1.0051 ± 0.0024	1.0033 ± 0.0017	1.0023 ± 0.0013

4.2.2 JRC estimation from roughness parameters

Several empirical laws found in the literature have been used to estimate the Joint Roughness Coefficient starting from the roughness parameters computed for each profile. Firstly, the equations were applied to the two orthogonal survey directions separately, as shown in figures 4.24–4.39 (a), and then the data were grouped and processed all together, as shown in figures 4.24–4.39 (b). The results are presented in the following graphs using error bars to show the variability given by the standard deviation of the input parameters. To increase the readability of the graphs, the empirical correlations are progressively numbered according to table 4.2.

Table 4.2: Relationship between correlation and equation used to compute JRC

	C1	C2	C3	C4	C5	C6	C7	C8	C9	C10	C11
Z_2	eq.2.9	eq.2.10	eq.2.11	eq.2.12	eq.2.13	-	-	-	-	-	-
R_p	-	-	-	-	-	eq.2.15	eq.2.16	eq.2.17	-	-	-
SF	-	-	-	-	-	-	-	-	eq.2.19	eq.2.20	-
D	-	-	-	-	-	-	-	-	-	-	eq.2.22

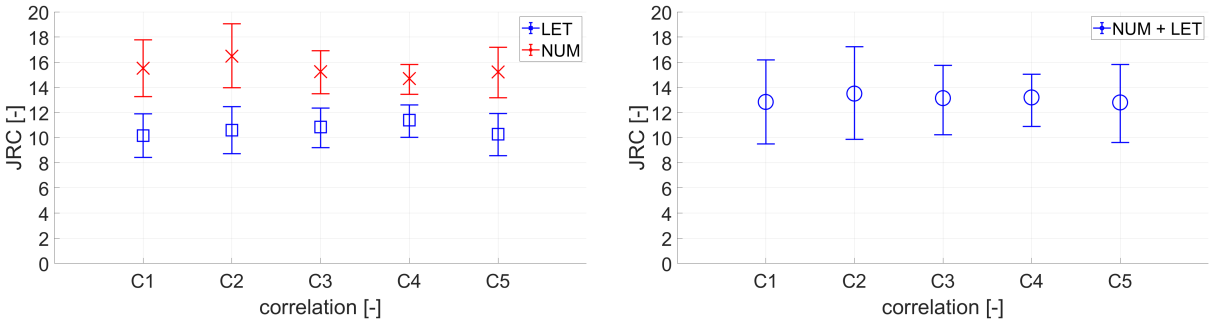

(a) (b)

Figure 4.24: JRC obtained from Z_2 for Porriño

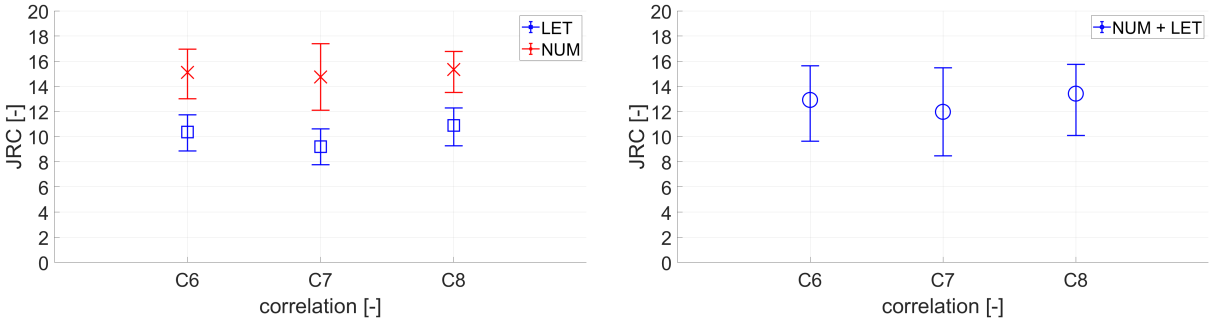

(a) (b)

Figure 4.25: JRC obtained from Rp for Porriño

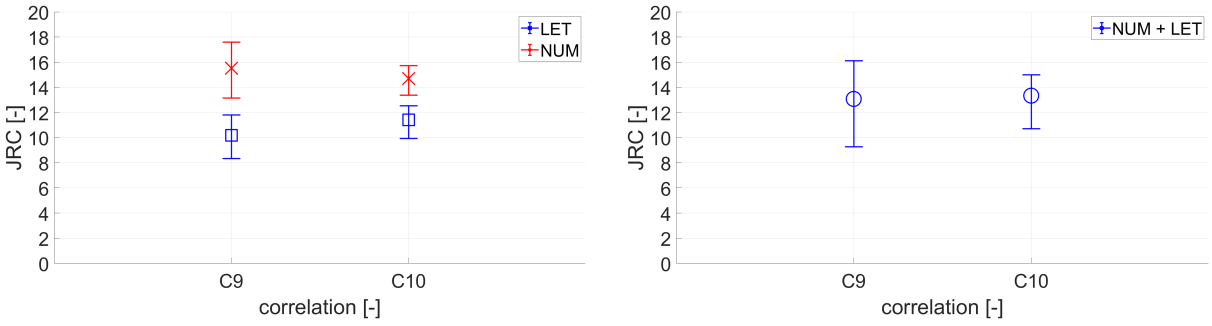

Figure 4.26: JRC obtained from SF for Porriño

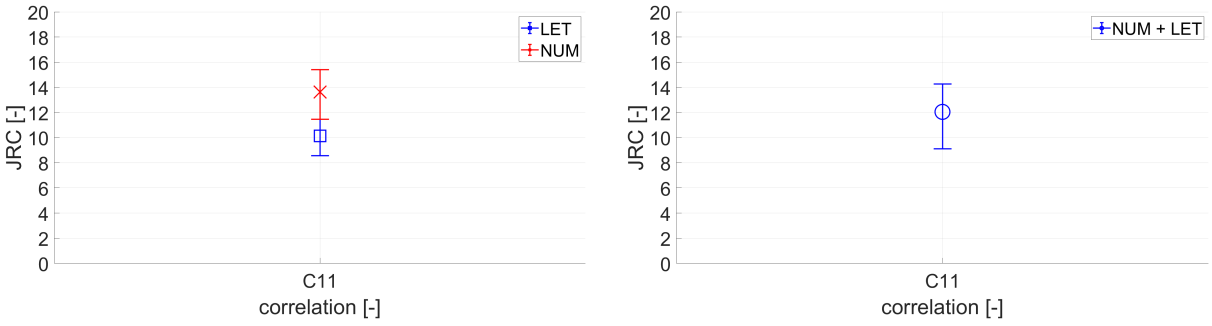

Figure 4.27: JRC obtained from D for Porriño

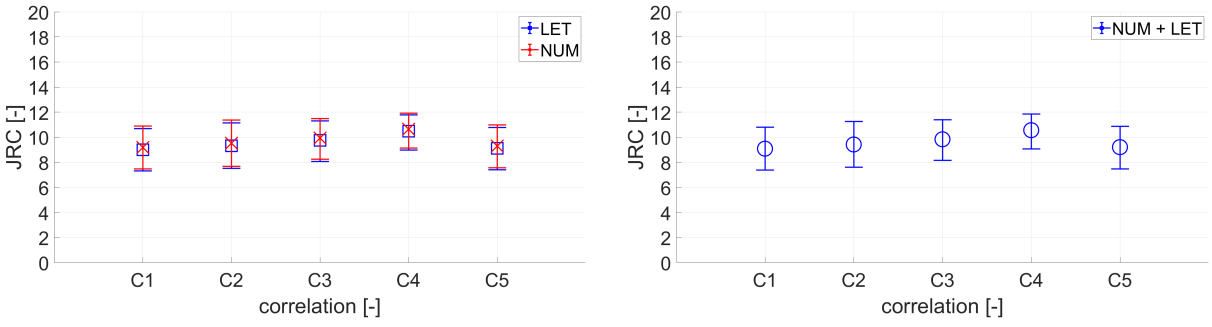

Figure 4.28: JRC obtained from Z_2 for Syenite

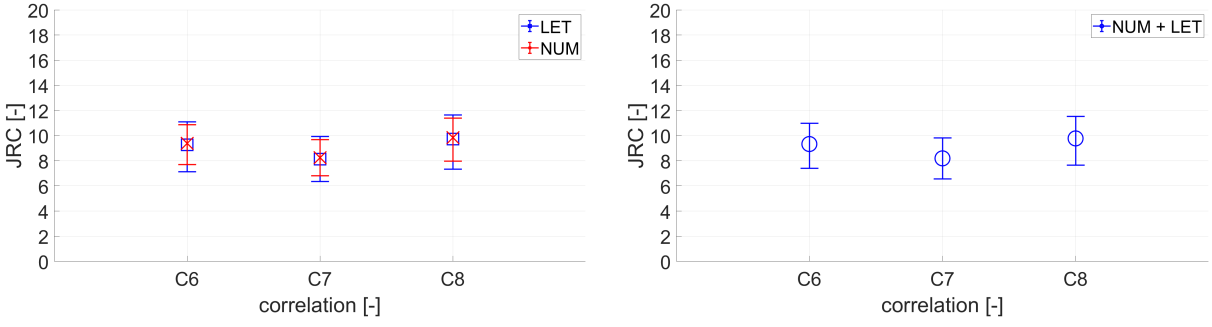

Figure 4.29: JRC obtained from Rp for Syenite

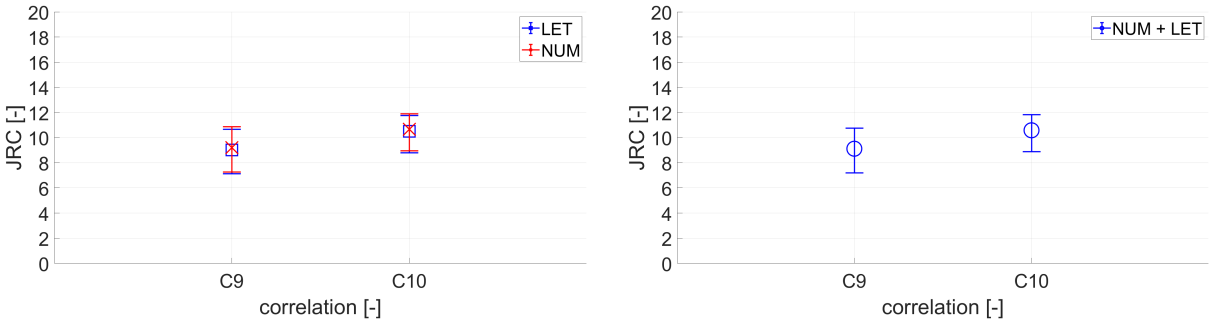

(a) (b)

Figure 4.30: JRC obtained from SF for Syenite

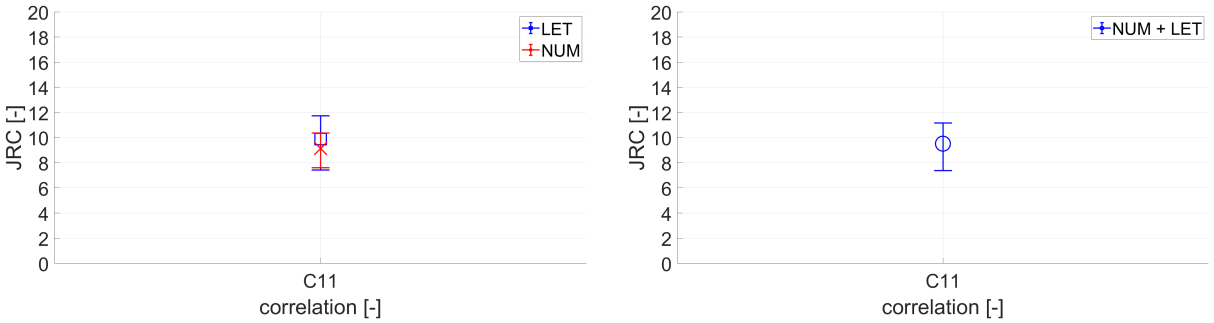

(a) (b)

Figure 4.31: JRC obtained from D for Syenite

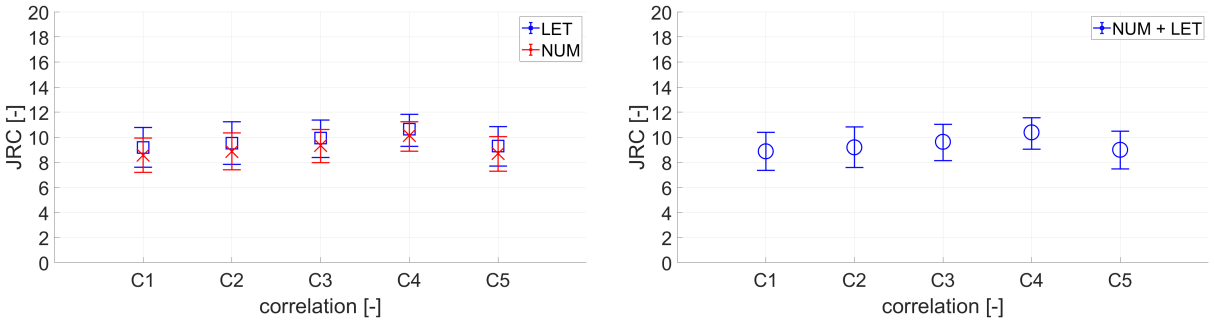

(a) (b)

Figure 4.32: JRC obtained from Z_2 for Absolute Black

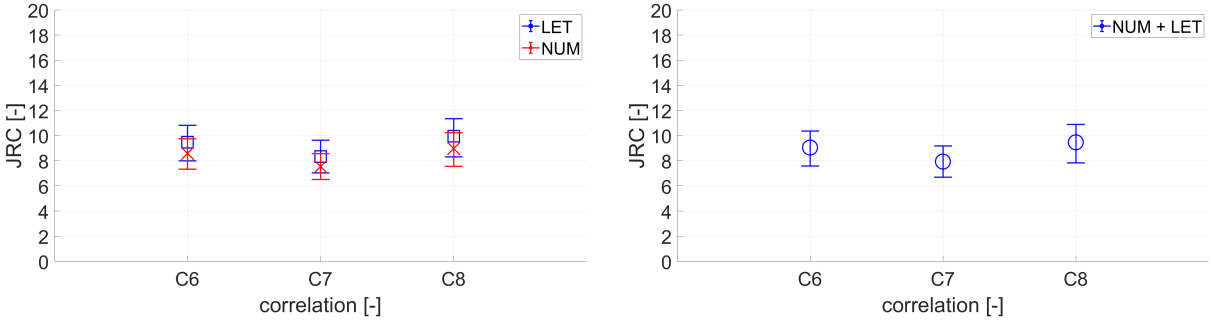

(a) (b)

Figure 4.33: JRC obtained from Rp for Absolute Black

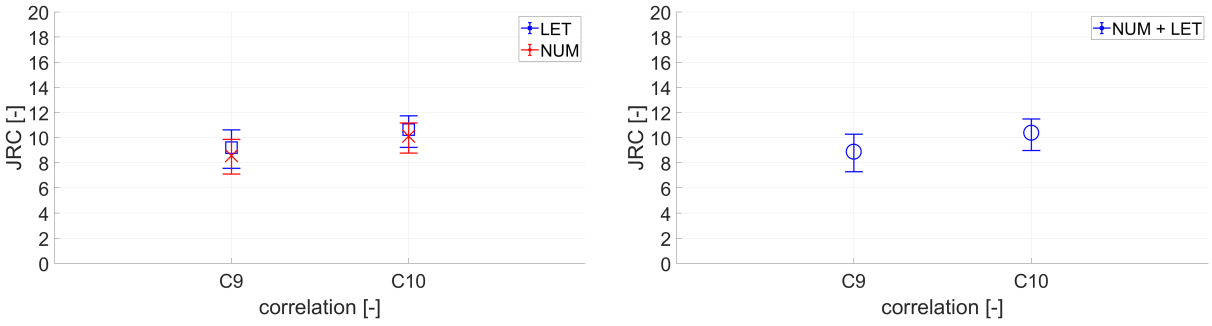

(a) (b)

Figure 4.34: JRC obtained from SF for Absolute Black

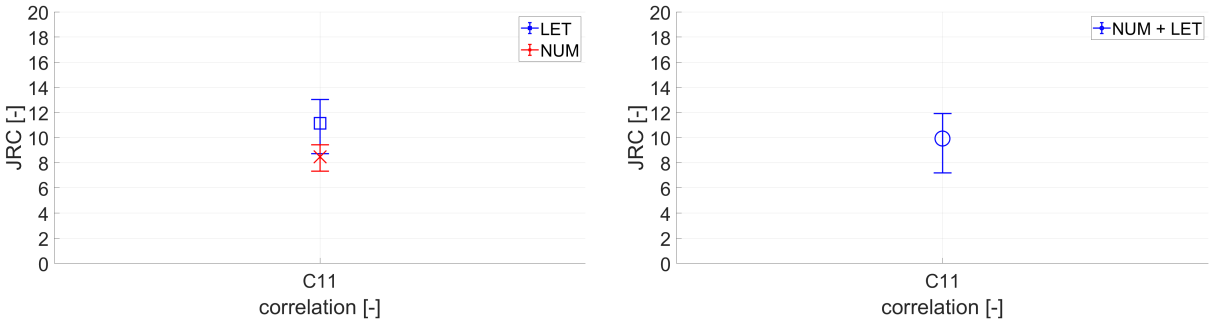

(a) (b)

Figure 4.35: JRC obtained from D for Absolute Black

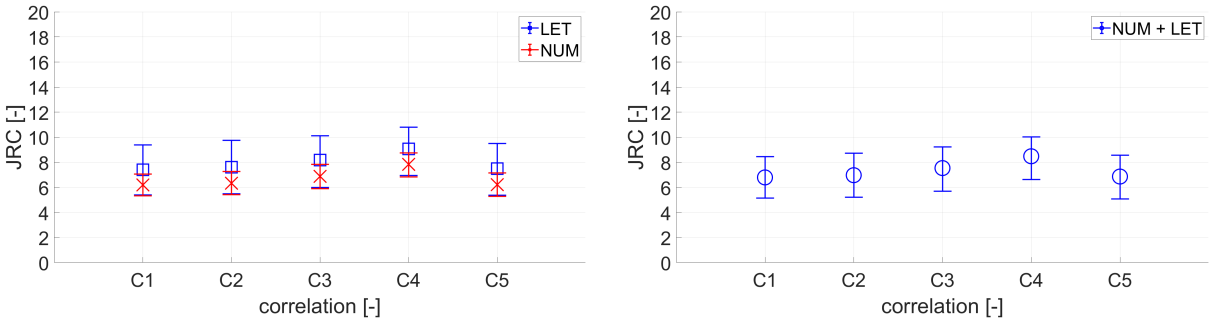

(a) (b)

Figure 4.36: JRC obtained from Z_2 for Carrara

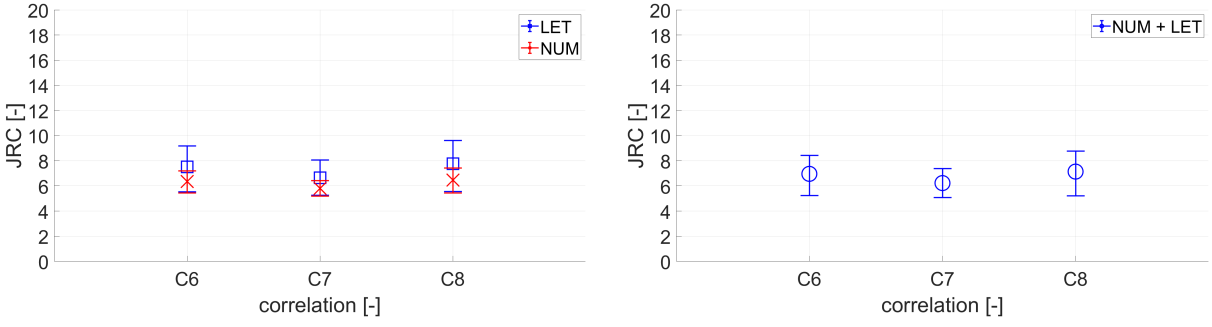

(a) (b)

Figure 4.37: JRC obtained from Rp for for Carrara

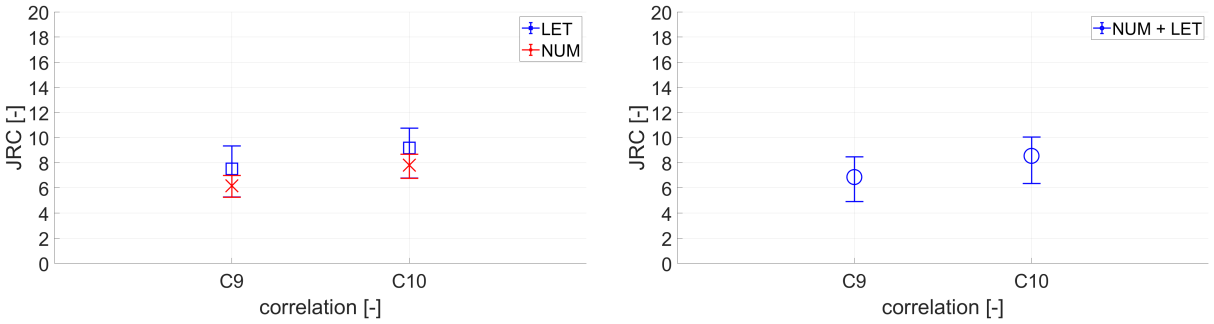

(a) (b)

Figure 4.38: JRC obtained from SF for Carrara

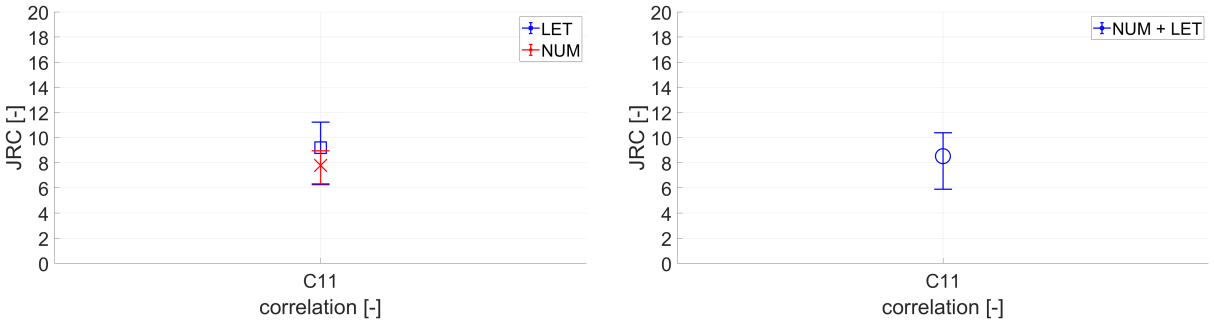

(a) (b)

Figure 4.39: JRC obtained from D for Carrara

4.2.3 JRC estimation from qualitative comparison with standard profiles

A qualitative comparison of the collected profiles with the standard profiles provided by Barton and presented in fig. 2.7, was carried out. The profiles were opportunely scaled, preserving the shape, at the width suggested by the author of 10 cm. A visual evaluation of the JRC was assessed and the results are presented in table 4.3.

Table 4.3: JRC from the qualitative comparison with the standard profiles provided by [9]

	JRC			
Profile	Porriño	Syenite	Absolute Black	Carrara
1	14	10	6	8
2	16	9	10	6
3	15	10	8	7
4	15	11	8	5
5	16	9	7	5
6	15	9	8	6
7	17	10	8	5
8	15	8	6	7
9	12	7	8	7
10	13	9	8	5
11	10	8	9	4
12	12	11	7	5
13	10	9	9	5
14	12	10	8	4
15	11	8	10	7
16	10	10	9	8
17	9	10	8	9
18	11	8	11	9
19	13	9	8	5
20	14	8	8	6
21	14	8	11	7
22	16	10	10	6
23	14	10	8	6
24	16	8	10	4
25	14	9	11	6
26	16	10	10	7
27	16	10	7	8
28	15	8	11	6
29	10	9	10	7
30	12	10	8	8
31	11	8	10	8
32	13	9	9	8
33	13	8	9	8
34	11	9	10	6
35	13	9	12	6
36	11	10	10	8
37	12	9	9	8
38	16	13	9	7
39	15	12	11	8
40	15	12	10	5
41	15	10	10	5
42	16	9	9	6
43	15	11	8	4
44	13	12	10	5
45	14	10	9	5
46	12	11	8	10
47	14	11	7	9
48	13	10	8	9
49	11	12	9	9
50	10	10	8	9
51	10	10	7	9
52	12	9	10	9
53	11	8	9	6
54	9	8	10	6
Average JRC	13	10	9	7

4.3 Discussion of the results

The analysis of the roughness parameters and their impact on the Joint Roughness Coefficient (JRC) gives an insight on the role of fracture mechanism in the formation of the roughness. As a matter of fact, a different roughness was measured, in some cases, for the two series of profiles of different direction of analysis. Being the "numbers" direction orthogonal and the "letters" direction parallel to the induced fracture propagation as previously shown in fig. 4.1, the latter gives higher values of JRC in Syenite, Absolute Black and Carrara.

Notably, Porriño exhibits a distinct behavior, with higher JRC values observed in the direction of numbers compared to the direction of "letters", as can be observed from figures 4.24–4.27 (a). This unexpected trend in Porriño suggests potential anisotropy in the fracture propagation process. One reason could be found in the fabric heterogeneity of the material and in minerals size: in fact Porriño has the coarsest minerals compared to the other analyzed lithotypes.

In the case of Syenite, as shown in figures 4.28–4.31 (a), no significant differences in JRC values were observed between the two orthogonal directions. This could suggest a more isotropic nature of fracture propagation given by the homogeneity of the composition itself, which allows the orientation of the profile to have a minimal impact on the roughness and consequently on the resulting JRC.

Absolute black and Carrara present a similar behavior with higher JRC values in the direction of "letters" compared to "numbers", as clearly visible in figures 4.32–4.35 (a) and 4.36–4.39 (a). This findings lead to a slightly anisotropic pattern in these lithotypes, where the fracture surface characteristics are more pronounced in one direction than the other, even if the mineralogical structure is very homogeneous.

Passing to the correlations between roughness parameters and JRC, it can be observed that correlations $C1$, $C2$ from Yu & Vayssade and $C5$ from Tatone & Grasselli provide very similar results in terms of JRC. $C3$ and $C4$ correlations lead to the highest absolute values of the coefficient. The correlations $C6$, $C8$ and $C9$ well match the values obtained with $C1$, $C2$, $C5$ while $C7$ tends to lower values of JRC . $C10$ from SF and $C11$ from D give higher values comparable to $C3$ and $C4$.

Moreover, these described trends are consistent between the lithotypes except for the "numbers" direction of Porriño samples. Nevertheless, this discrepancy is not attributed to the formulation itself but to the different roughness of the fracture in the orthogonal direction to the fracture propagation. This lead to consider that for high roughness of the surface (or profile) being analyzed, such as in the case of Porriño, the correlations of Z_2 can fail the prediction of JRC or at least can be less consistent and more variable, so attention must be paid in that case. Instead, the correlations with other parameters, such as R_p, SF and D, provide almost equal and reliable results between them.

On the contrary the same relationships do not provide the same reliability in JRC results for the "letters" direction of Porriño and for the other lithotypes in which the roughness is lower.

Considering the whole datasets of analyzed profiles, averaging the most reliable correlations according to this study ($C1$, $C2$, $C5$, $C6$, $C8$ and $C9$), the resulting JRCs are summarized in the following table:

Table 4.4: JRC from the qualitative comparison with the standard profiles provided by ISRM [9]

	Syenite	Absolute Black	Porriño	Carrara
JRC	9	9	13	7

The qualitative comparison of the roughness profiles with those provided by ISRM [9], shows quite similar results in terms of JRC.

The trend of the shear stiffnesses of the interfaces computed in the Chapter 3 and reported in the simplified table 4.5, is justified by the JRC values of each fracture surface. While Porriño presents the highest shear stiffness at the interface and the highest JRC values, Carrara has the lowest values in both findings. Syenite and Absolute Black have comparable results both in terms of shear stiffness and JRC. A correlation between the roughness, as evaluated trough the calculation of roughness parameters on many analyzed profiles and the dynamic stiffness of the interface seems to emerge from the results of the tests reported here.

Table 4.5: Normal and tangential stiffness of the fracture for each lithotype.

Lithotype	K_σ	K_τ
-	$\mathrm{TPa\,m^{-1}}$	$\mathrm{TPa\,m^{-1}}$
Syenite	91.5 ± 74.5	40.5 ± 22.8
Absolute Black	30.2 ± 9.0	51.0 ± 14.7
Pink Porriño	203.3 ± 104.9	270.4 ± 61.1
Carrara	95.2 ± 45.0	31.0 ± 13.7

Chapter 5

Image analysis of surfaces

5.1 Image acquisition procedure

The aim of this chapter is to investigate some petrographic aspects of the specimens, such as the mineralogical composition or the difference between the composition of a saw–cut surface and the fracture surface. Images of the rough surfaces of the fractured samples were taken in the Photographic Lab of the DISEG, using a specific setup as illustrated in fig. 5.1, with the camera fixed at a constant distance from the working plane. An example of the captured images is presented in fig. 5.2.

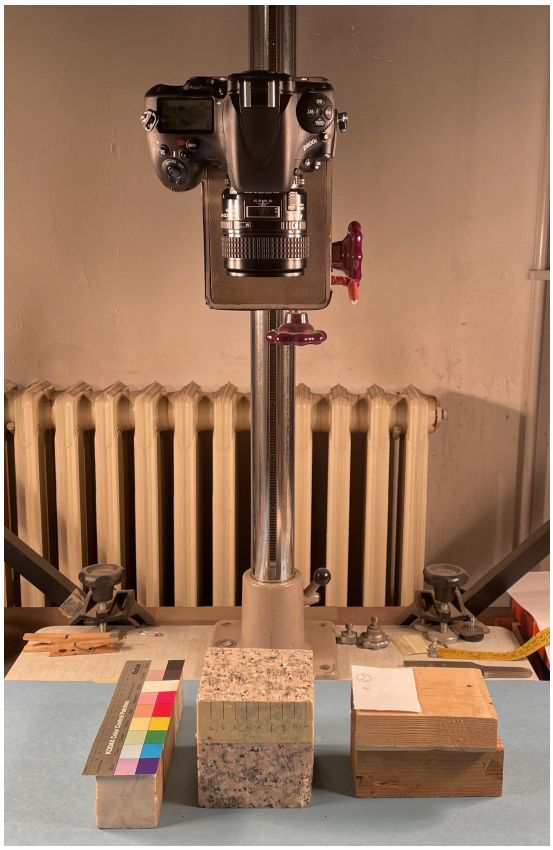

Figure 5.1: Setup of the camera in the Photographic Lab.

(a) (b)

Figure 5.2: Photos of the two sides of a splitting fracture in a Porriño sample. (a): side A; (b): side B.

In order to refer the images to the same local coordinate system (a process called "image registration" in photogrammetry), a geometrical setup built with the software Adobe Illustrator was adopted, to allow obtaining the center of the face of each half sample. Firstly, the corners of each half sample were obtained crossing the extensions of the sides. Then the diagonals were traced and the center was found. All the images were cropped using equal–size squares of 9.5cm of side, positioned in the center of the sample. The geometrical setup is shown in fig. 5.3.

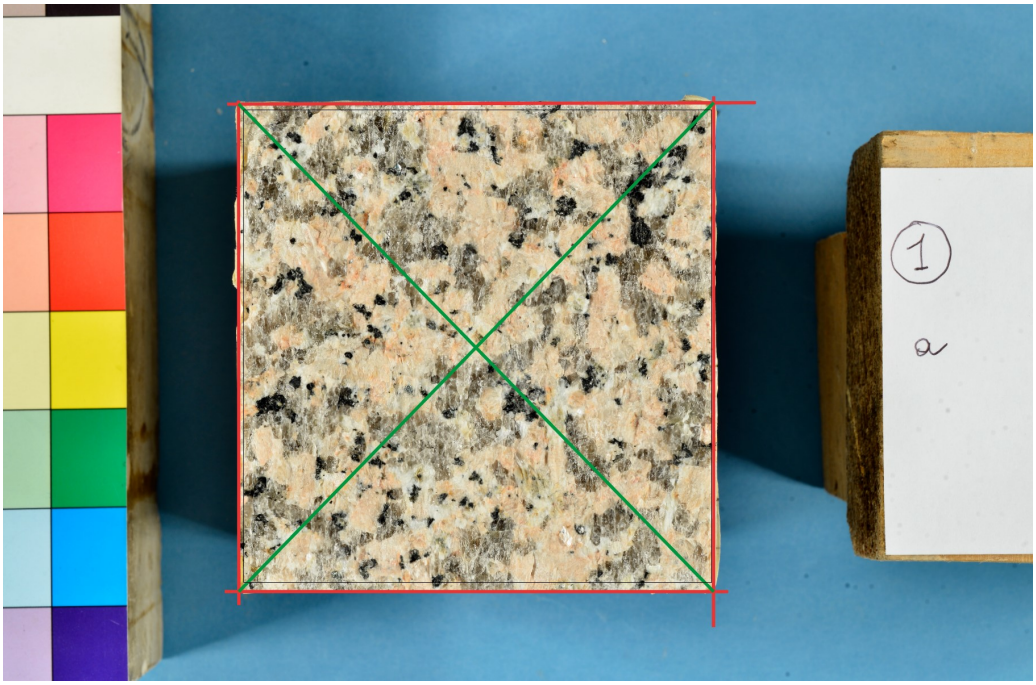

Figure 5.3: Geometrical setup to find the center of the Porriño sample.

The images related to the side "B" of the fracture surfaces are symmetric with respect to the side "A", so they are vertically mirrored and presented in fig. 5.4 and fig. 5.5 for the Porriño sample 1 and for the Syenite sample 1, respectively.

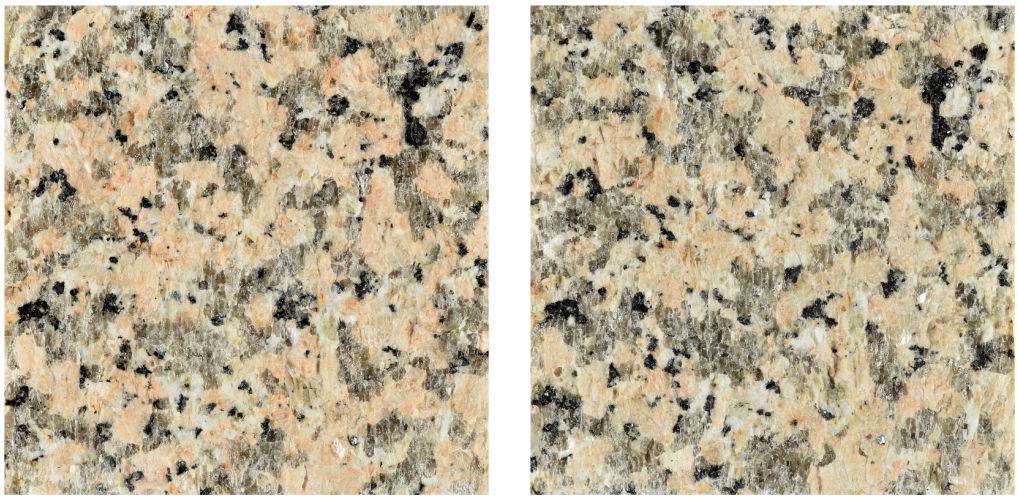

(a) (b)

Figure 5.4: Cropped image of the fracture surface of Porriño sample 1. (a): side A; (b): side B.

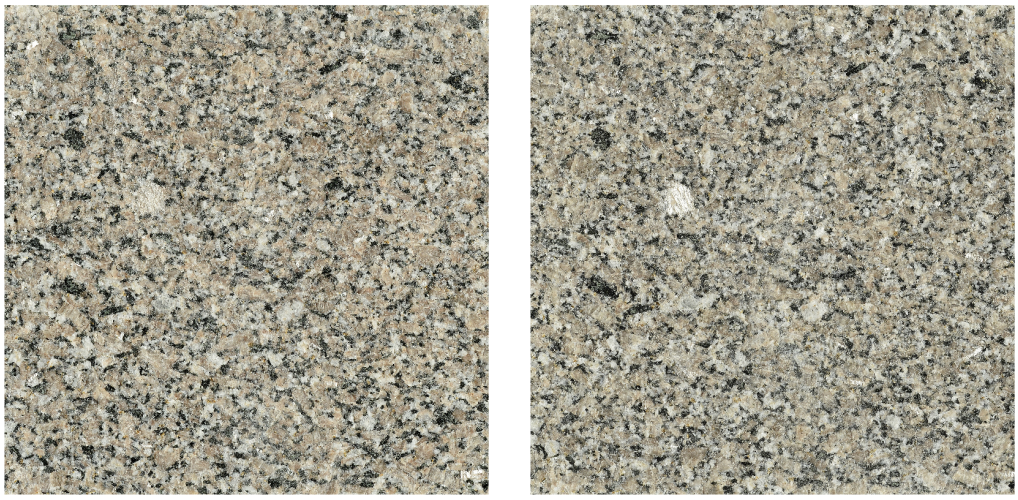

(a) (b)

Figure 5.5: Cropped image of the fracture surface of Syenite sample 1. (a): side A; (b): side B.

5.2 Mineralogical composition: results

The relative abundance of each mineral on the saw cut surfaces is considered representative of the volumetric mineralogical composition. This section is aimed at evaluate the influence of the fracturing process on the rough surfaces composition that could lead to different relative abundances of the minerals. In order to obtain the mineralogical composition of each surface, the images were processed using the software *ImageJ*, to allow the quantification of different colors corresponding to different mineral inclusions. The table 5.1 provides the mineral–color correlation adopted for this analysis, where the colors are chosen after a visual inspection of the surfaces.

Each image was converted to scale–grey colors and a color threshold is applied allowing to isolate the colors corresponding to different minerals, which abundance has to be evaluated. The *watershed* function allows the image segmentation, obtaining a complete separation of the particles. It is based on a topographic mapping process, where image intensity values are

Table 5.1: Mineral–color correlation adopted for Syenite and Porriño samples.

Mineral	Syenite	Porriño
Potassium feldspar	Grey/Violet	Pink
Mafic	Black	Black
Plagioclase	White	White
Quartz	-	Grey

considered as heights on a landscape. The process starts with the intensity gradient computation across the image that allow to identify potential watershed lines. Then the center of each object is used as starting point for *flooding*, which means to fill the map with imaginary water. The watershed lines which represents the boundaries between segmented regions are identified where flooding from different markers meets. Below, each photograph refers to a different isolated color whose pixels are white, while those that has no correspondence are black. The images processed by colors of the saw–cut surface of Porriño sample 1 are shown in fig. 5.6.

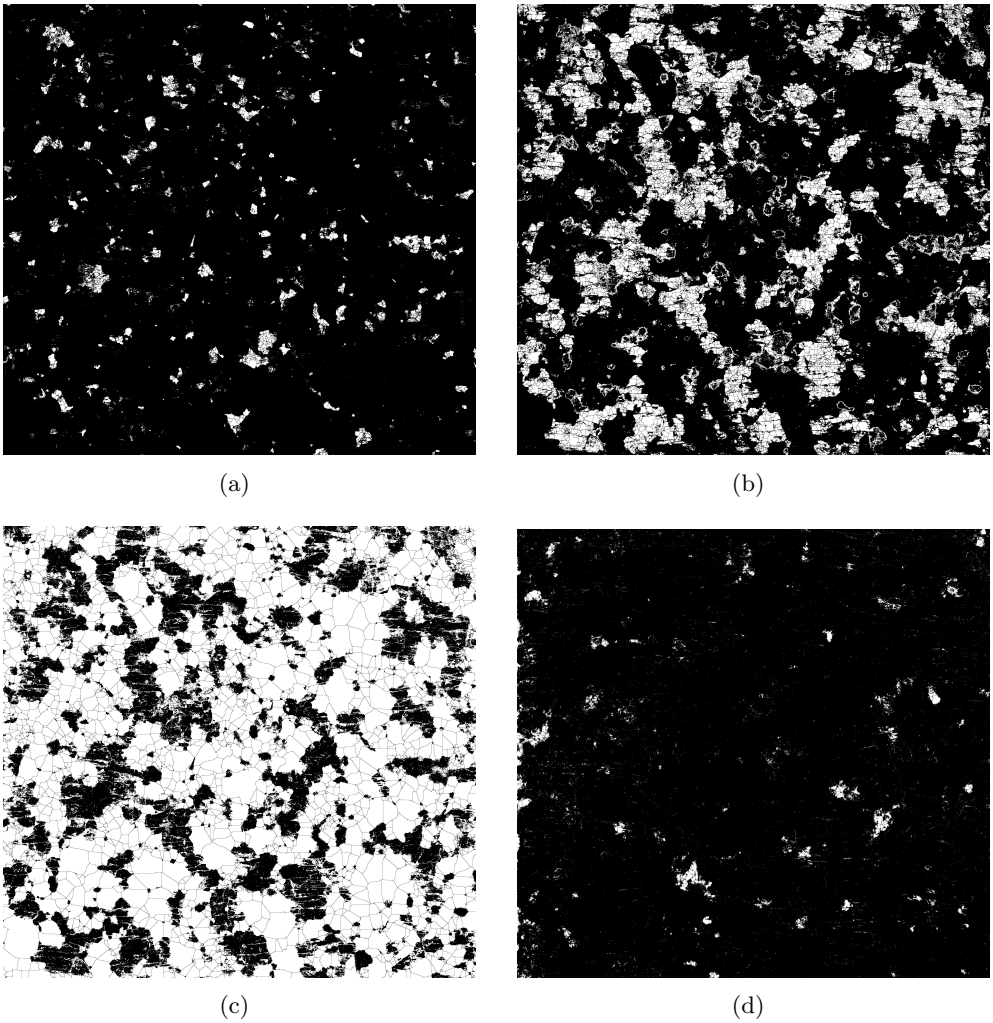

(a) (b)

(c) (d)

Figure 5.6: Color extraction using ImageJ of Porriño sample 1. Saw-cut surface. (a) black; (b) grey; (c) pink; (d) white.

The same process is applied to the rough fractures (side "A") and the processed pictures are shown in fig. 5.7. The other samples of Porriño are reported in the Appendix D for the sake of readability. The mineralogical compositions of both the saw–cut and the rough fractures are summarized in table 5.2.

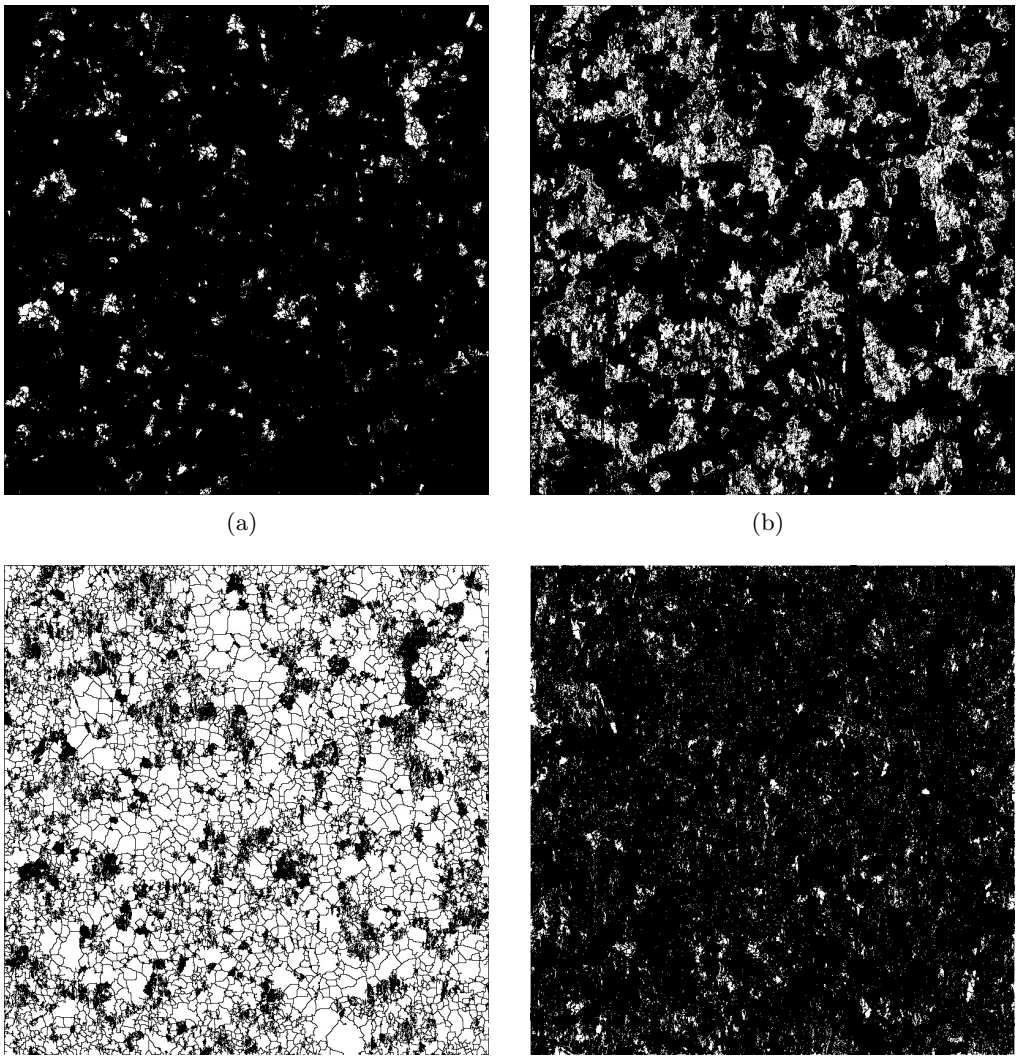

(a) (b) (c) (d)

Figure 5.7: Color extraction using ImageJ of Porriño sample 1. Fracture surface (side "A"). (a) black; (b) grey; (c) pink; (d) white.

Table 5.2: Mineral composition of Porriño samples.

			Porriño 1	Porriño 2	Porriño 3
Color	Mineral	Saw-cut surface	Fracture surface		
Pink	Potassium feldspar	68.3 %	73.3 %	68.3 %	68.4 %
Grey	Quartz	25.3 %	17.8 %	18.9 %	17.9 %
Black	Mafic	4.1 %	3.7 %	3.7 %	4.7 %
White	Plagioclase	2.3 %	5.2 %	9.1 %	9.0 %
		100.0 %	100.0 %	100.0 %	100.0 %

The pictures of the saw–cut surface and of the rough fracture of Syenite sample 1 are shown in fig. 5.8 and fig. 5.9, respectively. The other samples of Syenite are reported in the Appendix D for the sake of readability. For both surfaces the mineralogical compositions are summarized in table 5.3.

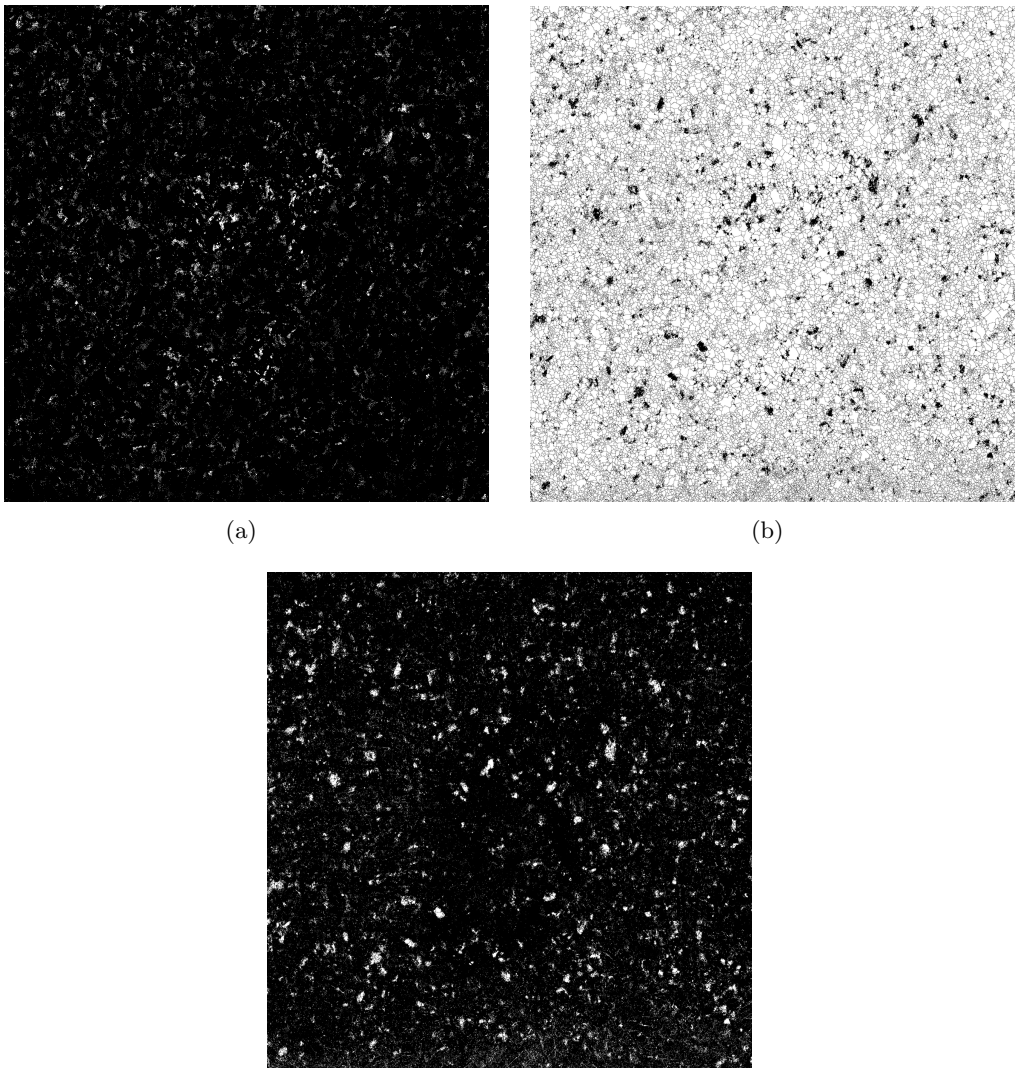

(a) (b)

(c)

Figure 5.8: Color extraction using ImageJ of the Syenite sample 1. Saw–cut surface. (a) black; (b) grey; (c) pink; (d) white.

Table 5.3: Mineral composition of Syenite samples.

			Syenite 1	Syenite 2	Syenite 3
Color	Mineral	Saw-cut surface	Fracture surface		
Grey/violet	Potassium feldspar	90.0 %	79.6 %	75.3 %	75.2 %
Black	Mafic	3.1 %	5.5 %	6.7 %	6.6 %
White	Plagioclase	6.9 %	14.9 %	18.0 %	18.2 %
		100.0 %	100.0 %	100.0 %	100.0 %

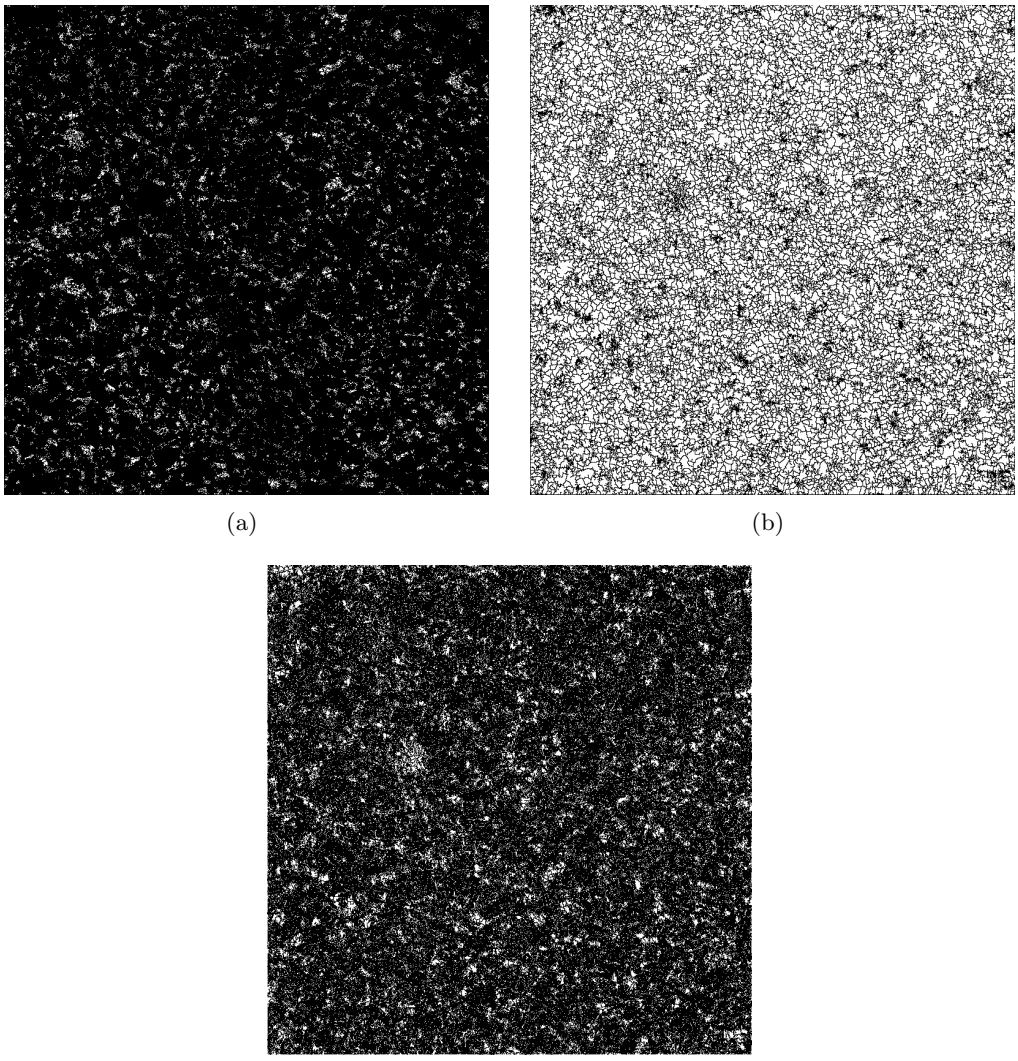

(a) (b)

(c)

Figure 5.9: Color extraction using ImageJ of the Syenite sample 1. Fracture surface. (a) black; (b) grey; (c) pink; (d) white.

5.3 Mismatching of the two faces of the fracture: results

The correlation of the two faces of the fracture is performed using the *Image Calculator* tool in *ImageJ*. Firstly, the images are resized with a sampling rate of 4 pixels for millimeter to avoid a possible error due to the alignment process of the image pairs. Then, the image difference is obtained by subtracting the RGB pixel values of the two images. This difference is composed of black pixels in the case of correlation (equal colors in source images) and white pixels in case of no correlation (different color in source images). An example of this type of operation is reported in fig. 5.10, where (a) shows low correlation between the compared pictures while (b) shows the total correlation which is obtained comparing an image with itself.

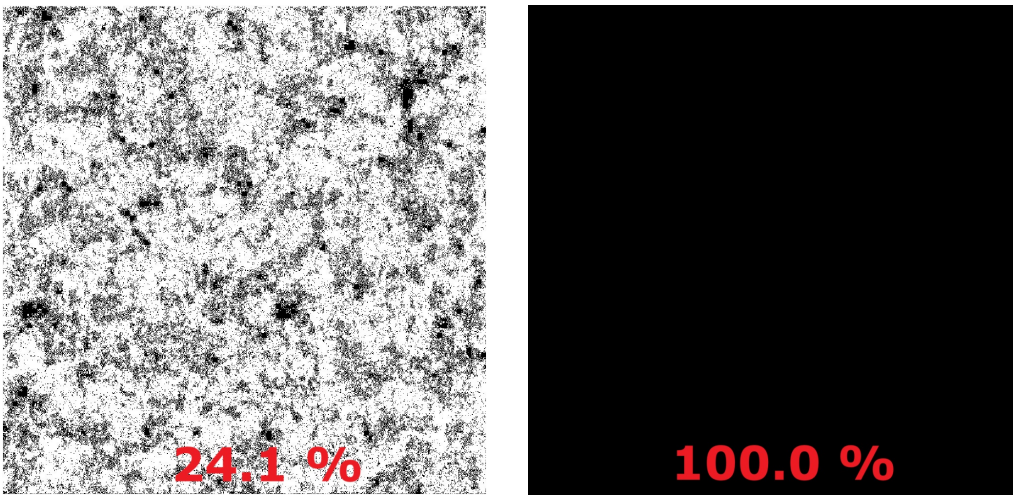

(a) (b)

Figure 5.10: Image correlation of the Porriño sample 1. (a) low correlation (24.1%); (b) total correlation (100.0%).

The correlations between the two faces of the fracture for the Porriño samples and the Syenite samples are presented in fig. 5.11 and fig. 5.12, respectively. The percentage of mismatching is shown in red in the figures.

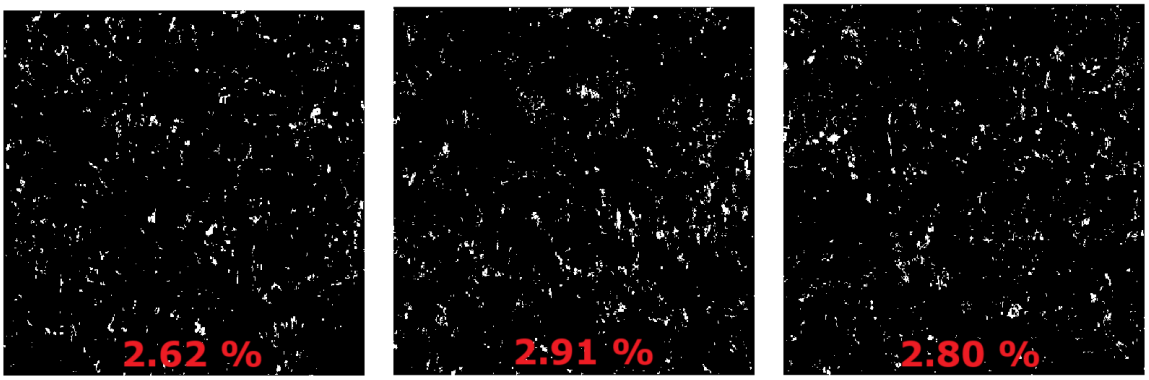

(a) (b) (c)

Figure 5.11: Mismatching of the two faces of the fracture in Porriño samples. (a) Porriño 1; (b) Porriño 2; (c) Porriño 3.

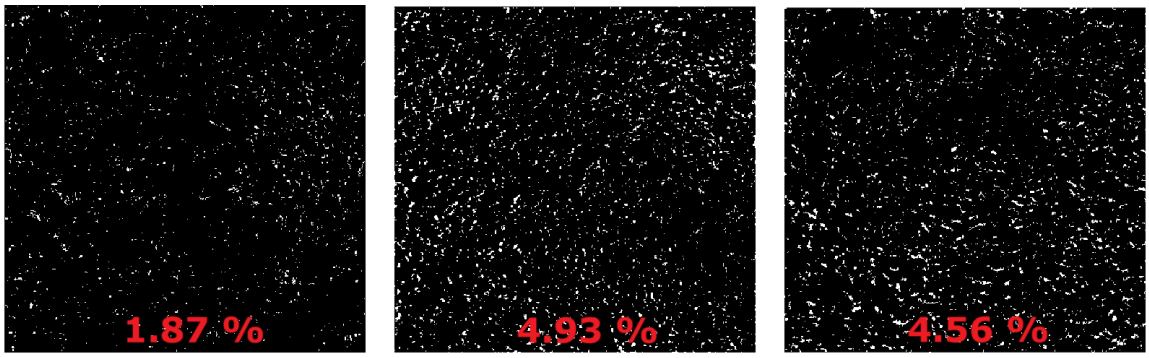

(a) (b) (c)

Figure 5.12: Mismatching of the two faces of the fracture in Syenite samples. (a) Syenite 1; (b) Syenite 2; (c) Syenite 3.

5.4 Discussion of the results

The analysis of the distribution of minerals on fracture surfaces and its comparison with the one of saw-cut surfaces is used in this thesis to investigate the process of fracture propagation, at the microscopic scale. The comparison has been done in terms of percentages of different minerals observed on the exposed faces and by analyzing the level of mismatch between the two sides of the fracture. In the first case, a variation in minerals percentages from saw-cut surface to fracture could reveal a preferential path of the fracture, determined by the properties of particular minerals, i.e. the fracture tends to develop avoiding minerals with greater resistance.

Porriño samples reveal a good match in minerals distribution between the saw cut surface and the rough fractures. *Potassium feldspar* (pink mineral) and *Mafic* (black mineral) have the same proportion. *Quartz* (grey mineral) has higher concentration in the saw cut surfaces at the expense of *Plagioclase* (white mineral) that has lower concentration. When comparing the rough fractures, the first sample shows higher content of *Potassium feldspar* (73.3% vs 68.3%, 68.4%) and lower content of *Plagioclase* (5.2% vs 9.1%, 9.0%). *Quartz* and *Mafic* are essentially present in the same proportion. In contrast, the rough fractures of Syenite samples show a notably higher concentration of *Plagioclase* and a lower presence of *Potassium feldspar* (violet) with respect to the saw cut surfaces. Moreover, the three rough fractures are very similar in composition with slightly high presence of *Potassium feldspar* in the first sample (79.6% vs 75.3%, 75.2%) at the expense of *Plagioclase* (14.9% vs 18.0%, 18.2%). Syenite shows higher variations between saw cut and rough surfaces, that could means a slightly higher mineral redistribution during fracturing, i.e. strong minerals are avoided by the fracture.

An in-depth analysis of color mismatch between the two sides of the fracture reveals a strong correlation, suggesting that a significant portion of minerals were truncated or separated along pre–existing weakness planes. This process effectively preserved the relative position of minerals, rendering them consistent on both sides of the rough fracture surfaces. In cases where no matching is observed, it indicates that the fracture has bypassed the minerals, avoiding their truncation or separation. This mechanism points out the complexities of fracture propagation and the ability of fractures to adapt to the geological heterogeneity within rock formations. Both samples exhibit differences of less than 5%, confirming what was observed before: almost all the minerals were truncated by the fracture development process.

Chapter 6

Conclusion

Following an introductory overview on the role of discontinuities in the mechanical behavior of rock masses in terms of strength and deformability, the present document describes the experimental lab activities conducted to evaluate the dynamic and static deformability of different rock specimens and to characterize the interfaces artificially obtained by inducing tensile fractures (Mode—I) within the specimens. The tests have been carried out on prismatic specimens and the analysis of their results has required in some cases ad hoc interpretations. In particular four different types of rocks were considered: Balma Syenite, Absolute Black Gabbro, Pink Porriño Granite and Carrara marble.

Ultrasonic P–wave and S–wave propagation tests have been performed on intact rock specimens in three orthogonal directions, measuring the arrival times of each wave. Using the equations presented in Chapter 2, the dynamic deformability properties such as Young's modulus and Poisson's ratio, have been evaluated.

Regarding the uniaxial compression tests, the specimens were prepared and the tests performed according to the standards provided by ISRM [9] and by UNI EN 14580/2005 [24] for the determination of the static elastic modulus of natural rock prisms. The obtained results in terms of static Young's modulus and Poisson's ratio were compared to the dynamic deformability properties given by the ultrasonic propagation tests, highlighting higher values in the dynamic case, as expected from literature.

Ultrasonic tests were repeated on the fractured rock samples, to evaluate the influence of the interfaces on the deformability of the rock samples. The interface stiffnesses were found to have a inverse correlation with the deformability properties of the intact rock specimens. Indeed, higher the elastic Young's modulus (static or dynamic) lower the interface normal or tangential stiffness.

A statistical analysis of the roughness profiles of the artificial interfaces was also carried out, using mathematical descriptors such as Z_2, RP, SF, D and using many empirical correlations available in literature to obtain an evaluation of the JRC for each profile. The results were treated once separately for each direction of analysis (parallel and orthogonal to the propagation direction of the induced fracture) and then grouped together. The correlations were found to have different reliability based on different level of roughness of the considered profiles. A summary of the more reliable equations according to the considerations made in this study was highlighted. In particular the correlations $C1$, $C2$, $C5$, $C6$, $C8$ and $C9$ were found to have low dispersion and good correspondence with the classical visual method of JRC evaluation. Furthermore, a correlation between the JRC obtained in this way and the dynamic shear stiffnesses of the interfaces was also outlined. In particular higher roughness (higher JRC) correspond to higher shear stiffness, as expected from literature.

Image analysis has been performed on the samples photographs to obtain the relative abundances of the minerals on the saw cut surfaces, representative of the volumetric composition of the rock, and on the rough fractures to highlight differences induced by the fracturing process.

A further comparison between the two sides of the fracture surfaces was made to catch if some minerals were truncated or bypassed by the splitting. The results shows that almost all the minerals were truncated, suggesting that they do not influence the fracturing process.

Finally, tilt tests were performed on the smooth surfaces to evaluate the base friction angle. The results were interpreted and correlated to the grain size of the materials, given that the fine-grained rocks show smaller angles and the coarse-grained ones show larger angles.

In conclusion, the considerations outlined in this document would be particularly valuable, and the procedure proposed in Chapter 4 with the set of probabilistic analysis proposed could represent a crucial input for design purposes. These analysis would enable the construction of a valuable design tool calibrated to the mechanical characteristics of the materials under examination. Furthermore, conducting additional ultrasonic propagation tests on specimens with varying confinement, would allow for a more in-depth assessment of the influence of the interfaces on the mechanical behavior of brittle rocks.

Bibliography

[1] Z. T. Bieniawski. *Engineering rock mass classifications: a complete manual for engineers and geologists in mining, civil, and petroleum engineering*. John Wiley & Sons, 1989.

[2] A.F.A. Babiker et al. "Non-associative limit analysis of the toppling-sliding failure of rock slopes." In: *International Journal of Rock Mechanics and Mining Sciences* 71 (Oct. 2014), pp. 1–11. DOI: 10.1016/j.ijrmms.2014.06.008.

[3] M.S. Diederichs. "When does brittle failure become violent? Spalling and rockburst characterization for deep tunneling projects." In: *Proceedings: World Tunneling Conference*. 2014.

[4] F.T. Suorineni, B. Hebblewhite, and S. Saydam. "Geomechanics challenges of contemporary deep mining: a suggested model for increasing future mining safety and productivity." In: *Journal of the Southern African Institute of Mining and Metallurgy* 114 (Dec. 2014), pp. 1023–1032. ISSN: 2225-6253.

[5] S.D. Priest. *Discontinuity Analysis for Rock Engineering*. Chapman & Hall, 1993. ISBN: 9780412476006.

[6] L. Zhang. *Engineering Properties of Rocks*. 2nd ed. Butterworth-Heinemann, 2016. ISBN: 9780128028339.

[7] N. Barton. "Suggested methods for the quantitative description of discontinuities in rock masses: International Society for Rock Mechanics." In: *Int J Rock Mech Min Sci Geomech Abstr* 15 (Jan. 1978), pp. 319–368.

[8] B. Tatone. "Quantitative Characterization of Natural Rock Discontinuity Roughness Insitu and in the Laboratory." PhD thesis. Sept. 2009, pp. 188–.

[9] International Society for Rock Mechanics. *The Complete ISRM Suggested Methods for Rock Characterization, Testing and Monitoring*. Addison-Wesley, 2007.

[10] E. Hoek. *Practical rock engineering*. 2006. URL: https://www.rocscience.com/assets/resources/learning/hoek/Practical-Rock-Engineering-Full-Text.pdf (visited on 09/30/2023).

[11] F.D. Patton and Don U. Deere. "Multiple modes of shear failure in rock and related materials." PhD thesis. University of Illinois at Urbana-Champaign Department of Geology, 1966.

[12] N. Bahrani and P. Kaiser. "Estimation of Confined Peak Strength of Crack-Damaged Rocks." In: *Rock Mechanics and Rock Engineering* 50 (Feb. 2017). DOI: 10.1007/s00603-016-1110-1.

[13] L. Carmignani. *Appunti di geologia applicata Vol.II*. CGT Centro di Geotecnologie dell'Università degli Studi di Siena, 2007.

[14] N. Barton. "Review of a new shear-strength criterion for rock joints." In: *Engineering Geology* 7.4 (Jan. 1973), pp. 287–332. DOI: 10.1016/0013-7952(73)90013-6.

[15] N. Barton and S. Bandis. "Effect of block size on the shear behavior of jointed rocks." In: *Proceedings - Symposium on Rock Mechanics* (Jan. 1982), pp. 739–760.

[16] N.O. Myers. "Characterization of surface roughness." In: *Wear* 5.3 (May 1962), pp. 182–189. DOI: 10.1016/0043-1648(62)90002-9.

[17] G. Zhang et al. "A new method estimating the 2D Joint Roughness Coefficient for discontinuity surfaces in rock masses." In: *International Journal of Rock Mechanics and Mining Sciences* 72 (Dec. 2014), pp. 191–198. DOI: 10.1016/j.ijrmms.2014.09.009.

[18] X. Yu and B. Vayssade. "Joint profiles and their roughness parameters." In: *International Journal of Rock Mechanics and Mining Sciences* 28.4 (July 1991), pp. 333–336. DOI: 10.1016/0148-9062(91)90598-g.

[19] Y. Li and R. Huang. "Relationship between joint roughness coefficient and fractal dimension of rock fracture surfaces." In: *International Journal of Rock Mechanics and Mining Sciences* 75 (Apr. 2015), pp. 15–22. DOI: 10.1016/j.ijrmms.2015.01.007.

[20] Heping Xie. "Fractal Estimation of Joint Roughness Coefficients." English. In: *Chinese Science Abstracts Series B* 14.2 Part B (1995), p. 55.

[21] C. Hellier. *Handbook of Nondestructive Evaluation*. McGraw-Hill Education, 2001. ISBN: 9780071399470.

[22] A.S. Birks, R.E. Green, and P. McIntire. "Ultrasonic Testing." In: Nondestructive testing handbook. American Society for Nondestructive Testing, 1991, pp. 383–431. ISBN: 9780931403040.

[23] G. Starzynski and R. Buczkowski. "Ultrasonic Measurements of Contact Stiffness Between Rough Surfaces." In: *Journal of Tribology* 136 (July 2014), pp. 1–6. DOI: 10.1115/1.4027132.

[24] *Natural stone test methods - Determination of static elastic modulus*. UNI 14580:2005. 2005.

[25] Z. P. Bažant, F. Lin, and H. Lippmann. "Fracture energy release and size effect in borehole breakout." In: *International Journal for Numerical and Analytical Methods in Geomechanics* 17.1 (), pp. 1–14. DOI: https://doi.org/10.1002/nag.1610170102.

[26] E. Brühwiler and F. H. Wittmann. "The wedge splitting test, a new method of performing stable fracture mechanics tests." In: *Engineering Fracture Mechanics* 35.1 (1990). Special Issue Fracture and Damage of Concrete and Rock, pp. 117–125. ISSN: 0013-7944. DOI: https://doi.org/10.1016/0013-7944(90)90189-N.

[27] A. T. Zehnder. "Modes of Fracture." In: *Encyclopedia of Tribology*. Springer, 2013, pp. 2292–2295. DOI: 10.1007/978-0-387-92897-5_258.

[28] M. Mooney. "A Theory of Large Elastic Deformation." In: *Journal of Applied Physics* 11.9 (Sept. 1940), pp. 582–592. DOI: 10.1063/1.1712836.

[29] R. S. Rivlin. "Large elastic deformations of isotropic materials IV. further developments of the general theory." In: *Philosophical Transactions of the Royal Society of London. Series A, Mathematical and Physical Sciences* 241.835 (Oct. 1948), pp. 379–397. DOI: 10.1098/rsta.1948.0024.

[30] L. R. Alejano et al. "ISRM Suggested Method for Determining the Basic Friction Angle of Planar Rock Surfaces by Means of Tilt Tests." In: *Rock Mechanics and Rock Engineering* 51.12 (Oct. 2018), pp. 3853–3859. DOI: 10.1007/s00603-018-1627-6.

[31] C. Yu, S. Ji, and Q. Li. "Effects of porosity on seismic velocities, elastic moduli and Poisson's ratios of solid materials and rocks." In: *Journal of Rock Mechanics and Geotechnical Engineering* 8 (Sept. 2015). DOI: 10.1016/j.jrmge.2015.07.004.

Appendix A

Ultrasonic tests on intact rock specimens

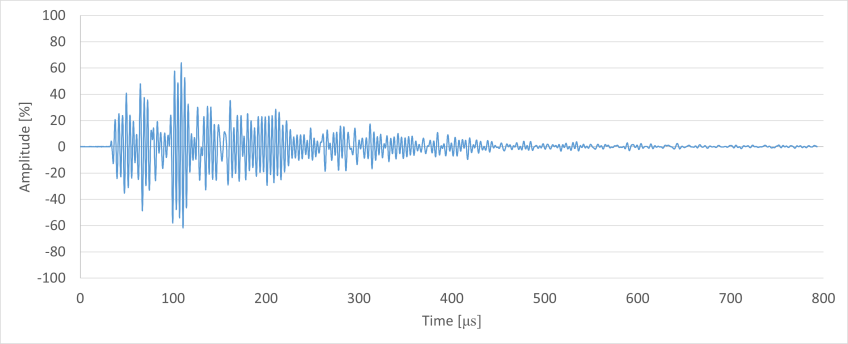

Figure A.1: Recorded signal of P-waves in direction “a” for Absolute Black sample 2

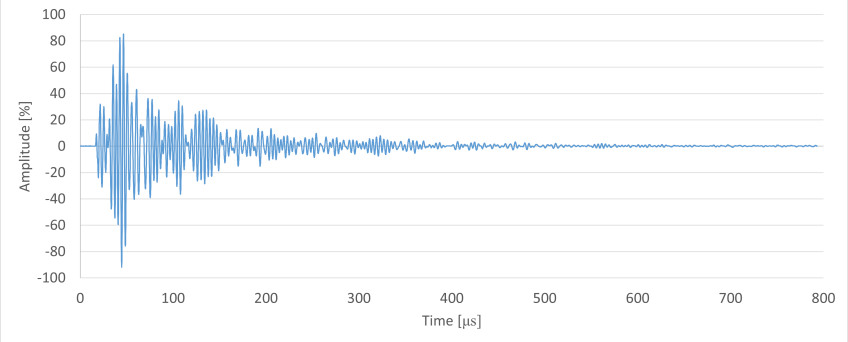

Figure A.2: Recorded signal of P-waves in direction “b” for Absolute Black sample 2

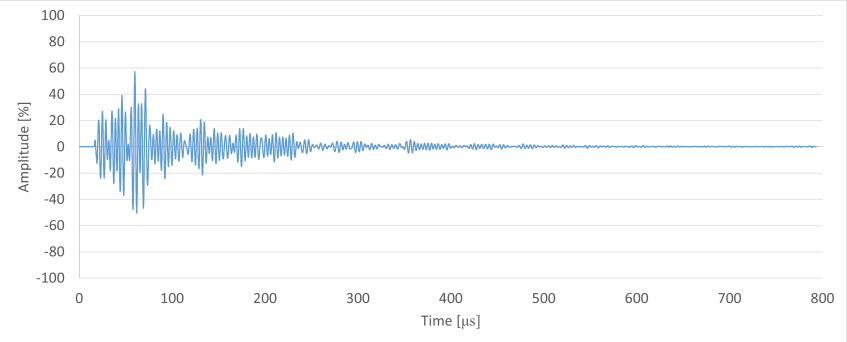

Figure A.3: Recorded signal of P-waves in direction “c” for Absolute Black sample 2

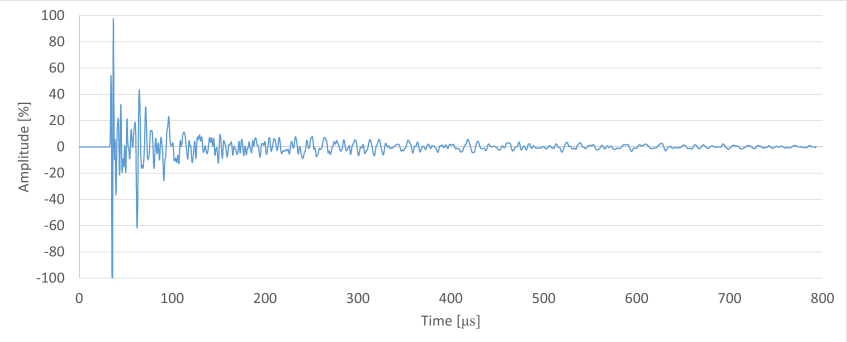

Figure A.4: Recorded signal on vibration plane “x” of S-waves in direction “a” for Absolute Black sample 2

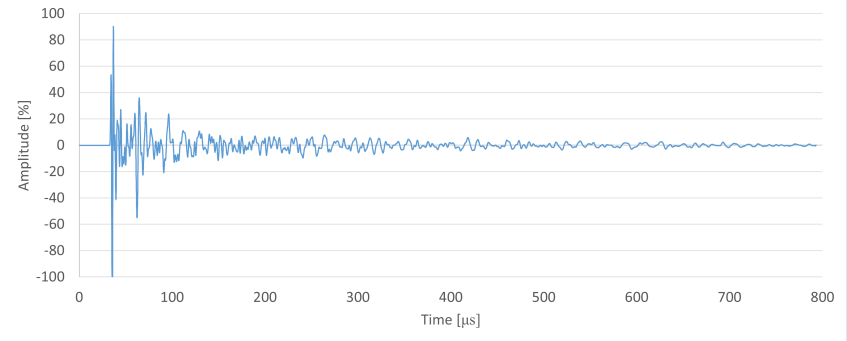

Figure A.5: Recorded signal on vibration plane “z” of S-waves in direction “a” for Absolute Black sample 2

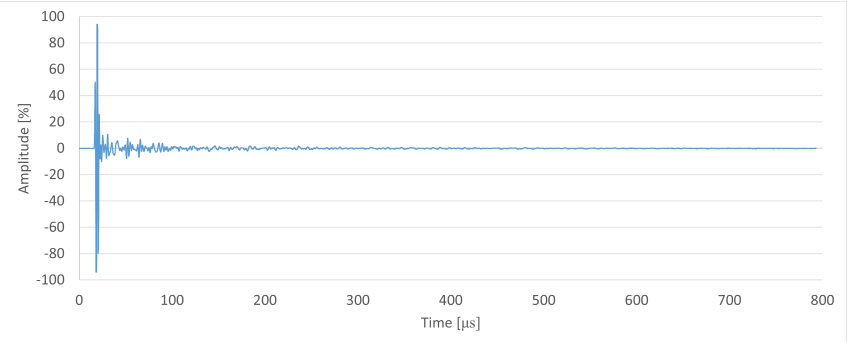

Figure A.6: Recorded signal on vibration plane “z” of S-waves in direction “b” for Absolute Black sample 2

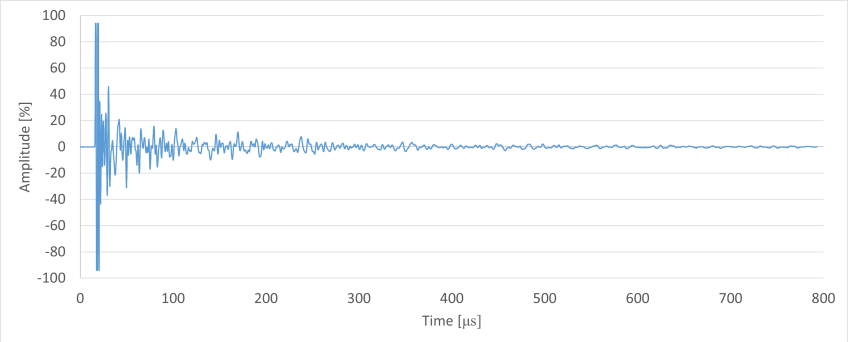

Figure A.7: Recorded signal on vibration plane "z" of S-waves in direction "c" for Absolute Black sample 2

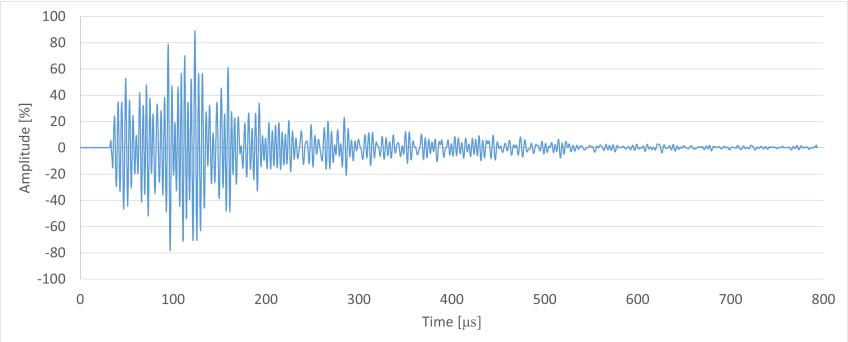

Figure A.8: Recorded signal of P-waves in direction "a" for Absolute Black sample 3

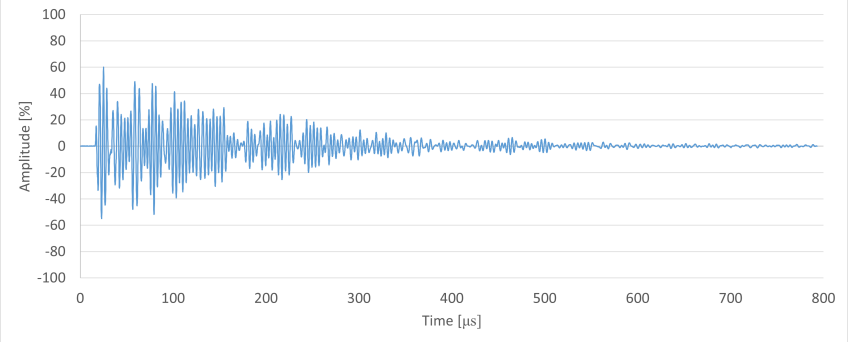

Figure A.9: Recorded signal of P-waves in direction "b" for Absolute Black sample 3

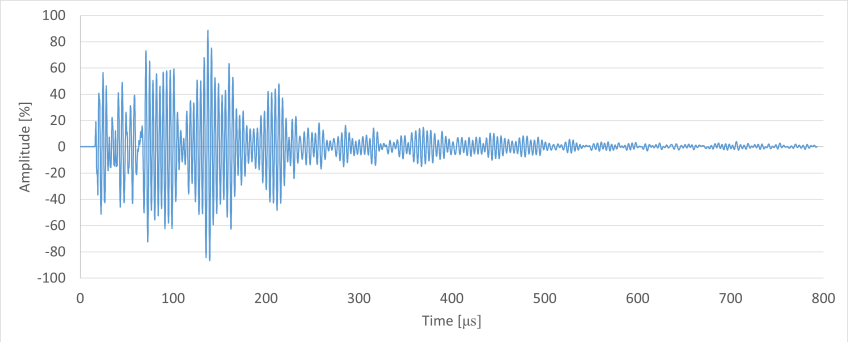

Figure A.10: Recorded signal of P-waves in direction "c" for Absolute Black sample 3

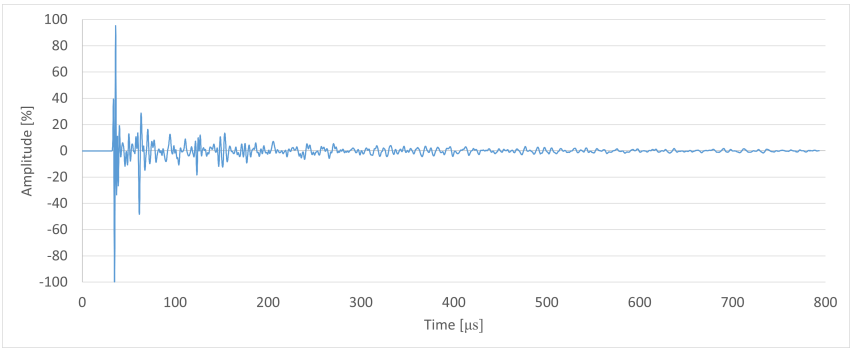

Figure A.11: Recorded signal on vibration plane “x” of S-waves in direction “a” for Absolute Black sample 3

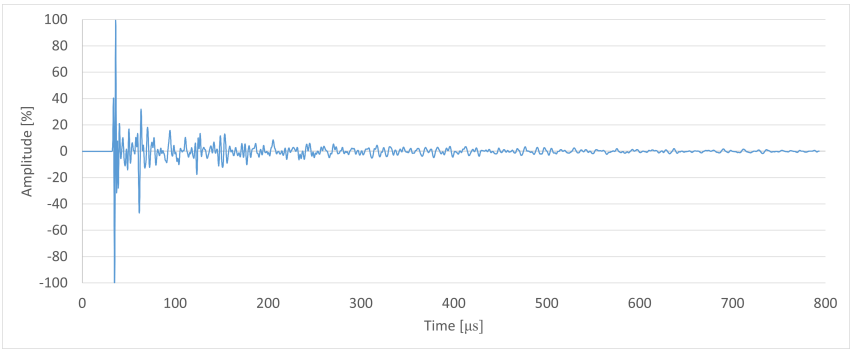

Figure A.12: Recorded signal on vibration plane “z” of S-waves in direction “a” for Absolute Black sample 3

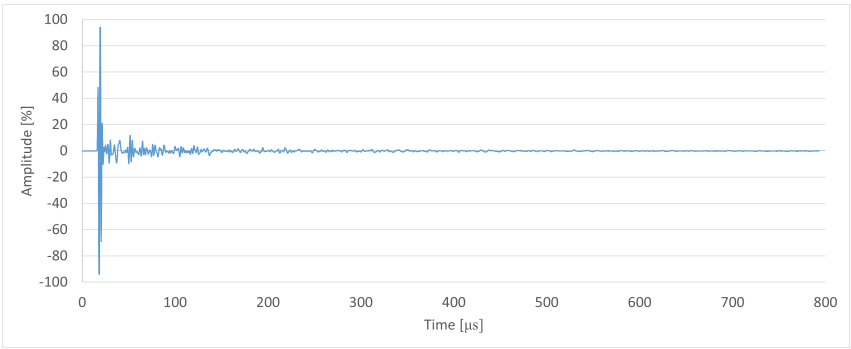

Figure A.13: Recorded signal on vibration plane “z” of S-waves in direction “b” for Absolute Black sample 3

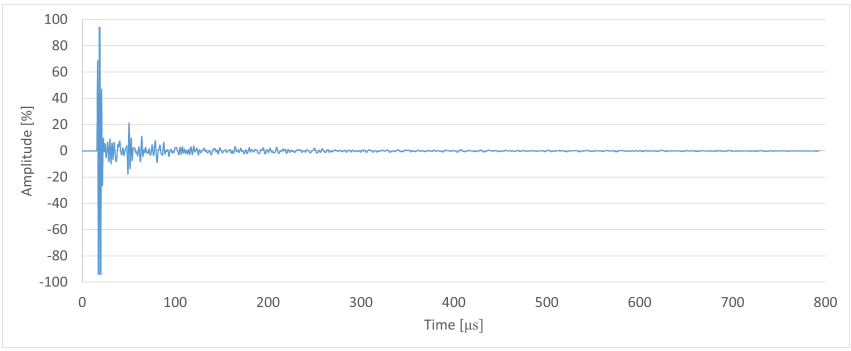

Figure A.14: Recorded signal on vibration plane “z” of S-waves in direction “c” for Absolute Black sample 3

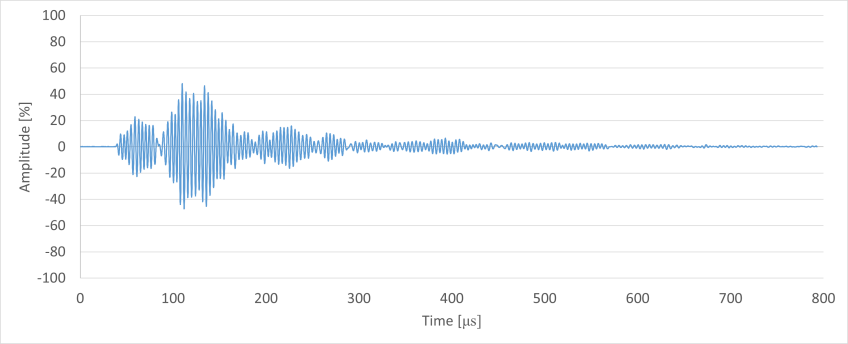

Figure A.15: Recorded signal of P-waves in direction “a” for Syenite sample 1

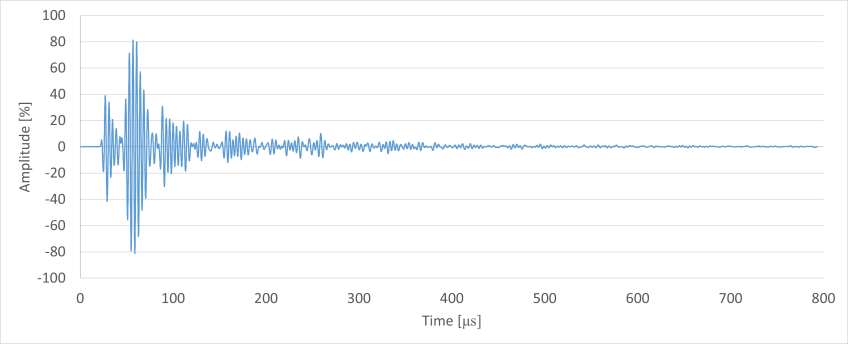

Figure A.16: Recorded signal of P-waves in direction “b” for Syenite sample 1

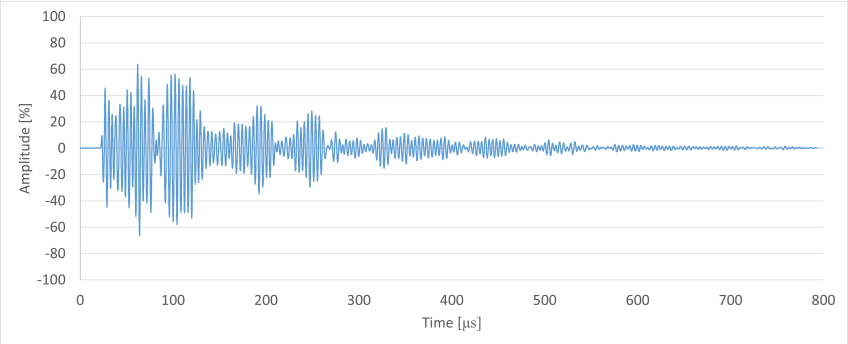

Figure A.17: Recorded signal of P-waves in direction “c” for Syenite sample 1

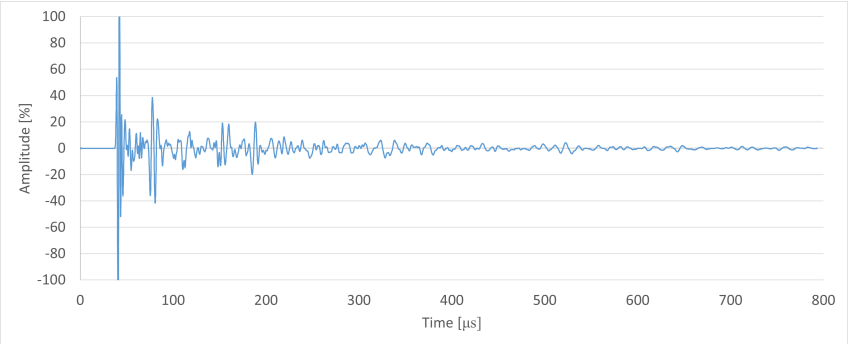

Figure A.18: Recorded signal on vibration plane “x” of S-waves in direction “a” for Syenite sample 1

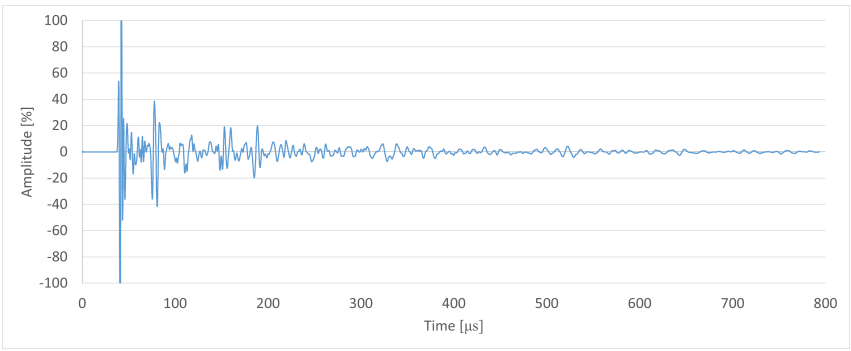

Figure A.19: Recorded signal on vibration plane "z" of S-waves in direction "a" for Syenite sample 1

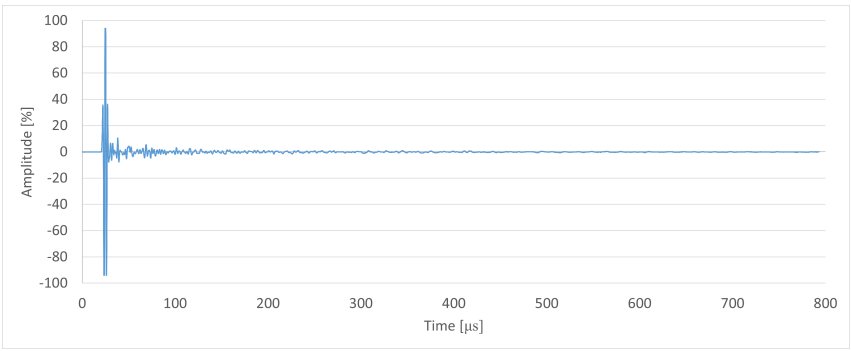

Figure A.20: Recorded signal on vibration plane "z" of S-waves in direction "b" for Syenite sample 1

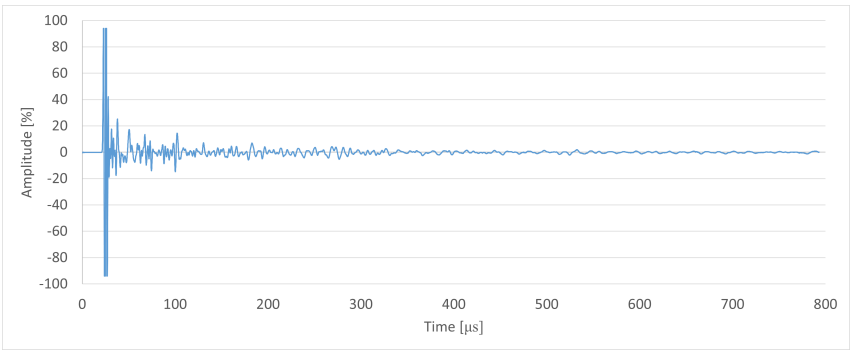

Figure A.21: Recorded signal on vibration plane "z" of S-waves in direction "c" for Syenite sample 1

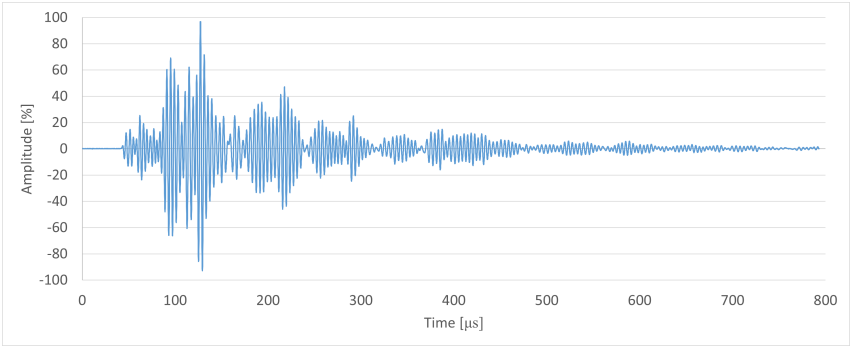

Figure A.22: Recorded signal of P-waves in direction "a" for Syenite sample 2

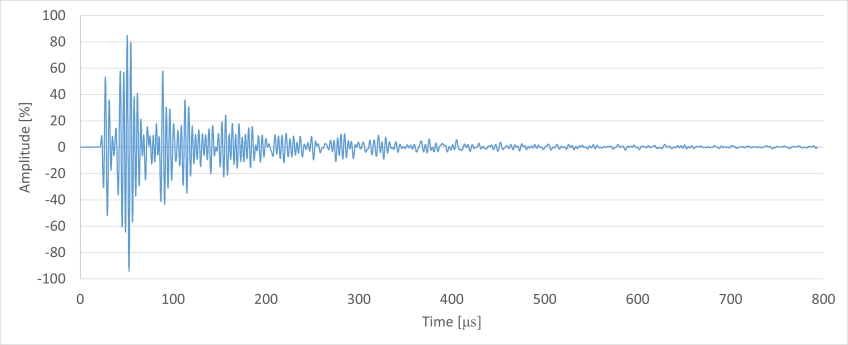

Figure A.23: Recorded signal of P-waves in direction “b” for Syenite sample 2

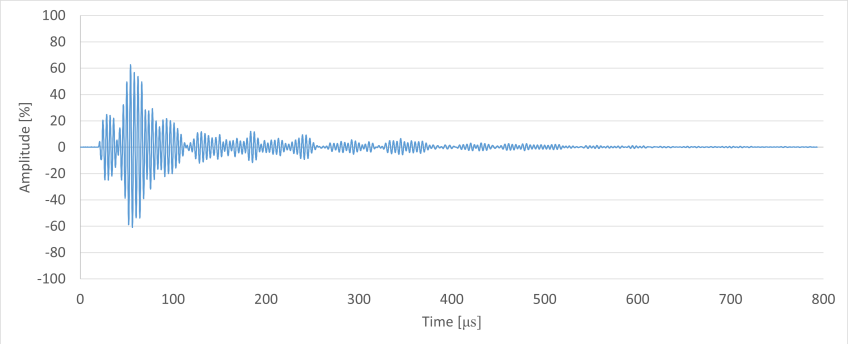

Figure A.24: Recorded signal of P-waves in direction “c” for Syenite sample 2

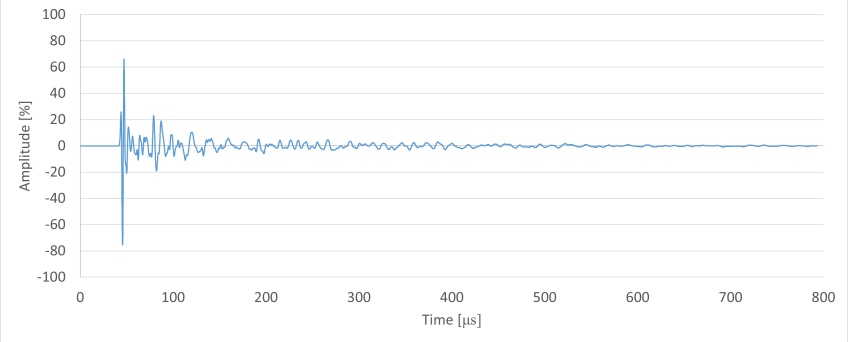

Figure A.25: Recorded signal on vibration plane “x” of S-waves in direction “a” for Syenite sample 2

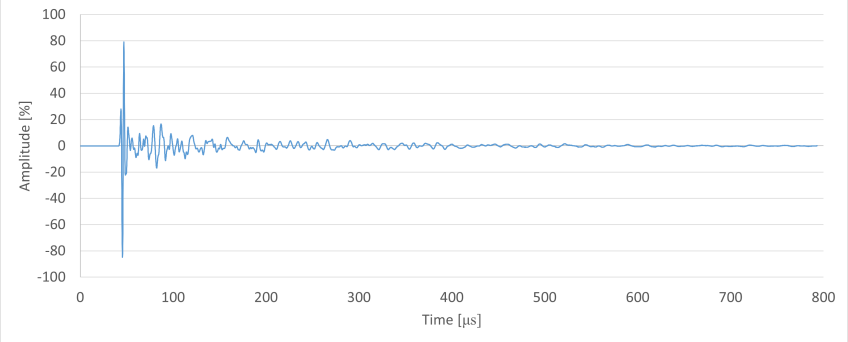

Figure A.26: Recorded signal on vibration plane “z” of S-waves in direction “a” for Syenite sample 2

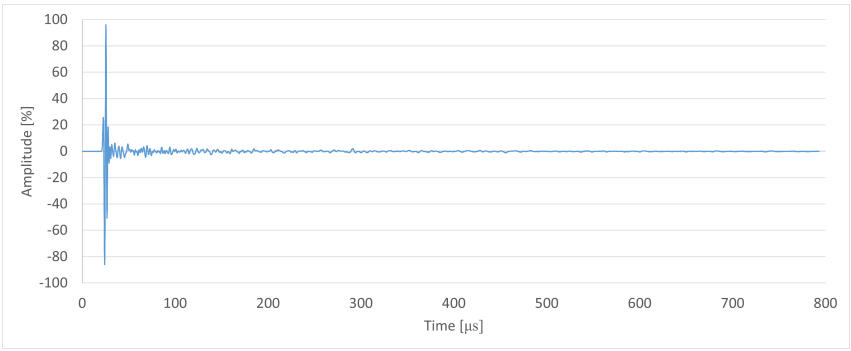

Figure A.27: Recorded signal on vibration plane “z” of S-waves in direction “b” for Syenite sample 2

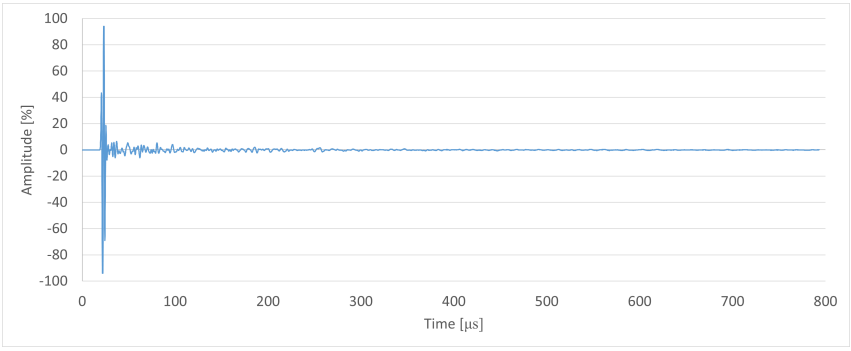

Figure A.28: Recorded signal on vibration plane “z” of S-waves in direction “c” for Syenite sample 2

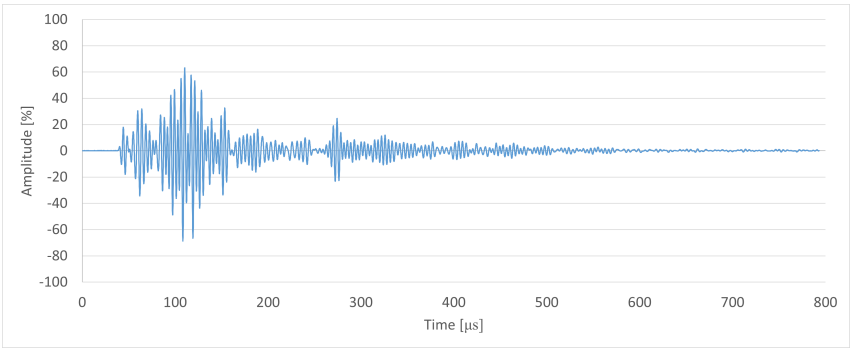

Figure A.29: Recorded signal of P-waves in direction “a” for Syenite sample 3

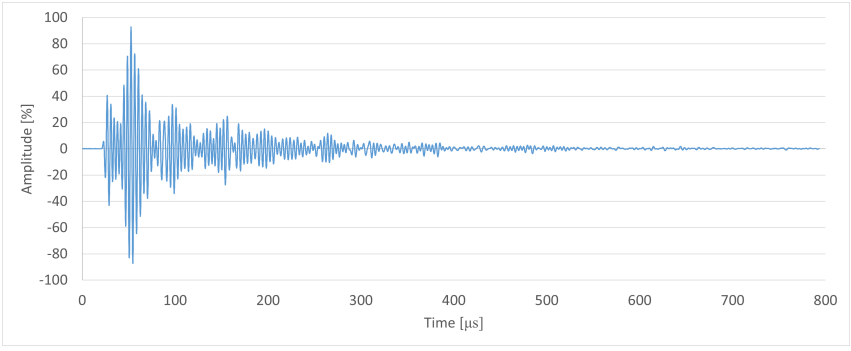

Figure A.30: Recorded signal of P-waves in direction “b” for Syenite sample 3

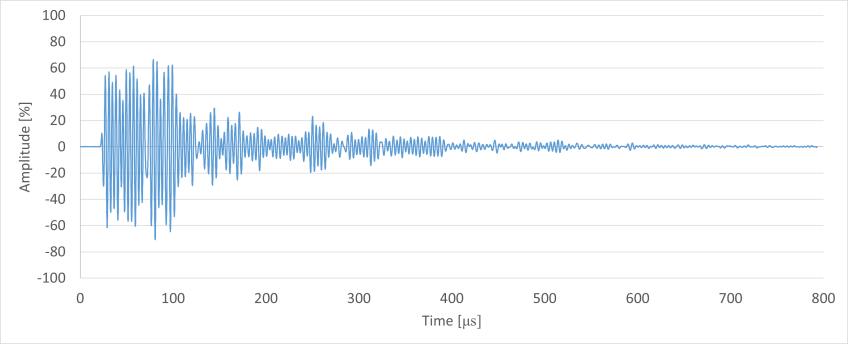

Figure A.31: Recorded signal of P-waves in direction “c” for Syenite sample 3

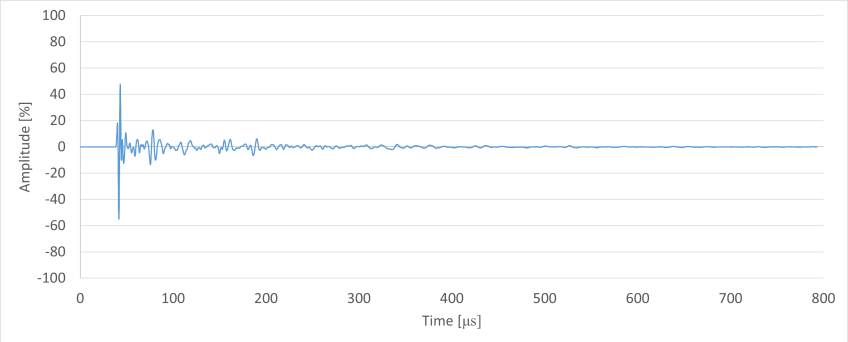

Figure A.32: Recorded signal on vibration plane “x” of S-waves in direction “a” for Syenite sample 3

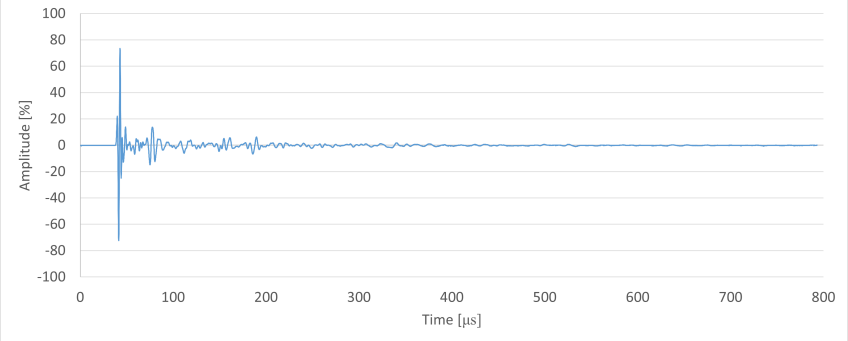

Figure A.33: Recorded signal on vibration plane “z” of S-waves in direction “a” for Syenite sample 3

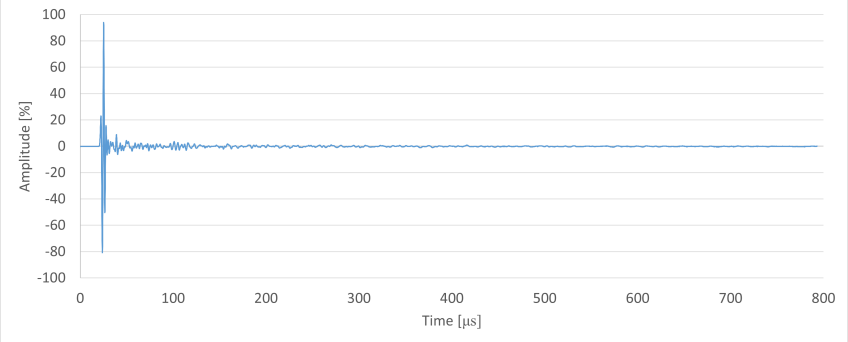

Figure A.34: Recorded signal on vibration plane “z” of S-waves in direction “b” for Syenite sample 3

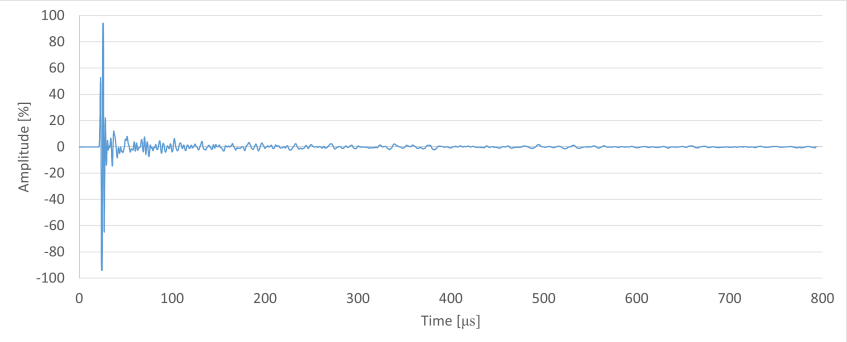

Figure A.35: Recorded signal on vibration plane "z" of S-waves in direction "c" for Syenite sample 3

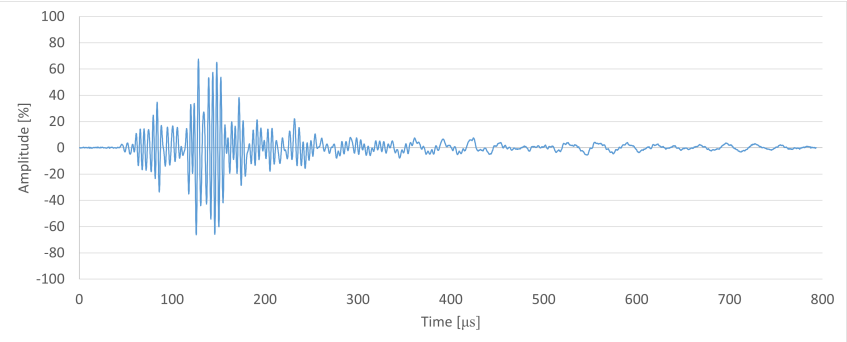

Figure A.36: Recorded signal of P-waves in direction "a" for Porriño sample 1

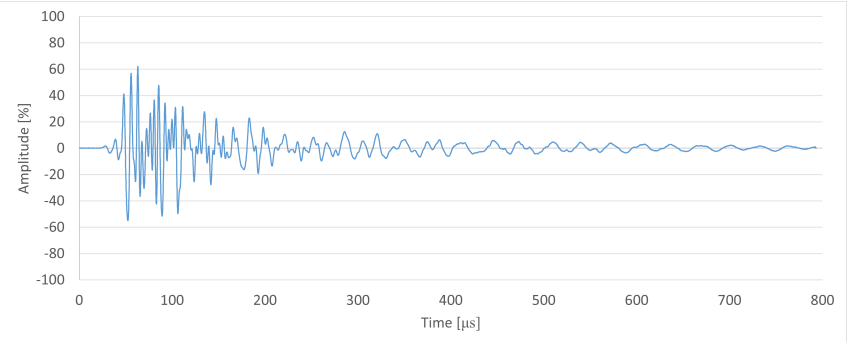

Figure A.37: Recorded signal of P-waves in direction "b" for Porriño sample 1

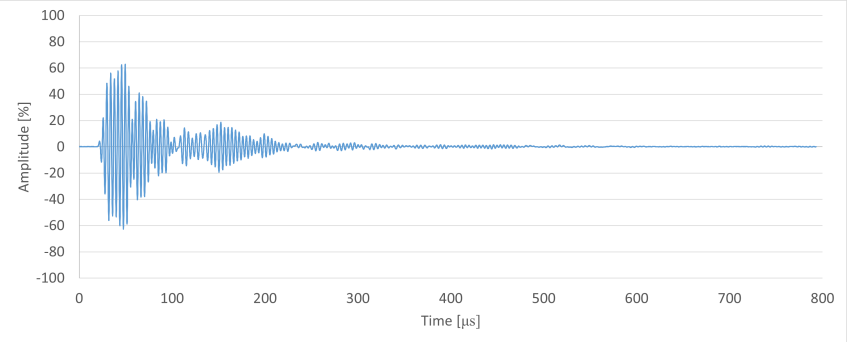

Figure A.38: Recorded signal of P-waves in direction "c" for Porriño sample 1

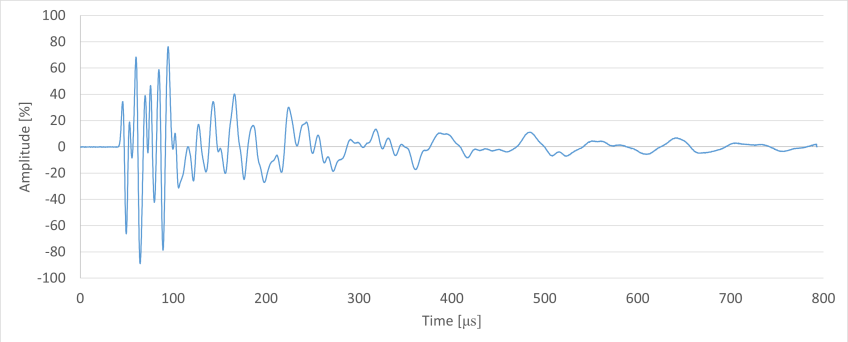

Figure A.39: Recorded signal on vibration plane "x" of S-waves in direction "a" for Porriño sample 1

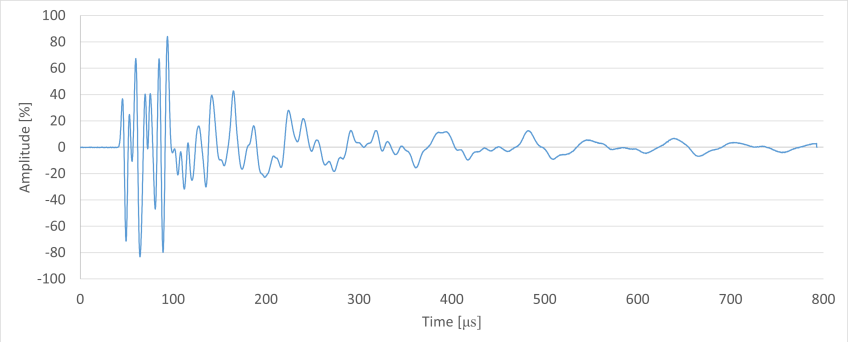

Figure A.40: Recorded signal on vibration plane "z" of S-waves in direction "a" for Porriño sample 1

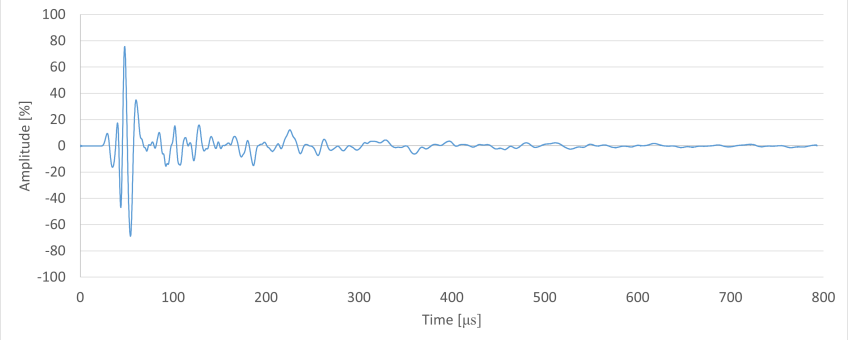

Figure A.41: Recorded signal on vibration plane "z" of S-waves in direction "b" for Porriño sample 1

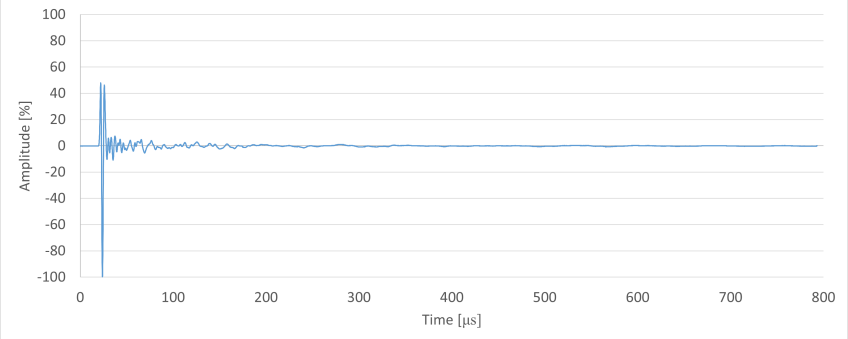

Figure A.42: Recorded signal on vibration plane "z" of S-waves in direction "c" for Porriño sample 1

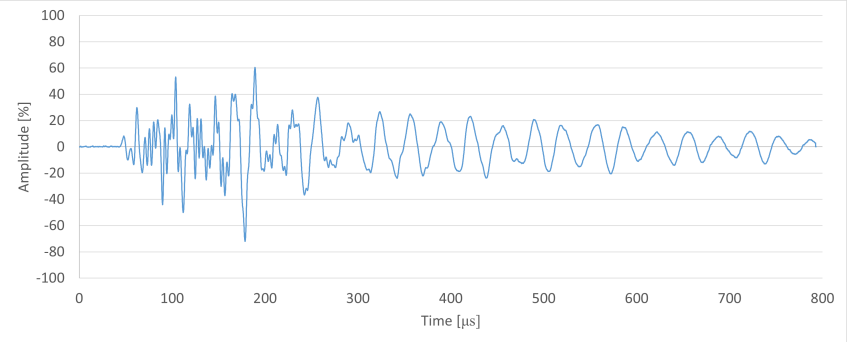

Figure A.43: Recorded signal of P-waves in direction “a” for Porriño sample 2

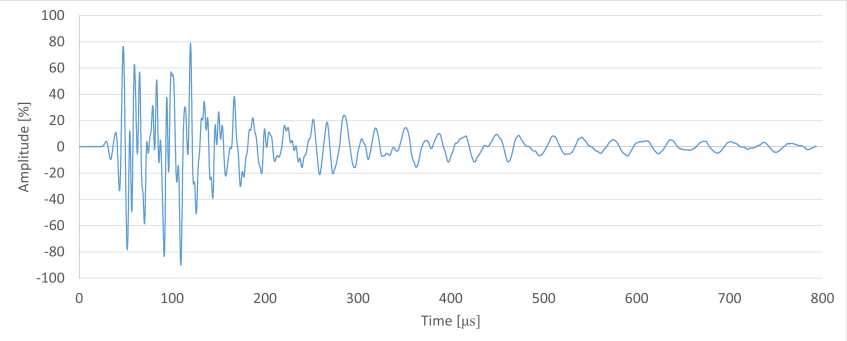

Figure A.44: Recorded signal of P-waves in direction “b” for Porriño sample 2

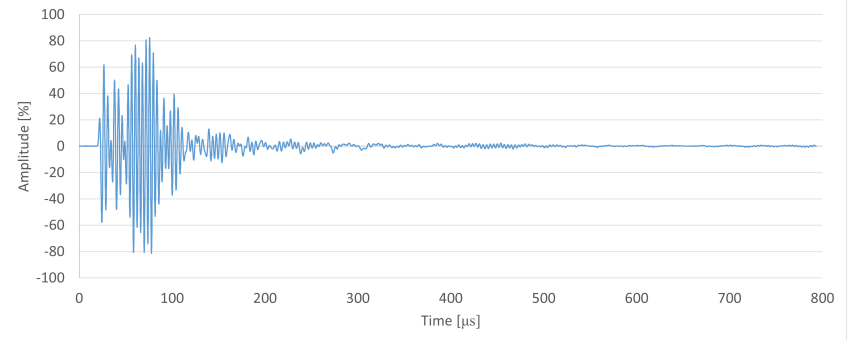

Figure A.45: Recorded signal of P-waves in direction “c” for Porriño sample 2

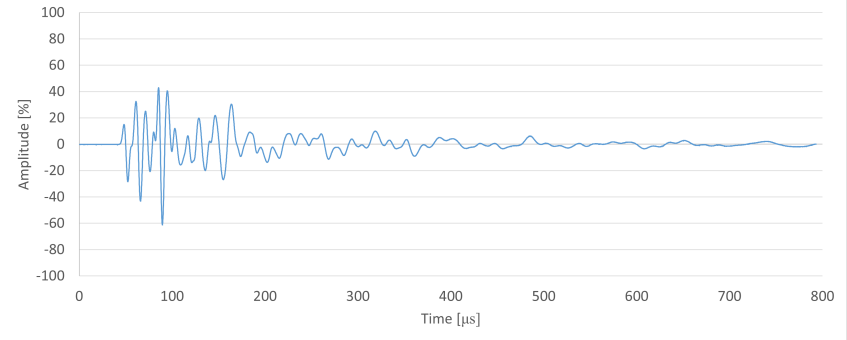

Figure A.46: Recorded signal on vibration plane “x” of S-waves in direction “a” for Porriño sample 2

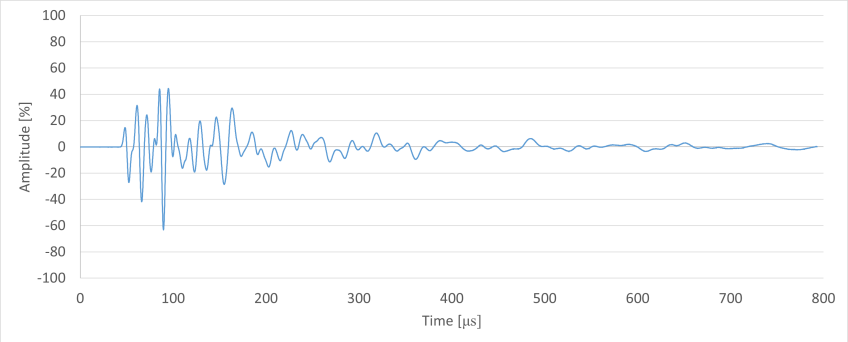

Figure A.47: Recorded signal on vibration plane "z" of S-waves in direction "a" for Porriño sample 2

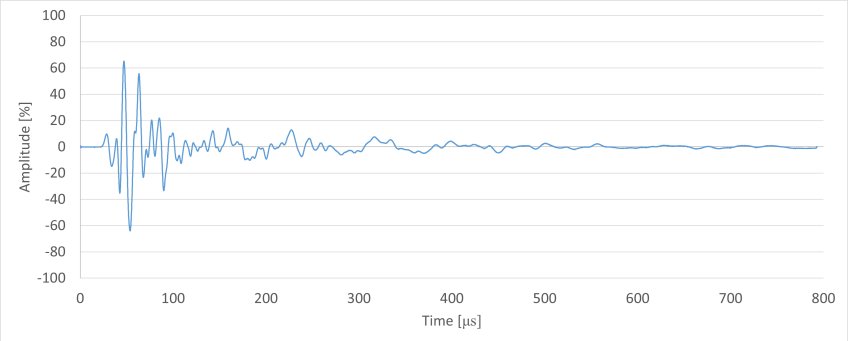

Figure A.48: Recorded signal on vibration plane "z" of S-waves in direction "b" for Porriño sample 2

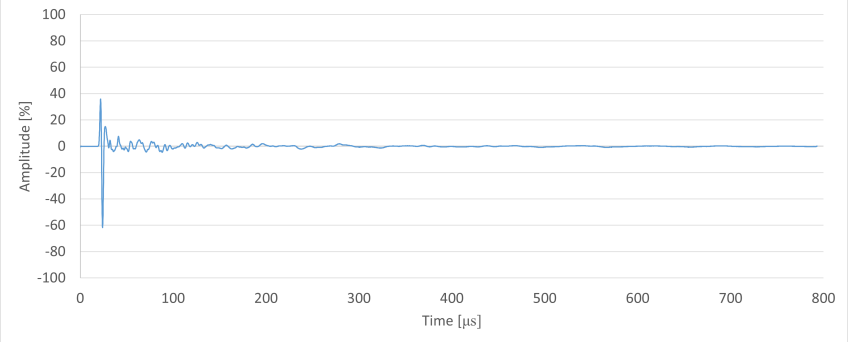

Figure A.49: Recorded signal on vibration plane "z" of S-waves in direction "c" for Porriño sample 2

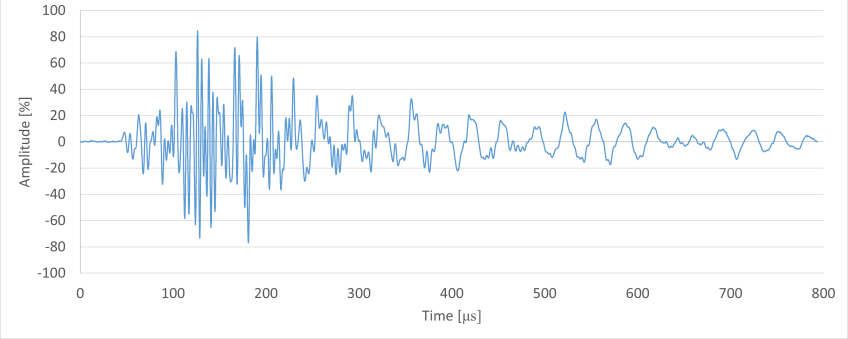

Figure A.50: Recorded signal of P-waves in direction "a" for Porriño sample 3

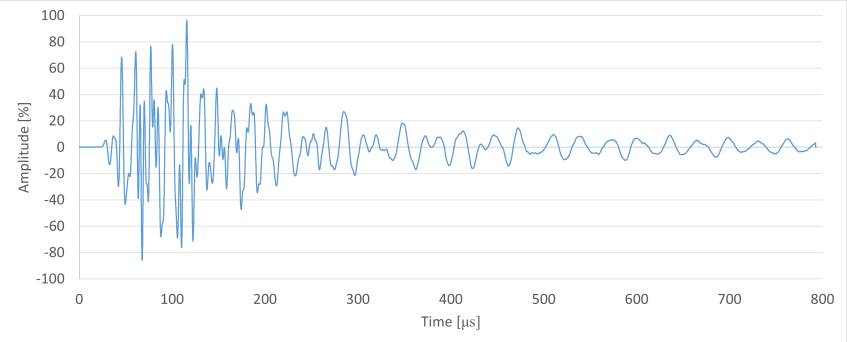

Figure A.51: Recorded signal of P-waves in direction “b” for Porriño sample 3

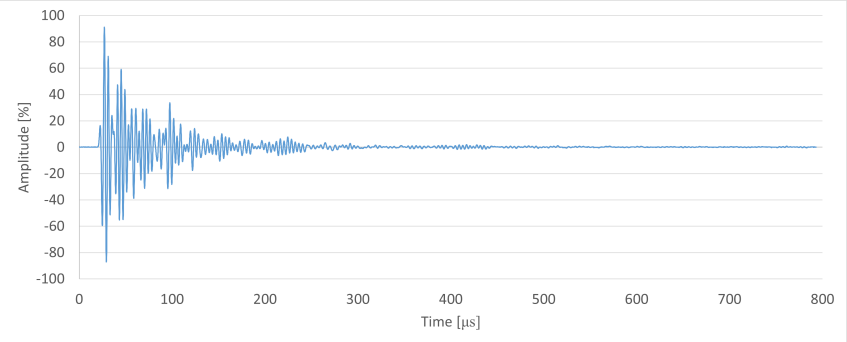

Figure A.52: Recorded signal of P-waves in direction “c” for Porriño sample 3

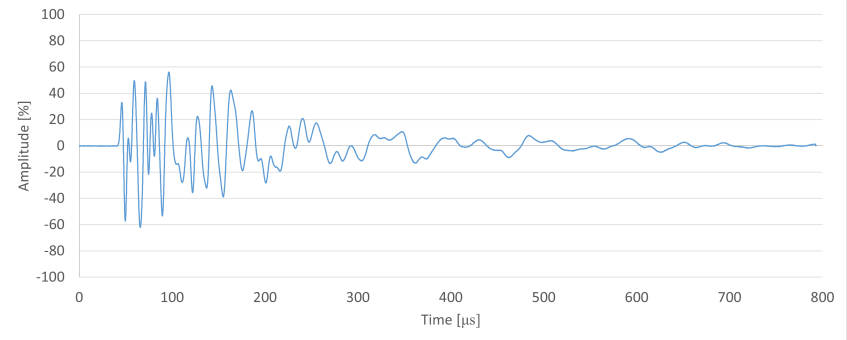

Figure A.53: Recorded signal on vibration plane “x” of S-waves in direction “a” for Porriño sample 3

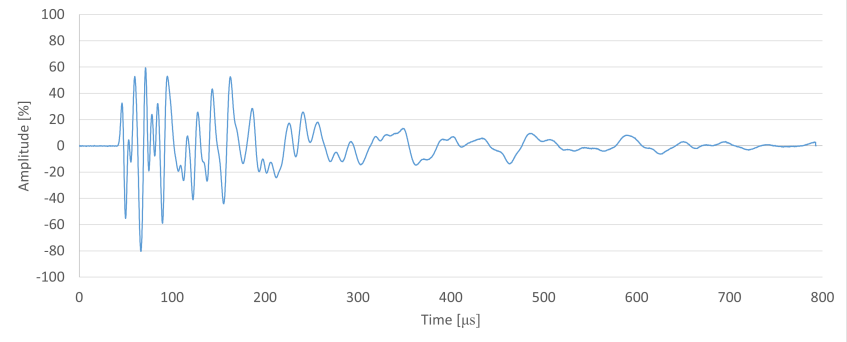

Figure A.54: Recorded signal on vibration plane “z” of S-waves in direction “a” for Porriño sample 3

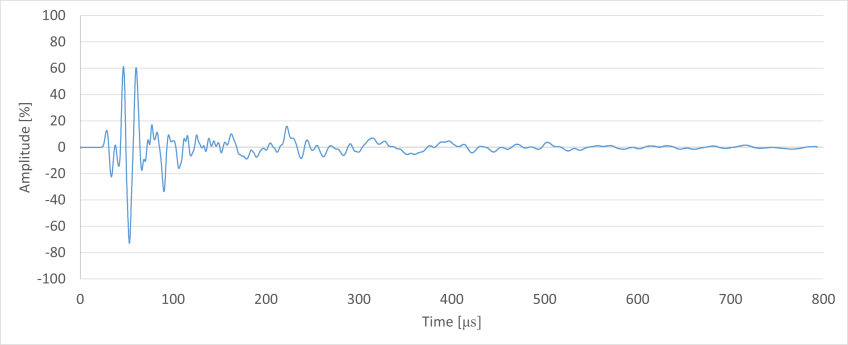

Figure A.55: Recorded signal on vibration plane "z" of S-waves in direction "b" for Porriño sample 3

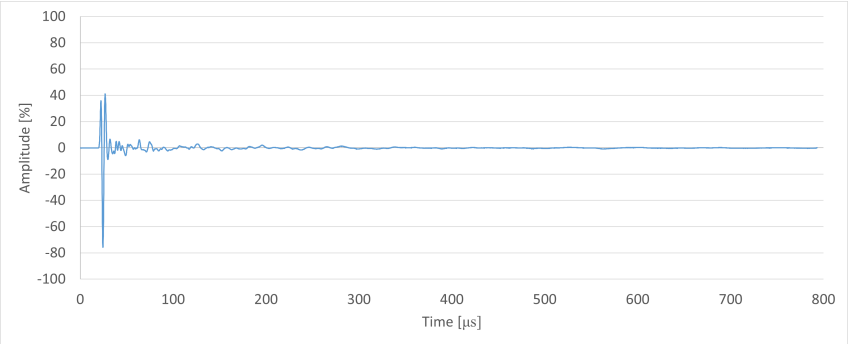

Figure A.56: Recorded signal on vibration plane "z" of S-waves in direction "c" for Porriño sample 3

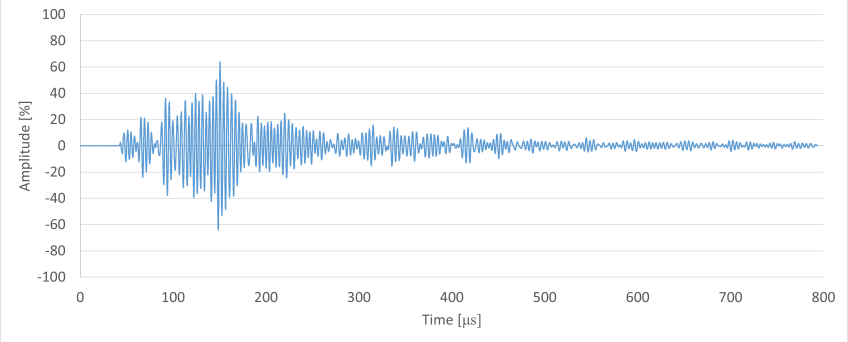

Figure A.57: Recorded signal of P-waves in direction "a" for Carrara sample 1

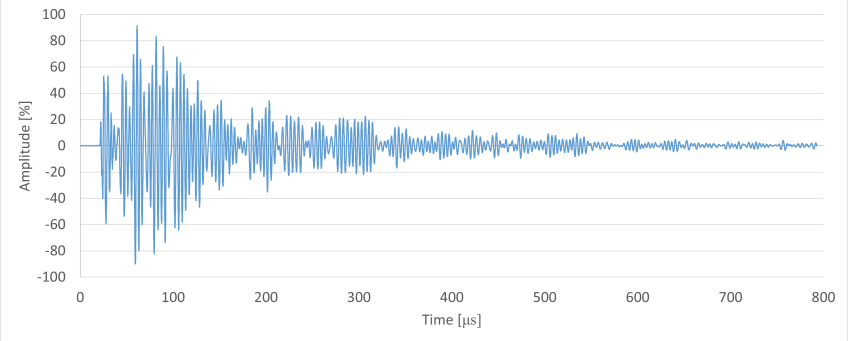

Figure A.58: Recorded signal of P-waves in direction "b" for Carrara sample 1

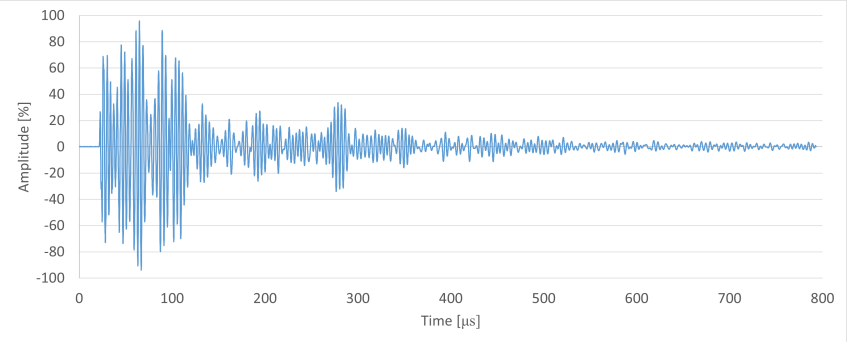

Figure A.59: Recorded signal of P-waves in direction “c” for Carrara sample 1

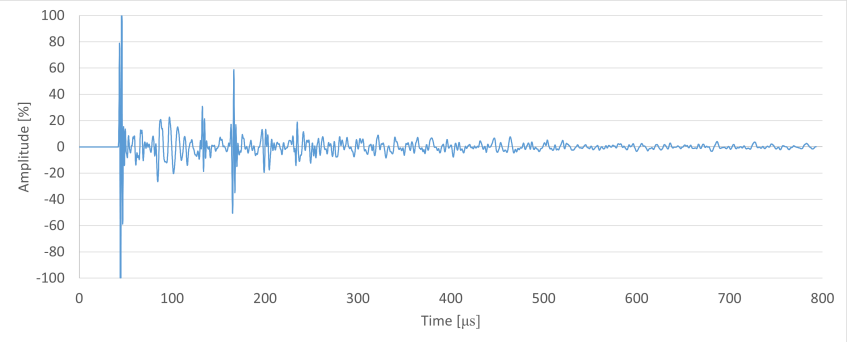

Figure A.60: Recorded signal on vibration plane “x” of S-waves in direction “a” for Carrara sample 1

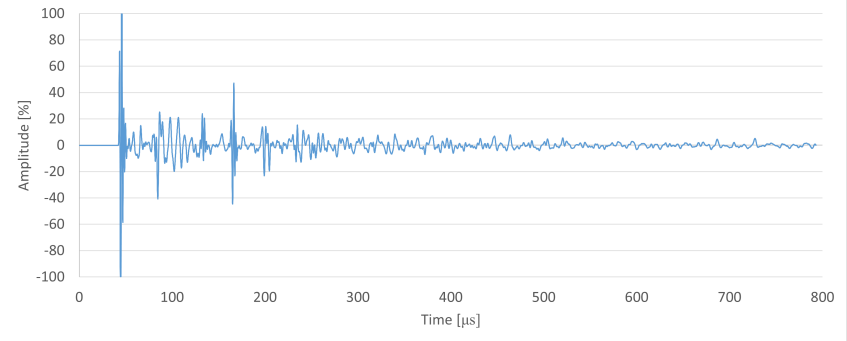

Figure A.61: Recorded signal on vibration plane “z” of S-waves in direction “a” for Carrara sample 1

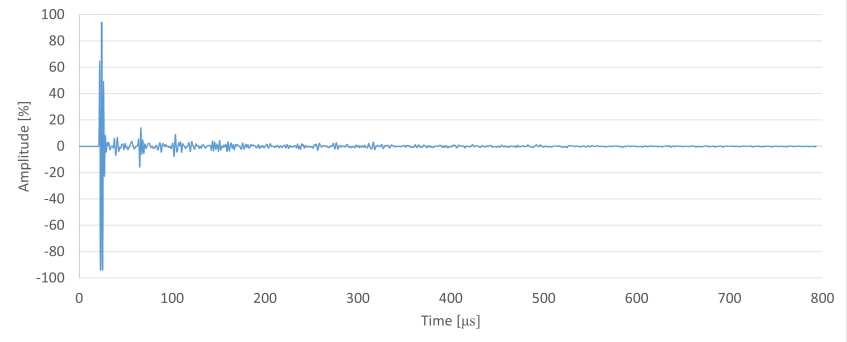

Figure A.62: Recorded signal on vibration plane “z” of S-waves in direction “b” for Carrara sample 1

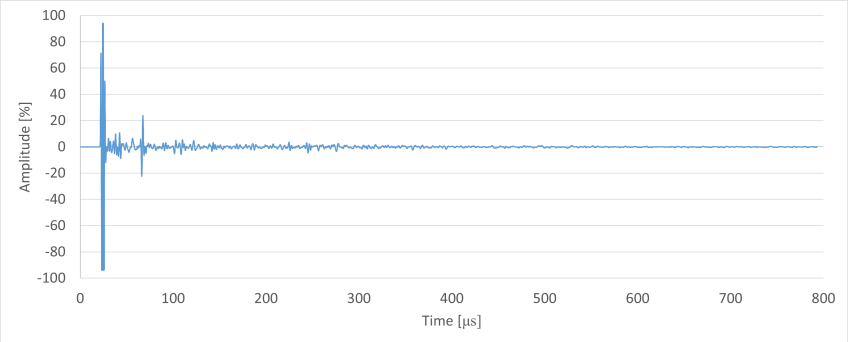

Figure A.63: Recorded signal on vibration plane "z" of S-waves in direction "c" for Carrara sample 1

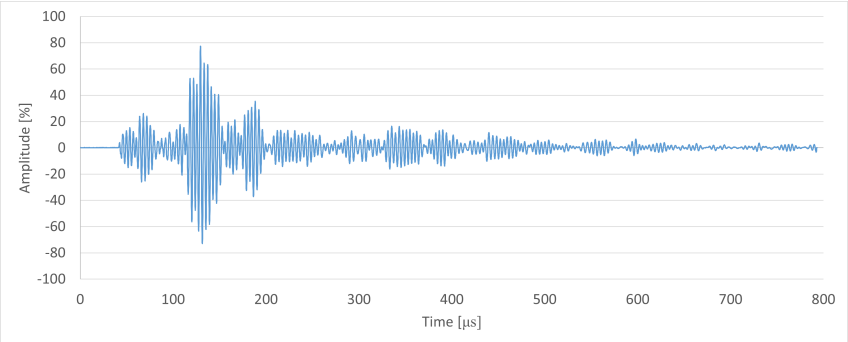

Figure A.64: Recorded signal of P-waves in direction "a" for Carrara sample 2

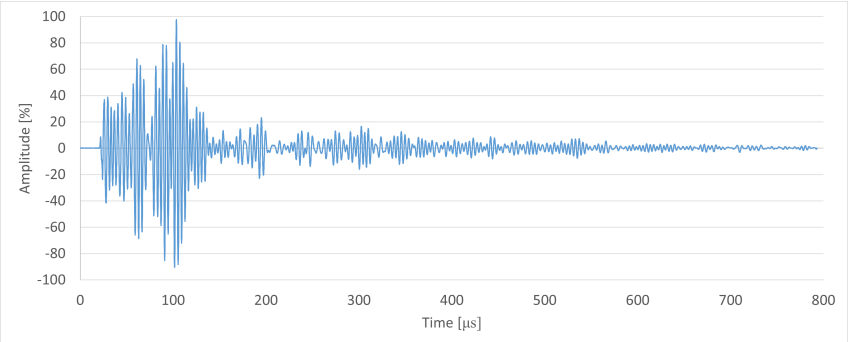

Figure A.65: Recorded signal of P-waves in direction "b" for Carrara sample 2

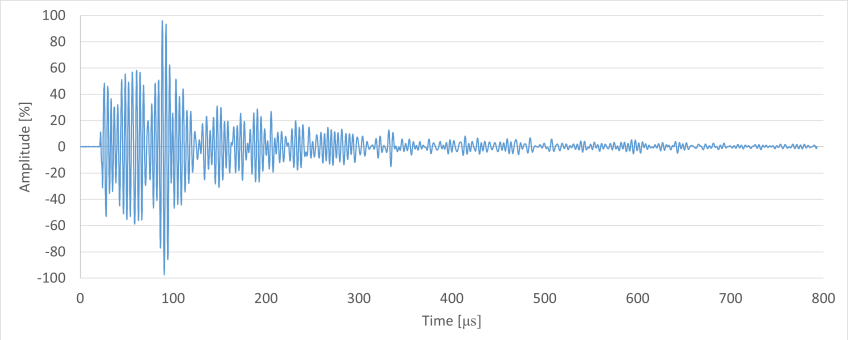

Figure A.66: Recorded signal of P-waves in direction "c" for Carrara sample 2

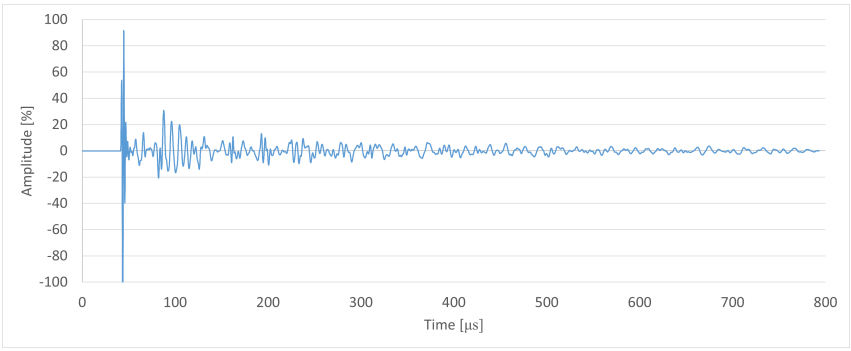

Figure A.67: Recorded signal on vibration plane “x” of S-waves in direction “a” for Carrara sample 2

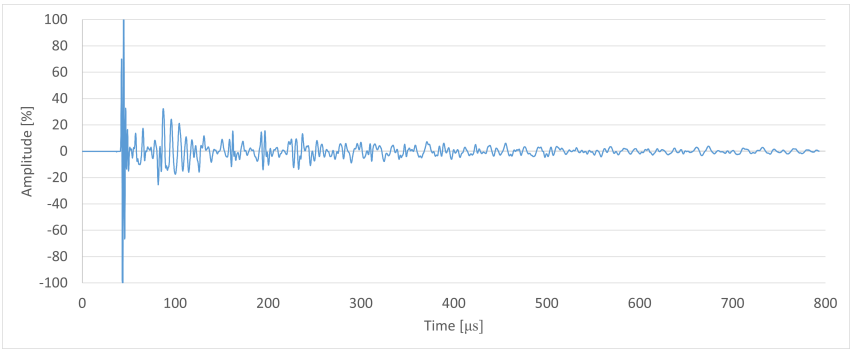

Figure A.68: Recorded signal on vibration plane “z” of S-waves in direction “a” for Carrara sample 2

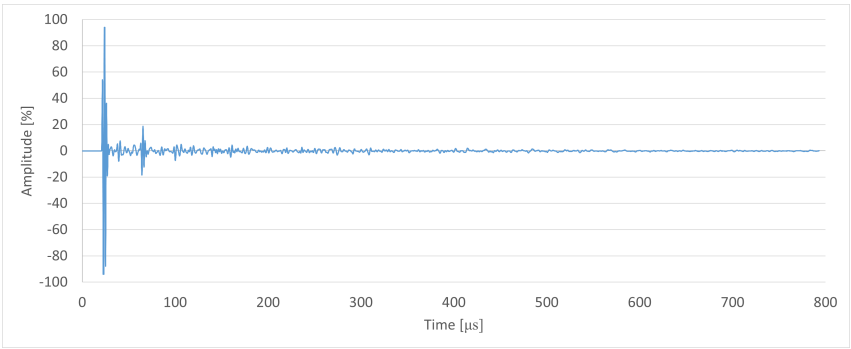

Figure A.69: Recorded signal on vibration plane “z” of S-waves in direction “b” for Carrara sample 2

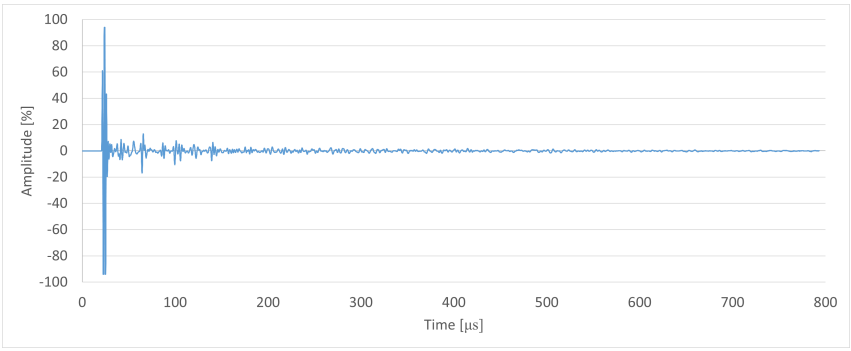

Figure A.70: Recorded signal on vibration plane “z” of S-waves in direction “c” for Carrara sample 2

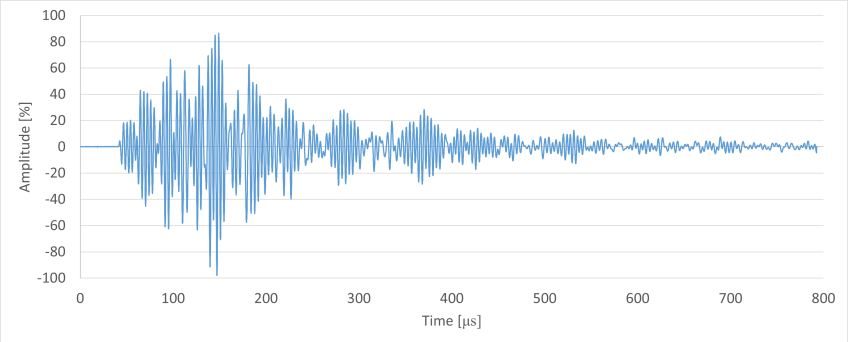

Figure A.71: Recorded signal of P-waves in direction “a” for Carrara sample 3

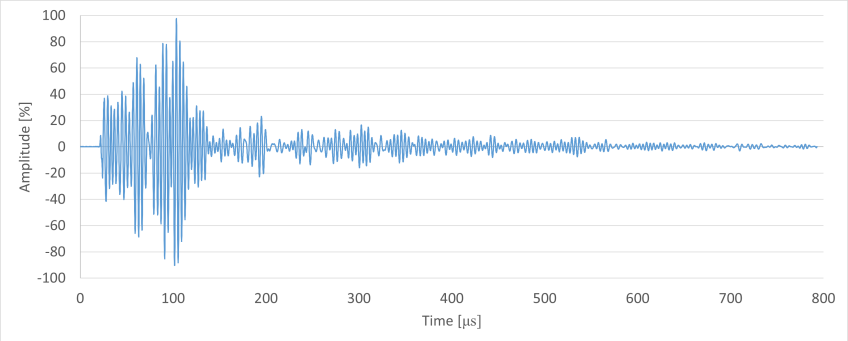

Figure A.72: Recorded signal of P-waves in direction “b” for Carrara sample 3

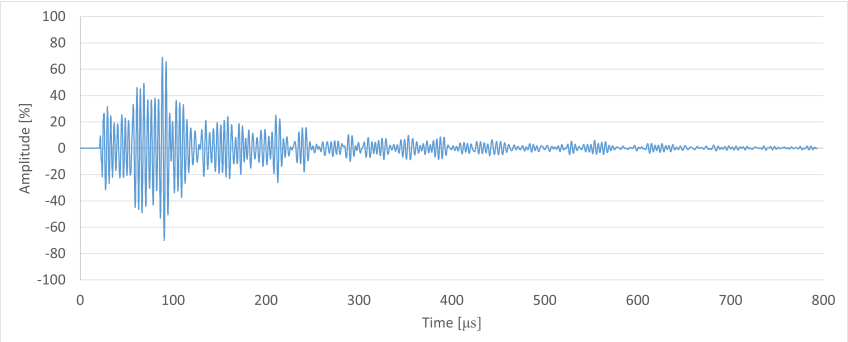

Figure A.73: Recorded signal of P-waves in direction “c” for Carrara sample 3

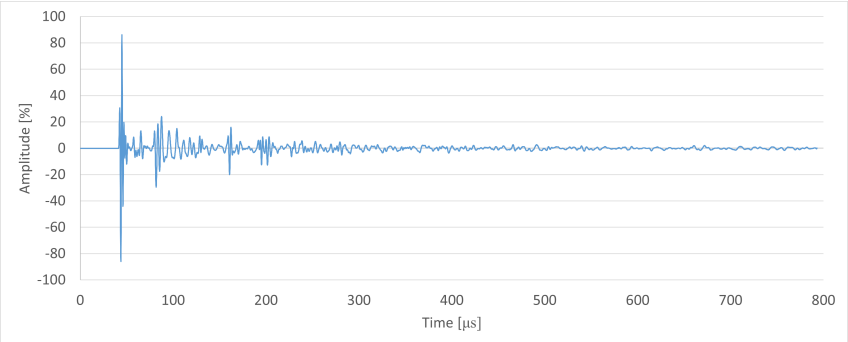

Figure A.74: Recorded signal on vibration plane “x” of S-waves in direction “a” for Carrara sample 3

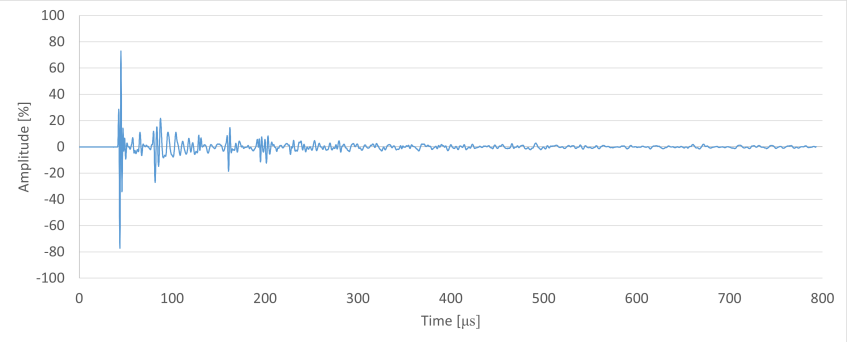

Figure A.75: Recorded signal on vibration plane “z” of S-waves in direction “a” for Carrara sample 3

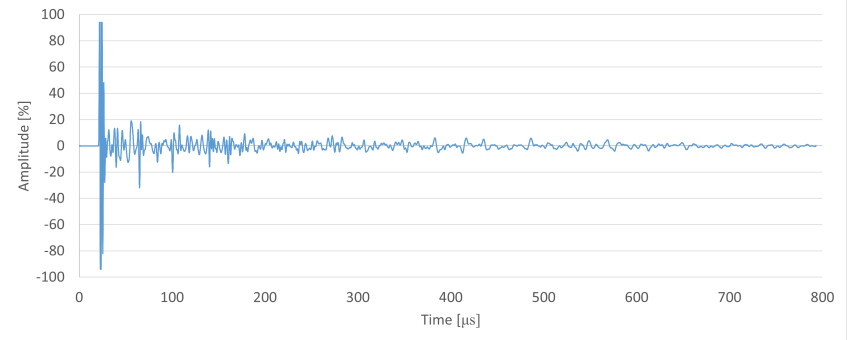

Figure A.76: Recorded signal on vibration plane “z” of S-waves in direction “b” for Carrara sample 3

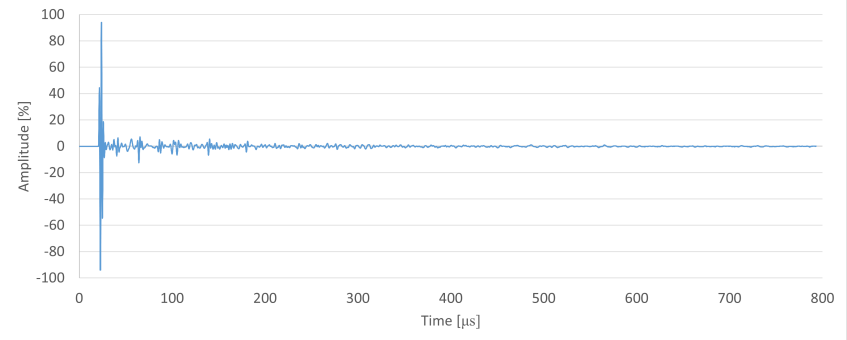

Figure A.77: Recorded signal on vibration plane “z” of S-waves in direction “c” for Carrara sample 3

Appendix B

Unconfined compression tests

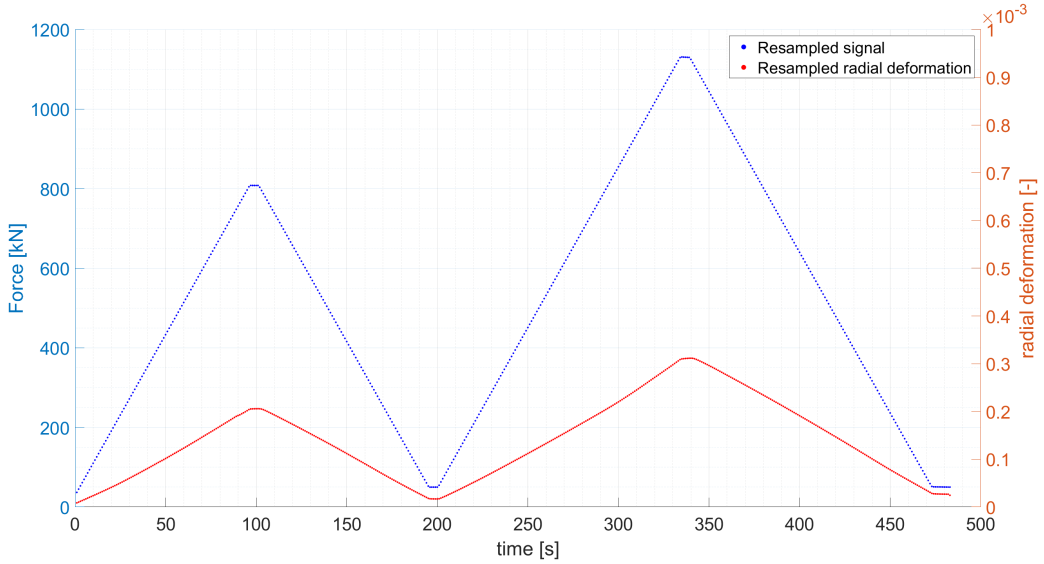

Figure B.1: Syenite sample 2. blue: force vs time; red: radial strain vs time.

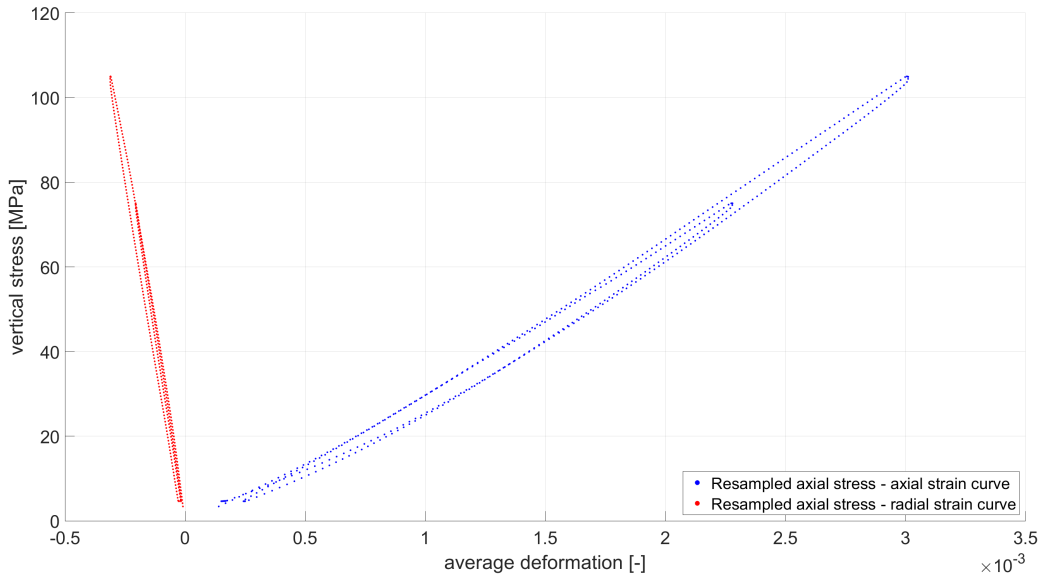

Figure B.2: Syenite sample 2. blue: stress vs axial strain; red: stress vs radial strain.

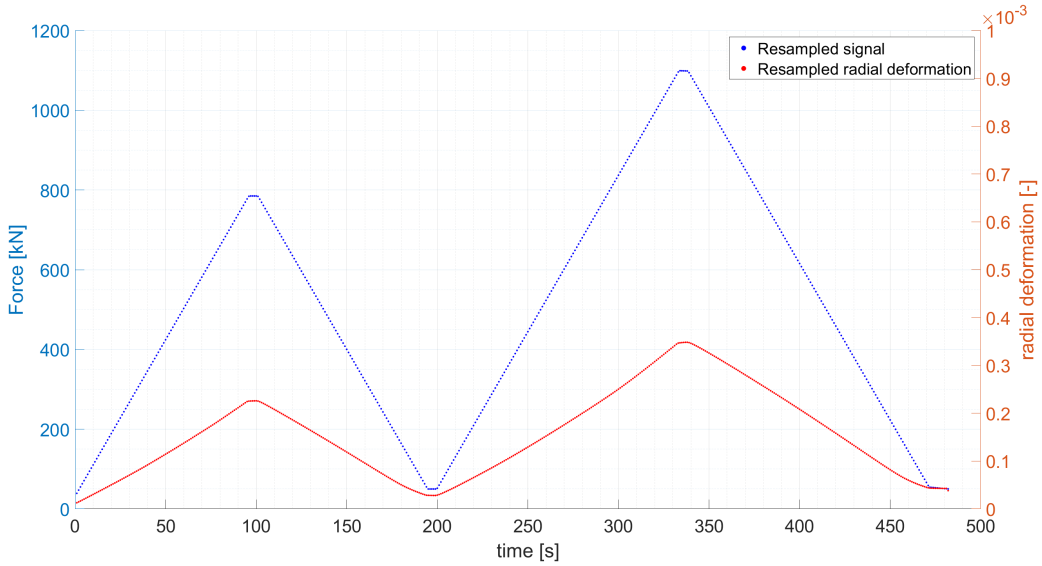

Figure B.3: Syenite sample 3. blue: force vs time; red: radial strain vs time.

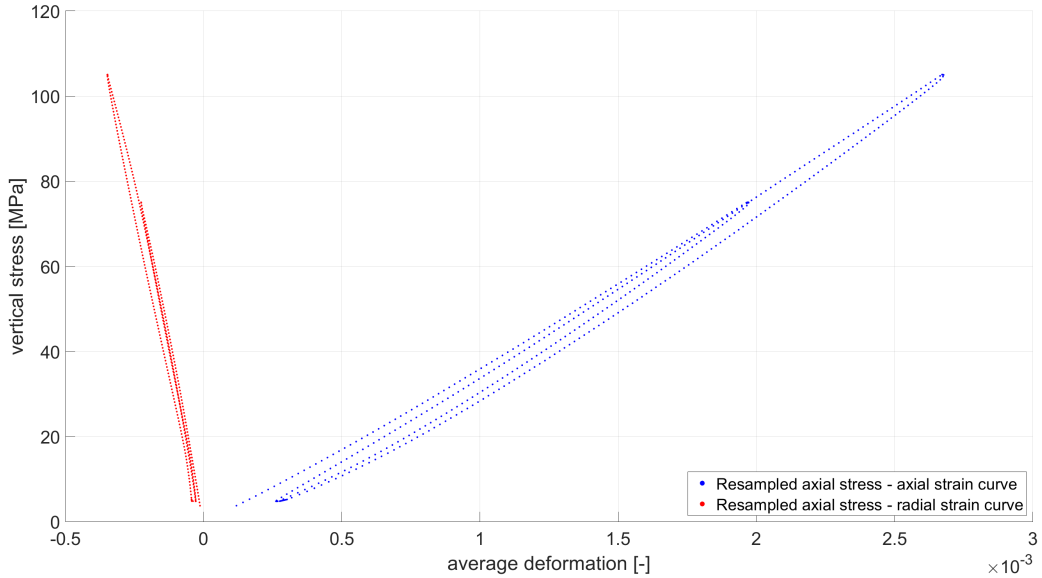

Figure B.4: Syenite sample 3. blue: stress vs axial strain; red: stress vs radial strain.

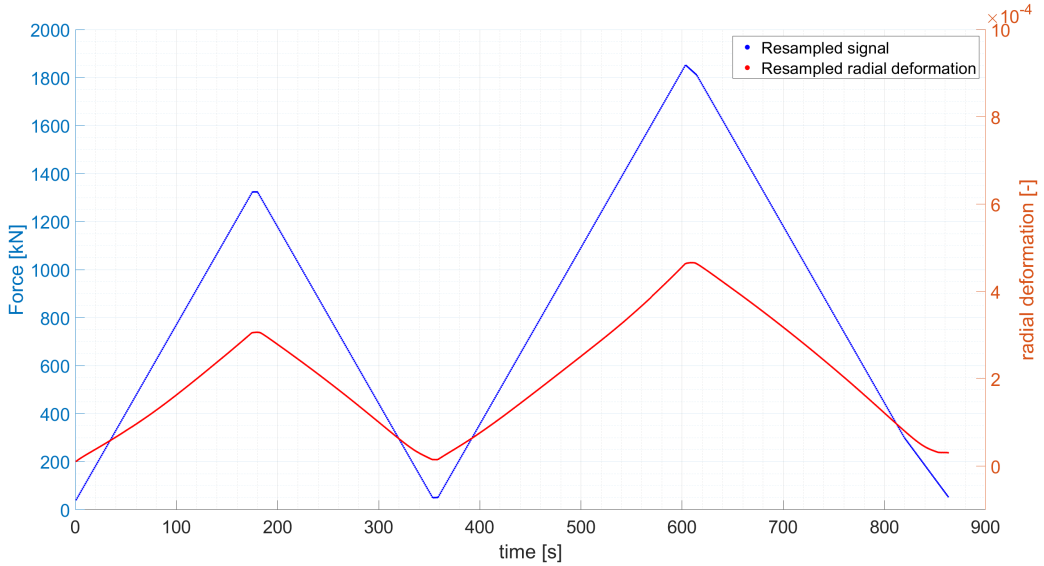

Figure B.5: Absolute Black sample 2. blue: force vs time; red: radial strain vs time.

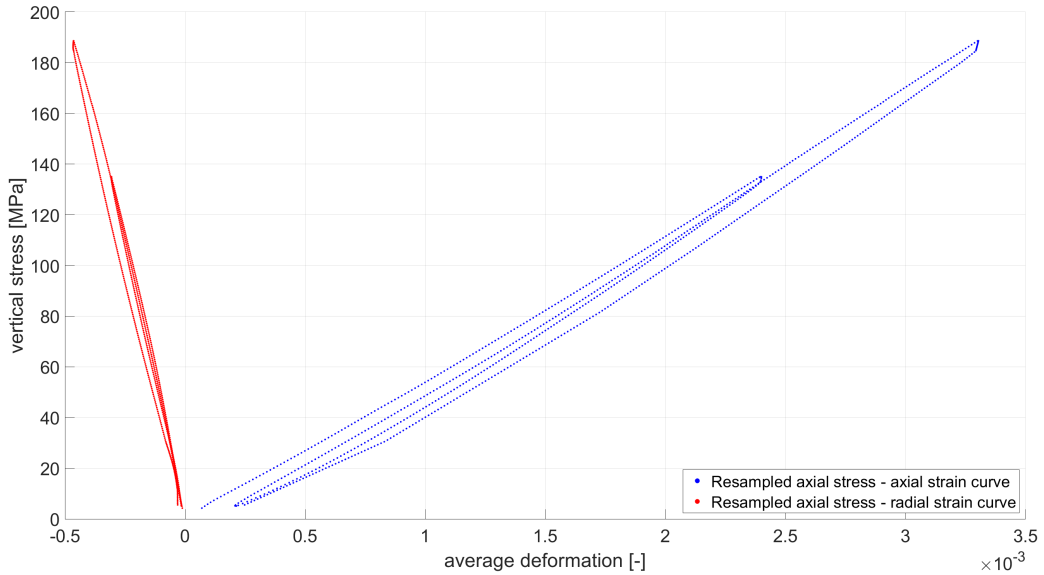

Figure B.6: Absolute Black sample 2. blue: stress vs axial strain; red: stress vs radial strain.

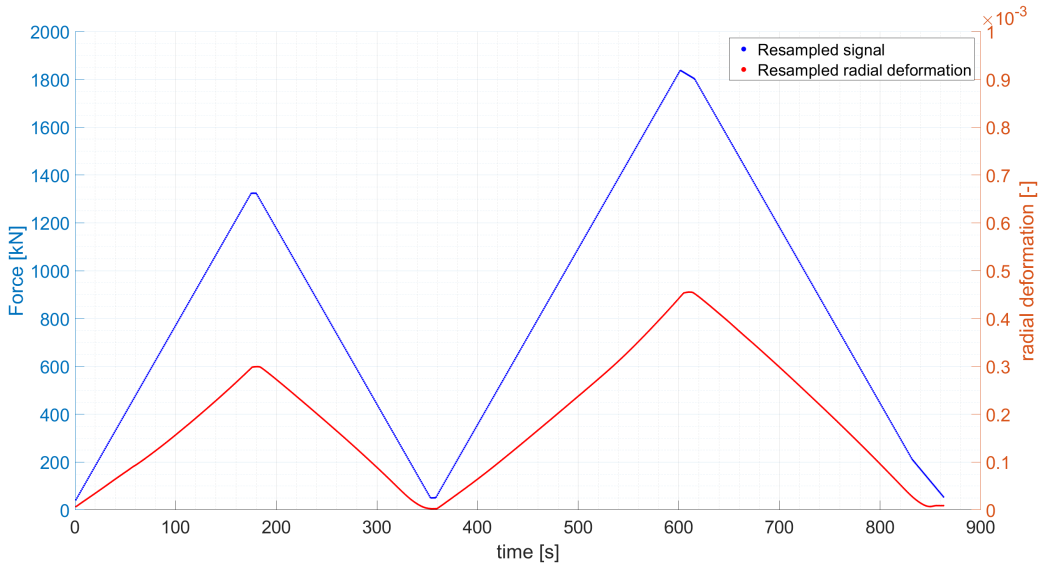

Figure B.7: Absolute Black sample 3. blue: force vs time; red: radial strain vs time.

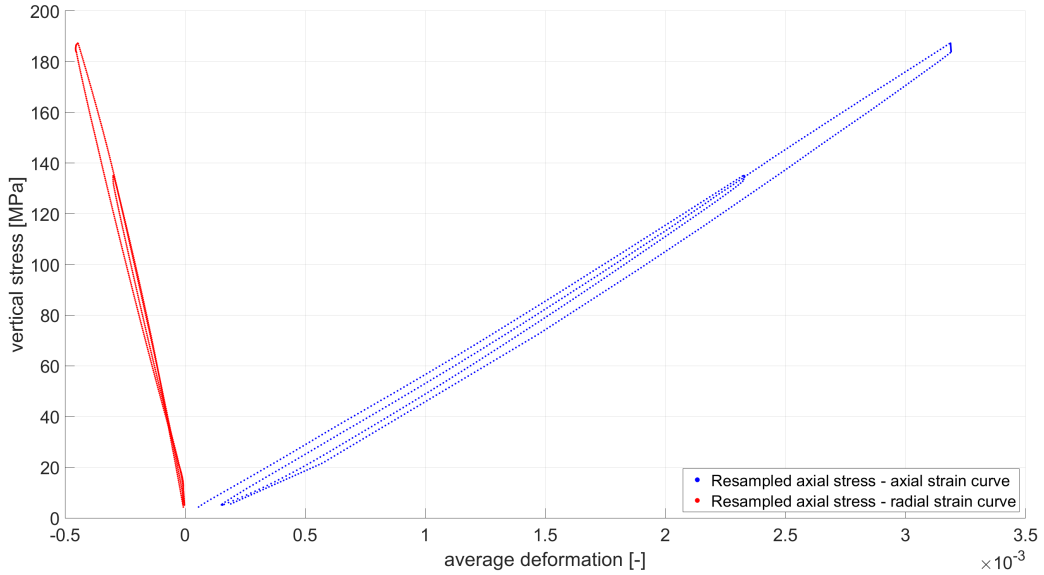

Figure B.8: Absolute Black sample 3. blue: stress vs axial strain; red: stress vs radial strain.

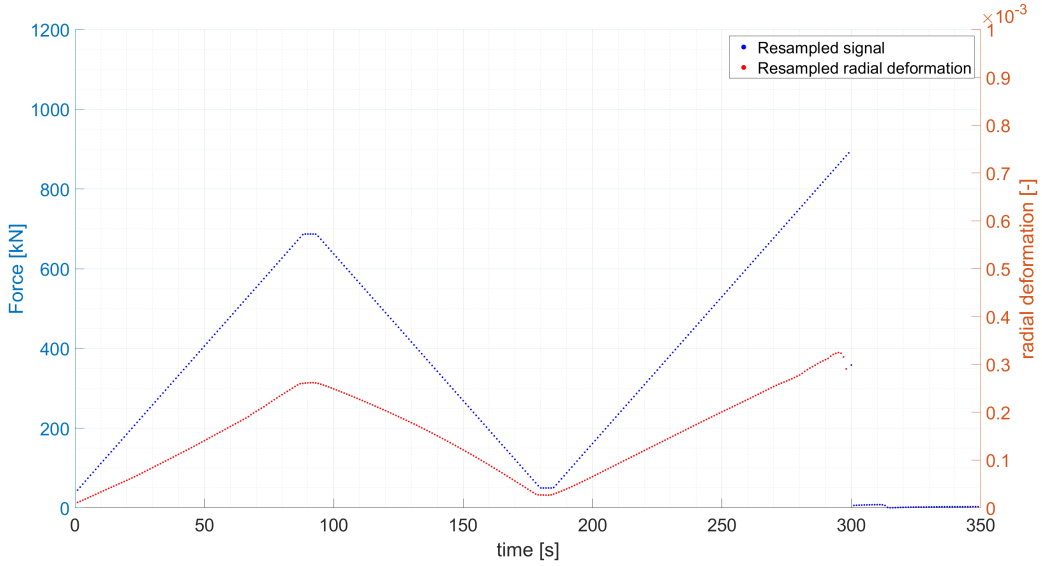

Figure B.9: Porriño sample 2. blue: force vs time; red: radial strain vs time.

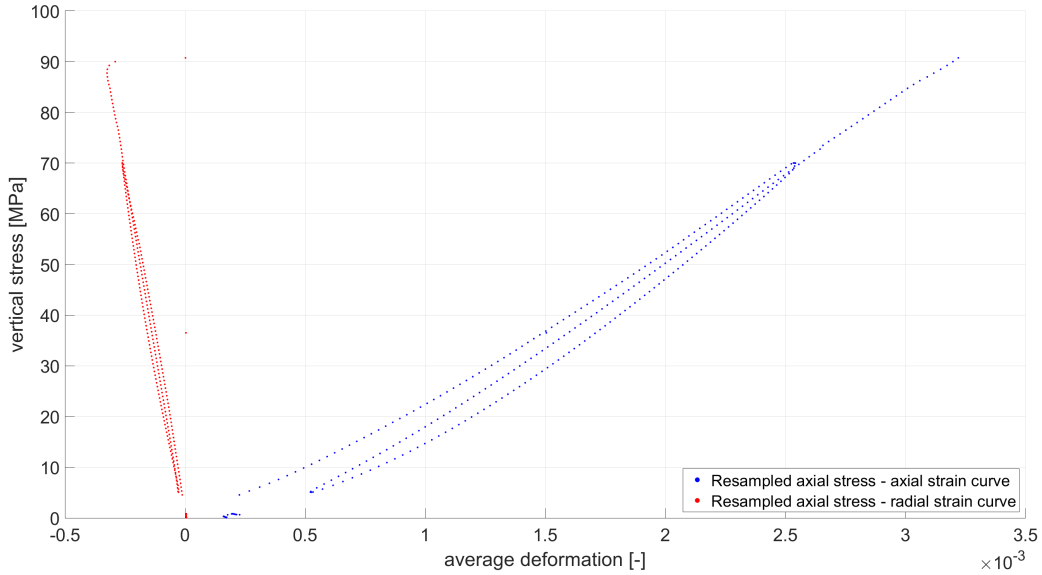

Figure B.10: Porriño sample 2. blue: stress vs axial strain; red: stress vs radial strain.

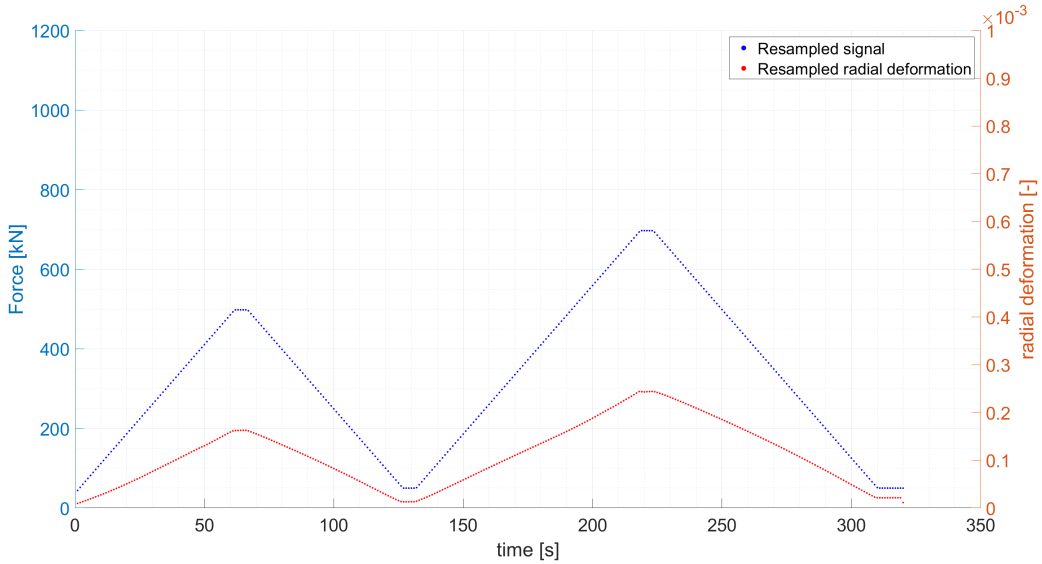

Figure B.11: Porriño sample 3. blue: force vs time; red: radial strain vs time.

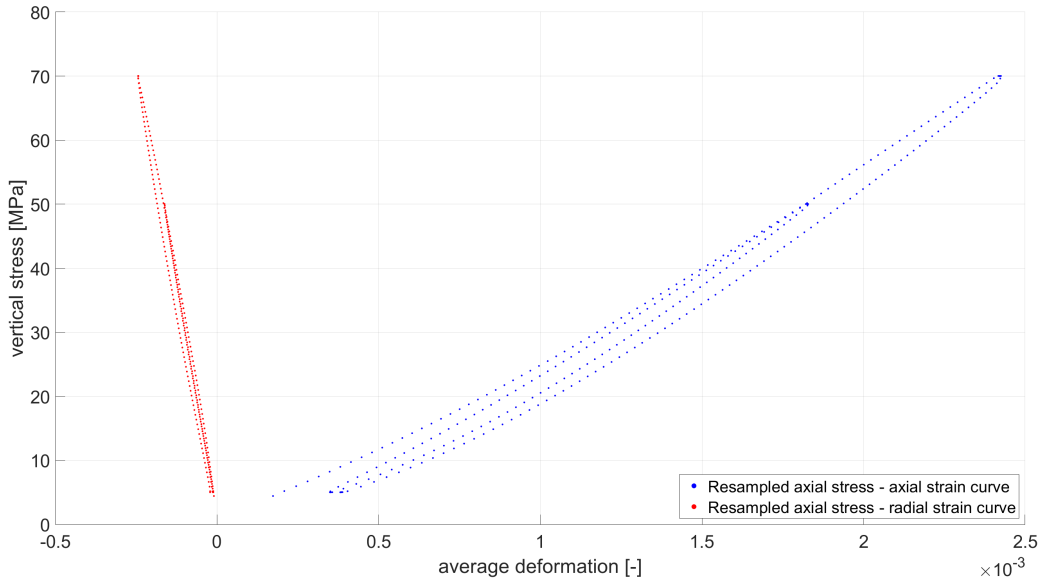

Figure B.12: Porriño sample 3. blue: stress vs axial strain; red: stress vs radial strain.

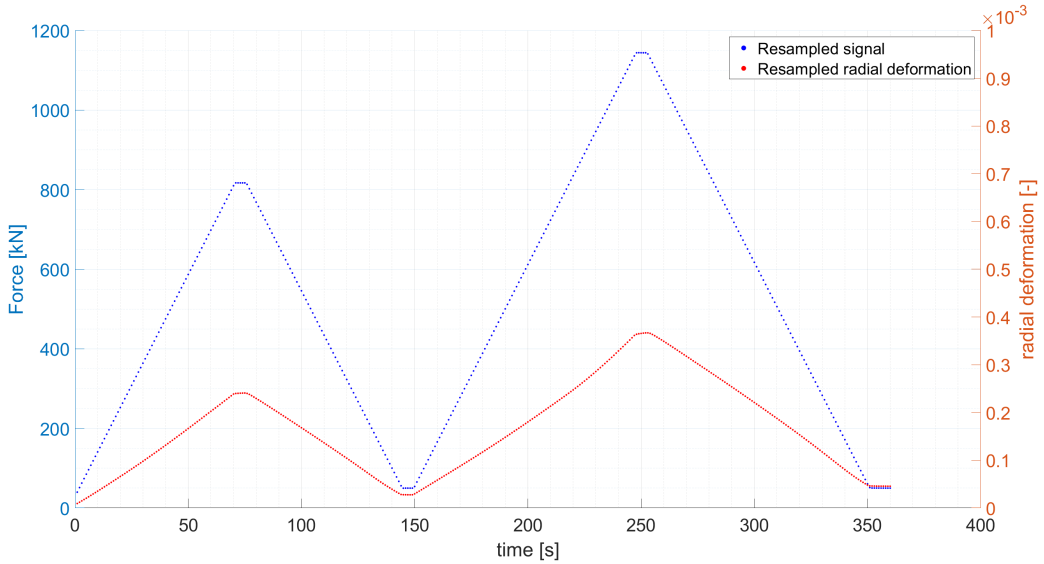

Figure B.13: Carrara sample 2. blue: force vs time; red: radial strain vs time.

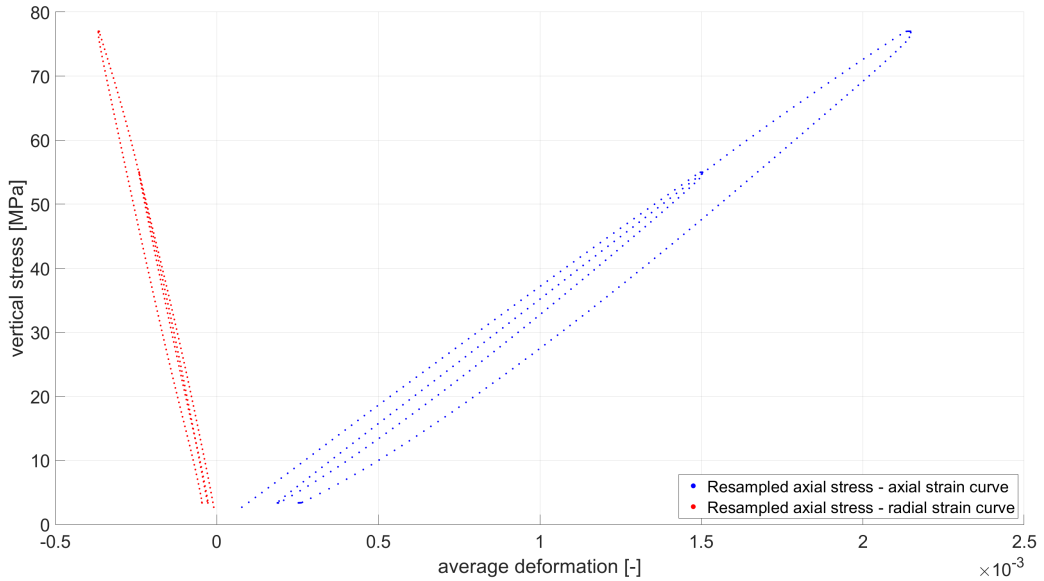

Figure B.14: Carrara sample 2. blue: stress vs axial strain; red: stress vs radial strain.

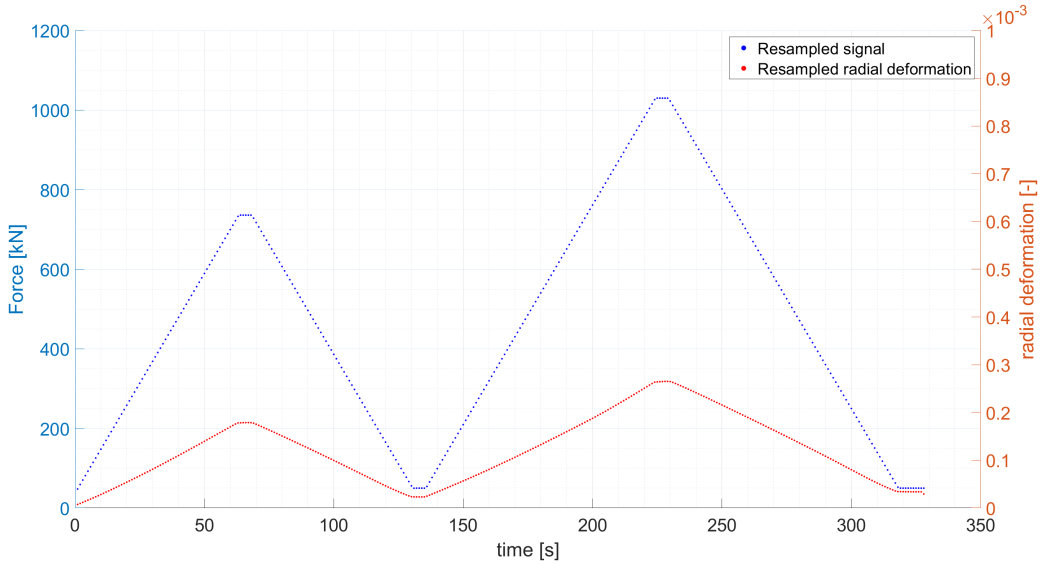

Figure B.15: Carrara sample 3. blue: force vs time; red: radial strain vs time.

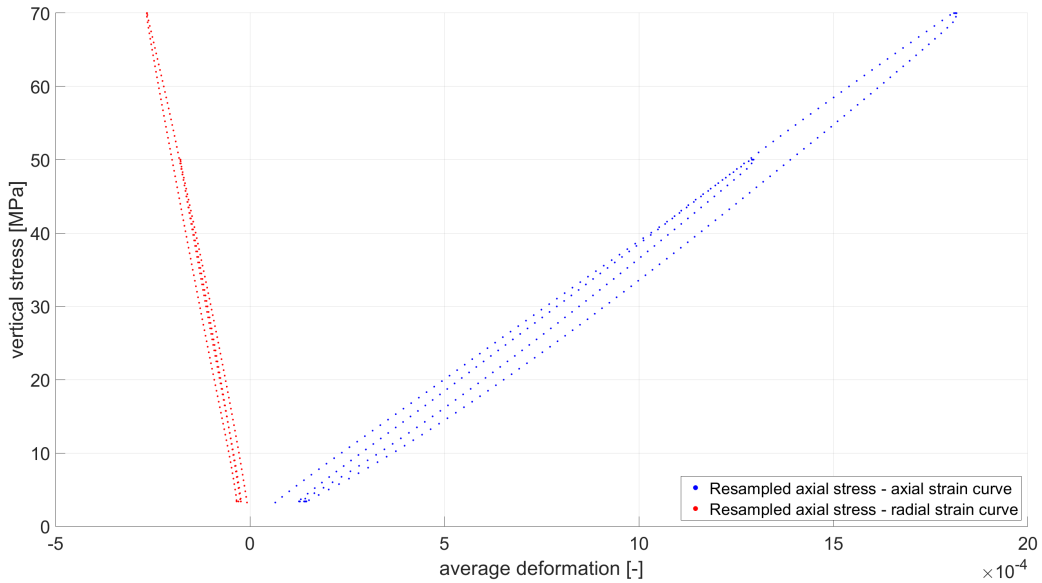

Figure B.16: Carrara sample 3. blue: stress vs axial strain; red: stress vs radial strain.

Appendix C

Ultrasonic tests on fractured rock specimens

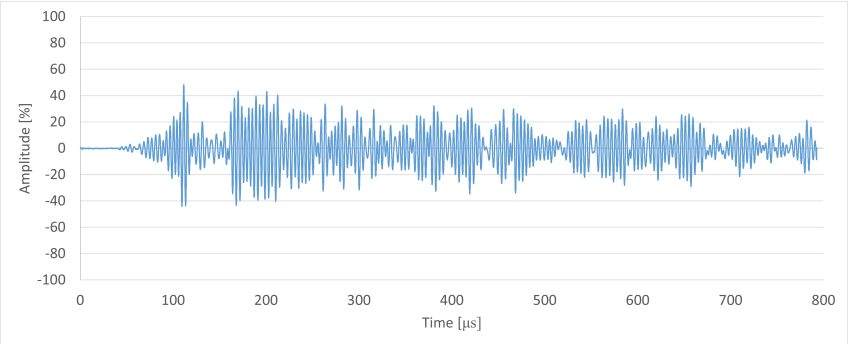

Figure C.1: Recorded signal of P-waves in direction "a" for Absolute Black sample 2 (rough surfaces).

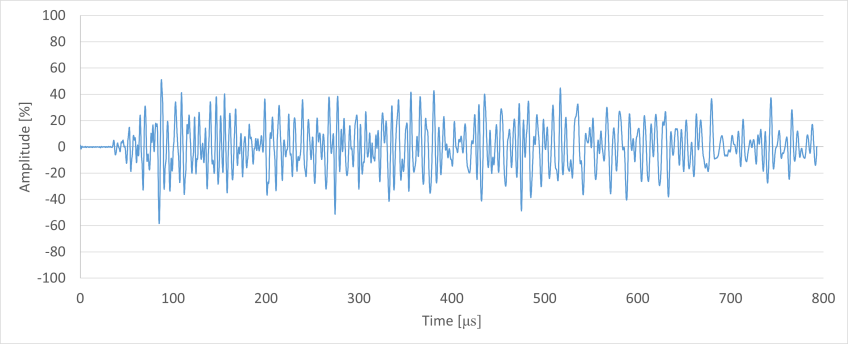

Figure C.2: Recorded signal on vibration plane "x" of S-waves in direction "a" for Absolute Black sample 2 (rough surfaces).

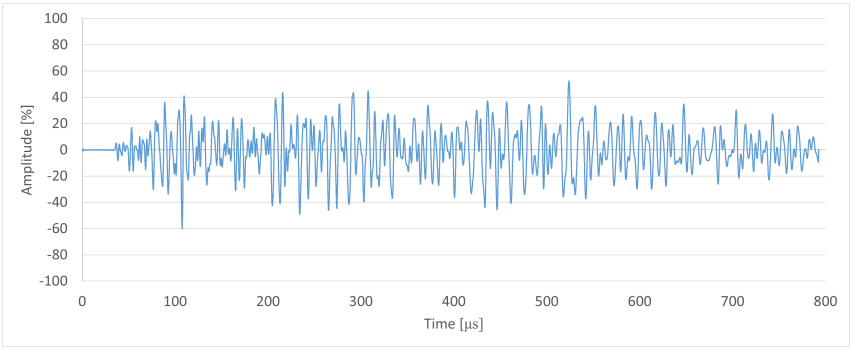

Figure C.3: Recorded signal on vibration plane "z" of S-waves in direction "a" for Absolute Black sample 2 (rough surfaces).

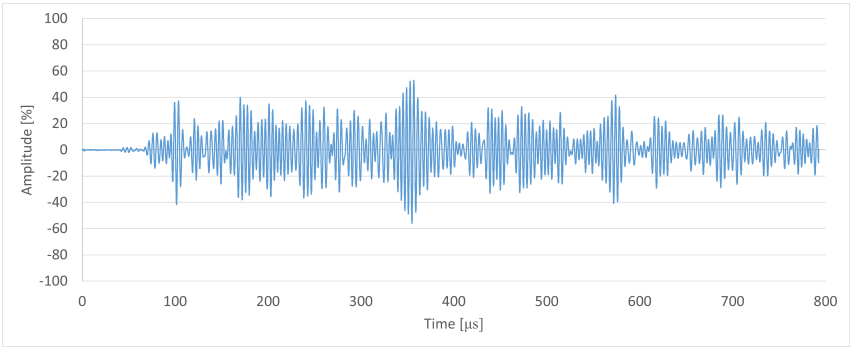

Figure C.4: Recorded signal of P-waves in direction "a" for Absolute Black sample 3 (rough surfaces).

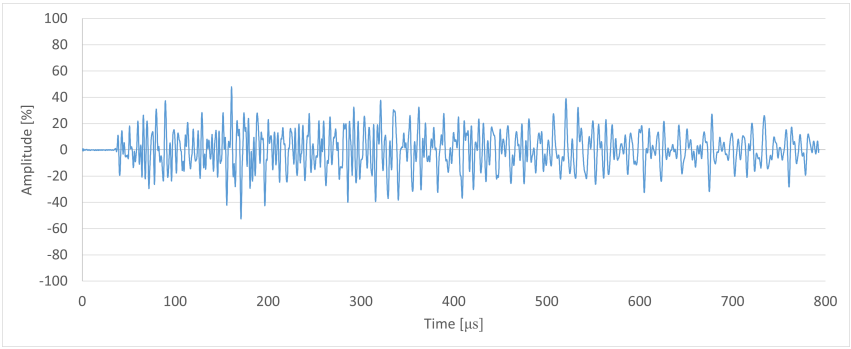

Figure C.5: Recorded signal on vibration plane "x" of S-waves in direction "a" for Absolute Black sample 3 (rough surfaces).

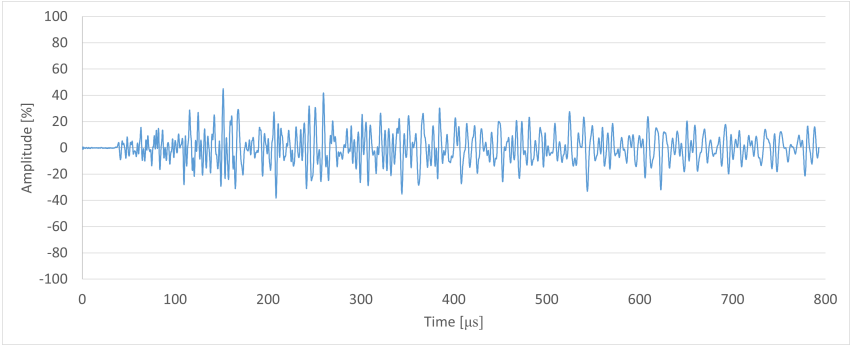

Figure C.6: Recorded signal on vibration plane "z" of S-waves in direction "a" for Absolute Black sample 3 (rough surfaces).

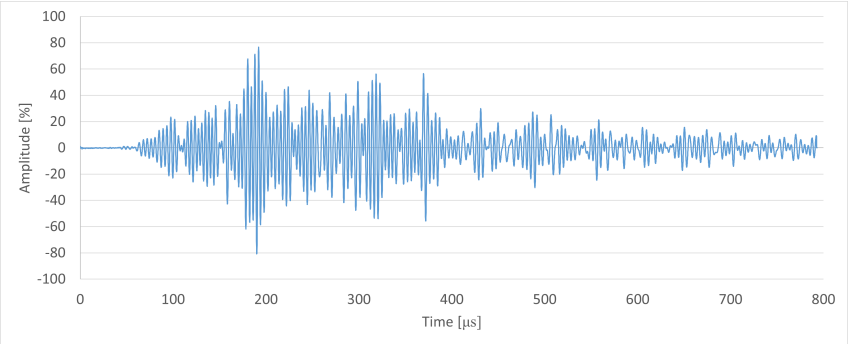

Figure C.7: Recorded signal of P-waves in direction “a” for Syenite sample 1 (rough surfaces).

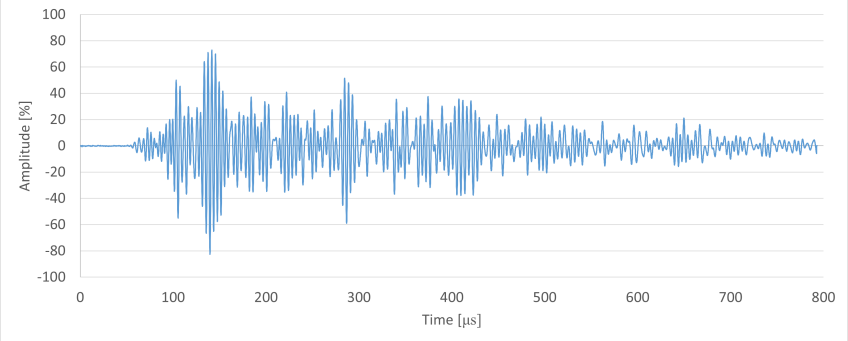

Figure C.8: Recorded signal of P-waves in direction “b” for Syenite sample 1 (flat surfaces).

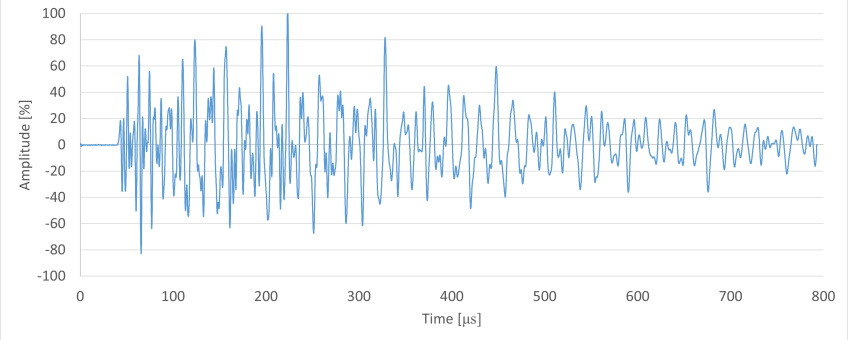

Figure C.9: Recorded signal on vibration plane “x” of S-waves in direction “a” for Syenite sample 1 (rough surfaces).

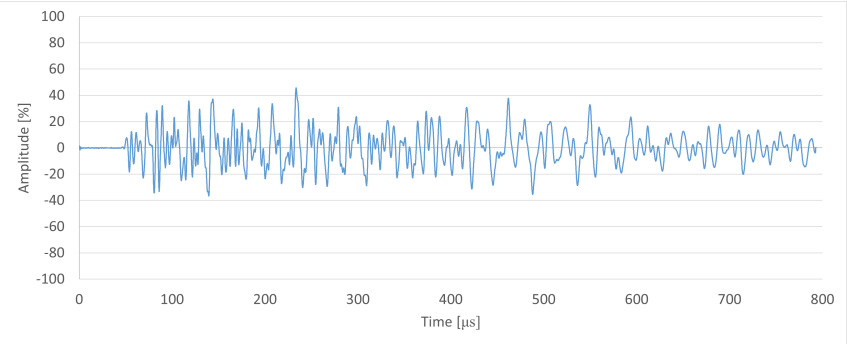

Figure C.10: Recorded signal on vibration plane "x" of S-waves in direction "b" for Syenite sample 1 (flat surfaces).

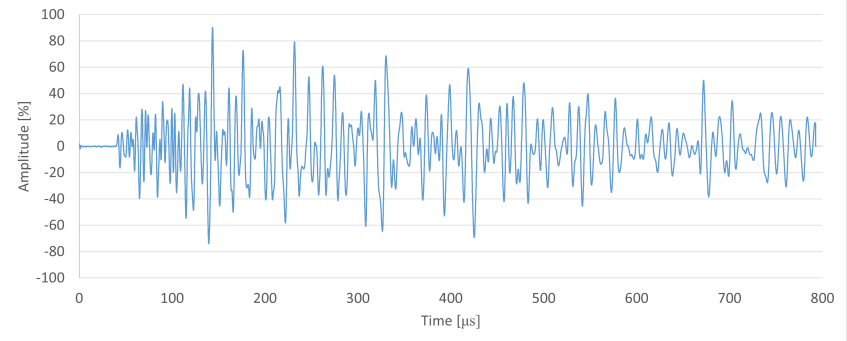

Figure C.11: Recorded signal on vibration plane "z" of S-waves in direction "a" for Syenite sample 1 (rough surfaces).

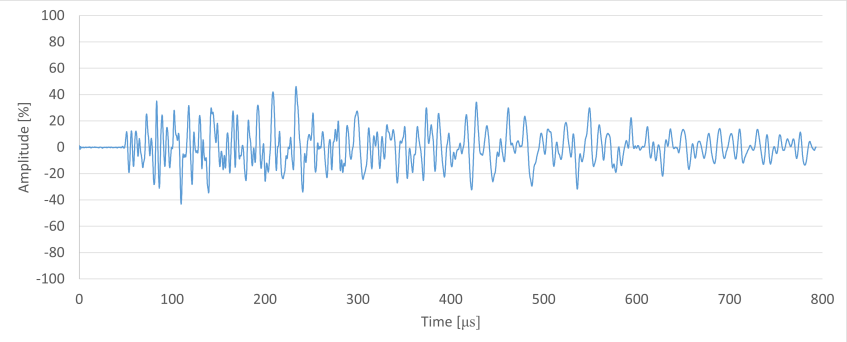

Figure C.12: Recorded signal on vibration plane "z" of S-waves in direction "b" for Syenite sample 1 (flat surfaces).

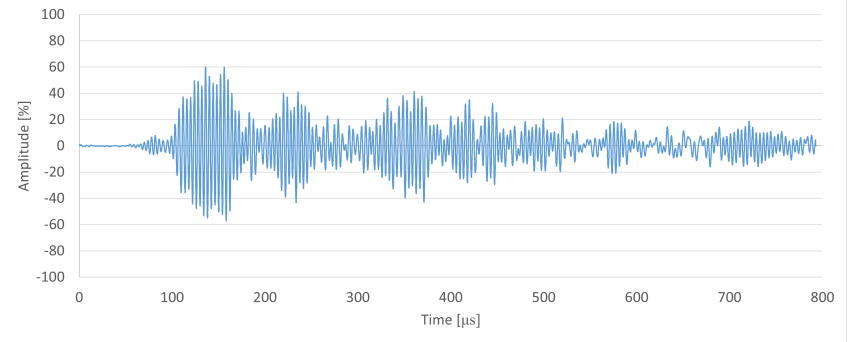

Figure C.13: Recorded signal of P-waves in direction "a" for Syenite sample 2 (rough surfaces).

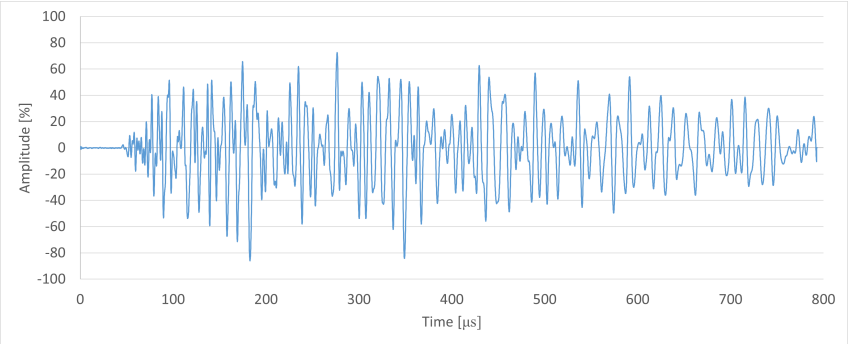

Figure C.14: Recorded signal on vibration plane "x" of S-waves in direction "a" for Syenite sample 2 (rough surfaces).

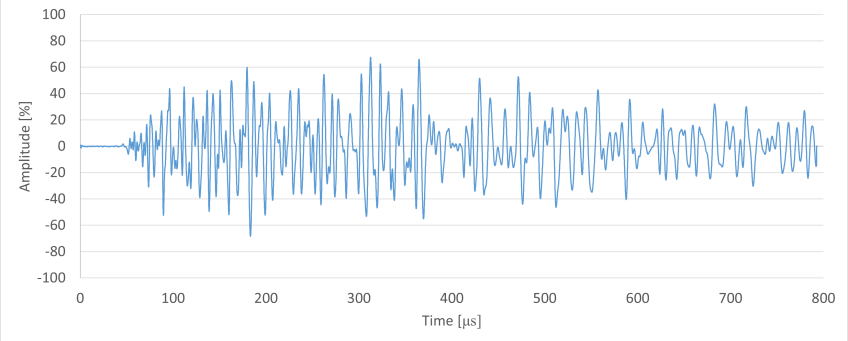

Figure C.15: Recorded signal on vibration plane "z" of S-waves in direction "a" for Syenite sample 2 (rough surfaces).

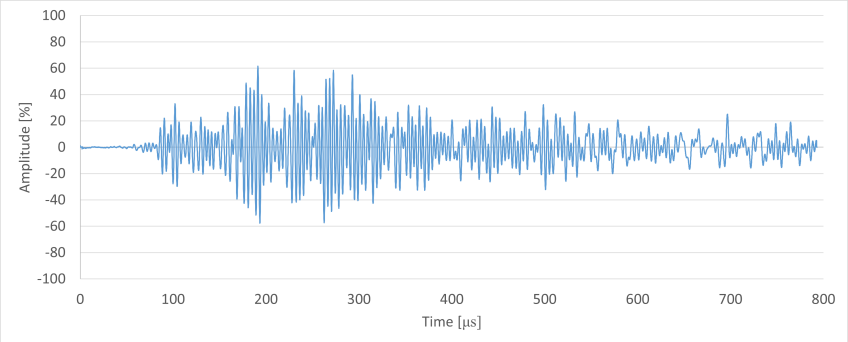

Figure C.16: Recorded signal of P-waves in direction "a" for Syenite sample 3 (rough surfaces).

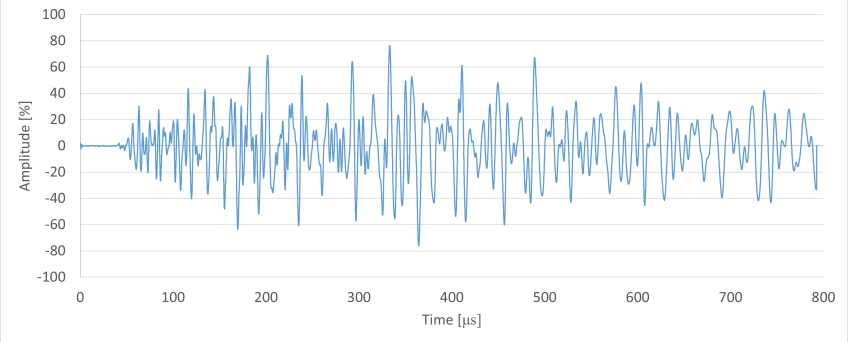

Figure C.17: Recorded signal on vibration plane "x" of S-waves in direction "a" for Syenite sample 3 (rough surfaces).

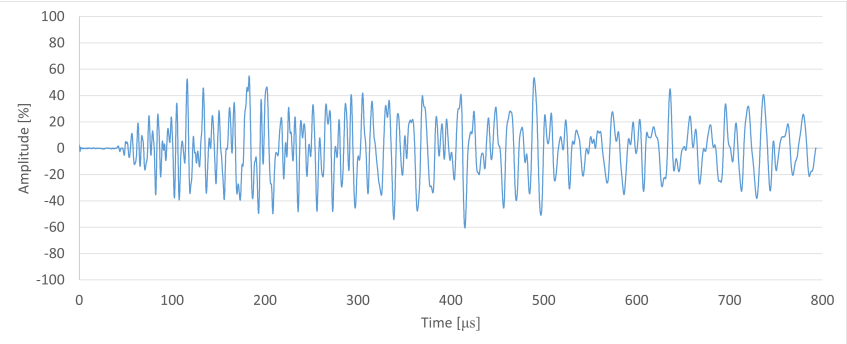

Figure C.18: Recorded signal on vibration plane "z" of S-waves in direction "a" for Syenite sample 3 (rough surfaces).

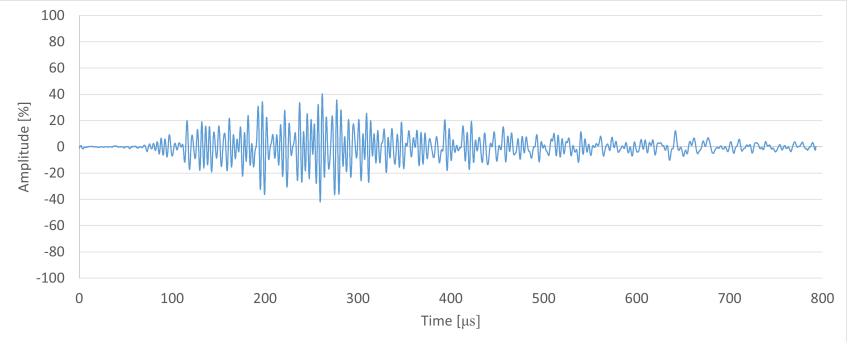

Figure C.19: Recorded signal of P-waves in direction "a" for Porriño sample 1 (rough surfaces).

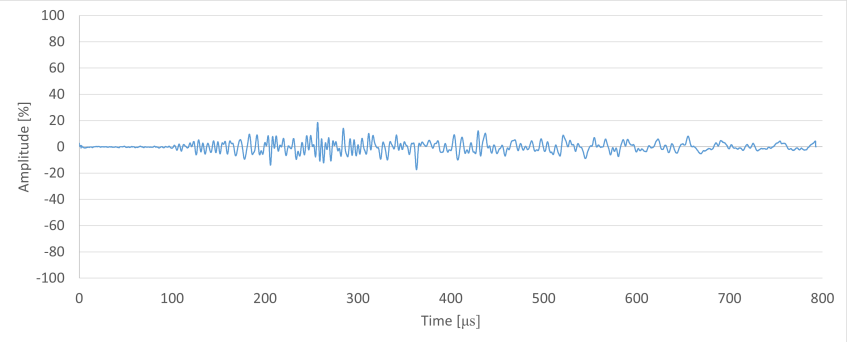

Figure C.20: Recorded signal of P-waves in direction "b" for Porriño sample 1 (flat surfaces).

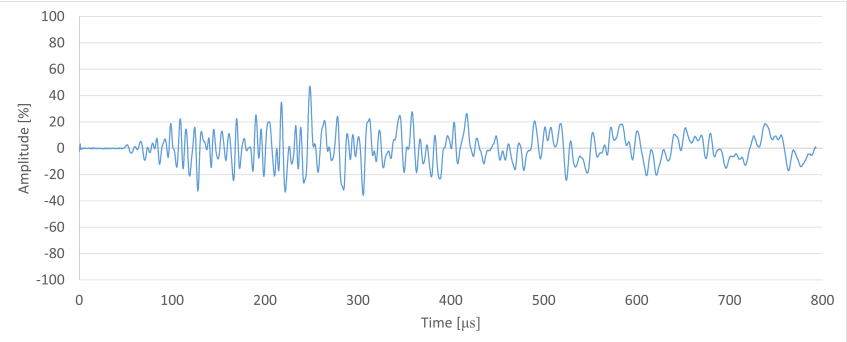

Figure C.21: Recorded signal on vibration plane "x" of S-waves in direction "a" for Porriño sample 1 (rough surfaces).

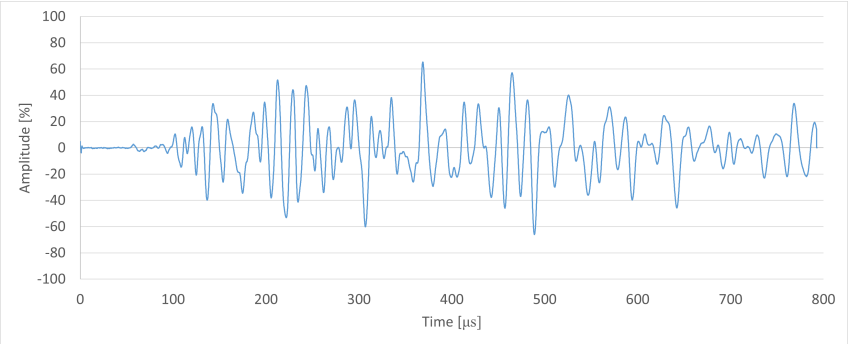

Figure C.22: Recorded signal on vibration plane "x" of S-waves in direction "b" for Porriño sample 1 (flat surfaces).

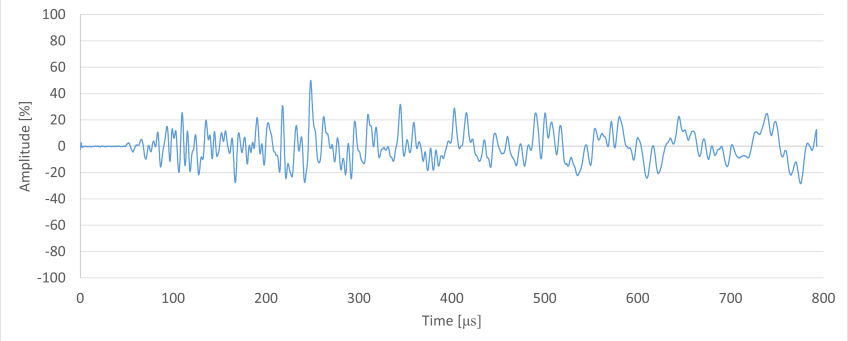

Figure C.23: Recorded signal on vibration plane "z" of S-waves in direction "a" for Porriño sample 1 (rough surfaces).

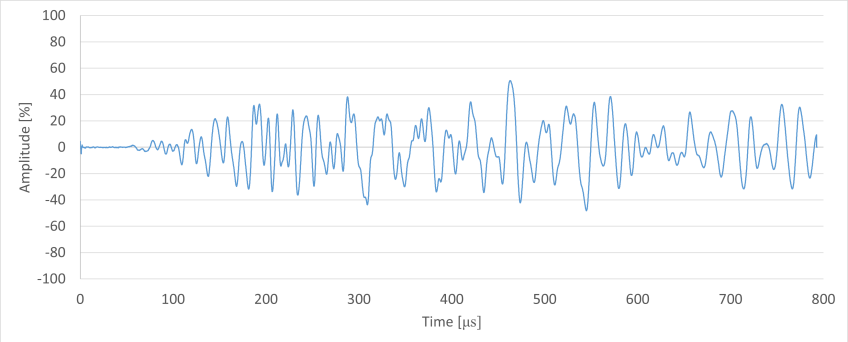

Figure C.24: Recorded signal on vibration plane "z" of S-waves in direction "b" for Porriño sample 1 (flat surfaces).

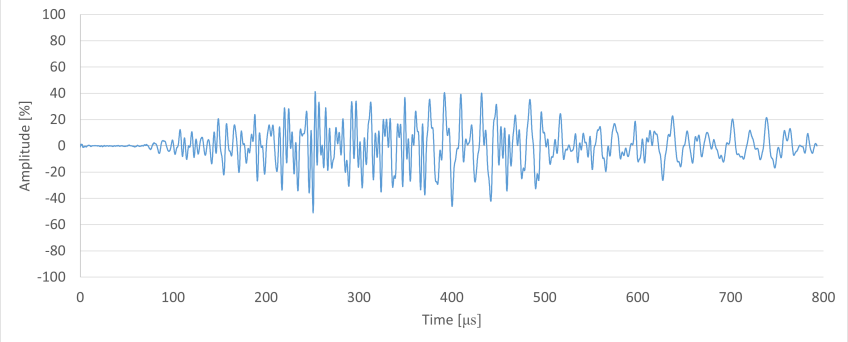

Figure C.25: Recorded signal of P-waves in direction "a" for Porriño sample 2 (rough surfaces).

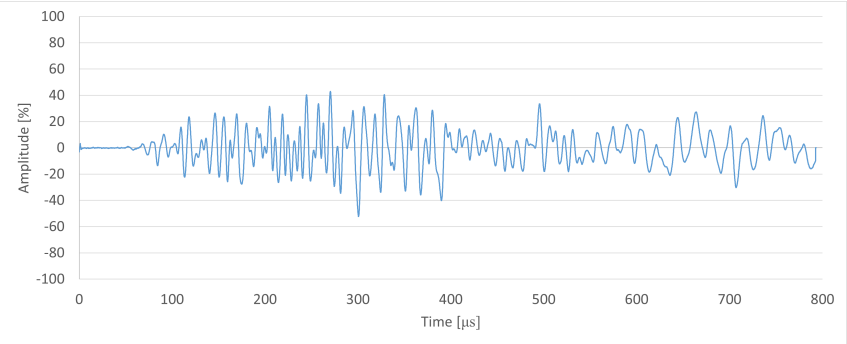

Figure C.26: Recorded signal on vibration plane "x" of S-waves in direction "a" for Porriño sample 2 (rough surfaces).

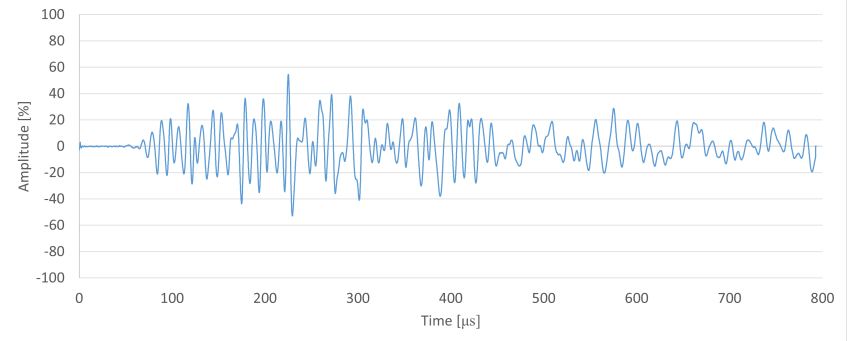

Figure C.27: Recorded signal on vibration plane "z" of S-waves in direction "a" for Porriño sample 2 (rough surfaces).

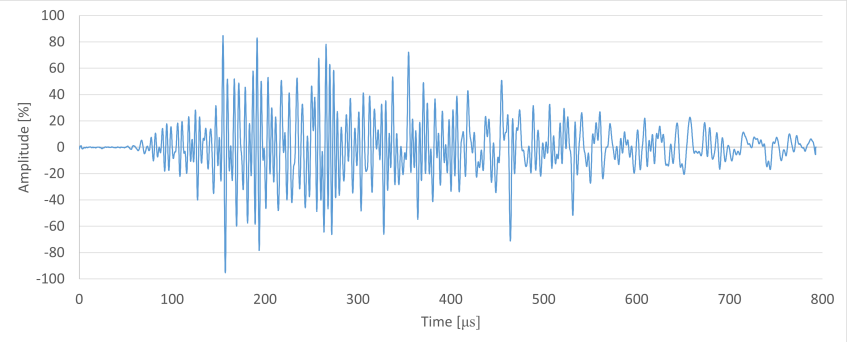

Figure C.28: Recorded signal of P-waves in direction "a" for Porriño sample 3 (rough surfaces).

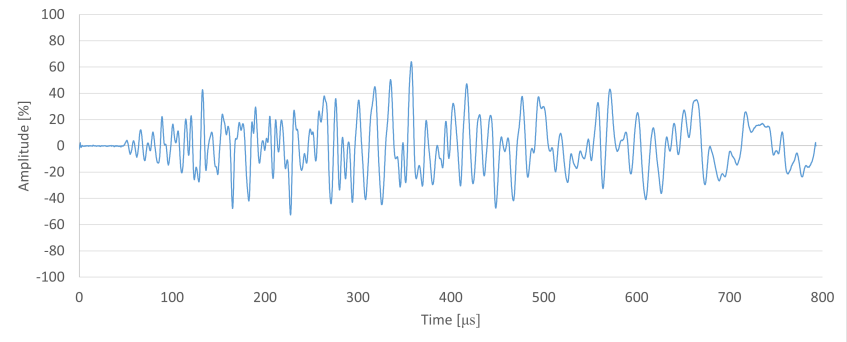

Figure C.29: Recorded signal on vibration plane "x" of S-waves in direction "a" for Porriño sample 3 (rough surfaces).

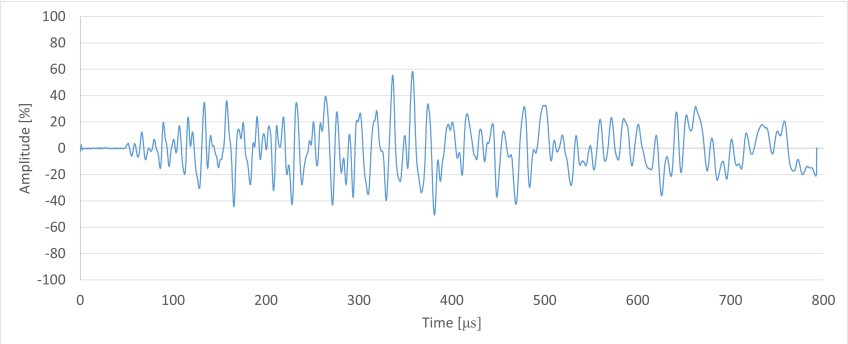

Figure C.30: Recorded signal on vibration plane "z" of S-waves in direction "a" for Porriño sample 3 (rough surfaces).

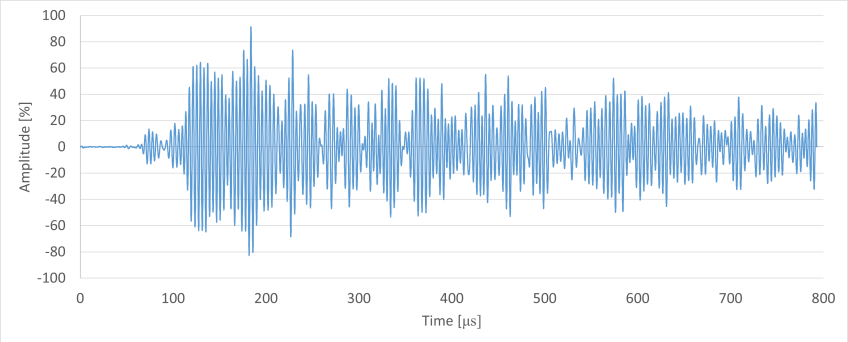

Figure C.31: Recorded signal of P-waves in direction "a" for Carrara sample 1 (rough surfaces).

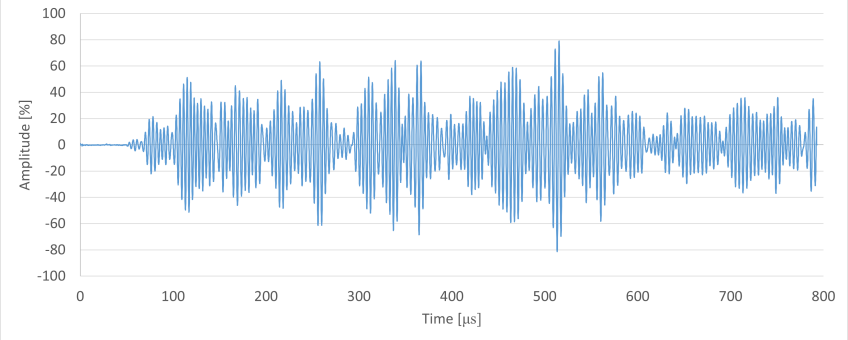

Figure C.32: Recorded signal of P-waves in direction "b" for Carrara sample 1 (flat surfaces).

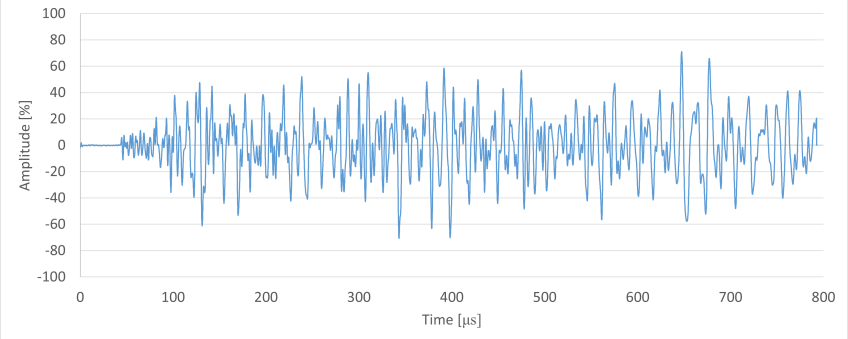

Figure C.33: Recorded signal on vibration plane "x" of S-waves in direction "a" for Carrara sample 1 (rough surfaces).

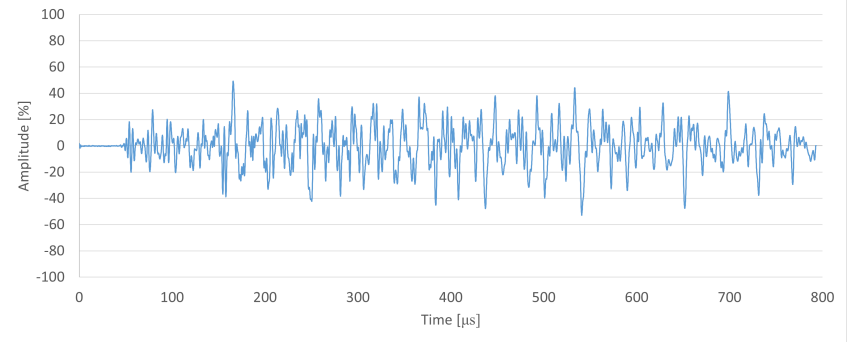

Figure C.34: Recorded signal on vibration plane "x" of S-waves in direction "b" for Carrara sample 1 (flat surfaces).

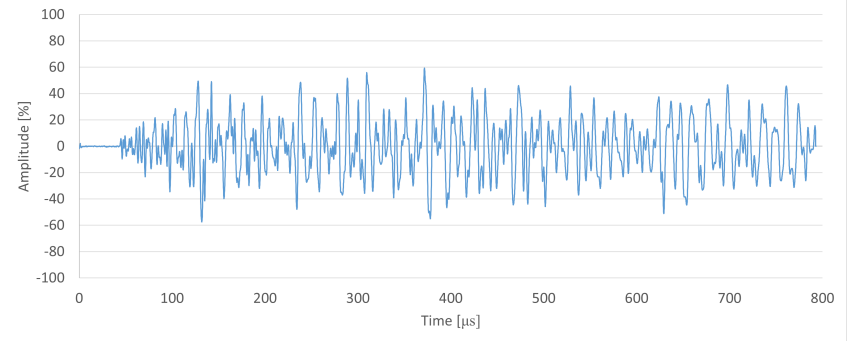

Figure C.35: Recorded signal on vibration plane "z" of S-waves in direction "a" for Carrara sample 1 (rough surfaces).

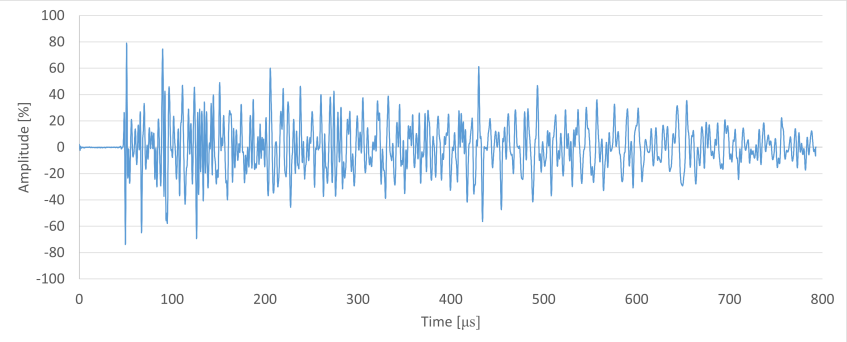

Figure C.36: Recorded signal on vibration plane "z" of S-waves in direction "b" for Carrara sample 1 (flat surfaces).

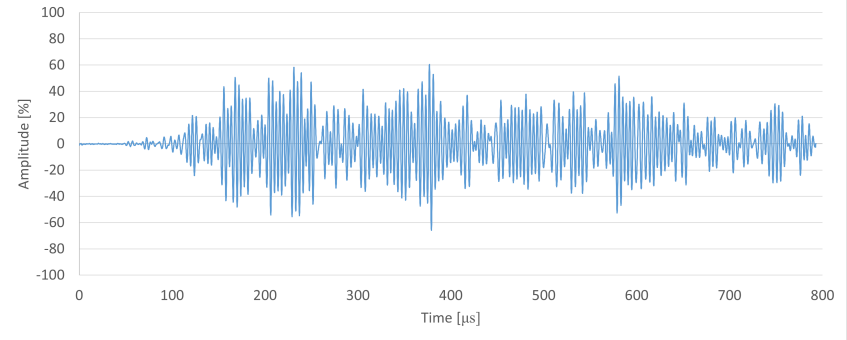

Figure C.37: Recorded signal of P-waves in direction "a" for Carrara sample 2 (rough surfaces).

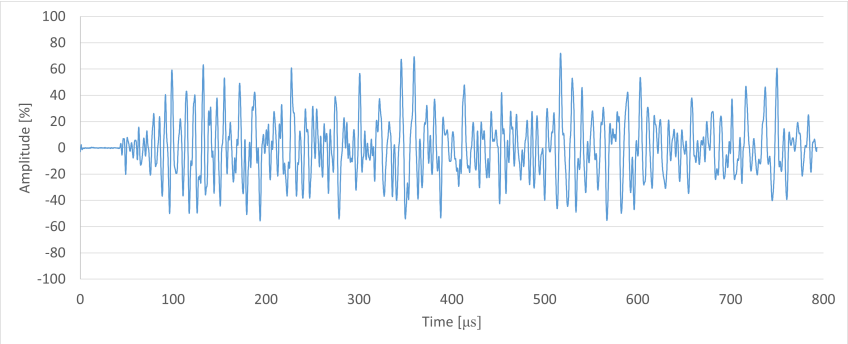

Figure C.38: Recorded signal on vibration plane "x" of S-waves in direction "a" for Carrara sample 2 (rough surfaces).

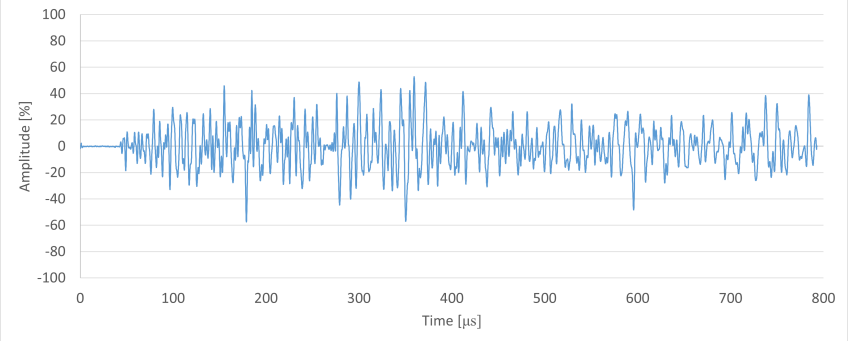

Figure C.39: Recorded signal on vibration plane "z" of S-waves in direction "a" for Carrara sample 2 (rough surfaces).

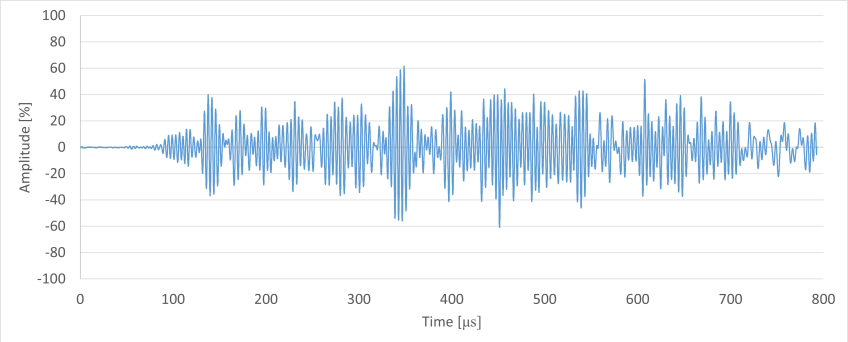

Figure C.40: Recorded signal of P-waves in direction "a" for Carrara sample 3 (rough surfaces).

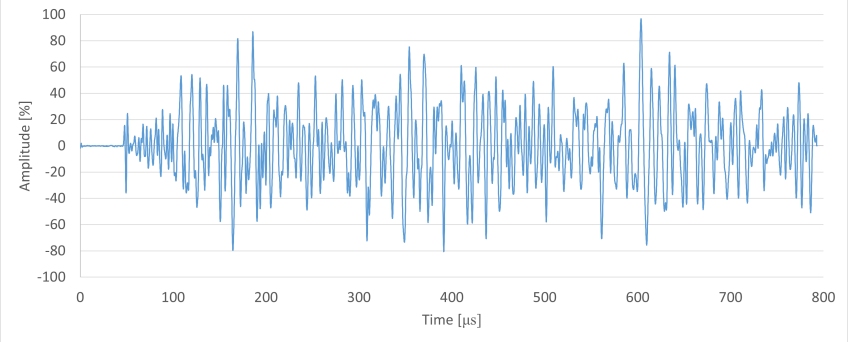

Figure C.41: Recorded signal on vibration plane "x" of S-waves in direction "a" for Carrara sample 3 (rough surfaces).

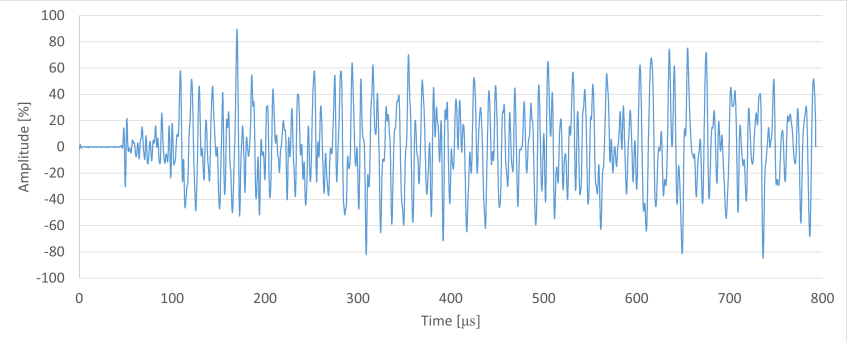

Figure C.42: Recorded signal on vibration plane “z” of S-waves in direction “a” for Carrara sample 3 (rough surfaces).

Appendix D

Mineralogical composition

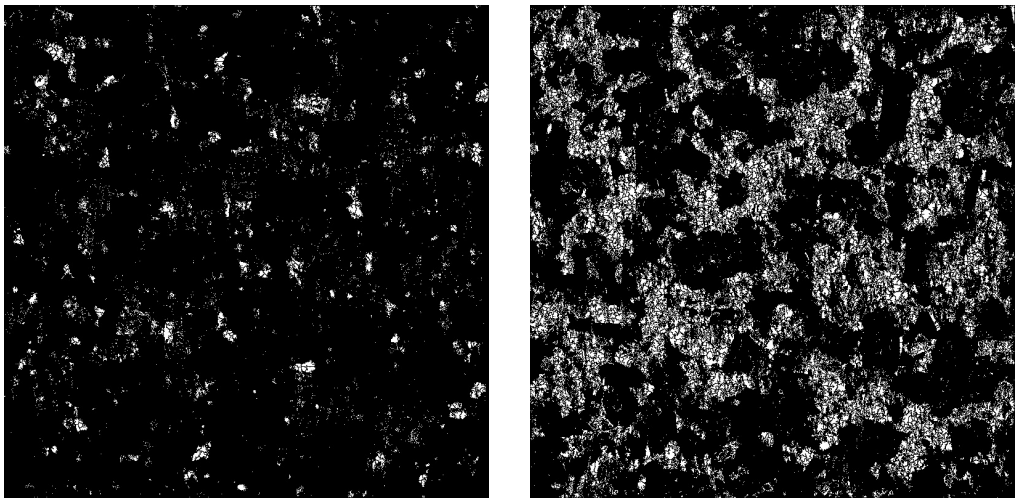

(a)

(b)

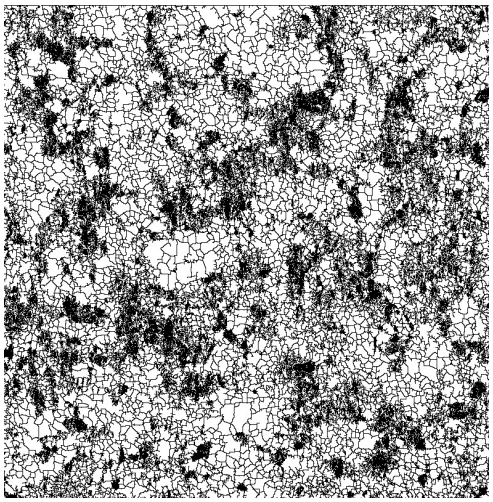

(c)

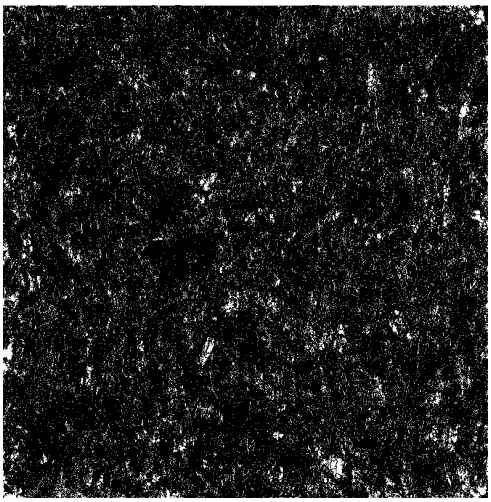

(d)

Figure D.1: Color extraction using ImageJ of Porriño sample 2. Fracture surface. (a) black; (b) grey; (c) pink; (d) white.

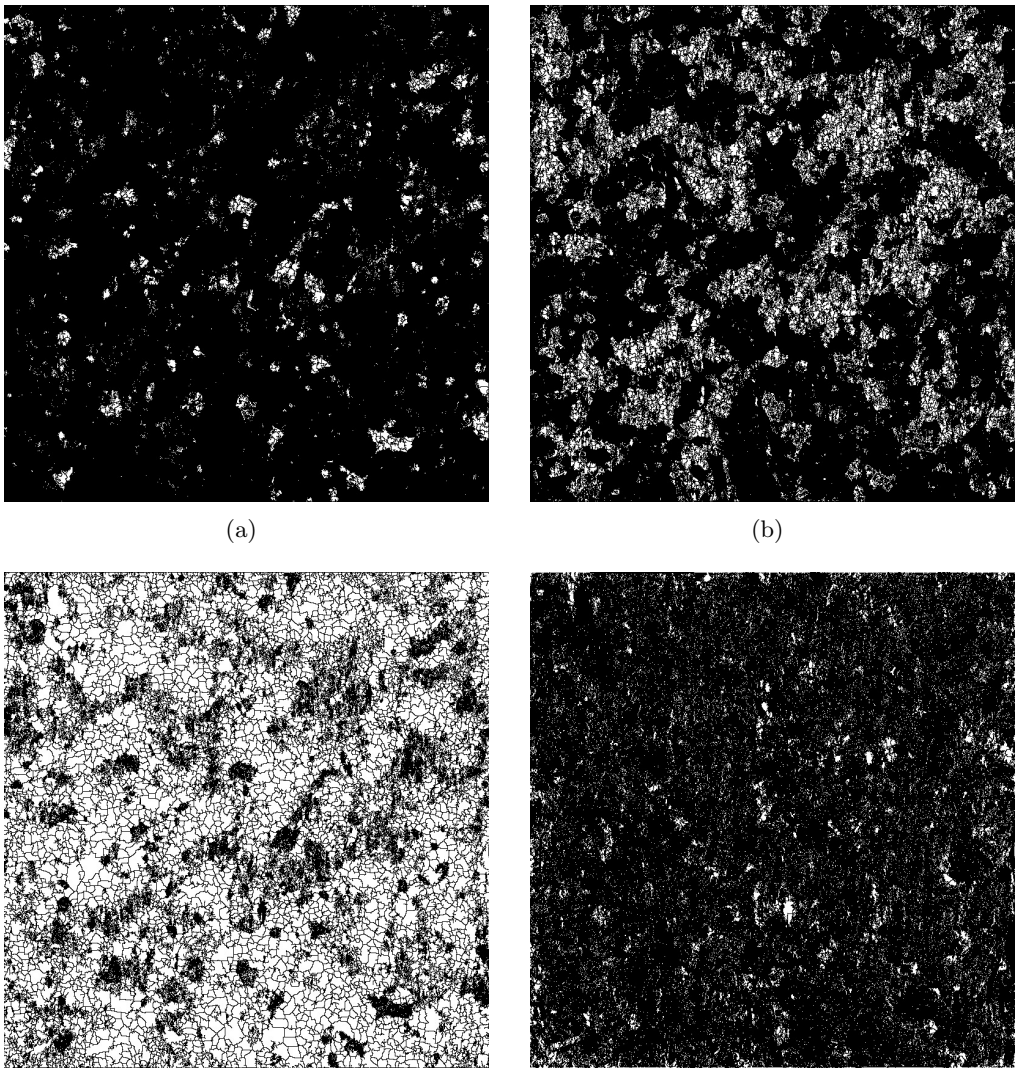

(a) (b)

(c) (d)

Figure D.2: Color extraction using ImageJ of Porriño sample 3. Fracture surface. (a) black; (b) grey; (c) pink; (d) white.

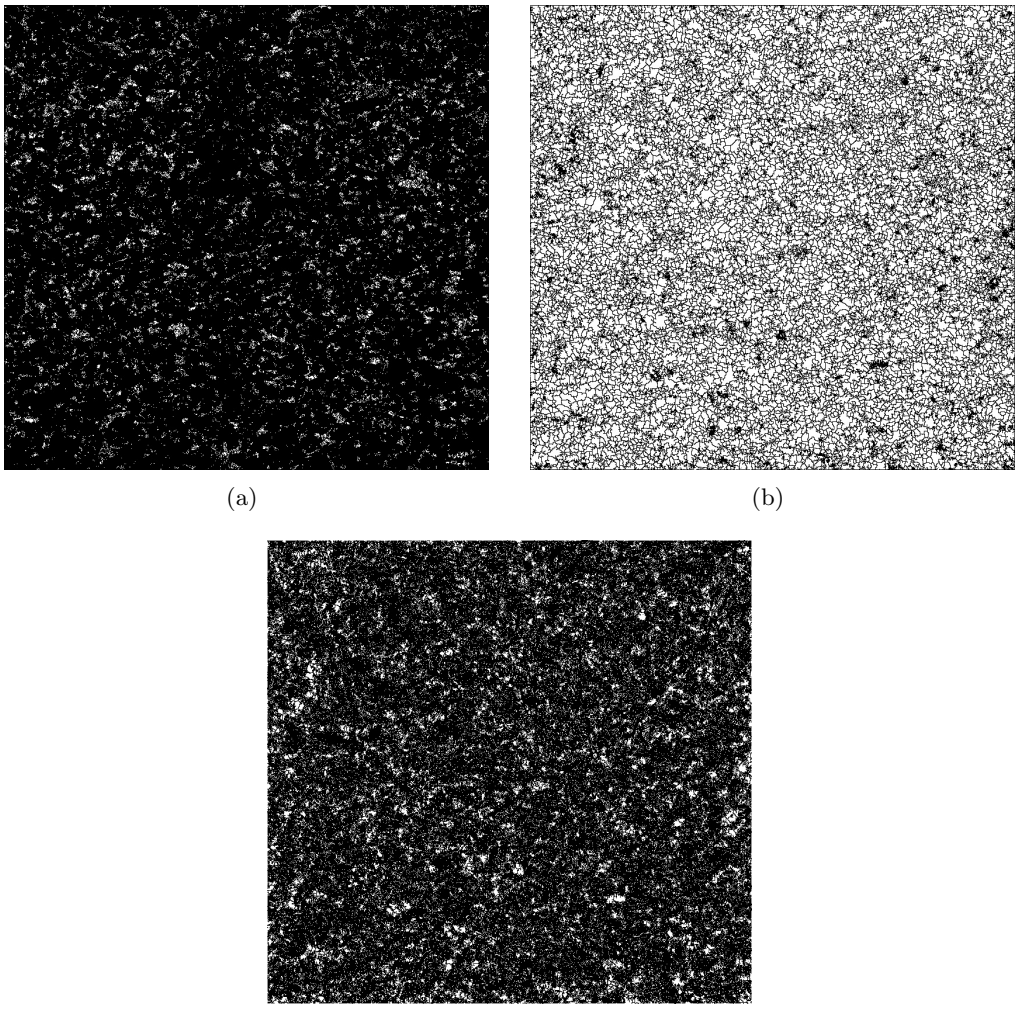

(a) (b)

(c)

Figure D.3: Color extraction using ImageJ of the Syenite sample 1. Fracture surface. (a) black; (b) grey; (c) pink; (d) white.

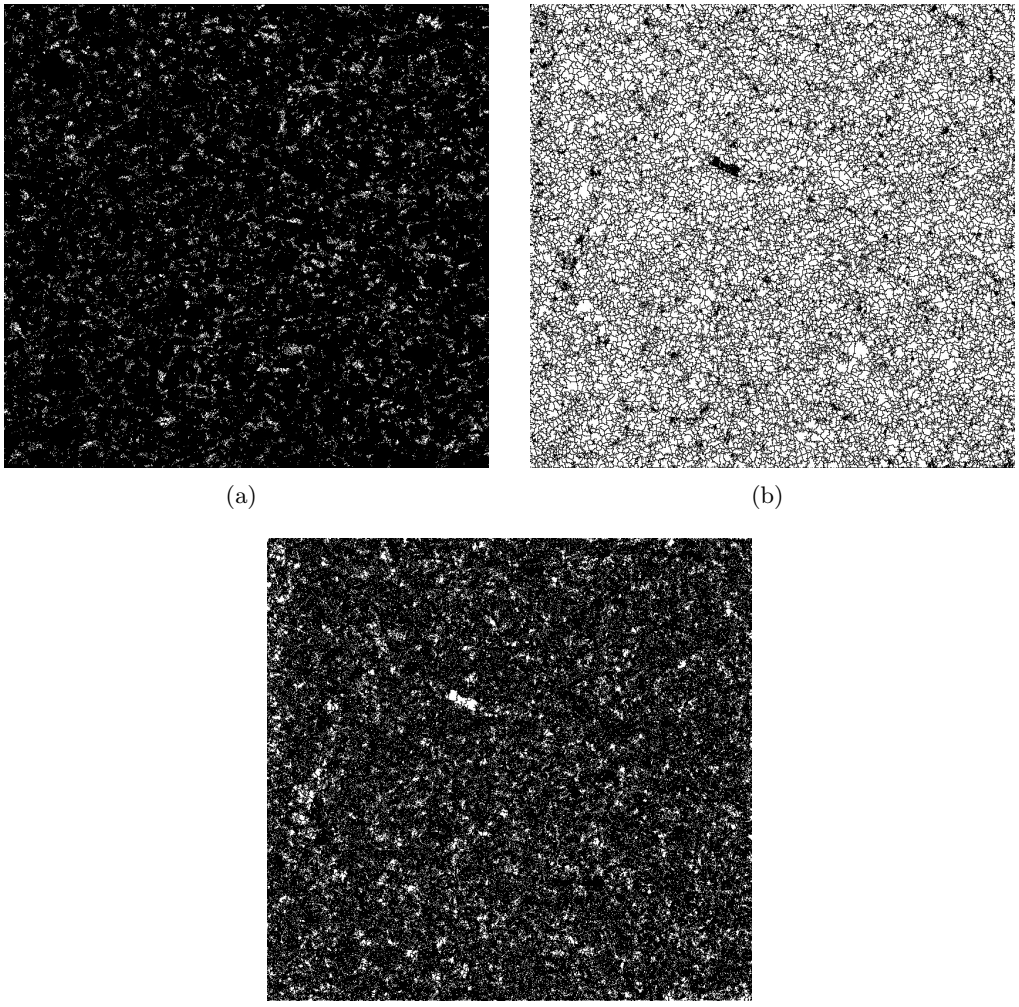

(a) (b)

(c)

Figure D.4: Color extraction using ImageJ of the Syenite sample 1. Fracture surface. (a) black; (b) grey; (c) pink; (d) white.